SYNTHESIS, CHARACTERISATION AND ADSORPTION PROPERTIES OF METAL-ORGANIC FRAMEWORKS AND THE STRUCTURAL RESPONSE TO FUNCTIONALISATION AND TEMPERATURE

John Patrick Stephen Mowat

A Thesis Submitted for the Degree of PhD
at the
University of St. Andrews

2012

Please use this identifier to cite or link to this item:
http://hdl.handle.net/10023/3195

Synthesis, Characterisation and Adsorption Properties of Metal-Organic Frameworks and the Structural Response to Functionalisation and Temperature.

University
of
St Andrews

A thesis presented for the degree of

Doctor of Philosophy

In the Faculty of Science of the University of St. Andrews

By John Patrick Stephen Mowat MChem (Hons)

July 2012

1. Candidate’s declarations:

I, John Mowat, hereby certify that this thesis, which is approximately 49,500 words in length, has been written by me, that it is the record of work carried out by me and that it has not been submitted in any previous application for a higher degree.

I was admitted as a research student in October, 2008 and as a candidate for the degree of *Doctor of Philosophy* in October, 2009; the higher study for which this is a record was carried out in the University of St Andrews between 2008 and 2012.

Date …………………… signature of candidate ………………………………

2. Supervisor’s declaration:

I hereby certify that the candidate has fulfilled the conditions of the Resolution and Regulations appropriate for the degree of *Doctor of Philosophy* in the University of St Andrews and that the candidate is qualified to submit this thesis in application for that degree.

Date …………………… signature of supervisor ………………………………

3. Permission for electronic publication: (*to be signed by both candidate and supervisor*)

In submitting this thesis to the University of St Andrews I understand that I am giving permission for it to be made available for use in accordance with the regulations of the University Library for the time being in force, subject to any copyright vested in the work not being affected thereby. I also understand that the title and the abstract will be published, and that a copy of the work may be made and supplied to any bona fide library or research worker, that my thesis will be electronically accessible for personal or research use unless exempt by award of an embargo as requested below, and that the library has the right to migrate my thesis into new electronic forms as required to ensure continued access to the thesis. I have obtained any third-party copyright permissions that may be required in order to allow such access and migration, or have requested the appropriate embargo below.

Date …………… signature of candidate ………………… signature of supervisor ………………

The following is an agreed request by candidate and supervisor regarding the electronic publication of this thesis:

Access to printed copy and electronic publication of thesis through the University of St Andrews.

Abstract

The synthesis of a scandium aluminium methylphosphonate $ScAl_3(CH_3PO_3)_6$ isostructural to the aluminium methylphosphonate AlMePO-α and with permanent microporosity is reported here for the first time. Structural characterisation of three lanthanide bisphosphonate structures (I,II,III) with the light lanthanides and N,N′-piperazine bis-(methylenephosphonic acid) and its 2-methyl and 2,5-dimethyl derivatives is described. The framework of structure type I shows considerable flexibility upon dehydration with a symmetry change from *C2/c*, a = 23.5864(2) Å, b = 12.1186(2) Å, c = 5.6613(2) Å, β = 93.040(2)°) in the hydrated state to $P2_1/n$, a = 21.8361(12) Å, b = 9.3519(4) Å, c = 5.5629(3) Å, β = 96.560(4)° after dehydration. This cell volume reduces by 27% on dehydration and is accompanied by a change in the conformation of the piperazine ring from chair to boat configuration. The structures of type I (hydrated and dehydrated) were refined against synchrotron powder X-ray diffraction data. Despite the reversible hydration and flexibility, the structures possess no permanent porosity.

Investigation of the solvothermal chemistry of scandium carboxylates identified routes to 7 framework structures 5 of which were previously unreported in the scandium system. Lower temperature solvothermal reactions using terephthalic acid (80 - 140°C using dimethylformamide and diethylformamide) yielded two scandium terephthalates, MIL-88B(Sc) and MIL-101(Sc), identified by laboratory X-ray powder diffraction. Whereas higher temperature (160 – 220°C), reactions gave MIL-53(Sc) and Sc_2BDC_3. Further study with the tri- and tetra-carboxylate linkers, trimesic acid, 3,3′,5,5′-azobenzenetetracarboxylic acid and pyromellitic acid yielded MIL-100(Sc), Sc-ABTC and Sc_4PMA_3 respectively. Structural identification of MIL-100(Sc) and Sc-ABTC was performed by means of X-ray powder diffraction analysis and of Sc_4PMA_3 by single crystal X-ray diffraction.

The structure of a small pore scandium terephthalate Sc_2BDC_3 was investigated as a function of temperature and of functionalization. *In situ* synchrotron X-ray diffraction data, collected on a Sc_2BDC_3 *in vacuo*, enabled a phase change from orthorhombic *Fddd* to monoclinic *C2/c* and the associated structural effects to be observed in detail. The orthorhombic structure displayed a negative thermal expansivity of 2.4×10^{-5} K^{-1} over the temperature range 225 – 523 K which Rietveld analysis showed to be derived from carboxylate group rotation. Motion within the framework was studied by ^2H wide-line and MAS NMR on deuterated Sc_2BDC_3 indicating π flips can occur in the phenyl rings above 298 K. The effects of functionalization on the Sc_2BDC_3 framework were investigated by reactions using the 2-amino- and 2-nitroterephthalic acid and gave evidence for a strong structural effect resulting from inclusion of the functional groups.

The structure of Sc_2BDC_3 and the functionalised derivatives were solved using Rietveld analysis on synchrotron X-ray powder diffraction data. $Sc_2(NH_2\text{-}BDC)_3$ was solved using the orthorhombic Sc_2BDC_3 framework starting model and, over the temperature range studied, stayed orthorhombic *Fddd*. $Sc_2(NO_2\text{-}BDC)_3$, was shown to be monoclinic *C2/c* over the same temperature range, a result of the steric effects of the bulky $–NO_2$ group in a small pore framework. Partial ordering of the functional groups was observed in both $Sc_2(NH_2\text{-}BDC)_3$ and $Sc_2(NO_2\text{-}BDC)_3$. The strength of interaction for the $Sc_2(NH_2\text{-}BDC)_3$ with CO_2 was higher than that of the parent Sc_2BDC_3 due to the strong $–NH_2\cdots CO_2$ interaction. Despite the inclusion of a relatively large $–NO_2$ group along the walls of a channel ~4 Å in diameter the $Sc_2(NO_2\text{-}BDC)_3$ still showed permanent microporosity to CO_2 (2.6 mmol g^{-1}) suggesting that there must be some motion in the $-NO_2$ group to allow the CO_2 molecules to diffuse through the channels.

The scandium analogue of the flexible terephthalate MIL-53, a competitive phase in the synthesis of Sc_2BDC_3, was prepared and characterised by Rietveld analysis on synchrotron X-ray powder diffraction data using a combination of literature structural models and models obtained from single crystal X-ray diffraction experiments. Experimental solid state ^{45}Sc, ^{13}C and ^{1}H NMR data combined with NMR calculations on the structural models produced from diffraction analysis were used to identify the hydrated (MIL-53(Sc)-H_2O), calcined (MIL-53(Sc)-CAL) and high temperature (MIL-53(Sc)-HT) structures of MIL-53(Sc). Further to this the 2-nitroterephthalate derivative, MIL-53(Sc)-NO_2, was prepared and characterised using single crystal X-ray diffraction. The adsorptive properties of the parent terephthalate and the functionalised derivative were compared and in both cases showed a breathing behaviour, exemplified by steps in the adsorption isotherms. MIL-53(Sc)-CAL was found to possess a closed pore configuration in the dehydrated state, a previously unreported structural form for the MIL-53 series, and its presence can be observed in the low pressure region of the CO_2 adsorption isotherm as a non-porous plateau.

The selectivity and separation properties of two MOFs, the nickel bisphosphonate, STA-12(Ni) and the scandium carboxylate, Sc_2BDC_3 were measured using breakthrough curves on mixtures of CH_4 and CO_2. The results showed both materials to be highly selective in the adsorption of CO_2 over CH_4. Column testing using a PLOT column of STA-12(Ni) and a packed column of Sc_2BDC_3 showed promising preliminary results with STA-12(Ni) displaying effective, baseline separation on low boiling point hydrocarbon mixtures (C_1 – C_4) while the smaller pore channels of Sc_2BDC_3 were effective in the size selective separation of higher boiling point branched and straight-chain hydrocarbons (C_5 – C_7).

Acknowledgments

First and foremost I would like to thank my supervisor, Professor Paul Wright, for his supervision from my undergraduate studies through to the opportunity to carry out this research. His knowledge, support and enthusiasm has been exceptional and the major factor in the success of this work. One could not ask for more from a supervisor.

I would also like to thank all the collaborators with whom I have worked throughout this project, their expertise and contribution to this work has been invaluable. I thank Dr. Stuart Miller for his friendship, guidance and mentoring, and for his work that formed a basis for this study. I am grateful to Dr. Sharon Ashbrook, Dr. John Griffin and Valerie Seymour for their prompt and thorough collection and analysis of solid-state NMR data. I thank Professor Alex Slawin and Dr. Stephen Moggach for their help and support with crystallography. For their help and support in the computer simulation of adsorption, I thank Dr. David Fairen-Jimenez, Dr. Tina Düren and Ana-Maria Banu. Mrs Sylvia Williamson is thanked for the collection of adsorption and thermal analysis data and for training on how to use on the instruments.

My thanks also go to all friends and colleagues within the Chemistry department including Charlotte Jones, Magdalena Lozinska, Juergen Kahr, Lewis Downie, Cameron Black, Laura Mitchell, members of the Wright group with special thanks to Michael Wharmby for proof-reading and generally bouncing ideas off. Beyond Chemistry, I would like to thank my best friend (and best man) David Armstrong and all the friends who made University an enjoyable and memorable experience with special thanks to William Barber, Barry Barkey and Damien Phillips.

Most importantly, I thank my wife Catherine for her love, support and encouragement without which, this thesis would not have been possible.

Finally I thank my parents, Philip and Deirdre Mowat, for their love and support throughout this project and my education as a whole and my Gran, Dorothy Mowat, for making me the person I am today and who will never be forgotten.

Dedication

This thesis is dedicated to my Gran, Dorothy Mowat (1918 - 2010) whose contribution to my life will be felt forever.

Publications arising from this work

1. *Lanthanide N,N'-piperazine-bis(methylenephosphonates) (Ln = La, Ce, Nd) that display flexible frameworks, reversible hydration and cation exchange*. John P. S. Mowat, John A . Groves, Michael T. Wharmby, Stuart R. Miller, Yang Li, Philip Lightfoot and Paul A. Wright. Journal of Solid State Chemistry, 182, 2009, 2769-2778.

2. *Synthesis and crystal chemistry of the STA-12 family of metal N,N'-piperazinebis(methylenephosphonate)s and applications of STA-12(Ni) in the separation of gases.* Michael T. Wharmby, Gordon M. Pearce, John P.S. Mowat, John M. Griffin, Sharon E. Ashbrook, Paul A. Wright, Lars-Hendrik Schilling, Alexandra Lieb, Norbert Stock, Sachin Chavan, Silvia Bordiga, Edder Garcia, Gerhard Pirngruber, Martin Vreeke, and Leszek Gora., Microporous and Mesoporous Materials, 2011, article in press, DOI: 10.1016/j.micromeso.2011.12.003

3. *Synthesis, characterisation and adsorption properties of microporous scandium carboxylates with rigid and flexible frameworks.* John P. S. Mowat, Stuart R. Miller, Alexandra M. Z. Slawin, Valerie R. Seymour, Sharon E. Ashbrook and Paul A. Wright., Microporous and Mesoporous Materials, 142, 2011, 322-333.

4. *Structural Chemistry, Monoclinic-to-Orthorhombic Phase Transition, and CO_2 Adsorption Behaviour of the Small Pore Scandium Terephthalate, $Sc_2(O_2CC_6H_4CO_2)_3$, and Its Nitro- And Amino-Functionalized Derivatives.* John P. S. Mowat, Stuart R. Miller, John M. Griffin, Valerie R. Seymour, Sharon E. Ashbrook, Stephen P. Thompson, David Fairen-Jimenez, Ana-Maria Banu, Tina Düren, and Paul A. Wright., Inorganic Chemistry, 50, 2011, 10844-10858.

5. *A novel structural form of MIL-53 observed for the scandium analogue and its response to temperature variation and CO_2 adsorption*. John P. S. Mowat, Valerie R. Seymour, John M. Griffin, Stephen P. Thompson, Alexandra M. Z. Slawin, David Fairen-Jimenez, Tina Düren, Sharon E. Ashbrook and Paul A. Wright., Dalton Transactions, 41, 2012, 3937-3941.

Table of Contents

Appendices, attached CD

1 Introduction

1.1 Overview

Porous solids have attracted considerable interest in recent years[1] primarily for applications in gas storage,[2-5] separation and purification.[6-8] In addition, they have been explored for use in a wide variety of other applications including magnetism[9], drug delivery[10] and catalysis.[11] The term porous solids encompasses a wide range of materials including zeolites, zeotypes, porous carbons and, more recently, metal organic frameworks[12] (MOFs), zeolitic imidazolate frameworks[13] (ZIFs) and covalent organic frameworks[14] (COFs). Zeolites, both naturally occurring and synthetic derivatives - in some ways the parent class of materials in porous solids - have many current commercial applications covering a broad range of areas from catalysis,[15] such as cracking of alkanes,[16] to use as adsorbents in household powder detergents.[17]

MOFs have attracted particular interest as adsorbents and have a number of potential advantages over zeolites and porous carbons which are the current industry standard.[18] Traditionally, zeolites have been chosen for their fixed size and adsorption properties[7], leading to use as molecular sieves (size selective process) and in gas separation e.g. N_2/O_2[19,20] (adsorption selective separations).

One of the main advantages of MOF materials over the conventional zeolites and porous carbons is in the tunability of the materials both pre-synthesis[21] and post-synthesis[22,23]. In MOF materials, it is possible to add functional groups, vary the framework forming metal cation and alter the pore size while retaining a particular framework topology, exemplified by the honeycomb-like structure of the isoreticular St. Andrews porous materials, STA-12(Ni)[24] and STA-16(Co)[25] (Figure 1.1). This versatility means that where traditional materials may be limited to a specific type of interaction (e.g. porous carbons are limited to separations involving only anhydrous components), MOF materials can be tuned. For example, a pore system that is delimited by hydrophobic organic linker molecule could be made hydrophilic by addition of an amine group to the linker.

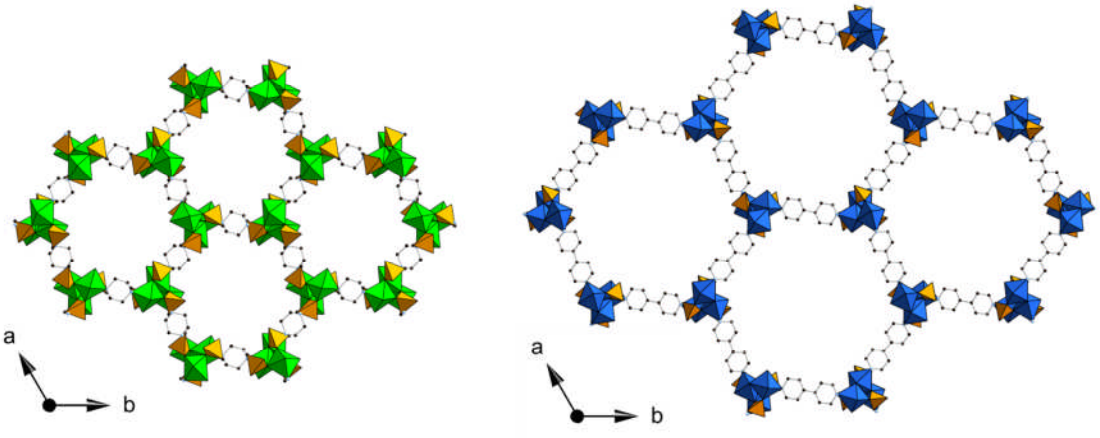

Figure 1.1: View down the hexagonal channels in the honeycomb like pore structure of metal bisphosphonates STA-12(Ni) (left) and STA-16(Co) (right). Metal octahedra are shown in green and blue for nickel and cobalt respectively. Phosphonate tetrahedra are shown in orange and black spheres represent the carbon atoms of the organic linker.

MOF materials, also referred to as hybrid porous solids[12] or coordination polymers,[26] consist of inorganic fragments joined with organic linking molecules (ligands). The inorganic fragments can consist of various different metal environments including isolated polyhedra,[27] clusters,[28] chains[29] and layers[30] which are linked by the organic molecules to form framework materials (Figure 1.2). MOF materials can crystallise over a wide range of particle sizes from microcrystalline powders (< 1 μm^3 particles) up to larger single crystals (> (150 μm)^3). As MOFs are crystalline, the pore systems are well defined throughout the material enabling better reproducibility and uniformity of sorption properties when compared with amorphous porous carbons and silicas.

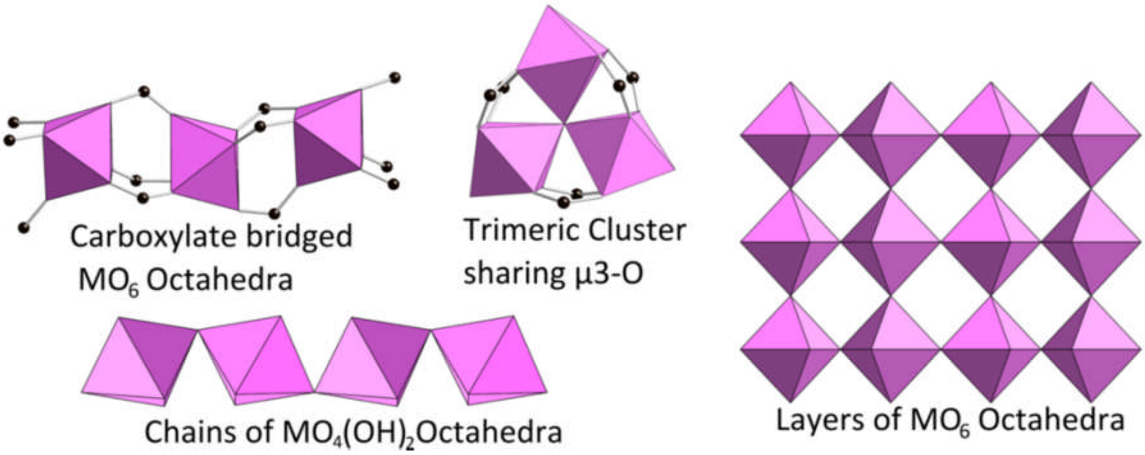

Figure 1.2: Examples of MOF building units. Metal octahedra are shown in pink with the carbon atoms of the carboxylate shown in black.

MOFs tend to be categorised by the type of functional group on the organic linker involved in the framework. The most studied classes are carboxylates, amines, and phosphonates. Ligands which contain the same functional groups but with a different organic connectivity, for example linear dicarboxylates (including benzene-1,4-dicarboxylate, biphenyl-4,4′-dicarboxylate etc.) can lead to a series of isoreticular materials which are topologically identical but the organic linking molecule is extended.[31] This is exemplified by the MOF-5 structure[32] (also referred to as IRMOF-1) and series of related frameworks IRMOFs 2-16[31] where the same $Zn_4O(CO_2)_6$ clusters form the inorganic core, whilst the ligand between the carboxylate groups is varied with retention of the cubic network of channels (Figure 1.3).

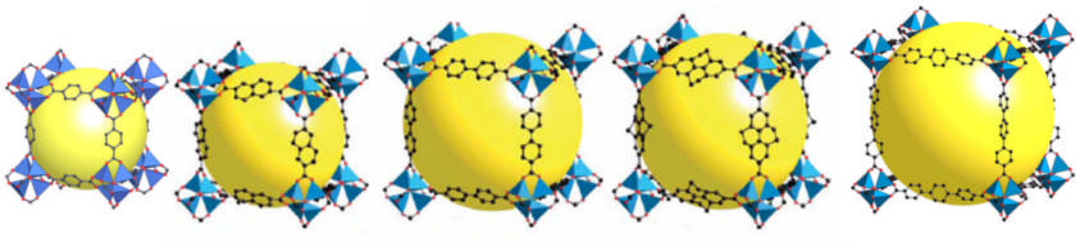

Figure 1.3: IRMOF series including (from left to right) IRMOF-1,8,10, 12 and 16, where the $Zn_4O(CO_2)_6$ clusters are pillared by dicarboxylate linkers of increasing length.[31] Yellow spheres indicate the location of the cavities in the cubic cage.

Another important characteristic of porous solids with regards to adsorption and separation is the surface area. In general, for an adsorbed species, the interaction between the guest species and the surface of an adsorbent is much greater than the guest - guest interaction. A series of isoreticular materials with increasing surface area, but constant host-guest interactions, can adsorb an increased quantity of a given species. MOF materials have reported very high surface areas, for example 4100 m^2g^{-1} for the MIL-101 structure[4] and 4500 m^2g^{-1} for MOF-177[33] which at the time were not only some of the largest surface areas reported for MOF materials but also the highest for all known materials.

One area in which traditional materials still have advantages is in the thermal stability. Zeolites can, in some cases, be heated to temperatures in excess of 1000°C in air without degradation[34] which can allow for applications in the separation (or purification) of gases such as flue gas[35] or high temperature catalysis.[15] MOF materials tend to have significantly lower thermal stability than zeolites but some examples of MOFs with strong metal - ligand bonds and stable organic components have shown thermal stability, in air, greater than 550°C in a porous MOF[27] and over 600°C in a higher density non-porous MOF.[36]

1.2 Zeolites and Zeotypes

The name zeolite is derived from the greek words 'zeo' and 'lithos' translating as boiling stones and was the result of the work by the Swedish mineralogist Axel Fredrick Cronstedt.[37] He observed that a naturally occurring mineral, stilbite, visibly lost water upon heating. Zeolites are crystalline aluminosilicates where the tetrahedral AlO_4 and SiO_4 centres create porous arrangements of rings, channels and cages. An example of a typical zeolite structure (zeolite A) is shown in Figure 1.4.

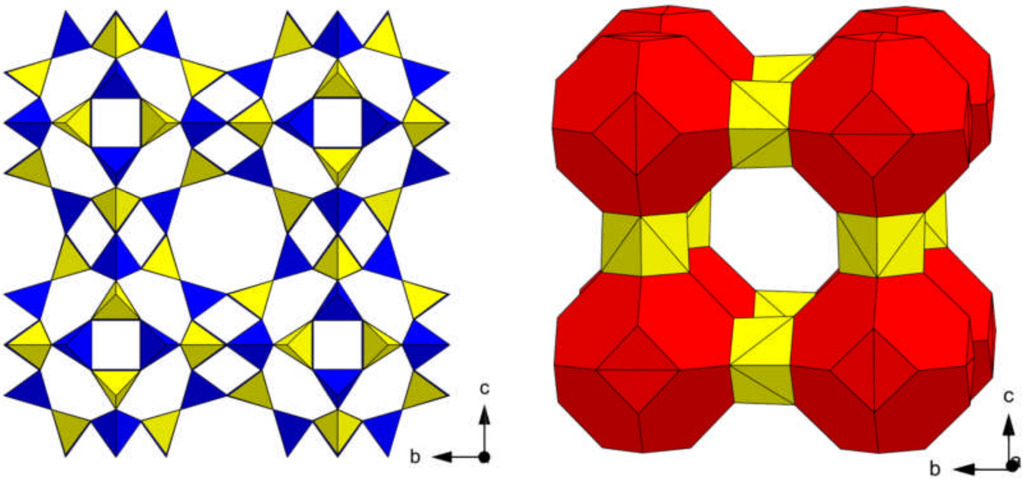

Figure 1.4: Model of a typical zeolite (zeolite A) represented by tetrahedral units *(left)* and using a polyhedral representation of the cages *(right)*. Extra framework water and sodium cations omitted for clarity.[38]

Due to the charges on the cations, Si^{4+} and the Al^{3+}, when aluminium replaces silicon, additional cations must also be present to maintain the overall charge balance with the chemical formula $(M^{n+})_{x/n}(AlO_2)_x(SiO_2)_y \cdot Z(H_2O)$. The additional cations are not present within the framework (lattice) itself but can be involved in the stabilization of intermediate species such as rings and cages during synthesis. These stabilized units form the building units of the material and as such play an important role in the production of synthetic zeolite materials. The first novel zeolite framework was produced in the 1940s by Barrer.[39] This work triggered an explosion of growth in the field and with it the development of industrial applications starting with Union Carbide in the 1950s.

The next major development in porous solids came with the work of Flanigen and co-workers with the synthesis of aluminophosphates (AlPO) during the early 1980s.[40] The introduction of the phosphorus meant that the framework did not need the additional cations to stabilize the charge with the formula unit $(AlO_2)^{-}(PO_2)^{+}$ creating an charge neutral framework. This development was further extended to include many other elements both incorporated into the conventional aluminosilicate frameworks and in the synthesis of novel framework architectures with different chemical compositions, commonly referred to as zeolite-like or zeotype materials.[41]

1.3 Metal Phosphonates and Bisphosphonate MOFs.

1.3.1 AlMePOs

The aluminium methylphosphonates AlMePO-α and AlMePO-β structures (Figure 1.5) reported by Maeda and co-workers[42,43] were an early example of aluminium organophosphonates and were shown to demonstrate porosity comparable to zeolites such as ZSM-5.[44]

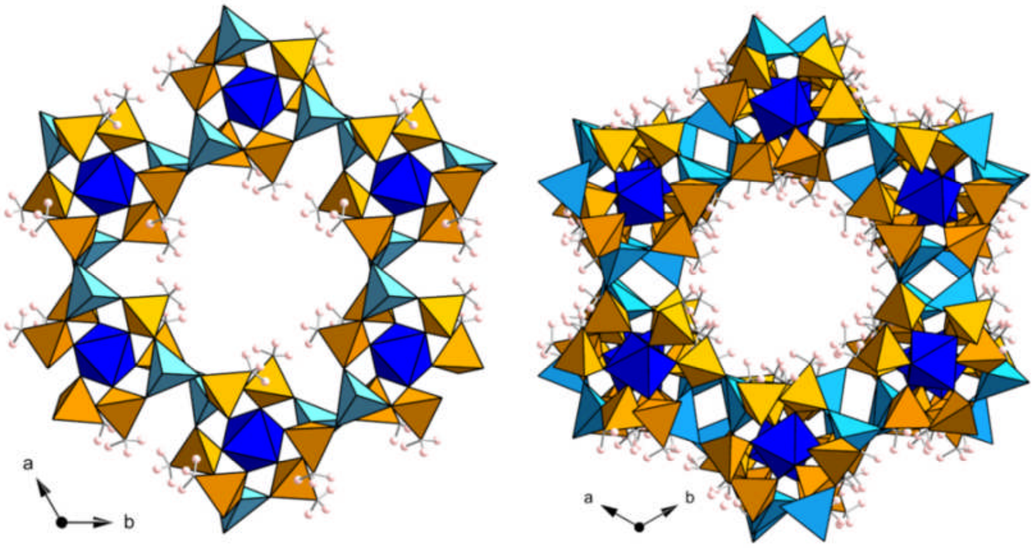

Figure 1.5: Structure of the AlMePO-α (left) and AlMePO-β (right) viewed down the pore channel, parallel to the c-axis in both cases. Aluminium polyhedral are shown in blue, bark blue for octahedral and light blue for tetrahedral coordination. Phosphonate tetrahedra are shown in orange and pink spheres represent the hydrogen atoms of the methylphosphonate.

AlMePO-β is prepared via a hydrothermal route to produce large crystals, which can be transformed to AlMePO-α by heating in a nitrogen stream saturated with water vapour at 500°C. The internal surfaces of the channels in the AlMePO materials differ from aluminophosphates, being hydrophobic due to the –CH_3 groups lining the walls.

Work carried out by Gonzalez and co-workers[45] involving the dynamics of aromatic molecules in the AlMePO systems has shown that there is potential for their use as a separation medium. NMR studies on deuterated benzene and toluene species dosed onto the dehydrated forms of the AlMePO polymorphs showed that the benzene species was able to rotate freely in the more cylindrical channels of the AlMePO-α form whereas in the α form, the motion restricted to flipping between three symmetry related sites on the pore. Toluene however is unable to tumble freely and is thought of as rotating in a cone around the para-axis of the molecule. These data were combined with molecular dynamics simulations to approximate the motion of the dosed molecules within the system (Figure 1.6).[45] A subsequent study by Herdes *et al.* on AlMePO-α investigated the selective adsorption of ethyl chloride from a mixture with vinyl chloride on the same material.[46]

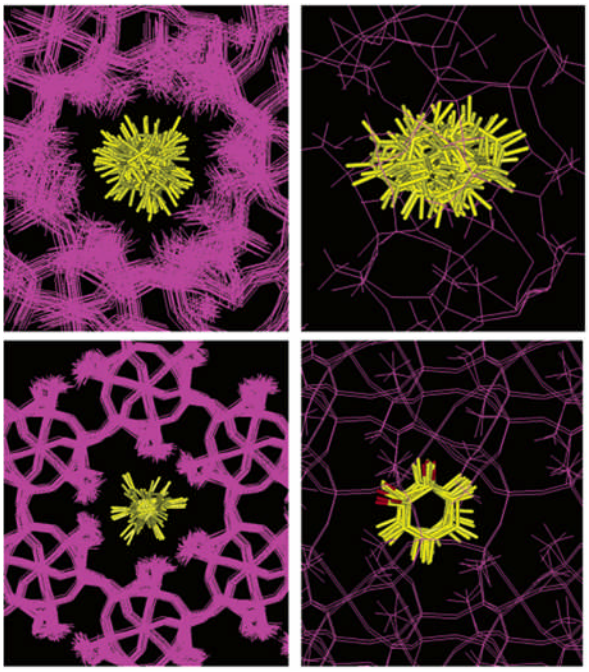

Figure 1.6: Trajectory of benzene molecules within the pores of AlMePO-β (*above*) and AlMePO-α (*below*). The structure is viewed along the channel axes (*left*) and perpendicular to these axes (*right*). The location of benzene in AlMePO-β is shown every 2.5 × 10^{-12} s for the full length of the 1 × 10^{-10} s simulation. The location of benzene in AlMePO-α is shown every 5 x 10^{-12} s during the full 1 x 10^{-10} of the simulation. The orthogonal view of the motion of benzene in AlMePO-α is shown every 5 x 10^{-13} s between 1.25 x 10^{-11} and 1.70 x 10^{-11} s.[45]

1.3.2 Metal Bisphosphonates

The next major development in phosphonate-based systems, following the interest in methylphosphonates, was to connect two phosphonate groups with an organic molecule, extending the building unit. This can range from a simple methylene group to a phenyl ring or more complex multi-ring systems such as those shown in Figure 1.7.[47]

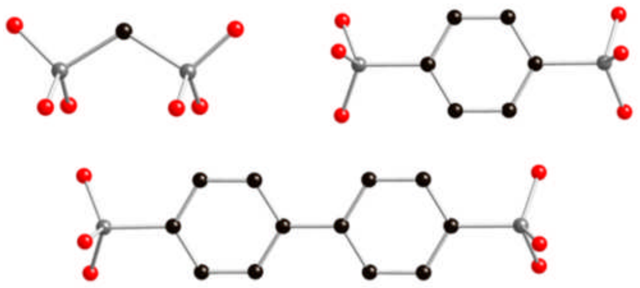

Figure 1.7: Examples of simple bisphosphonate molecules

This organic linkage in the framework reduces the thermal stability of the resulting framework but allows for greater control of the internal surfaces as well as the potential for greater and more accessible porosity. Simple organic synthesis can be used to add functional groups to the linker molecules, such as amino and nitro groups, thus modifying the properties for applications such as gas adsorption.[21]

The piperazine-derived family of bisphosphonate ligands has been particularly successful in the preparation of porous frameworks.[24,48] Of particular interest to this study are the piperazinebis(methylenephosphonic acid) and the 2-methylpiperazine and 2,5-dimethylpiperazine derivatives shown in Figure 1.8.

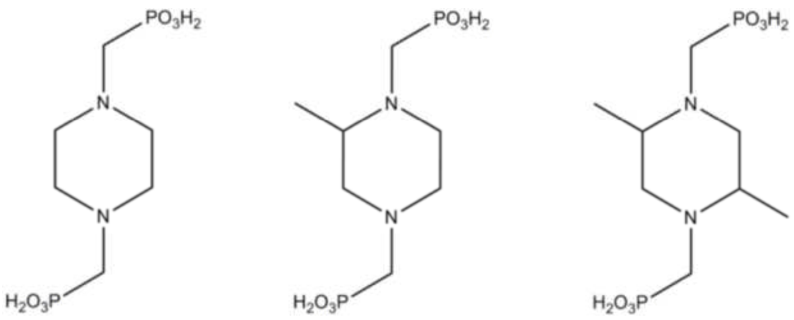

Figure 1.8: Piperazine-bis(methylenephosphonic acid) linker (H_4L) *(left)*, the 2-methyl-piperazine derivative (H_4L') *(middle)* and the 2,5-dimethyl- derivative (H_4L'')*(right)*.

The first large pore framework reported with the piperazine-based linker (H_4L) was the phosphonate STA-12(Ni) (Figure 1.9).[24,49] The framework is composed of helical chains of edge sharing nickel octahedra together with the phosphonate tetrahedra from the bisphosphonate linker. The resulting inorganic chains are bridged through the piperazine-based bisphosphonate to three other chains creating a honeycomb like array of unidirectional channels. The hexagonal channels have a cross-sectional diameter of 9 Å which in the as-synthesised state are filled with physisorbed water.

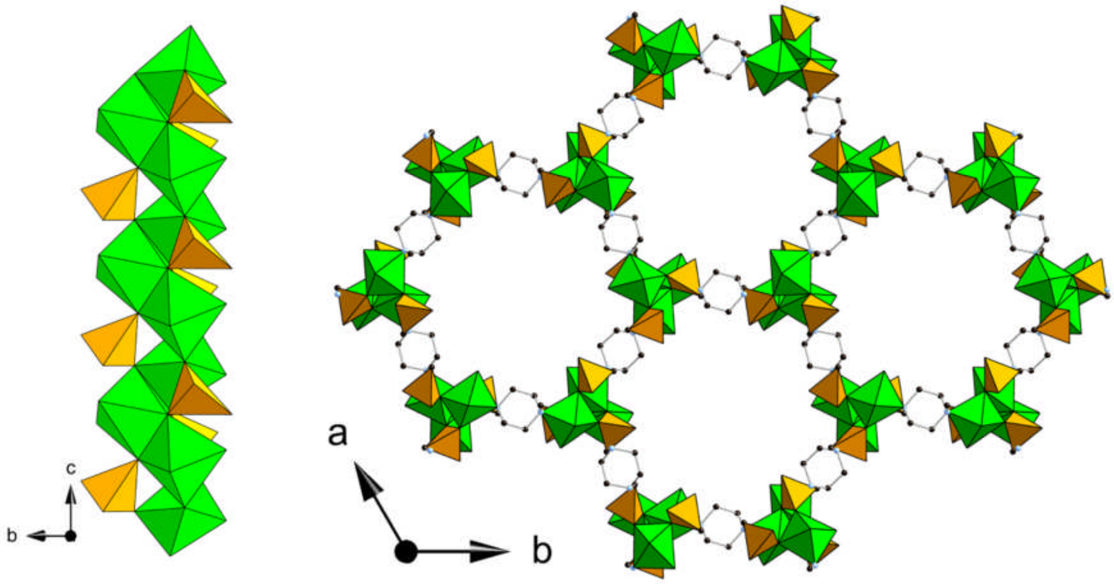

Figure 1.9: Helical nickel phosphonate chains *(left)* and hexagonal channels *(right)* of the STA-12(Ni) framework. Nickel octahedra are shown in green and phosphonate tetrahedra are shown in orange, black spheres represent the carbon atoms of the organic linker

The nitrogen atom from the piperazine ring is involved in the metal coordination along with four phosphonate oxygen atoms and the oxygen of a water molecule, resulting in a distorted octahedral geometry around the metal. The dehydration behavior of STA-12 has been studied by synchrotron PXRD. On dehydration, the water molecule is lost from the each metal cation causing a twisting of the metal phosphonate chains. This structural change is observable as a change in colour from green, in the as-prepared material, to yellow/brown, in the dehydrated state.

The isoreticular analogue of the STA-12 framework topology was later prepared with the extended bipiperidine derivative of the bisphosphonate linker.[25] This structure, STA-16 (Figure 1.10), shows an increased pore diameter of 18 Å (from 9 Å in STA-12) and is the largest pore size reported in metal phosphonate systems.

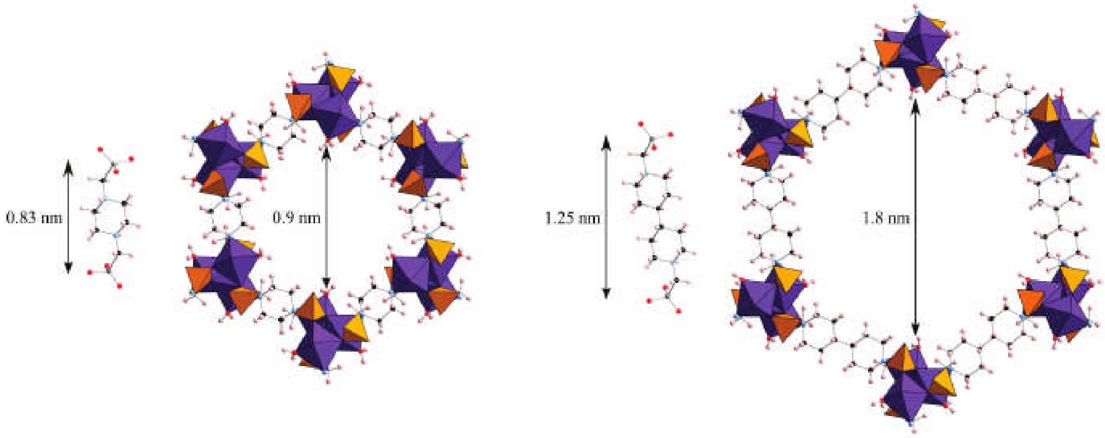

Figure 1.10: Comparison of the ligand and pore size in the STA-12(Co) And STA-16(Co) structures.[25] Cobalt octahedra are shown in purple and phosphonate tetrahedra are shown in orange, black and pink spheres represent the carbon and hydrogen atoms of the organic linker.

Nitrogen adsorption data on STA-16, combined with non-local DFT calculations for N_2 at 77 K show that the permanent porosity of the material can be represented by a cylindrical pore of diameter 18.5 Å approaching that of the mesoporous regime (20-500 Å).[25] Indeed the N_2 adsorption isotherm shows an inflection at low pressure (0.025 p/p_0) indicative of the capillary condensation observed in mesoporous materials. The large and accessible columnar channels of STA-16 mean that the material may be of use in the storage or separation of large molecules, where other MOFs with similar porosity tend to have large mesoporous cavities limited by the 'windows' between cages.

1.4 Carboxylate MOFs

1.4.1 Divalent Carboxylates

The divalent metal carboxylate based frameworks MOF-5 and HKUST-1 are examples of prototypical MOF materials and triggered a huge growth in the field of metal-organic frameworks. A keyword search for "metal-organic frameworks" registers >1,600 publications in 2010 and >2,000 for 2011, a strong indication of the worldwide interest in this area and indicates that the growth is continuing. More recent work on divalent carboxylates with longer and more complex organic components is pushing the limits of gas adsorption and storage properties with the highest surface areas and lowest densities of all known crystalline materials.

1.4.1.1 MOF-5 & MOF-177

MOF-5 is an early and heavily studied example of a MOF material.[32] The material is an example of a cubic 3-dimensional extended lattice composed of Zn_4O inorganic clusters connected by terephthalate linkers (Figure 1.11).

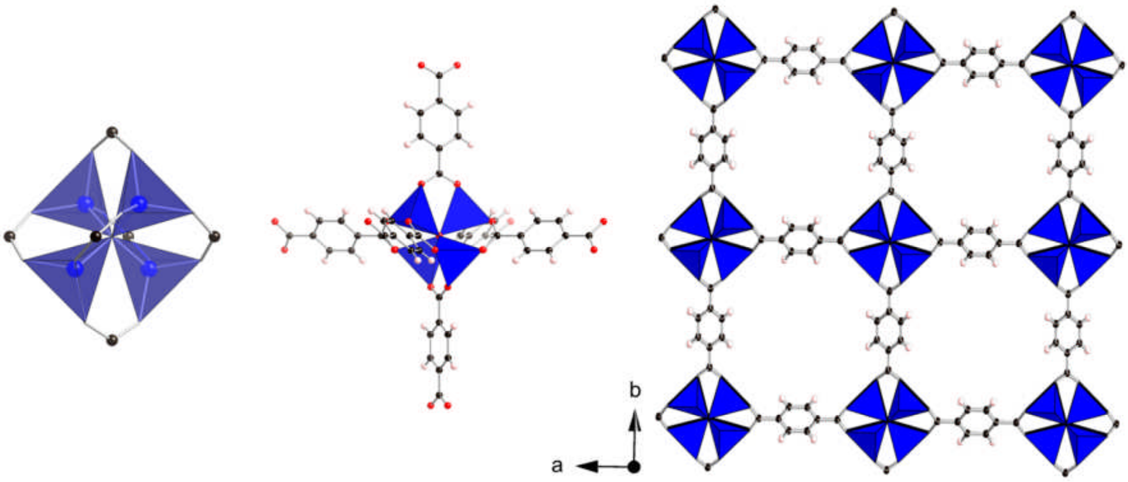

Figure 1.11: MOF-5 assembly, $Zn_4O(CO_2)_6$ cluster *(left)*, octahedral geometry of terephthalate molecules *(middle)* and 3D cubic lattice *(right)*. Zinc tetrahedra are shown in blue. Black spheres represent the carbon atoms of the organic linker

Each cluster involves 6 carboxylate groups of 6 terephthalate molecules bridging zinc atoms leading to an octahedral type arrangement around the cluster which, when expanded in three dimensions, reproduces the cubic arrangement of the material. The structure is retained upon solvent removal and the literature states that the Langmuir surface area (a monolayer-equivalent surface area) is stated to be of the order of 3000 m^2g^{-1}, significantly higher than that of most zeolites and at the time, among the highest of all known materials. One downside to the large open pore structure is the potential for interpenetration of 2 frameworks. In the case of MOF-5 and the IRMOF family of isoreticular structures[31] (see Figure 1.3 above), if the pore size is sufficient to contain a Zn_4O cluster and the dicarboxylate is of sufficient length, then the formation of a second extended lattice can occur within the first. This interpenetration or catenation of two frameworks results in a significant reduction in the porosity as the majority of the void space in the cage is filled with the other framework. Examples of interpenetration are reported for some members of the IRMOF series as shown in Figure 1.12. [31]

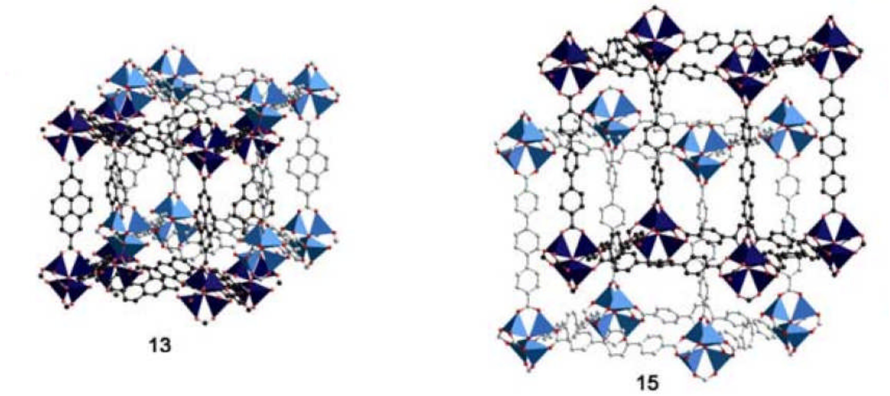

Figure 1.12: Interpenetration of the low density cubic lattices in IRMOF-13 (*left*) and IRMOF-15 (*right*).[31]

MOF -177 is another example of a MOF material containing the tetrahedral Zn_4O cluster but with a more complex and extended tricarboxylate linker.[33] The carboxylate molecule in this case in the large BTB molecule where BTB = benzene- 1,3,5-tribenzoic acid. This large yet rigid tri-carboxylate unit connects to the cluster in the same manner as in the MOF-5 structure but as there are three carboxylate units and a triangular geometry, this produces a more spherical porous cage structure rather than the cubic pore geometry in MOF-5.[32]

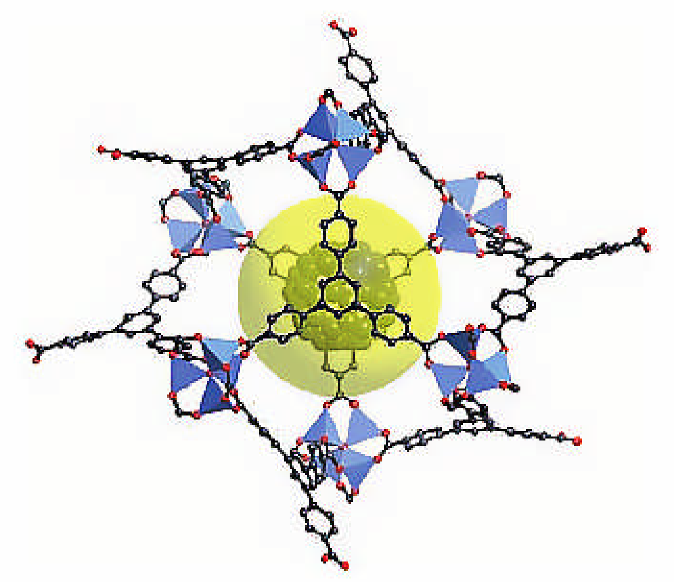

Figure 1.13: Single cage from the zinc carboxylate, MOF-177.[33]

MOF-177 has been shown to have the one of the largest surface areas of known materials to date (Figure 1.13). Literature states a Langmuir surface area value of 4500 m^2g^{-1} with N_2 adsorption giving a type I isotherm with adsorption of 1350 mg g^{-1} between 0.4 and 1 P/P_0.[50] These values show that MOF-177 is a highly porous open framework MOF material with a 3-dimensionally connected array of porous cages.

1.4.1.2 HKUST-1

HKUST-1 is another early example of a divalent carboxylate MOF (Figure 1.14).[51] Reported around the same time as MOF-5, HKUST-1 is a copper 'paddlewheel' based MOF where two copper ions form a dimeric unit with four bridging carboxylates creating a square planar geometry around two adjacent copper sites. The two copper ions in the paddlewheel coordinate to the oxygen of two water molecules to create a double square pyramidal geometry for the two metal sites in the hydrated form of the structure. Activation of the material prior to adsorption studies results in the removal of the terminal water molecules resulting in a coordinatively unsaturated metal site.

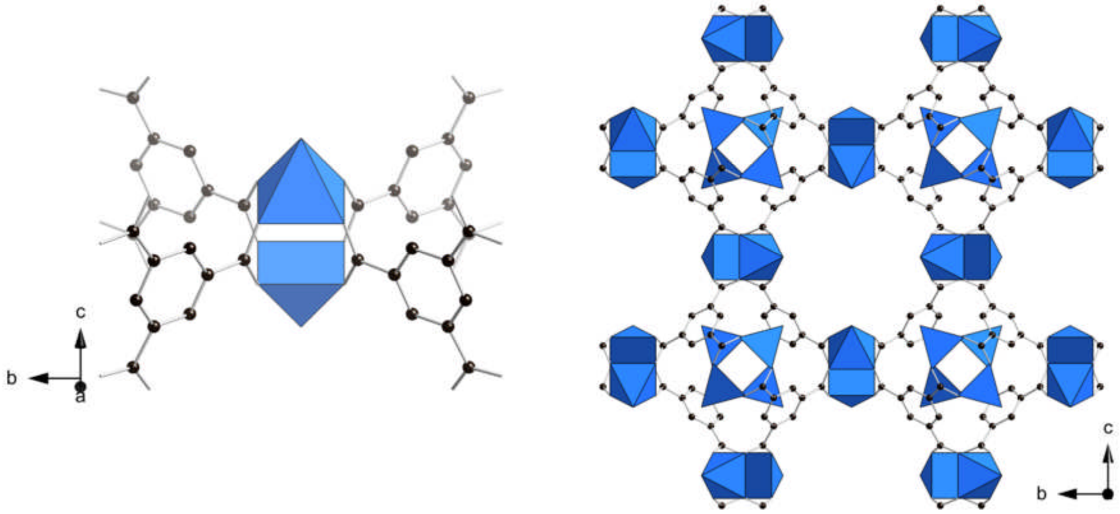

Figure 1.14: Individual $Cu_2(CO_2)_4(H_2O)_2$ 'paddlewheel' cluster coordinated by trimesic acid (*left*) and the porous cubic framework (*right*) of HKUST-1.[51] Blue polyhedra represent the square pyramidal CuO_5. Black spheres represent the carbon atoms of the organic linker

The rigid, porous structure of the HKUST-1 framework combined with the accessibility of the activated metal sites upon dehydration has led to a lot of interest in adsorption, separation and catalysis applications.[52-54]

1.4.2 High surface area materials

Metal-organic frameworks currently boast the highest reported surface areas of any known materials.[55] MOFs with exceptionally high surface areas are of interest in applications such as hydrogen storage. The weak intermolecular interactions between the hydrogen molecules mean that the dominating interaction is the between the hydrogen molecules and the surface of the material therefore the higher the surface area the greater the adsorption capacity for hydrogen. Physisorption is more energetically efficient than other storage methods such as metal hydrides which, although they have a density of stored hydrogen that is greater, require a higher temperature and therefore greater energy cost to release the hydrogen. Some of the highest surface area MOFs reported to date are based on the inorganic units of the prototypical MOF materials MOF-5 and HKUST-1 (described above) but with more complex extended organic linkers, examples of which are shown in Figure 1.15.[55,56]

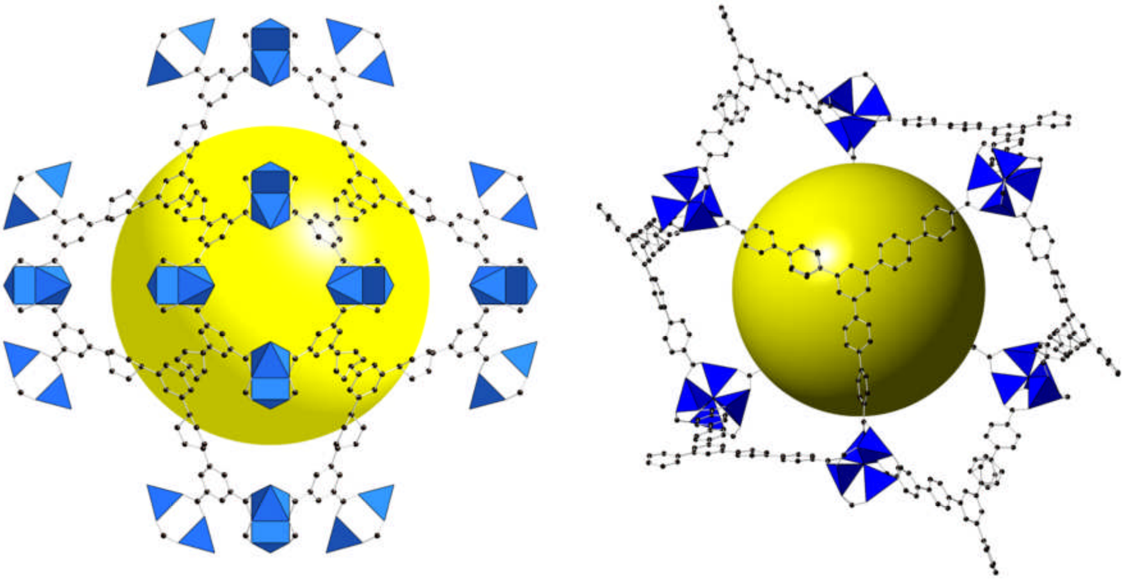

Figure 1.15: MOFs with ultrahigh porosity: NOTT-112[55] (*left*) and MOF-200[54] (*right*)

1.4.2.1 CPO-27 / MOF-74

While surface area and pore volume is important to the adsorption properties of MOF materials, another consideration is the availability of coordinatively unsaturated metals sites. The divalent metal carboxylate CPO-27(M) (where M = Co,Ni) was reported by Dietzel and co-workers,[57] while at a similar time work by Rosi *et. al.* produced the isostructural zinc analogue, referred to as MOF-74.[58] The divalent metal and 2,5-dihydroxyterephthalic acid linker form a honeycomb like array of hexagonal channels (Figure 1.16). The inorganic component is a helical chain of edge sharing NiO_6 octahedra where each metal is bound to two oxygens from hydroxyl groups on the ligand, three oxygens from carboxylate groups and one water molecule.[57] MOF-74 was prepared using DMF as the solvent and as such, has terminal DMF molecules bound to the free metal sites on the chain.[58]

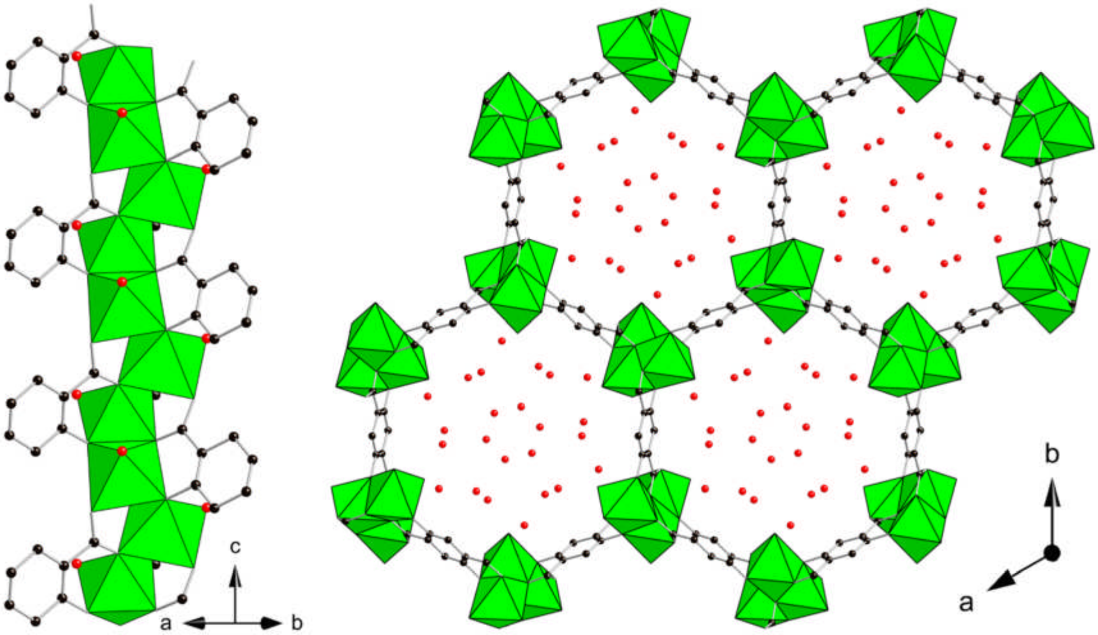

Figure 1.16: Single chain (*left*) and view along the hexagonal channels (*right)* of the nickel dihydroxyterephthalate, CPO-27(Ni).[57] Nickel octahedra are shown in green, black spheres represent the carbon atoms of the organic linker and red spheres the oxygen of adsorbed water molecules.

The helical chains of CPO-27(Ni) are separated by the planar dihydroxyterephthalic acid linker. This organic molecule acts as a rigid pillar between chains with each linker bound to three different metal sites from each chain. Removal of the solvent molecules from the terminal metal sites creates five-coordinate metal cations with little freedom to rotate or distort the chain to change the coordination environment. This unfavourable coordination environment means that the activated metal site has a high enthalpy of adsorption and is readily filled by adsorbed guest species. The chain is topologically identical to that of the nickel bisphosphonate STA-12(Ni) (Figure 1.9 above) but differs upon dehydration where the additional flexibility of the bisphosphonate linker allows the chain to twist and distort reducing the accessibility of the coordinatively unsaturated metal site. The availability of this metal site in the CPO-27 framework has been explored for a number of different adsorption applications involving gases such as CO_2, H_2 and NO.[59-61]

1.4.3 Trivalent Carboxylates

Some of the most widely studied of all metal organic frameworks are trivalent metal carboxylate materials. Extensive work in this area has provided an understanding of the crystal chemistry of a wide variety of the trivalent first row transition metals

1.4.3.1 MIL-47 & MIL-53

The vanadium terephthalate MIL-47, first reported by Barthelet and co-workers,[62] is an example of a metal organic framework consisting of infinite corner sharing metal chains of VO_6 octahedra bridged by the linear terephthalate organic linker. This connectivity results in the formation of large diamond shaped channels, as shown in Figure 1.17.

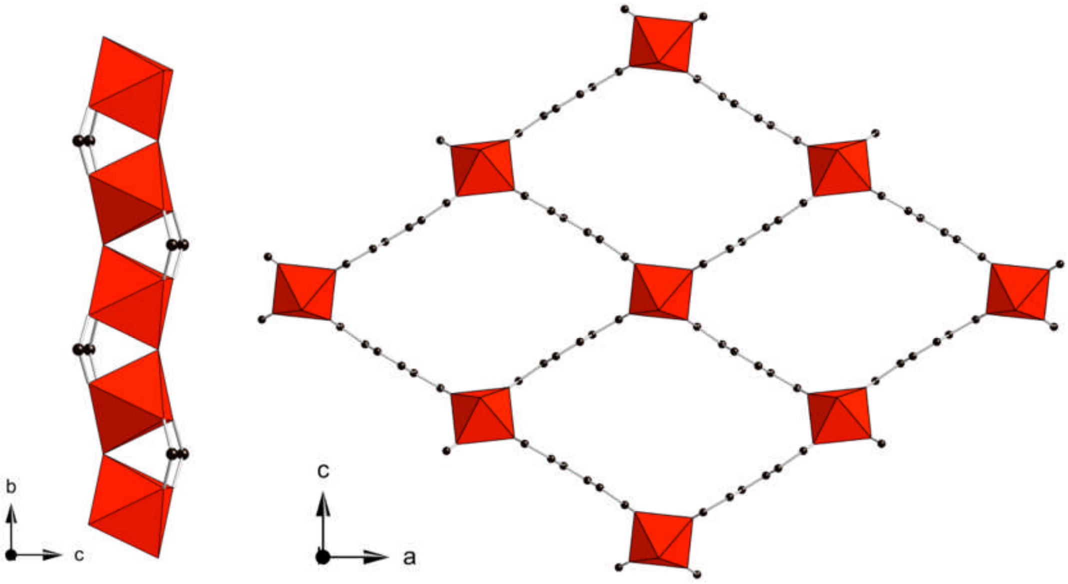

Figure 1.17: Corner sharing vanadium chains (*left*) and view along the rhombic channels (*right)* of the vanadium terephthalate, MIL-47(V).[62] Vanadium octahedra are shown in red, black spheres represent the carbon atoms of the organic linker.

The channels in as-prepared vanadium MIL-47 contain some residual guest terephthalic acid and is reported as having the formula $V^{III}(OH)(CO_2\text{-}C_6H_4\text{-}CO_2)$ and a hydroxide μ_2-OH ion forming the infinite chains. Activation of the solid by heating in a tube furnace at 573 K for 24 hours results in deprotonation of the hydroxide on the chains to form a μ_2-oxo and oxidation of the vanadium, to give $V^{IV}O(CO_2\text{-}C_6H_4\text{-}CO_2)$ as the formula for the activated material. The activated MIL-47(V) is anhydrous at room temperature under ambient pressure, as the channels are hydrophobic, being lined with phenyl rings and with no accessible metal sites or favourable hydrogen bonding positions the channels are hydrophobic.

MIL-53 was first reported with chromium[29] (Cr^{3+}) and shortly after with aluminium[63] (Al^{3+}) with terephthalic acid as the linker. MIL-53 (Figure 1.18) is isostructural with MIL-47, the main difference is that MIL-53 only contains the trivalent metal and a μ_2-hydroxide bridge whereas the activated MIL-47 is the tetravalent V^{4+} with μ_2-oxo bridging. As the activated form of the MIL-53 contains the metal hydroxide chains, the channels are hydrophilic with the hydroxide protons available for hydrogen bonding.

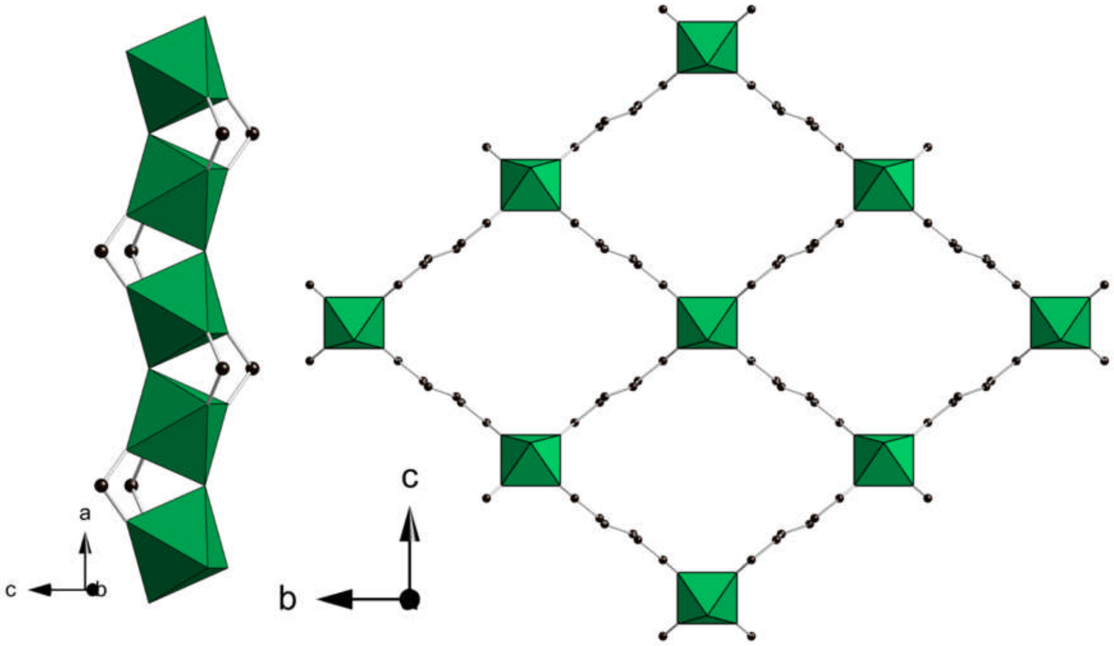

Figure 1.18: Corner sharing chromium hydroxide chains (*left*) and large pore (dehydrated) framework of MIL-53(Cr) (*right*). Chromium octahedra are shown in green, black spheres represent the carbon atoms of the organic linker.

When activated MIL-53(Cr or Al) is exposed to moisture, X-ray diffraction shows the material adopts a ‘closed’ structure, due to the strong hydrogen bonding interaction between the hydroxyl groups of the inorganic chains and the adsorbed water molecules.[63] As a result of this hydration behavior, the unit cell volume reduces by ~30 %, fully reversible upon subsequent dehydration (Figure 1.19). Such large structural changes, in response to adsorption of gas or solvent molecules, is commonly referred to as ‘breathing’.

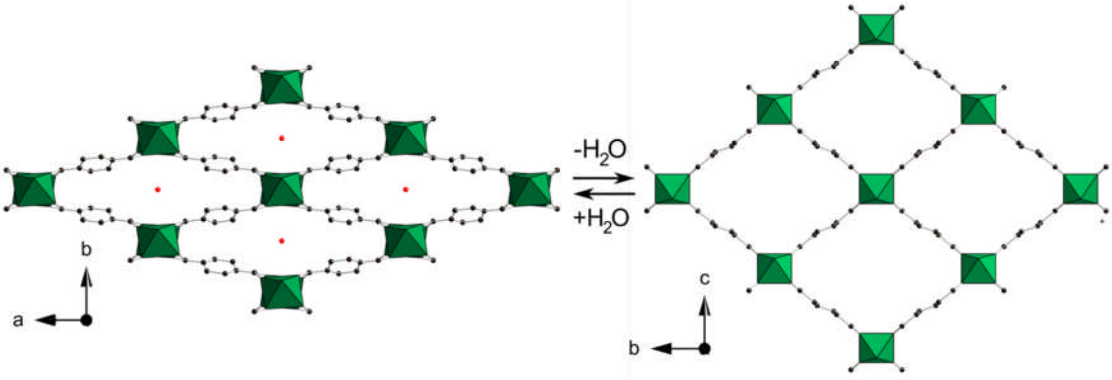

Figure 1.19: MIL-53(Cr) in the hydrated (narrow pore) state (*left)* and in the dehydrated (large pore) state (*right*). Chromium octahedra are shown in green, black spheres represent the carbon atoms of the organic linker.

Since the initial reports of the chromium and aluminium MIL-53, extensive work has been undertaken in this area, and the range of MIL-53 materials now extends to: Cr^{3+}, Al^{3+}, Fe^{3+}, Ga^{3+}, In^{3+}, and (as a result of this work) Sc^{3+}). The major developments in understanding the breathing and flexibility of the MIL-53(M) as well as the synthesis and characterization of MIL-53(Sc) will be discussed in detail in Chapter 6.

1.4.3.2 MIL-68

Work by Barthelet and co-workers also identified MIL-68, another trivalent metal terephthalate (Figure 1.20).[64] The framework is a polymorph of the MIL-47/MIL-53 structure with the chemical formula, $M^{III}OH(CO_2\text{-}C_6H_4\text{-}CO_2)$ initially reported for V^{3+} and later with In^{3+} and Ga^{3+}. In this case the metal hydroxide chains connect to form two types of unidirectional channels, triangular and hexagonal in shape, creating a 'kagome lattice' like network of pore channels. The cross-sectional diameters of the triangular and hexagonal channels are 6 Å and 17 Å respectively.

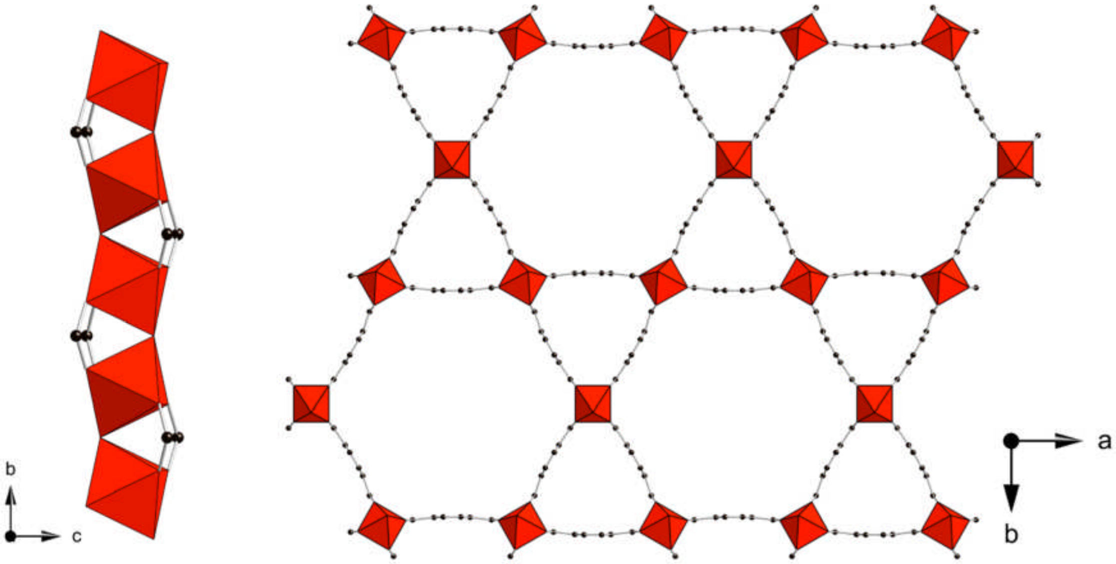

Figure 1.20: Corner sharing vanadium chains (*left*) and large pore framework of MIL-68(V) (*right*).[64] Vanadium octahedra are shown in red, black spheres represent the carbon atoms of the organic linker.

N,N'-Dimethylformamide (DMF) solvent molecules were observed in the smaller triangular channels of as-prepared MIL-68(In) reported by Volkringer *et. al*,[65] disordered over two positions, with hydrogen bonding between the oxygen of the DMF and the hydroxyl group of the inorganic chain. The solvent was removed by calcination at 200°C overnight in a furnace. The activated samples were stored under inert atmosphere to prevent rehydration which would lead to hydrolysis and ultimately decomposition of the structure. Adsorption studies on the indium and gallium forms of MIL-68 give a value for the BET surface area of 1117(24) m^2 g^{-1}, 746(31) m^2g^{-1} and 603(22) m^2g^{-1} for the gallium, indium and vanadium forms respectively. A number of activation procedures were attempted and NMR analysis used to verify complete removal of guest molecules to obtain the surface area results. The BET values suggest that the indium and vanadium analogues were not fully activated prior to adsorption. Notably, a recent computational study of the theoretical surface area, gave a value of 3333 m^2g^{-1} for MIL-68(V) suggesting that there may still be activation issues with all the MIL-68 derivatives, rendering some of the porosity inaccessible.

1.4.3.3 MIL-88

Further study on the metal carboxylate systems of trivalent iron and chromium yielded a series of materials referred to as MIL-88(A-D). First reported as an iron fumarate,[66] and based on the trimeric building unit (Figure 1.21) obtained on the crystallization of iron (and chromium) acetate, MIL-88 is a family of isoreticular materials prepared with dicarboxylate linkers.[67]

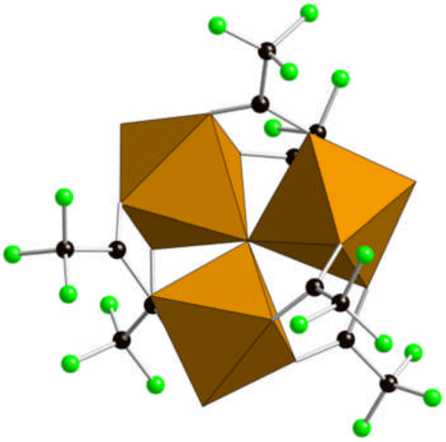

Figure 1.21: Iron trimer unit with bridging trifluoroacetate anions. Iron octahedra are shown in brown, black and green spheres represent the carbon and fluorine atoms of the organic linker respectively.

Reactions using the metal acetate trimeric building unit are thought to proceed via a ligand exchange mechanism where the acetate of the starting material is replaced with a longer linear dicarboxylate to create the three dimensional framework. MIL-88 is an isoreticular series with increasing length of dicarboxylate forming the same network topology prepared using the fumaric acid (MIL-88A), terephthalic acid (-88B), naphthalene-2,6-dicarboxylic acid (-88C) and 4,4'-biphenyldicarboxylic acid (-88D) (Figure 1.22). The framework consists of both one dimensional channels, and trigonal bipyramidal cages. Solvent exchange experiments on the terephthalate form, MIL-88B, show that large organic molecules such as lutidine and butanol are able to enter the framework and induce an increase in cell volume over the dried material.[67]

The three metals in the trimeric cluster share a μ_3-O and are bridged to the adjacent metals with 4 carboxylate groups leaving a coordinatively unsaturated metal site pointing into the cages within the framework. To maintain charge balance in the material, there must be one negatively charged species on the cluster, either a hydroxide or fluoride (depending on the synthesis conditions) occupying one of the unsaturated metal sites and the other two could be water or exchanged solvent species.

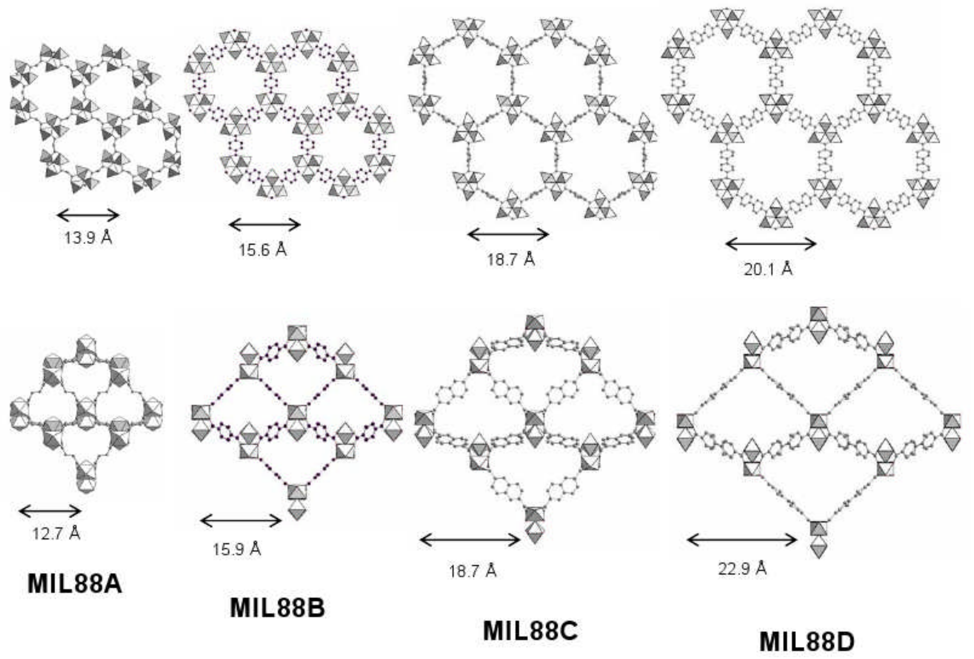

Figure 1.22: MIL-88(Fe or Cr) series with the fumarate, terephthalate, naphthalate and biphenyldicarboxylate linkers respectively.[67]

MIL-88(Cr and Fe) also exhibits a breathing behaviour in response to solvent exchange and gas adsorption. The mechanism for the breathing is similar to that observed in the MIL-53 where there is a hinge like motion around the axis of the two oxygen atoms of the carboxylate. The observed expansion and contraction of the unit cell volume is, however, much greater than that observed in MIL-53. As the trimeric units are connected in three dimensions, rather than the columnar rows of terephthalates connecting the chains in MIL-53, the change occurs over all three axes resulting in a cell volume expansion for the terephthalate form (MIL-88B) of 125 % from the fully dried form (1500 Å^3) to the most open form observed upon methanol solvation (3375 Å^3) (Figure 1.23).[67]

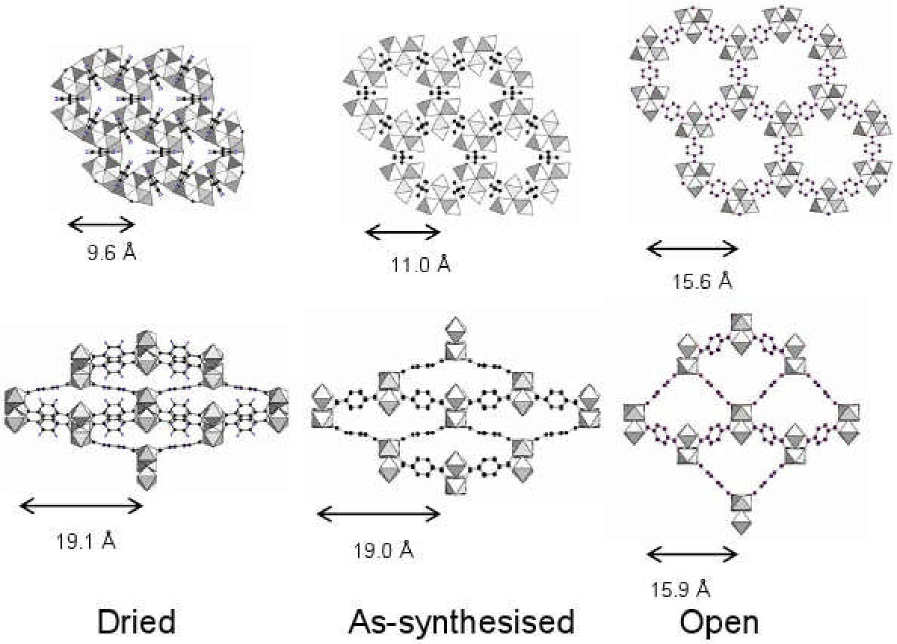

Figure 1.23: Open and closed MIL-88(Fe or Cr)[67]

1.4.3.4 MIL-100 & MIL-101

MIL-100 and MIL-101 comprise the same trimeric building unit as the MIL-88 (above).[68-70] The rigid carboxylate linkers connect trimers such that they form a super-tetrahedra which is the main building unit of the material (Figure 1.24). The difference between the two structures is that the MIL-100[70] is prepared with trimesic acid where the super-tetrahedral unit has a trimesate on the face of each tetrahedra whereas, the MIL-101[68] is prepared with terephthalic acid and consists of tetrahedra with a terephthalate on each edge with the trimeric units on the vertices.

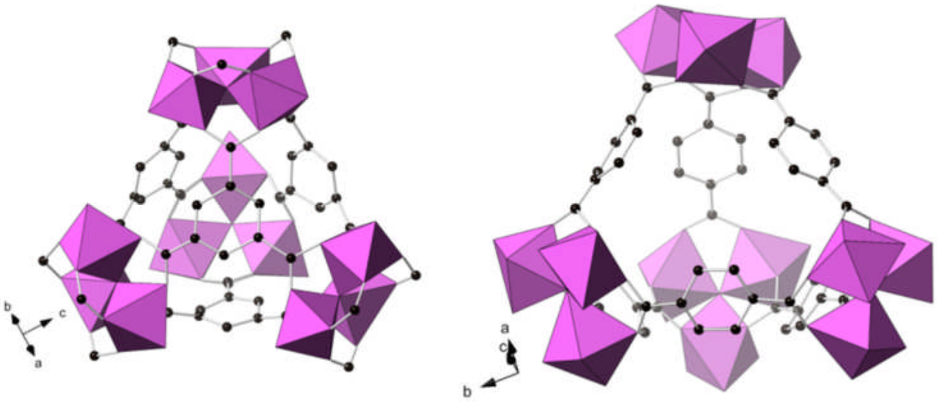

Figure 1.24: MIL-100 & MIL-101 super-tetrahedral units. Metal octahedra are shown in pink, black spheres represent the carbon atoms of the organic linker.

The two structures share the same overall network connectivity of tetrahedral units, in zeolite nomenclature the MTN topology, a framework type reported for the zeolite ZSM-39[71] where the AlO_4 and SiO_4 tetrahedra are replaced by 'super-tetrahedral' building units. The difference in size between the metal tetrahedra of ZSM-39 and the super-tetrahedral unit of the MIL-100 and MIL-101 means that the pore size is also significantly larger. The structures contain two types of cage with porosity into the mesoporous region. The internal diameter of the cages in MIL-101(Cr) is 29 Å for the smaller cage and 34 Å for the larger. The smaller cage is accessible through microporous pentagonal windows with a cross-sectional diameter of 1.2 nm, and the larger cage through both the pentagonal windows and larger hexagonal windows of diameter 1.6 nm (Figure 1.25).

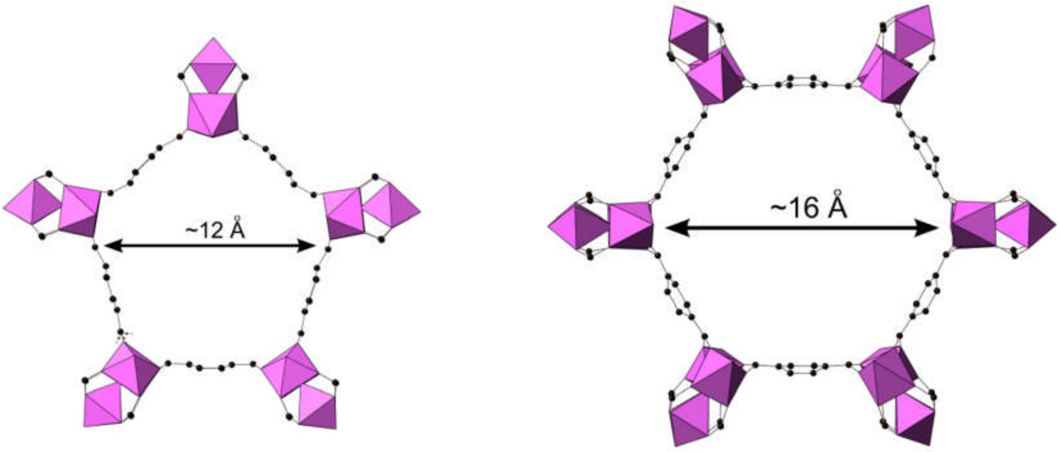

Figure 1.25: 'Windows' between cages in the MIL-101(Cr) structure. Metal octahedra are shown in pink, black spheres represent the carbon atoms of the organic linker.

The MIL-101 structure is best represented by comparison to the zeolitic MTN network (Figure 1.26), a framework type reported for the zeolite ZSM-39. Where the zeolite contains AlO_4 and SiO_4 tetrahedra, in MIL-101(Sc) these are replaced my much larger 'super-tetrahedral' units (Figure 1.27).

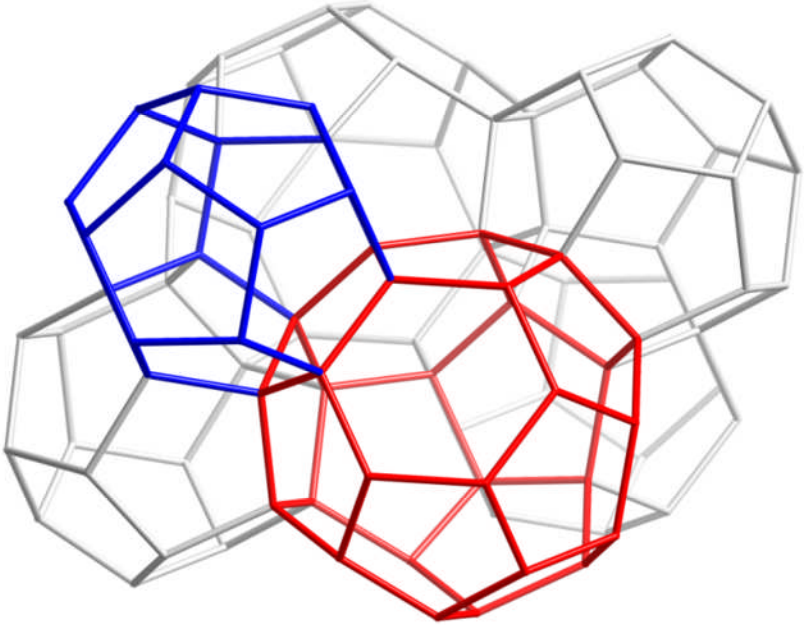

Figure 1.26: MTN network with a single smaller cage (blue) and larger cage (red) identified. Each vertex represents the centre of a tetrahedral unit, either an AlO_4 or SiO_4 tetrahedra in ZSM-39 or the super-tetrahedral building unit of MIL-101.

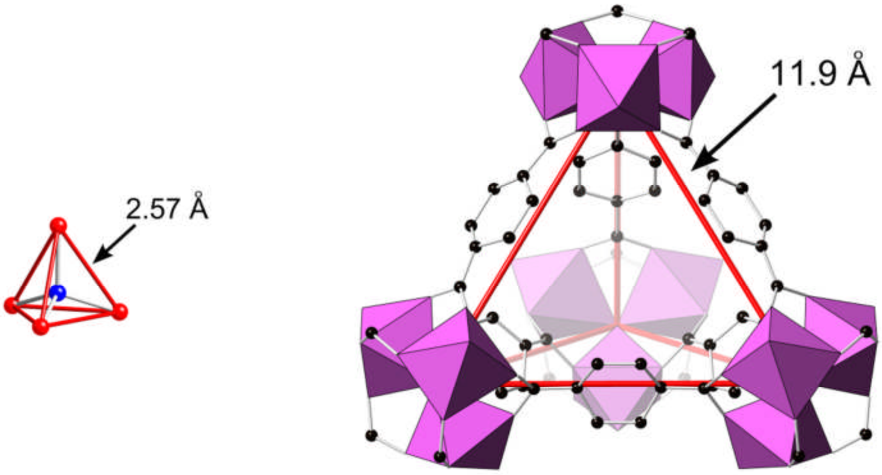

Figure 1.27: Tetrahedral units from the ZSM-39 zeolite and MIL-101(Cr) MOF which share the MTN topology. Metal octahedra are shown in pink, black spheres represent the carbon atoms of the organic linker.

The relative size of the tetrahedral units in MIL-101(Cr) creates a highly accessible porous network of cages accessible through pentagonal and hexagonal windows between cages. The same trimeric units as in MIL-88 (Figure 1.21) are present in the structure, with three terminal coordination sites. One terminal site must be occupied by a negatively charged anion (either hydroxide or fluoride - hydrofluoric acid is used in the synthesis) to balance the charge on the framework. The remaining two sites are occupied by H_2O molecule, as evidenced by IR studies of the material.[72] Removal of these terminal H_2O molecules results in the formation of Lewis acidic free metal sites. The MIL-101 structure requires multi-stage activation to render the full volume accessible. Terephthalic acid molecules from the original synthesis can become trapped in the cages and must be removed. There are various activation methods reported for the material but the most effective involves first treating the material in hot ethanol for 8 hours followed by dispersion in aqueous ammonium fluoride and washing in hot water.[4] Following this activation, the BET surface area of the MIL-101(Cr) is reported at 4230 m^2g^{-1}. Recent work on MIL-101(Cr) has explored a range of applications including the incorporation of catalytically active species such as polyoxometalates[73] within the cages and also the use of MIL-101 in the chromatographic separations of substituted aromatics.[74]

1.4.4 Framework flexibility in MOFs

Flexiblility in MOF systems typically refers to reversible crystal-to-crystal transitions where the framework connectivity of the bulk material is retained but a change occurs in the geometry of the framework components.[12] This could be as simple as a rotation within an organic molecule (changing the internal surface with minimal volume change) or as complex as a 3-dimensional hinging motion increasing the overall unit cell volume. This type of flexibility is not unique to MOF systems. Some zeolite frameworks are known to have a degree of flexibility, typically arising from exchanging out the cations which stabilize certain framework components such as ring systems between cages. A good example of this flexibility is observed in the zeolite-rho structure.[75]

Flexibility in MOFs can occur in a number of ways, some common examples are represented in Figure 1.28 (below). Example A is observed for the MIL-53 series in 2D[29,63] (Figure 1.19) and as a 3D example in MIL-88 (Figure 1.23). Example B is a case where a layered structure can be reversibly separated by intercalation of a gas or solvent between the layers.[26] Example C is typical of interpenetrated frameworks where the void space and 3D connectivity is such that two fully connected frameworks can exist within each other. In materials such as MOF-508[76] and some members of the IRMOF series discussed earlier (Figure 1.3), there can be translation of one framework with respect to the other, again driven by the adsorption of gas or solvent molecules. The final example shown (D) is representative of a case where the flexibility arises from rotational flexibility of the organic ligand pillaring the layers.[26] In this case rigid layers are separated by the flexible linker which can expand and contract in response to the adsorption and desorption of guest molecules.

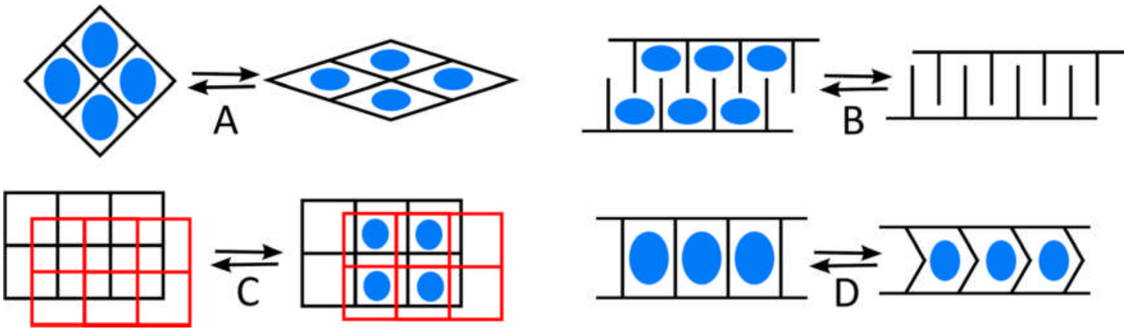

Figure 1.28: Schematic representation of the modes of flexibility observed in MOF structures.

1.4.5 Scandium Chemistry and MOF synthesis

1.4.5.1 General scandium chemistry

The existence of scandium as an element was first proposed by Dimitri Mendeleev when he created the periodic table and predicted the presence of an element that he proposed would resemble boron in it properties and he called it ekaboron. Scandium oxide was isolated by Swedish mineralogist Lars Frederick Nilson in 1876 from euxenite and gadolinite minerals from scandanivia, the name scandium derives from the latin *Scandia* meaning Scandinavian. Scandium is not a rare element on Earth. The abundance in the Earth’s crust is stated as being similar to that of more readily available elements such as cobalt and lead but the deposits are more dispersed and minerals containing scandium as the main constituent are rare. One of the main sources of scandium is uranium or rare earth mining where the scandium is a byproduct, sold as scandium oxide. The main application of scandium to date is in scandium-aluminium alloys used in some aircraft bodies. The presence of a small amount of scandium <1 % limits the grain growth that occurs when welding aluminium and results in a stronger alloy without the need for rivets although it is still more expensive than titanium alloys currently in use.

The chemical behaviour of scandium is similar to that of aluminium and yttrium. Naturally occurring scandium is exclusively the ^{45}Sc isotope a quadrupolar nuclei which has a nuclear spin of 7/2. A major advantage of this is that it permits the use of solid-state NMR analysis of scandium materials, providing information on the local structure of the solids.

In organic chemistry, scandium triflate is commonly used as a Lewis acid catalyst, prepared by reaction of scandium oxide with trifluoromethanesulfonic acid (referred to as triflic acid).[77,78] This is used as a recyclable, homogenous, Lewis acid catalyst, which unlike most common Lewis acidic compounds, is not deactivated in the presence of water.[77] In terms of ionic radius, scandium sits between indium and the first row transition metals.[79]

Extensive literature studies have been conducted on the other trivalent metals in the exploratory synthesis of novel MOFs, yielding a wide range of framework topologies. Scandium, being towards the larger and lighter end of the scale, presents as an excellent choice of trivalent ion for MOF synthesis (Figure 1.29).

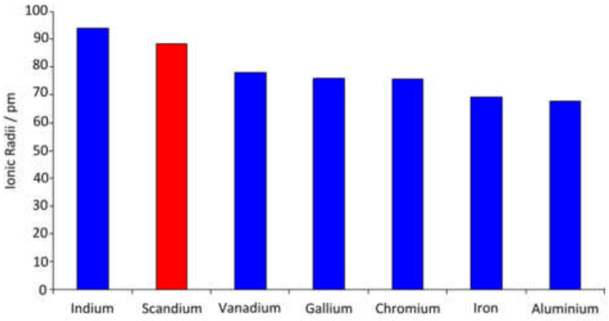

Figure 1.29: Comparison of the ionic radii of trivalent metals commonly used in carboxylate MOF syntheses.

1.4.5.2 Scandium in porous materials

Scandium bearing open framework materials were first reported as recently as 2002. Bull et. al. synthesised a scandium sulphate phosphate,[80] prepared hydrothermally and characterized by single-crystal X-ray diffraction, electron diffraction and solid-state NMR (Figure 1.30). The framework was templated using the cyclen macrocycle

(1,4,7,10-tetraazacyclododecane) resulting in a cubic arrangement of interconnected cages. At a similar time, the work of Riou et. al. in Versailles yielded an ethylenediammonium templated scandium phosphate (Figure 1.30).[81] This material, solved using single-crystal X-ray diffraction and solid-state NMR, is composed of corner shared ScO_6 octahedra and HPO_4 tetrahedra formed around the ethylenediammoniun organic template.

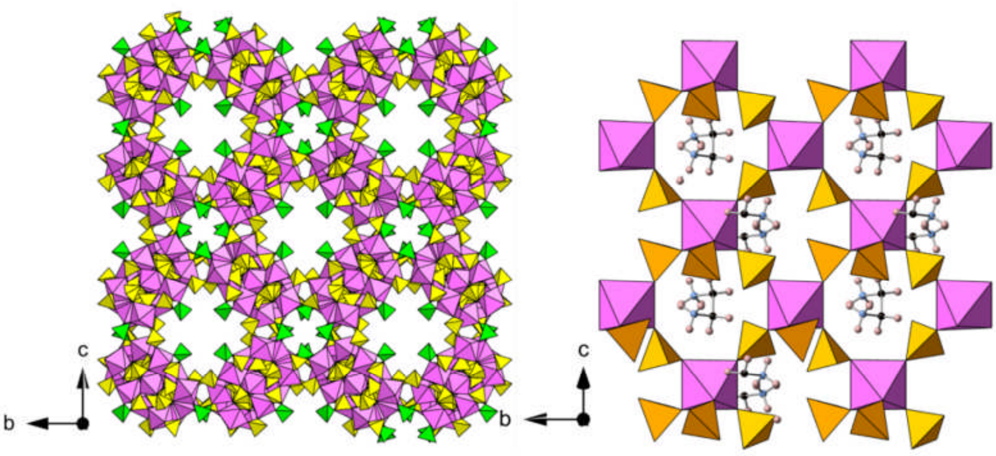

Figure 1.30: The first scandium based open framework materials. The scandium sulphate phosphate of Bull *et al.*[80] (*left*) and scandium phosphate of Riou *et al.*[81] (*right*). Scandium octahedra are shown in pink, sulphate tetrahedra in green and phosphonate tetrahedra in orange. Black, green and pink spheres represent the carbon, nitrogen and hydrogen atoms of the organic structure directing agent respectively.

These materials show that scandium is a suitable element for the preparation of open framework materials. Indeed, since 2002, scandium has been reported with a wide range of anionic framework components including phosphates, phosphites, phosphonates, bisphosphonates and carboxylates.

1.4.5.3 Scandium MOFs

Prior to this work there were few reports of scandium containing metal-organic frameworks. The first scandium based metal-organic framework was reported by Perles *et al.*[82] The framework is composed of layers of Sc_2O_{11} corner sharing dimers separated by the dicarboxylate linker succinic acid ($O_2CC_2H_4CO_2$) shown in Figure 1.31.

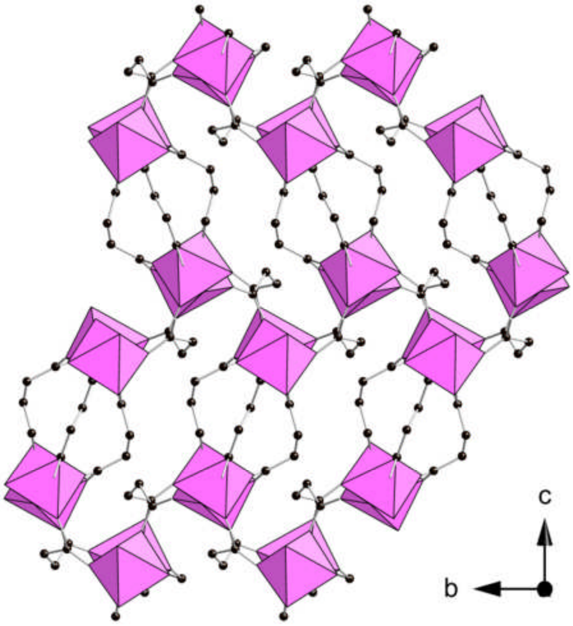

Figure 1.31: The first scandium MOF, a scandium succinate reported by Perles *et al*.[82] Scandium octahedra are shown in pink, black spheres represent the carbon atoms of the organic linker.

Although not permanently porous, catalytic studies showed that the scandium succinate was active in the Friedel-Crafts acylation of anisol (with acetic anhydride, 30 % yield after 24 hours) and the reaction of benzaldehyde with trimethyl orthoformate, (70 % yield after 4 hours) producing the dimethyl acetyl. Thermogravimetric analysis of the materials showed thermal stability of over 500°C under nitrogen gas. This represents a high thermal stability for an organic bearing framework and is representative of the strong scandium – oxygen bonds.

The first reporting of a permanently porous scandium based MOF was the scandium terephthalate Sc_2BDC_3.[27] The structure is composed of chains of octahedral Sc^{3+} bridged by terephthalate dianions shown in Figure 1.32. Along the chain, each scandium is separated by three bridging carboxylates of the terephthalates in each direction creating a chain of isolated ScO_6 octrahedra. This arrangement of linkers means that each chain is connected to six adjacent chains creating an array of microporous triangular channels, each delimited by the phenyl rings of the terephthalate linker. The fully coordinated metal centres and the strong Sc-O bonds result in high thermal stability in metal-organic framework materials.

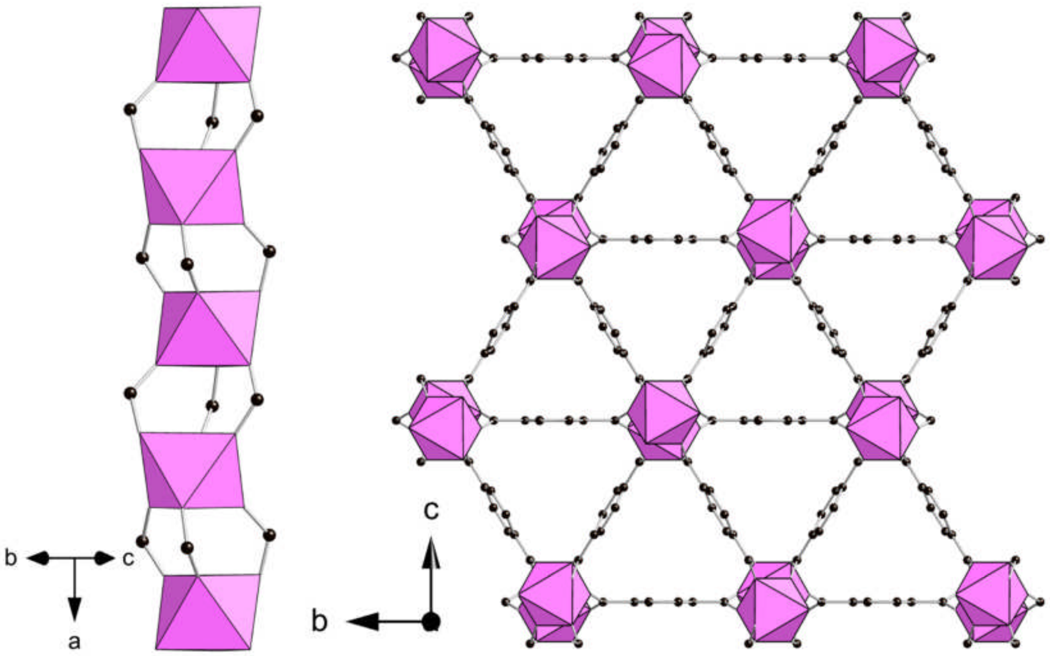

Figure 1.32: The small pore terephthalate Sc_2BDC_3 showing a single chain (*left*) and viewed down the triangular channels (*right*). Scandium octahedra are shown in pink, black spheres represent the carbon atoms of the organic linker.

Single crystal diffraction studies on Sc_2BDC_3, reported by Miller et. al,[83] describe in detail the structural response of the framework to adsorption of carbon dioxide and fuel related gases. The small microporous channels along with the hydrophobic nature of the pore surface make Sc_2BDC_3 an interesting candidate for separation experiments and will be discussed further in Chapter 5.

The other notable example of a scandium bearing metal-organic framework prior to this study was the scandium derivative of the MIL-88 network topology reported by Dietzel and coworkers[84] (with the 2,5-dihydroxyterephthalic acid) (Figure 1.33). This work is of particular interest as it was the first report of the scandium trimer unit and suggests that other networks which contain this unit could be possible. Thermogravimetric analysis showed an unusually low thermal stability with mass loss occurring from ~140°C with *in situ* X-ray diffraction showing a rapid decrease in crystallinity at this temperature point - with only 002 and 004 reflections observable. Although the framework topology suggests that there should be significant porosity, attempts to access the porosity with nitrogen gas at 77 K were unsuccessful. The structure was solved by single-crystal X-ray diffraction.

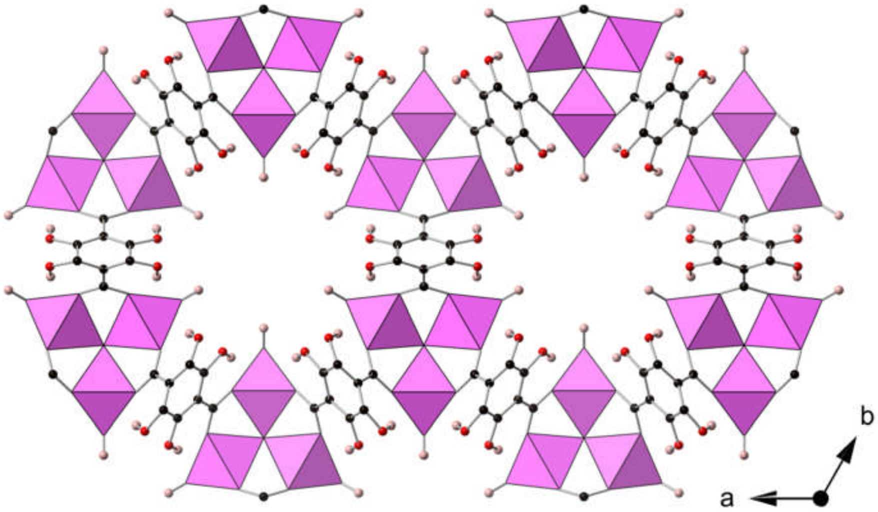

Figure 1.33: View down the channels of the scandium 2,5-dihydroxyterephthalic acid with the MIL-88 framework. Scandium octahedra are shown in pink, black, red and pink spheres represent the carbon, oxygen and hydrogen atoms of the organic linker respectively.

1.5 Column Chromatography

To date there are very few commercial applications known for MOF materials. One application where MOF materials could offer advantages over conventional materials is in chromatographic separations. MOFs offer many potential benefits over the current industrial standard including a tunable organic pore surface, large range of pore sizes and lower activation temperatures. The organic functionality can determine if a pore cavity is hydrophilic or hydrophobic, chiral or achiral and in the case of MOFs with sufficient pore size, molecules can be grafted onto the framework post-synthetically to modify the behaviour.

1.5.1 MOF-508

Prior to this work there was limited literature on the use of MOFs in chromatography. The first example of a MOF used in gas chromatography (GC) was a zinc based amine carboxylate, with the formula $Zn(BDC)(4,4'\text{-}Bipy)_{0.5}$ referred to as MOF-508.[76] The structure of MOF-508 is unusual as it consists of two interpenetrating flexible networks which can reversibly transform between a dense phase (MOF-508b) and an open phase (MOF-508a), with channels 4.0 × 4.0 Å, in response to addition of guest molecules. The framework consists of 2D layers of zinc paddlewheel clusters connected by the terephthalate linkers creating a square grid like arrangement which is pillared to adjacent layers by the 4,4’-bipyridine linkers on the axial sites of the paddlewheel. The large cubic cavities in the material allow another network to form within the first where the paddlewheel clusters sits in the middle of a cages, created by the first framework, and the linker molecules connect the clusters through the square shaped windows (Figure 1.34).

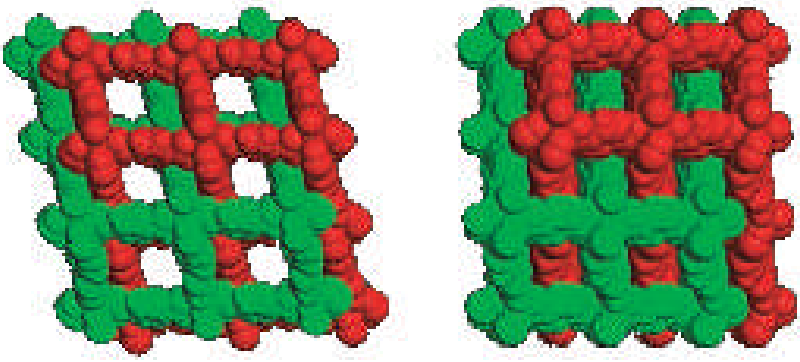

Figure 1.34: Structure of MOF-508a (*left*) and MOF-508b (*right*) showing the flexibility in the structure with the two interpenetrating networks coloured red and green[76]

This material was investigated in the separation of natural gas mixtures, linear alkanes and of linear-branched alkane mixtures. The experiment used a packed column, 120 cm long, containing 3 g of MOF-508 crystals ranging in size from 25-100 µm. The GC equipment used helium as the carrier gas at 60 psi and a temperature range of 40-150°C. The column was effective in the separations reported as shown in Figure 1.35.[76]

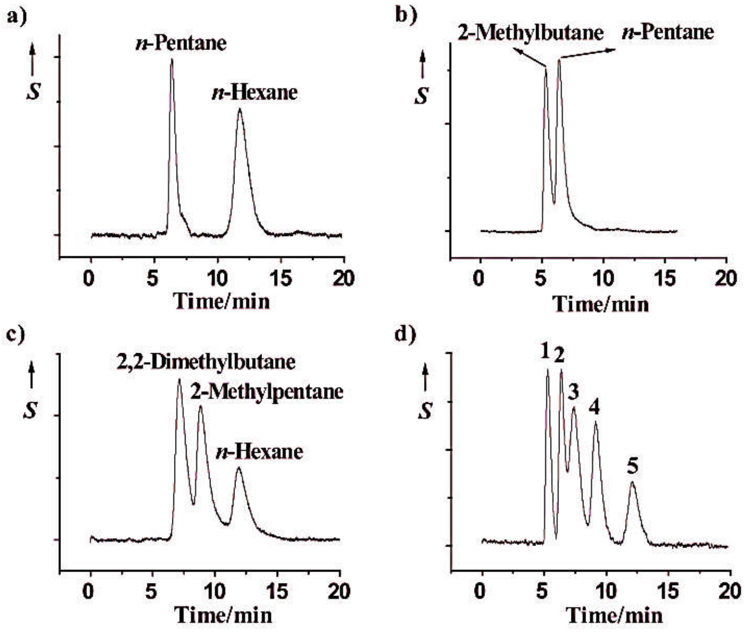

Figure 1.35: Chromatograms of alkane mixtures separated on a MOF-508 column: a) separation of n-pentane and n-hexane, b) separation of 2-methylbutane and n -pentane, c) separation of 2,2-dimethylbutane, 2-methylpentane, and n-hexane, and d) separation of an alkane mixture containing 2-methylbutane (1), n -pentane (2), 2,2-dimethylbutane (3), 2-methylpentane (4), and n -hexane (5). S = thermal conductivity detector response.[76]

The small pore channels of the MOF-508 structure and the van der Waals interactions with the pore wall are stated to be the main contributors to the observed retention times, with pore channels accessible only to the linear parts of the alkane and not the branched sections.

Although the separations measured for this material were successful, the flexibility and interpenetration observed in the structure could lead to problems, both in manufacturing and under use in the GC environment. As the active structure is stated to be the open form MOF-508a, with narrow linear channels lined with phenyl rings, a more rigid framework with similar pore chemistry could be a more suitable candidate.

1.5.2 MIL-47

Another significant example of MOFs in chromatography is the use of MIL-47(V) in the separation of xylene isomers reported by Alaerts et. al.[85] The separation of *para*-xylene *meta*-xylene and ethylbenzene is a challenging separation currently utilising ion exchanged zeolite X and Y. Before testing MIL-47(V) in a column experiment, the selectivities for three candidate materials were determined from bulk measurements of uptake from binary mixtures in batch experiments. These included MIL-47(V), MIL-53(Al) and $Cu_3(BTC)_2$. From these results, MIL-47(V) showed the most promising results and was tested in a column packed with MIL-47(V) crystals. Chromatographic testing, using a pulse chromatography experiment in the liquid phase with a 4 $mLmin^{-1}$ hexane flow, showed three well resolved peaks for the ethylbenzene, *meta*-xylene and *para*-xylene respectively (Figure 1.36).

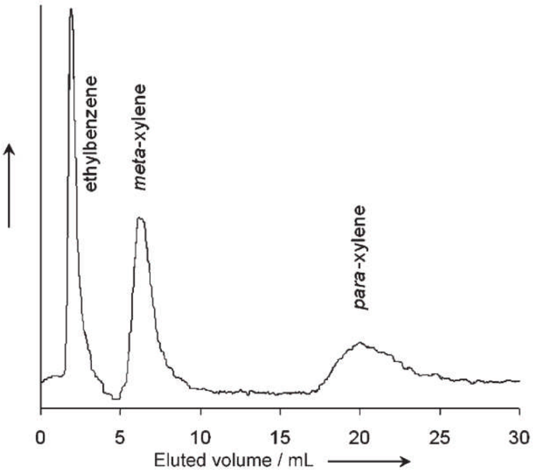

Figure 1.36: Chromatographic separation of a mixture of ethylbenzene, meta-xylene, and para-xylene on a column packed with MIL-47(V) in the liquid phase, with hexane as the desorbent at 298 K. The signal intensity of the refractive index detector is shown versus the eluted volume.[85]

The high selectivity could not be explained by the difference in interaction energies between the different components, as zero coverage adsorption enthalpies measured in the gas phase were reported as being identical. Instead, the packing of molecules in the structure was found to be the critical difference leading to the observed selectivity. For example, *para*-xylene, which eluted last in the experiment, was found to have a more efficient packing in the sterically restricted channels with strong π-π interactions between adsorbed *para*-xylene molecules. Positions for each of the molecules in the MIL-47(V) structure were identified by Rietveld refinement of X-ray powder diffraction data on the solids saturated with the relevant aromatic species.

1.5.3 MIL-101

A subsequent study, also using xylene isomers and ethylbenzene, used the large pore MIL-101(Cr) as the stationary phase.[74] In contrast to the previous examples which used packed columns, the MIL-101(Cr) was prepared as a coated capillary column. This type of column, referred to as porous layer open tubular (PLOT) or wall coated open tubular (WCOT) involves a thin film of the stationary phase on a the inner surface of a capillary column. The advantage of this technique is the small quantity of material required to prepare the column. The column was prepared by the dynamic coating method where a suspension of MIL-101 in ethanol was passed though the column by gas pressure leaving a thin film of the microcrystalline particles as a coating, SEM images of this coating are shown in Figure 1.37.

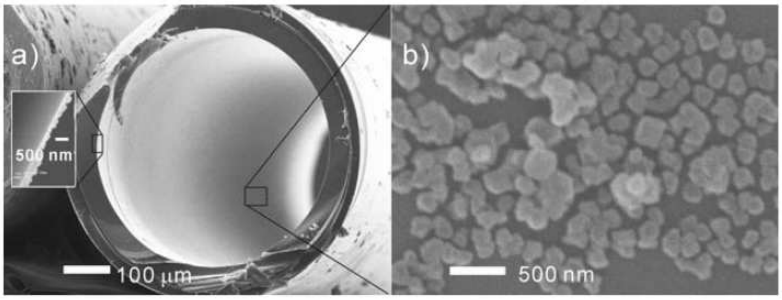

Figure 1.37: SEM images of the cross-section of the column (*left*) and the MIL-101 deposited on the inner surface of the capillary.[74]

The column showed well resolved, baseline separated peaks with theoretical plates calculated to be 3800 plates m^{-1} (Figure 1.38). The GC trace was collected on a 15 m × 0.53 mm (internal diameter) column at 160°C under a nitrogen flow of 3 $mLmin^{-1}$. Also of interest is that only 1 mg of MIL-101 was used in the preparation of the column.

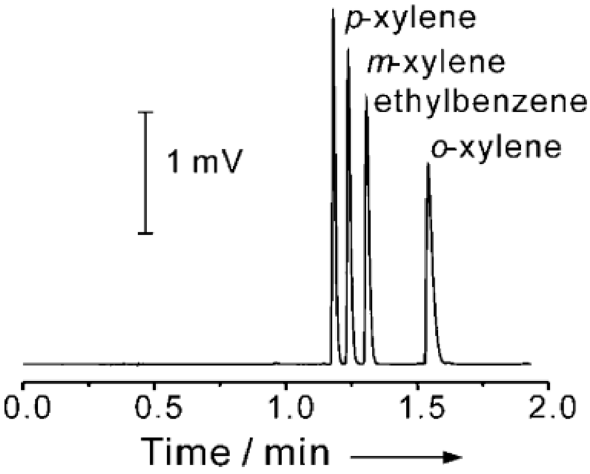

Figure 1.38: GC separation of xylene isomers and ethylbenzene on a MIL-101 coated capillary column (15 m long 0.53 mm i.d.) at 160°C under a N_2 flow rate of 3 mL min^{-1}.[74]

1.5.4 Column summary

The literature on metal-organic framework based column preparations has shown that the PLOT type columns, with the stationary phase coating the internal surface of the capillary column, show the most promise for future development. The main advantage of this method over the packed column approach is the significantly smaller quantity of MOF required. The PLOT column approach, coupled with the use of the large pore MIL-101 as the stationary phase, has shown promising baseline separation of peaks using a mixture of xylene isomers and ethyl benzene which are challenging to separate by current methods. These results show MOFs to be suitable candidate materials for use in this environment where materials could be chosen or modified to specific operating requirements.

1.6 Aims

The principal aim of this work was to investigate the effects of structural flexibility and functionalization on the adsorption and separation properties of metal-organic framework materials.

The work focused on two classes of materials, phosphonates and scandium carboxylates where the synthesis of novel scandium carboxylates and functionalisation of novel and existing materials was the major area of the research.

Novel materials were characterized using X-ray diffraction, solid-state NMR, chemical analysis (CHNS) and thermogravimetric analysis (TGA). Porosity of the materials was characterized by nitrogen and carbon dioxide adsorption to determine optimal weight percent mass uptake and surface area including both volumetric and gravimetric analysis techniques.

Materials with suitable porosity progressed for further adsorption study utilising techniques such as zero-length column and breakthrough curves to determine suitable separation applications. Ultimately separation experiments were carried out using a packed or capillary column in a gas chromatography set-up to investigate the use of porous metal organic framework materials in the separation of small gas molecules and short-chain hydrocarbons.

2 Experimental Methods

2.1 Synthesis Methods

Materials in this work were synthesised via a hydrothermal or solvothermal route. The starting mixture consisted of a metal oxide or salt, organic ligand and any structure-directing agents (SDA), dissolved or dispersed in solvent. The mixtures were stirred thoroughly, transferred to a PTFE lined stainless steel autoclave (examples of which are shown in Figure 2.1), sealed and heated in an oven. The products were filtered and washed with solvent (typically the solvent used in the synthesis) and dried at 50 °C in a drying oven. Exceptions to this were when the solvent used was a high boiling point organic solvent such as N,N'-Dimethylformamide (DMF). The solid products were washed thoroughly with ethanol after filtration or stirred in an excess of the solvent to exchange any solvent coordinating to the metal sites.

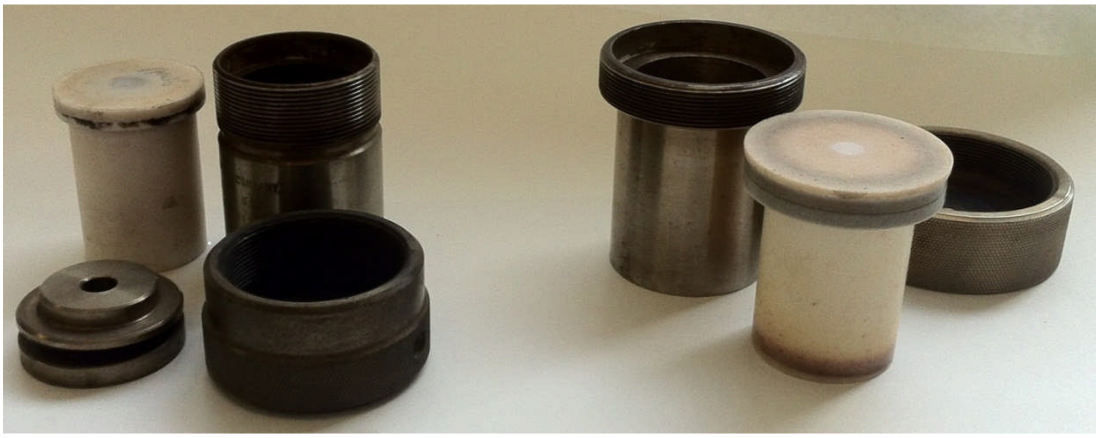

Figure 2.1 Example of autoclaves used in this study. The Parr type, 23 mL autoclave (*left*) and a 40 mL autoclave made in-house (*right*).

The MOF materials that exhibit flexibility on solvent exchange needed special treatment before single-crystal diffraction data could be collected. When crystals were produced, it was necessary to treat the materials as if they were air-sensitive to ensure that there was no loss of crystallinity due to solvent loss on drying. These samples were sealed in a sample vial under the same solution used in the crystallization (commonly referred to as 'mother liquor') and transferred directly to a poly-fluorinated oil used to mount the single-crystals on a diffractometer for data collection. The structural models resulting from the single-crystal data on the as-synthesised form of the solid can then be refined using information on the unit cell and volume from powder X-ray diffraction and adsorption measurements to further model the behavior and to understand the flexibility or response to solvent exchange or desolvation.

2.2 Characterisation of Materials

2.2.1 X-ray Diffraction

X-ray diffraction (XRD) is the principal technique for obtaining information on long range order within crystalline framework materials. A crystal is a solid consisting of a three dimensional periodic array of atoms or molecules. The array of equivalent points or lattice points of a crystalline solid can be represented by a repeat unit known as a unit cell (Figure 2.2). A unit cell can in turn be described by a combination of an asymmetric unit, the minimum set of atoms required to produce the full structure, and the symmetry elements of a space group. Any plane of lattice points can be described using the Miller indices (hkl) where the plane described is orthogonal to the direction (h,k,l).

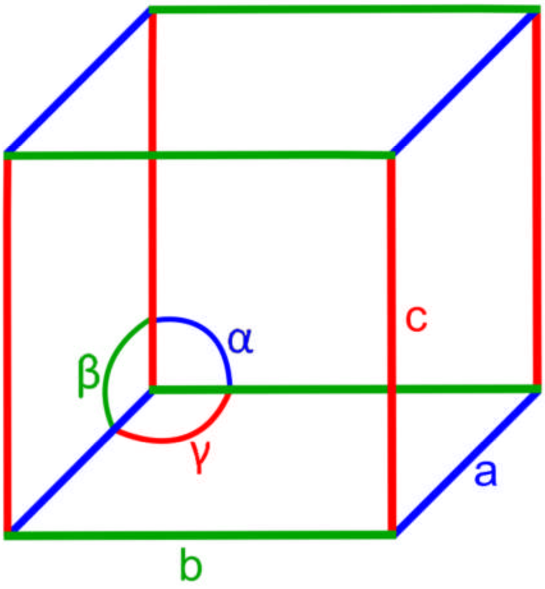

Figure 2.2 The unit cell with lengths a,b,c and angles α, β, γ

Mathematically there are a finite number of ways in which three dimensional lattices can be represented. There are seven crystal systems in total. Within the crystal systems there is lattice centering; Primitive (P) where the lattice points are on the cell corners; Body-centering (I) with lattice points on the cell corners and an additional point in the centre of the cell. Single face centering (A, B or C) where there are lattice points on the cell corners and an additional point in the centre of one face; Face-centering (F) with lattice points on the cell corners and one additional point at the centre of each face. This would give a total of 42 lattice types (seven crystal systems each with six lattice centering options) but as a number of these are equivalent to each other, the result is 14 distinct lattices referred to as Bravais lattices (Table 2.1).

Lattice Systems	Defined by	14 Bravais lattices
Triclinic	$a \neq b \neq c\,;\ \alpha \neq \beta \neq \gamma$	P
Monoclinic	$a \neq b \neq c\,;\ \alpha = \gamma = 90° \neq \beta$	P C
Orthorhombic	$a \neq b \neq c\,;\ \alpha = \beta = \gamma = 90°$	P C I F
Tetragonal	$a = b \neq c\,;\ \alpha = \beta = \gamma = 90°$	P I
Rhombohedral	$a = b = c\,;\ \alpha = \beta = \gamma \neq 90°$	P
Hexgonal	$a = b \neq c\,;\ \alpha = \beta = 90°\, \gamma = 120°$	P
Cubic	$a = b = c\,;\ \alpha = \beta = \gamma = 90°$	P I F

Table 2.1: The 7 lattice systems and the associated Bravais lattices.

Thirty two point groups, sets of symmetry operations comprising mirror planes, rotations, translations and inversions, when applied to an atom or group of atoms, produce the unit cell. The combination of the Bravais lattice and the point group gives what is referred to as the space group of a given material. There are a total of 230 unique space groups which can be used to represent a crystal structure.

Powder and single crystal X-ray diffraction were the principal techniques of this project used in the analysis and characterisation of the synthesised materials. It is also possible to use these techniques to understand the structural effects of processes such as adsorption and dehydration on the observed framework motif. Powder diffraction data were used for phase identification and also for structure elucidation in the case of materials where single crystals did not form readily. As the data obtained are one dimensional, where possible high resolution X-ray diffraction data was obtained from synchrotron radiation sources and, combined with computational and elemental analysis, used to determine structural information. Single crystal data gives a complex 3 dimensional output of reflections that can be processed by computational methods to directly obtain a model for the structural properties of a material and is the primary method of structural characterisation in systems where single crystals are obtained.

2.2.1.1 Single Crystal X-ray Diffraction

The concept of X-ray diffraction by crystals was originally proposed by Max von Laue (who conducted the first experiments) and later developed by William and Laurence Bragg. In X-ray diffraction a regular array of identical lattice planes in a crystalline solid act as a diffraction grating and the observed scattering of the incident X-rays occurs constructively where the path length difference is equal to an integer number of wavelengths, as described by Bragg's law (a schematic representation is shown in Figure 2.3).

$$n\lambda = 2d\sin\theta \qquad (1)$$

Constructive interference occurs where the path difference is an integer number of wavelengths $(AB + BC = n\lambda)$

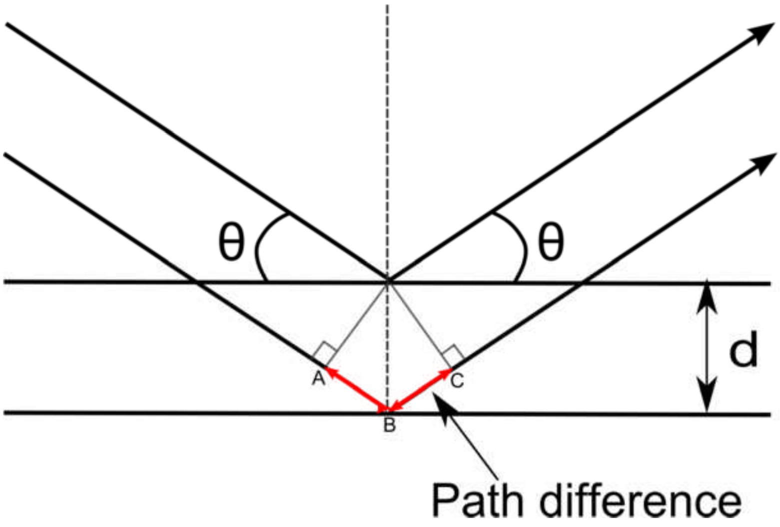

Figure 2.3: Schematic representation of Bragg's law.

Single crystal X-ray diffraction relies on the same principle as powder diffraction but in this case a single crystal is mounted on a goniometer, a device which allows the crystal to be rotated in three dimensions and a series of 2 dimensional diffraction images are collected, using a CCD detector, stepwise over a known range to ensure enough information is collected to determine the structure. The next step involves taking the series of images and indexing the spots to determine the unit cell dimensions and subsequently the space group. Once the space group is known, Fourier transforms are applied to the data to relate the intensity of the diffraction spots (I) to the structure factor (F):

$$\mathrm{I_{hkl}} \propto |\mathrm{F_{hkl}}|^2 \qquad (2)$$

As the intensity is proportional to the square of the structure factor it means that the phase of (F) cannot be determined directly, this is commonly referred to as the 'phase problem'. Experimental diffraction patterns represent scattering from parallel planes (hkl) and are dependent on the type and location of atoms within the unit cell (xyz).

$$F_{hkl} = \sum f_n e^{2\pi i(hx+ky+lz)} \qquad (3)$$

Where f_n is the atomic scattering factor for each atom (n)

The scattering is further influenced by thermal vibration (or positional disorder) of atoms in the unit cell.

$$F_{hkl} = \sum f_n e^{2\pi i(hx+ky+lz)} \cdot e^{\frac{-8\pi^2 U_n \sin^2\theta}{\lambda^2}} \qquad (4)$$

Where U_n is the temperature factor of the atom, a measure of the displacement around the point (xyz) and can be isotropic (spherical) or anisotropic (elliptical).

To obtain a structure, the electron density at points in the cell must be calculated.

$$\rho_{xyz} = \frac{1}{V}\sum_{hkl} |F_{hkl}| e^{-2\pi i(hx+ky+lz)} \qquad (5)$$

To overcome this 'phase problem' there are various statistical methods available, the most notable of these is the 'Direct Methods' approach developed by Hauptman and Karle. Direct Methods assumes that a structure is composed of discrete atoms with associated electron density and that the electron density cannot take a negative value. These assumptions combined with the amplitudes of the structure factor means that a probable phase can be determined. The SHELX[86] and SIR[87] software suites which implements Direct Methods were used to determine the atomic positions from any single crystal data sets collected.

Before powder diffraction analysis, the samples were ground so there were small crystallites and rotated in the X-ray beam during sample collection. The result of this process is that the sample can be thought of as an average of all possible orientations of the crystallites with respect to the X-ray beam and the diffraction images produced will therefore be an average of the series of spots that would be produced from a single crystal resulting in a series of diffraction cones attributable to the lattice vectors in reciprocal space. A schematic representation of single crystal and powder X-ray diffraction is shown in Figure 2.4.

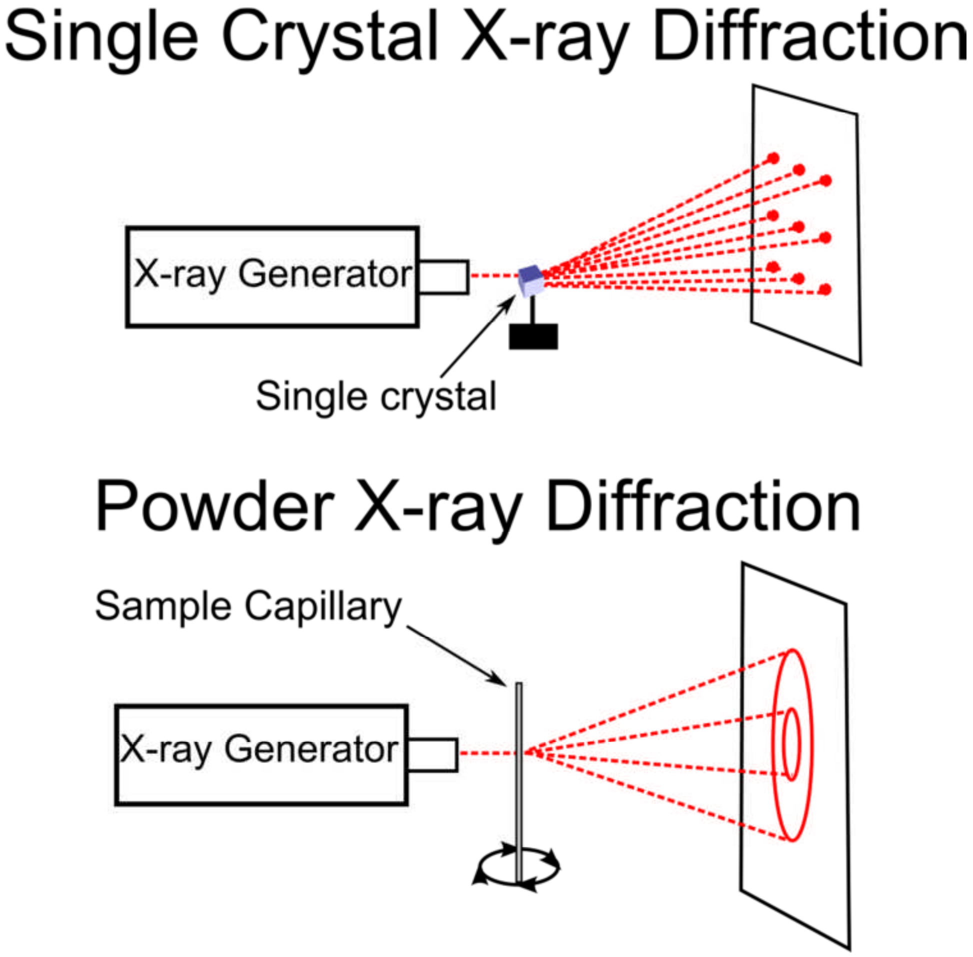

Figure 2.4: Schematic of single crystal and powder X-ray diffraction.

Powder XRD is an effective means of initial sample screening and phase identification in crystalline MOF materials. In large crystal and microcrystalline samples, comparison of patterns obtained experimentally with either theoretical patterns (produced from published structures or single crystal data) or other experimental patterns gives information on the products obtained and, in the case of samples containing single crystals, ensures the crystal analysed is representative of the bulk phase. As a result of the averaging of the diffraction spots into cones, it is more difficult to obtain phases from the powder X-ray diffraction patterns making the structure solution much more challenging than from single crystal data.

From indexing the peaks observed in the diffraction pattern, it is possible to determine the unit cell dimensions and therefore the lattice system, from systematic absences it may also to possible to identify one or more candidate space groups. The position of the peaks together with the intensity is input using a number of search algorithms the most notable of which are ITO,[88] DICVOL[89] and TREOR[90]. Software is available to attempt structure solution directly from powder X-ray diffraction data, programs such as EXPO[91] combine the indexing algorithm with direct methods and simulated annealing to obtain a model or partial model directly from the powder diffraction pattern. This approach is best used in combination with detailed elemental and density analysis on the materials under study. If the density and elemental composition of a material is known, it is possible to calculate the contents of the unit cell. This information is then used to construct the simulated cell and fill it to the desired composition, either as individual atoms or as larger rigid body fragments if a molecule or inorganic unit is known to be present in the material.

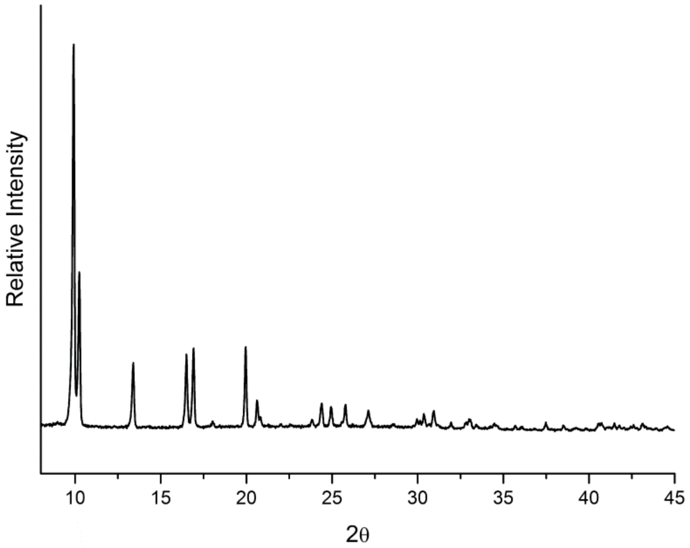

Figure 2.5 Example powder X-ray diffraction pattern collected on a capillary containing a scandium terephthalate sample, using a Stoe STADI/P diffractomoter.

Powder data was collected either in-house on a Stoe STADI/P diffractometer (an example of which is shown in Figure 2.5) in transmission mode with primary monochromation and Cu Kα_1 X-radiation or collected at a synchrotron facility such as Diamond Light Source beamline I11 which is configured for high resolution powder diffraction. Samples were ground into fine powder to prevent preferred orientation effects and mounted between two Mylar discs or placed in a 0.5 mm or 0.7 mm quartz capillary. A typical X-ray powder diffraction pattern obtained from a Stoe STADI/P diffractometer is shown in Figure 2.5.

Single crystal data was collected on a Rigaku Mercury CCD diffractometer using monochromated Mo Kα radiation or the ACTOR SM automated system utilising a sealed tube X-ray source and a CCD detector.

2.2.2 Rietveld Refinement and Le-Bail method

As well as using powder X-ray diffraction as a screening tool, it is also possible to use the data to evaluate a structural model. Rietveld refinement is a technique used to relate a structural model to experimentally obtained diffraction data (neutron and/or powder X-ray diffraction data). As the Rietveld method requires a starting structural model, preferable in reasonably good agreement with the experimental data, it is a refinement technique rather than a structure solution method. Structural models for Rietveld refinement in this study were primarily obtained by modifying a literature structural model (of a similar material) or directly from a single-crystal structure solution in the case of bulk phase analysis.

It is often advisable to use the Le-Bail method of unit cell refinement prior to the Rietveld analysis. The Le-Bail method is independent of the unit cell contents and is used to determine if it is possible to fit the diffraction pattern using only the unit cell and symmetry proposed for the model. As the difference between an experimental diffraction pattern and a pattern calculated from the model is based on the full diffraction pattern calculation, it is important to start with a model where the unit cell and symmetry is as close to the experimental pattern as possible.

Rietveld refinement uses a least squares method to minimize the difference between an experimental diffraction pattern and a calculated pattern.

$$M = \sum w(I_o - I_c)^2 \tag{6}$$

Where I_o and I_c are the observed and calculated intensities. The weighting w is based on the calculated errors for each reflection and the sum is over the full data set.

The main statistics reported for how well the data matches the model are the reduced χ^2, R_p and R_{wp}.

$$\chi^2 = \frac{M}{(N_{obs} - N_{var})} \tag{7}$$

Here N_{obs} is the total number of observations in the pattern and the N_{var} is the number of variables in the least squares refinement and the optimum value for χ^2 is 1.0. R_p and R_{wp} are the calculated residuals, again a measure of the difference between the calculated and experimental pattern with the value tending to zero as the refinement fit improves.

$$R_p = \frac{\sum |I_o - I_c|}{\sum I_o}$$

and

$$R_{wp} = \sqrt{\frac{M}{\sum w I_o^2}}$$

2.2.3 NMR

Solid state nuclear magnetic resonance (NMR), has been used in this study to aid in the structural characterisation of the MOF materials. Where X-ray diffraction gives information on long-range order, NMR gives information on the local environment of each unique atom. A combination of the two techniques can be invaluable in the determination of structural details of the materials studied.

NMR works on the principle that nuclei with a non-zero nuclear spin possess nuclear spin (I) and angular momentum (P) generating an associated (non-zero) magnetic moment (μ)

$$\mu = \gamma \mathrm{P} \tag{8}$$

Where γ is the gyromagnetic ratio of the nucleus.

The nuclear spin quantum number (I) can be any multiple of ½ for $I \geq 0$ creating $(2I+1)$ discrete values for the angular momentum.

Using hydrogen (^{1}H) with one proton and spin $I = ½$ as an example, the magnetic moments arising from the spins can be thought of as individual magnets. These magnetic moments can be aligned (either parallel or anti-parallel) when an external magnetic field is applied. The lower energy state (spin state (x), Figure 2.6) will have a slight excess of spins relative to the higher energy state.

$$\Delta E = \gamma \hbar B_0 \tag{9}$$

Where $\hbar$ is the reduced Planck's constant and B_0 is the applied magnetic field.

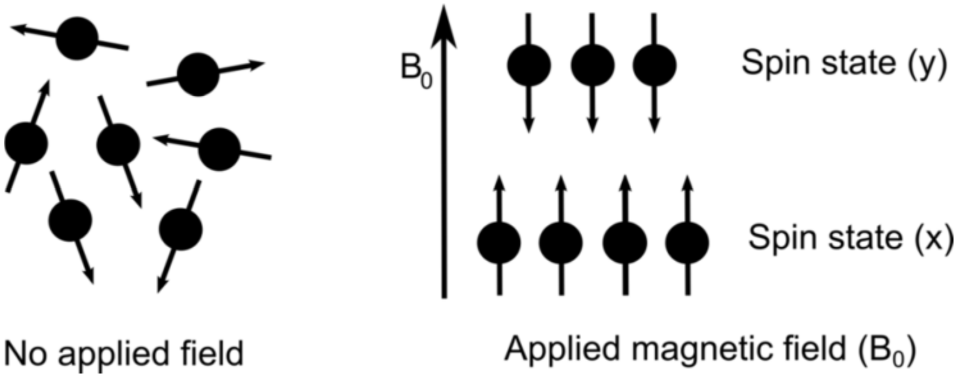

Figure 2.6: Alignment of nuclear spins in the presence of an external magnetic field.

Although aligned with the external magnetic field, the magnetic moment precesses around the axis of the applied field (Figure 2.7), by convention taken to be the z-axis, proportional to the strength of the field (B_0).

$$\omega = \gamma B_0 \tag{10}$$

Where ω is known as the Larmor frequency

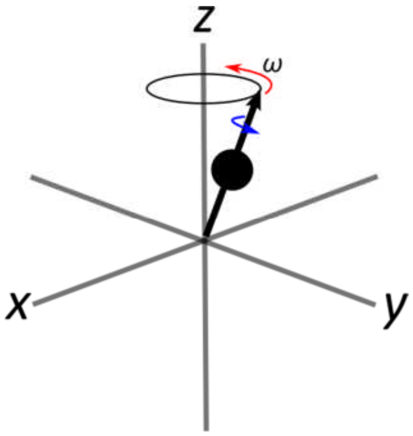

Figure 2.7: Precession of a magnetic moment around the axis of the applied field.

The result is that the net magnetisation of a spin system under study can be thought of as a single magnetic moment, referred to as the bulk magnetisation vector (Figure 2.8), M_0, along the z-axis and parallel to the applied magnetic field (B_0).

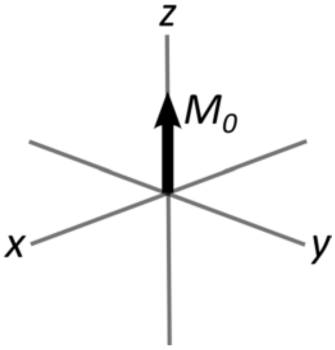

Figure 2.8: Bulk magnetization vector.

Radiofrequency (RF) pulses can be used to move the bulk magnetisation vector (Figure 2.9), M_0, away from the z-axis. The extent to which it is moved is controlled by the duration of the RF pulse. The angle, θ, through which the vector M_0 moves is related to the field strength, B_1, and duration, t_p, of the RF pulse by the following equation:

$$\theta = \gamma t_p B_1 \tag{11}$$

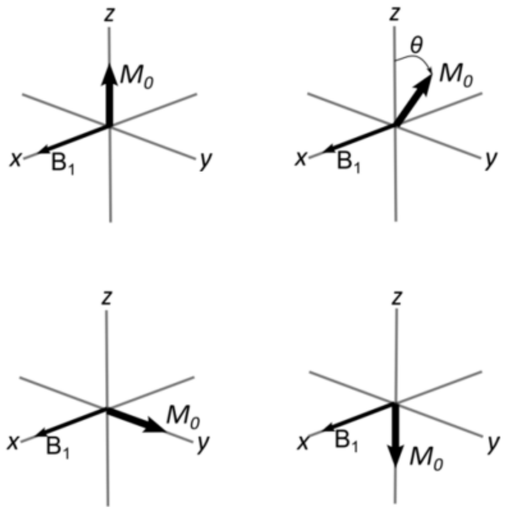

Figure 2.9: Representation of the change in the bulk magnetization vector as a result of a radiofrequency pulse B_1.

Following the RF pulse, the NMR signal is detected by means of an oscillating voltage in a coil surrounding the sample, upon relaxation from the excited state to the thermal equilibrium. Two main processes of relaxation are observed:

1: Longitudinal relaxation (T_1): spin – also known as lattice relaxation or the decay constant for repopulation of the energy levels to the thermal equilibrium level

2: Transverse relaxation (T_2): also known as spin-spin relaxation or the decay constant for the net bulk magnetisation vector in the x-y plane to return to zero.

The detected signal, free induction decay (FID) is Fourier transformed to produce the frequency spectrum of the signal known as the NMR spectrum.

2.2.3.1 Dipolar Broadening

Dipolar interactions are the interaction of a nuclear spin with the magnetic field of an adjacent nuclear spin. This through space interaction can result from heteronuclear or homonuclear species and is one effect responsible for broadening solid state NMR spectra. In solution, molecules experience continuous Brownian motion that results in an averaging of the dipolar interactions over the different orientations whereas in the solid state, if the sample is static, the spins couple resulting in a broad signal.

Dipolar coupling frequency

$$B_{jk} = \frac{\mu_0}{4\pi}\frac{\gamma_j\gamma_k\hbar}{r_{jk}^3}[1 - 3\cos^2\theta] \tag{12}$$

Anisotropic dipolar interactions can be suppressed by rotating the sample around an axis, 54.74° to the applied magnetic field. At this angle, $[1 - 3\cos^2\theta] = 0$ and the broadening of the spectra due to the dipolar interaction is reduced. This is known as magic-angle spinning (MAS). To average the interaction to zero, the rate of spinning must be greater than the magnitude of the interaction – the width of the static powder spectra, below this value additional signals are observed in the spectra known as spinning sidebands.

2.2.3.2 Quadrupolar Interactions

Nuclear spins with $I > 1/2$ have a non-spherical charge distribution resulting in an electric quadrupole moment. The interaction of this quadrupolar moment with electric field gradients can lead to extremely broad lines in the NMR spectra but can also give useful information about the coordination environment around the species under study. The quadrupole interaction may be of the order of 10's of MHz which is not insignificant compared to the Zeeman splitting of the order of 10-100's of MHz (Figure 2.10).

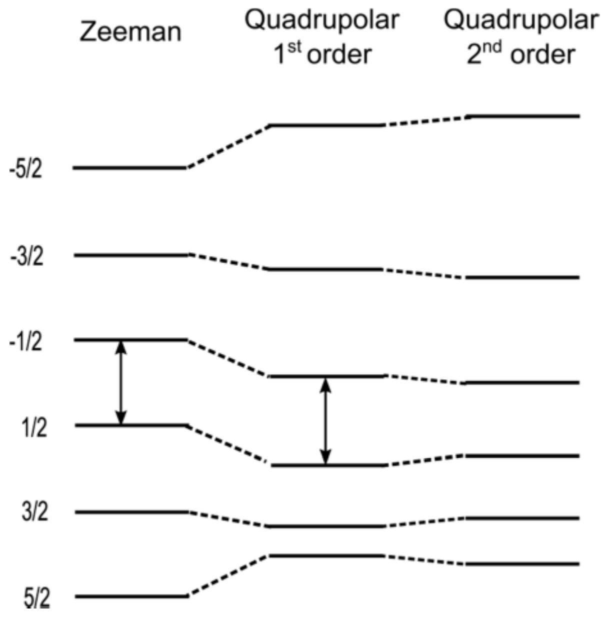

Figure 2.10: Zeeman splitting and degeneracy of energy levels for a spin 5/2 nucleus.

The First order quadrupolar interaction can be averaged or minimized by increasing the spin rate of MAS and by increasing the magnetic field strength. Importantly, the central transition – indicated by the arrows in Figure 2.10 – is not influenced by the first order quadrupolar interaction and has the same magnitude as the Zeeman interaction. The satellite transitions are visible as broadening of the spectra or as spinning sidebands if the spectral lines are resolved. The second order quadrupolar interaction cannot be averaged to zero by MAS.

There are a number of methods which can be employed to minimise the influence of the second order quadrupolar interactions. One option is to use advanced rotor technology to spin the sample around two axes simultaneously known as double rotation (DOR) at the magic angle (54.74°) and at 30.54°. Another technique, dynamic angle spinning (DAS), uses sequential spinning at two different angles. The final method, and most relevant to this study, is Multiple Quantum Magic Angle Spinning (MQMAS). This technique uses pulse sequences to excite multiple quantum coherences such as triple quantum (3Q) and 5Q coherences (Figure 2.11).

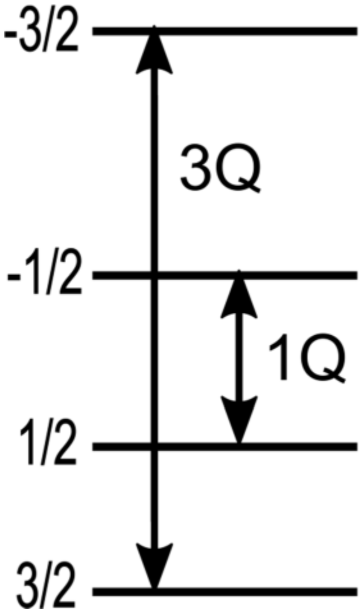

Figure 2.11: Triple quantum excitation

Although the 3Q excitation cannot be observed directly, it can be converted to a 1Q coherence for direct observation. Although the contribution of the second order components are non-zero they are different and as such can be used to separate the isotropic and second order effects. The result of the analysis is a 2D spectrum that suppresses the broadening observed for the quadrupolar nuclei and can be done carried out using standard MAS equipment (Figure 2.12).

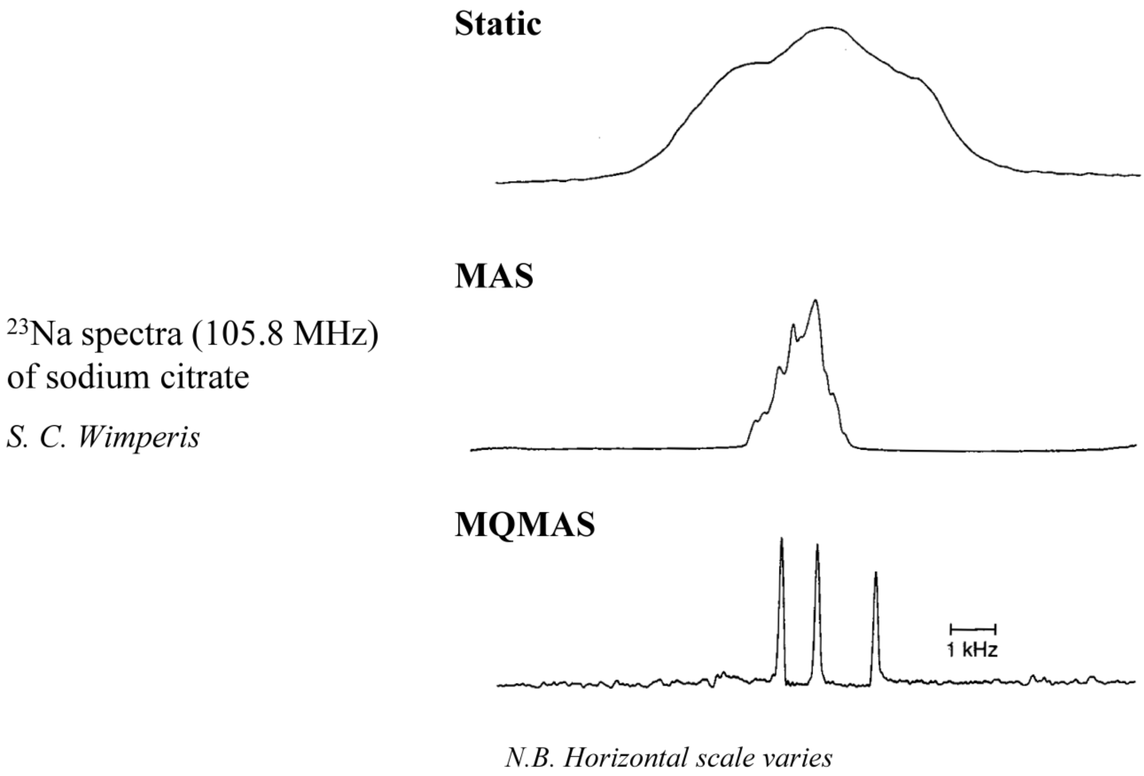

Figure 2.12: Additional information can be obtained by advanced techniques such as MAS and MQMAS.

Solid state NMR spectra were acquired using a Bruker Avance III spectrometer equipped with a wide-bore 14.1 T magnet yielding Larmor frequencies of 156.375 MHz, 242.937 MHz and 145.762 MHz for ^{27}Al (I = 5/2), ^{31}P (I = 1/2) and ^{45}Sc (I = 7/2) respectively. Samples were packed into conventional 4 mm ZrO_2 rotors and magic angle spinning (MAS) rates of 12.5 kHz (^{27}Al and ^{31}P) and 10 kHz (^{45}Sc) were used. Chemical shifts were referenced to 1M $Al(NO_3)_{3\ (aq)}$, H_3PO_4 and 0.2M $ScCl_{3\ (aq)}$.

One dimensional ^{27}Al, ^{31}P and ^{45}Sc MAS NMR were obtained using single pulse experiments with typical pulse lengths of 1.8 µs, 5 µs and 1.5 µs respectively. Typical power of the radiofrequency pulse used was 0 dB (Bruker power attenuation rating in decibels) with 24 scans (^{27}Al), 4 dB with 24 scans (^{31}P) and 0 dB with 64 scans (^{45}Sc). Spectral analysis was performed using the Topspin 2.1 program.

2.2.4 Chemical Analysis (CHNS and EDX)

Chemical analysis was used to determine the composition of materials both for phase identification and to aid in structure solution. Elemental analysis, carried out using a CE instruments EA 1110 CHNS analyser, will be used to determine the relative amount of carbon, nitrogen and hydrogen present in the synthesised materials. The presence of the metals and other heavy atoms will be identified using a JOEL 5600 SEM with an Oxford INCA Energy 200 EDX system.

2.3 Adsorption

MOF materials can range from non-porous dense phase materials through to low-density highly porous cage like structures demonstrating porosity in the mesoporous region. One important characteristic of MOF materials is the surface area. When looking at potential applications, the internal structure of the porous materials must be considered. Separations may be possible in materials where pore channels are accessible to only one species of a mixture or a species has a stronger interactions with the pore surface. Alternatively catalysis may only be possible if the substrate in question can access the available free metal sites. As a result it is important to know the crystallographic structure of the material to propose possible experiments and also verify with experimental data to ensure the materials behaves as expected.

One of the challenges with measuring the surface area of MOF materials is that the assumptions used when calculating conventional surface areas are not valid in the case of MOF materials. The Langmuir surface area calculations assume that:

i: Solid surface is uniform and contains a number of equivalent sites each of which may be occupied by only one molecule of adsorbate.

ii: A dynamic equilibrium exists between the gas (at pressure, P) and the adsorbed layer at constant temperature.

iii: Adsorbate molecules from the gas phase are continually colliding with the surface. If they impact a vacant adsorption site, they form a bond and stick. If they strike a filled site they are reflected back into the gas phase.

iv: Once adsorbed, the molecules are localised and the enthalpy of adsorption per site remains constant regardless of coverage.

This leads to the Langmuir adsorption isotherm equation for associative adsorption which predicts how the fractional monolayer coverage θ of adsorbate changes with P.

$$\theta = \frac{N_S}{N} = \frac{KP}{1+KP} \left(K = \frac{k_a}{k_d}\right) \tag{13}$$

Rearrangement of equation (13) gives the form of a straight line:

$$\left(\frac{P}{N_S}\right) = \frac{1}{NK} + P\left(\frac{1}{N}\right) \tag{14}$$

Where a plot of $\left(\frac{P}{N_S}\right)$ vs (P) gives a straight line graph with gradient $\left(\frac{1}{N}\right)$ and intercept $\left(\frac{1}{NK}\right)$

As there is assumed to be only monolayer coverage of the surface:

$$S_A = N \times A_m \tag{15}$$

The main restriction of the Langmuir surface area calculated from (14) is that there is assumed to be only monolayer coverage and that all sites are of equivalent energy. In MOF materials where there are 1,2 or 3 dimensional channels and combinations of metal sites and organic units, there will many possible sites all with different energy. MOF materials also demonstrate porosity that can only be attributed to multilayer adsorption and therefore the Langmuir surface area calculations are invalid.

An alternative to the Langmuir isotherm is the Brunauer Emmett and Teller (BET) isotherm. The BET isotherm is an extension of the Langmuir isotherm to multilayer adsorption. The assumptions for the BET isotherm are as follows:

i: Adsorption of first adsorbate layer is assumed to take place on an array of surface sites of equal energy.

ii: Second layer adsorption can only take place on the first, third on top of second, etc and when P = P_0 an infinite number of layers will form.

iii: At equilibrium, the rates of condensation and evaporation are the same for each individual layer.

iv: When the number of adsorbed layers is greater than or equal to two, the equilibrium constants are equal and the value of $\Delta H^0_{AD} = -\Delta H^0_{VAP}$. For the first layer the enthalpy of adsorption is as in the langmuir case. Summation of amount adsorbed in all layers leads to the BET equation.

$$\frac{P}{N_s\,(P_0-P)} = \frac{1}{NC} + \left(\frac{C-1}{NC}\right) \times \frac{P}{P_0} \tag{16}$$

Where

$$C \approx e^{\left(\frac{\Delta H_D^0 - \Delta H_{VAP}^0}{RT}\right)} \quad \Delta H_D^0 = \text{enthalpy of desorption} = -\Delta H_{AD}^0$$

Although the assumptions used in the BET isotherm are still not strictly true of MOF systems, work by Snurr *et. al*[92] – on the applicability of BET for determining the surface area of MOF materials – has shown that it is possible to get good agreement between the BET surface area calculations and the results obtained experimentally (Figure 2.13). This result is more significant for the material studied due to the fact that the MOF-5 structure contains arrays of square pores, an arrangement that means the assumption of multilayer formation cannot occur directly as the first few layers would render the centre of the pore inaccessible.

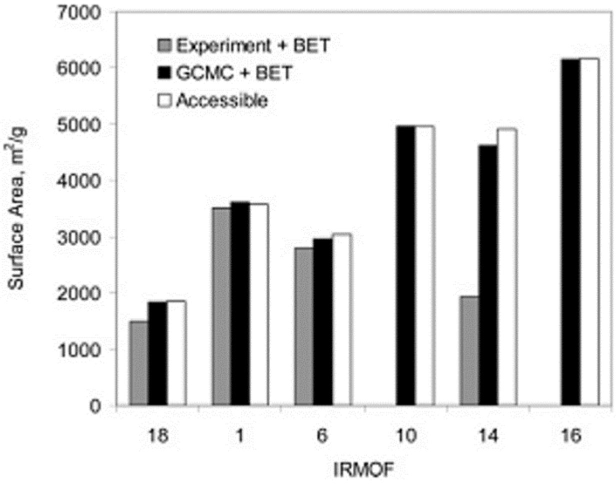

Figure 2.13 Literature example of molecular modelling comparison of the BET method of surface area calculation to that derived from Monte Carlo integration method for the IRMOF series of materials.[92]

Another modelling technique to calculate the accessible surface area of a MOF material uses a Monte Carlo integration technique where a probe molecule (nitrogen sized) is effectively 'rolled' over the framework surface produced from the crystal structure where the diameters of the framework atoms are taken from the DREIDING force field. As the simulations of the adsorption is being run, it is possible to take 'snapshots' of the material to observe where in the structure the calculations approximate the adsorbed molecules to be located (Figure 2.14).

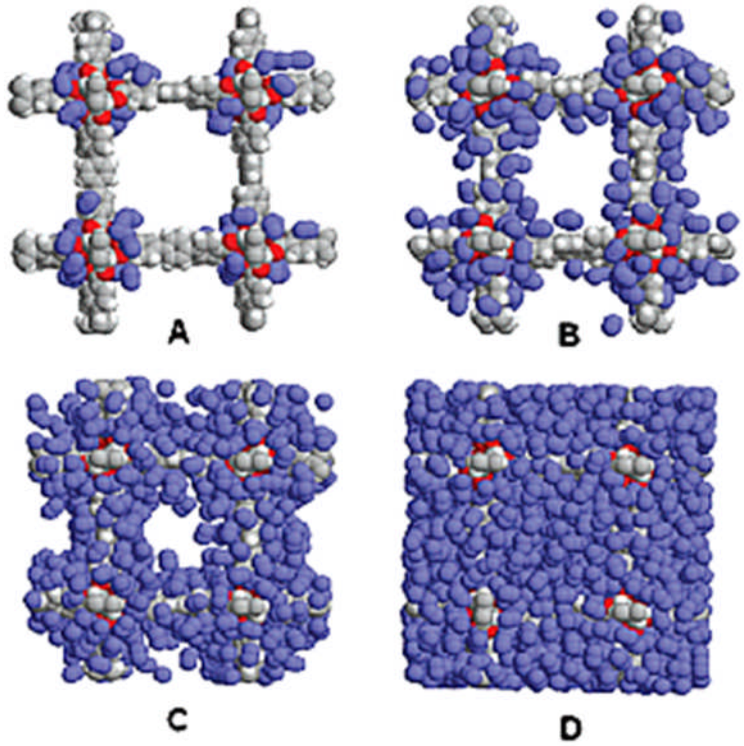

Figure 2.14 Step-by-step snapshots of the simulated adsorption isotherm indicating the more favourable adsorption locations for a given quantity of adsorbed species.[92]

The snapshots, although they are simulated, can be compared with energy profiles to more accurately determine the manner in which the adsorbed molecules fill the framework and may ultimately be possible to determine how effective a particular framework may be in terms of separations.

2.4 Computational Modelling

2.4.1 Structure optimization

As stated previously, one of the advantages of investigating scandium based framework systems is the NMR active ^{45}Sc nucleus. As the spin is 7/2, it is quadrupolar and as such interpreting the solid-state NMR spectra can be complex. One method of interpreting the solid-state NMR data is to use a structural model obtained from X-ray diffraction to calculate the NMR spectra and compare the results obtained with the experimental spectra. This process often involves first running a geometry optimization before the NMR calculations. Often with good quality single-crystal data it is not necessary to run the geometry optimization, but with lower resolution data such as powder diffraction data from a laboratory diffractometer (where geometric constraints are required to maintain chemically reasonable bond lengths in the Rietveld refinement) it can improve the model and show better agreement with the recorded spectra. This optimisation technique is particularly useful for framework materials where large, strongly scattering metals and weaker scattering organic components make up the framework. The organic ligands in this study such as the terephthalic acid which has a rigid phenyl core benefit from this optimisation where the distance restraints applied to the model in the Rietveld refinement process can result in small deviations from the optimum geometry for the rigid bodies.

Where necessary in this study, the CASTEP software package was used in collaboration with the research group of Dr. Sharon Ashbrook to geometry optimize the framework models and calculate the NMR parameters. CASTEP is a periodic planewave pseudopotential code for density functional theory calculations. This calculation is used to construct a wave function for the full system of electrons in a magnetic field.

2.4.2 Adsorption simulation

Another area where computer simulation is important is in adsorption studies. Experimental gas adsorption studies are time and labour intensive requiring many hours or often days of instrument time to collect data. In some experimental situations, equilibration time can be upwards of 5 hours per point on the isotherm and are routinely in the 30 – 180 minute range per point for microporous solids where a minimum of 20 – 30 adsorption and desorption points are required to accurately represent the isotherm. In situations where a large number of gases are to be studied, it is possible to simulate the adsorption process using a molecular simulation process. MUSIC is multipurpose simulation code used to simulate adsorption and diffusion developed by Randall Snurr and co-workers. MUSIC uses Monte Carlo moves to simulate the adsorption process where molecules are randomly inserted, translated, rotated or deleted. The interaction of the guest species and the framework is represented using Lennard-Jones potentials for the interatomic interactions with the parameters for the framework from the Dreiding force field. Mulliken partial charges for the framework atoms which can be calculated using the CASTEP code can also be used to better represent te framework charges. In each case a large number of Monte Carlo steps are performed (~ 1×10^7) until the system reaches equilibrium at which point a snapshot of the positions is obtained to represent a single configuration at that particular stage in the adsorption process. Comparison of this simulated data to the experimental adsorption can then be used to assess the accuracy of the simulation and if necessary small changes can be made to the framework model used or the force fields used to represent it to better simulate the real world uptake. This correction is usually required if the simulation results are lower than that observed experimentally as the simulation cell represents a rigid and idealized model of the structure which would only be matched by a materials which was fully activated with no structural distortion upon activation. If the simulated result is lower than the experimental, it usually means that either the force field used does not accurately represent the framework or that the framework model is not representative of the material upon adsorption of the guest species. In the case of flexible framework materials (Figure 2.15), it has been shown that a structural response can be induced by sufficient pressure of an adsorbed species such as CO_2.

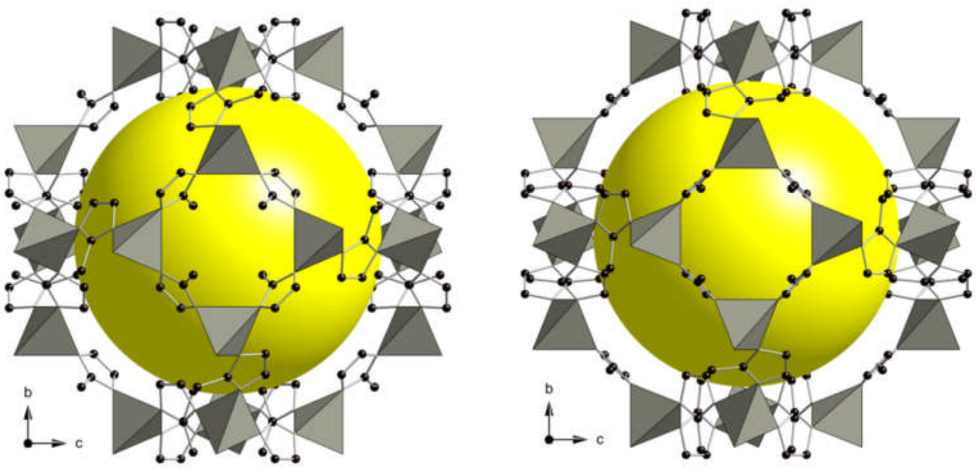

Figure 2.15: Low pressure structure (*left*) and high pressure structure (*right*) for the zinc imidazolate framework ZIF-8 observed over the course of a CO_2 adsorption isotherm. Grey tetrahedra represent the ZnN4 tetrahedra. Black spheres represent the carbon atoms of the linker.

Once accurate representation of example experimental isotherms is achieved, other gases can be simulated including mixtures to measure the selectivity of a material for different species.

2.5 Columns and Chromatography

2.5.1 ZLC

One of the techniques that will be used to study the adsorption and separation over the

MOF materials uses Zero Length Columns (ZLC). A technique introduced in the late 1980's by Eic and Ruthven,[93] ZLC can be used to measure intraparticle diffusion in porous materials.

ZLC experiments are carried out using very small quantities of sample material. Experiments on NaX and silicalite used <1 mg of sample (100 µm crystals) contained between 2 nickel sinters (producing the column of effectively zero length) and inserted into the gas flow and maintained at constant temperature.[94,95] The adsorbent is equilibrated with the sorbate at a known partial pressure and at a given time (t=0) the sorbent is purged with a helium gas flow of sufficient rate to ensure low sorbate concentration at the crystal surface to ensure that the diffusion is being measured and not the convective effects.

The following equations[96] represents a linear system with uniform spherical particles where the effluent concentration C is given by:

$$\frac{C}{C_0} = \sum_{n=1}^{\infty} \frac{2L}{[\beta_n^2 + L(L-1)]} \exp\left[\frac{-n^2\beta_n^2 Dt}{R^2}\right] \tag{17}$$

In the long-time region the higher order terms in equation (1) vanish so the equation approaches the asymptote:

$$\frac{C}{C_0} = \frac{2L}{[\beta_1^2 + L(L-1)]} \exp\left[\frac{-\beta_1^2 Dt}{R^2}\right] \tag{18}$$

Which is linear when plotted as $\ln\left(\frac{C}{C_0}\right)$ vs t.

If the value of L (Where $= \frac{1}{3}\frac{F}{KV_S}\frac{R^2}{D}$) is sufficiently high then even if the initial loading is outside the Henry's Law range, the limiting slope will yield the limiting time constant $\left(\frac{D_0}{r_c^2}\right)$

Other forms of experiment are also possible using the ZLC set-up. Tracer exchange experiments where instead of a pure helium purge, a deuterated sorbate of the same partial pressure is used to measure the response to the flow and subsequently the ratio of concentration in the adsorbed and gaseous phases.

2.5.2 Breakthrough Curves

Breakthrough curves are used as another analytical technique to determination the potential adsorptions and separations possible over a material of interest.[97] The term breakthrough curve refers to a measure of the response of an initially adsorbate free sample bed to an influent of time-independant composition. Initially the sample bed is purged with inert gas and at a given time (t = 0) the gas flow is switched to an influent flow. At this time a concentration front moves through the test bed, hindered by adsorption in the test sample, to a detector (mass spectrometer). The time taken for the influent to reach the detector (breakthrough) is measured giving an indication of the quantity of sorbent adsorbed, while the shape of the curve gives information about the adsorbate - sorbent interaction. A theoretical breakthrough curve is shown in Figure 2.16.

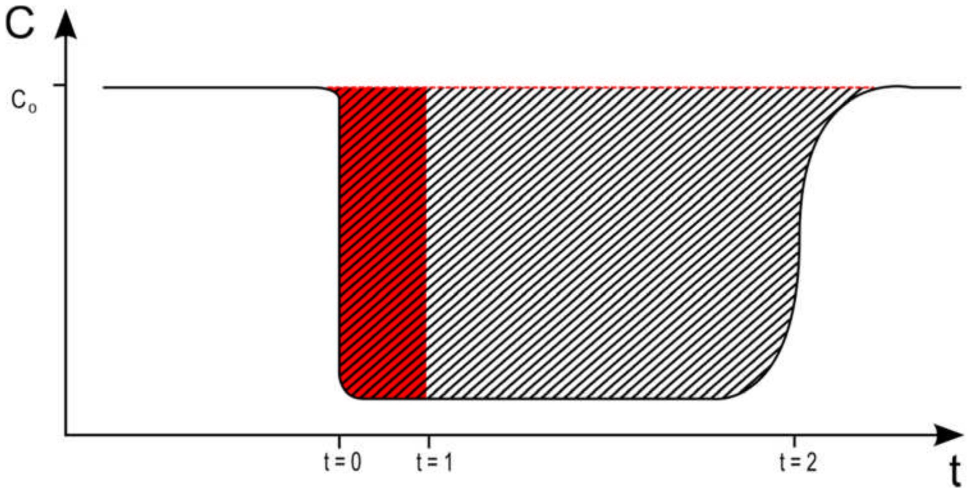

Figure 2.16 Typical example of a breakthrough curve. Shaded region represents the volume of sorbate adsorbed by the test bed, red area indicates correction required for the influent to reach detector without adsorption interaction.[97]

As stated previously, the shape of the breakthrough curve gives information on the nature of the adsorbate - sorbent interaction. The shape of the curve observed is directly related to the equilibrium isotherm as shown in Figure 2.17. The curve represents the resultant wavefront as it leaves the column. A favourable interaction between sorbate and adsorbant means that a high-concentration front travels faster than a slow concentration front and as such will be self-sharpening or compressive. An unfavourable interaction will be the opposite, the lower concentration in the front will move faster and as a consequence the wave will be dispersed (Figure 2.17).

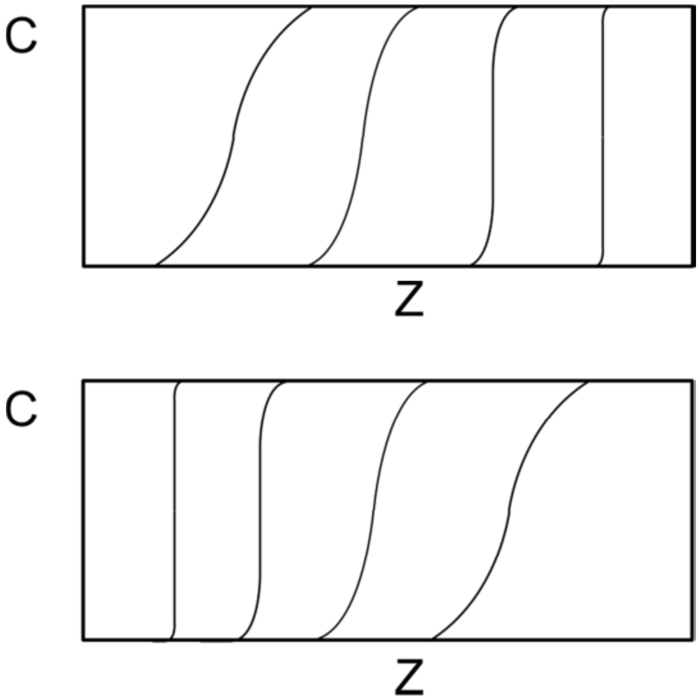

Figure 2.17 Example of the types of wavefront observed in the column. Top image shows successive representations of a self-sharpening wavefront caused by favourable sorbateadsorbent interaction. Lower image represents a dispersive wavefront arising from an unfavourable interaction. Z is the position in the column.[97]

3 Synthesis, Characterisation and Applications of Metal Phosphonates

3.1 Scandium substituted AlMePOs

The shape and size of the pore channels of the aluminium methylphosphonates, AlMePO-α and AlMePO-β, are of interest for use as a separation medium in column separation experiments. The two polymorphic structures contain aluminium in both octahedral and tetrahedral coordination in the ratio 1:3, with the formula $Al(o)Al(t)_3(PO_3CH_3)_6$, and create pore channels lined with $–CH_3$ groups. As discussed in the introduction, the pore channels are of sufficient size to adsorb aromatic molecules such as benzene but with restricted dynamics within the pore. With the aim of modifying the pore size of the AlMePO structure, experiments were carried out to investigate the incorporation of scandium into the octahedral sites to produce the $ScAl_3(CH_3PO_3)_6$ which, due to the larger radius of the scandium cation, should have a larger pore diameter than the original material.

In a typical synthesis of AlMePO-β, aluminium hydroxide and 1,4-dioxane is added to an aqueous solution of the methylphosphonic acid precursor in the ratio $Al(OH)_3:CH_3PO_3H_2:C_4H_8O_2:H_2O$ = 1:1.5:0.5:40. The aqueous mixture is stirred and transferred to a PTFE lined autoclave and heated at 160°C. Removal of the 1,4-dioxane template is performed by heating the sample at 450°C for 12 hours in a flow of dry nitrogen. The AlMePO-α polymorph is produced by topotactic transformation of AlMePO-β under a rapid flow of nitrogen saturated with water vapour described by Carter *et al.*[98] and Maeda *et al.*[99] It is possible to prepare the AlMePO-α phase directly but the product tends to demonstrate very low porosity compared with the sample produced via transformation from AlMePO-β.

A series of hydrothermal reactions were carried out using different scandium sources to investigate the possibility of incorporating scandium into the octahedral sites of the AlMePO structure. As well as varying the scandium source, reactions using the dimethyl ester of methylphosphonic acid (dimethyl methylphosphonate, DMMP) were investigated as an alternative to the more expensive methylphosphonic acid. The conditions are presented in Table 3.1.

Metal Source		Phosphonate source	Solvent	SDA	Ratio Al : Sc : P : SDA : H_2O	Temp /°C	Time /h	Product
Al	Sc							
Al_2O_3	$ScCl_3$	$CH_3PO_3H_2$	H_2O	1,4-Dioxane	0.75:0.25:1.5:0.5:40	160	48	AlMePO-β
$Al(OH)_3$	$ScCl_3$	$CH_3PO_3H_2$	H_2O	1,4-Dioxane	0.75:0.25:1.5:0.5:40	160	48	ScAlMePO-α
$Al(OH)_3$	$Sc(NO_3)_3$	$CH_3PO_3H_2$	H_2O	1,4-Dioxane	0.75:0.25:1.5:0.5:40	160	48	ScAlMePO-layered phase
$Al(OH)_3$	Sc_2O_3	$CH_3PO_3(CH_3)_2$	H_2O	1,4-Dioxane	0.75:0.125:1.5:0.5:40	160	48	ScAlMePO-α
$Al(OH)_3$	$Sc(NO_3)_3$	$CH_3PO_3(CH_3)_2$	H_2O	1,4-Dioxane	0.75:0.25:1.5:0.5:40	160	48	AlMePO-layered phase
$Al(OH)_3$	$Sc(NO_3)_3$	$CH_3PO_3(CH_3)_2$	H_2O	1,4-Dioxane	0.75:0.25:1.5:0.5:80	160	48	ScAlMePO-α + AlMePO-β

Table 3.1: Gel compositions and reaction conditions for the preparation of scandium substituted aluminium methylphosphonates

Initial phase identification of the products using powder XRD indicated that the ScAlMePO-α polymorph formed directly, identified by a shift in the XRD pattern (Figure 3.1) to lower 2θ representing a larger unit cell, due to the increased size of the Sc^{3+} cation over the Al^{3+} (88.5 pm and 67.5 pm respectively)[79].

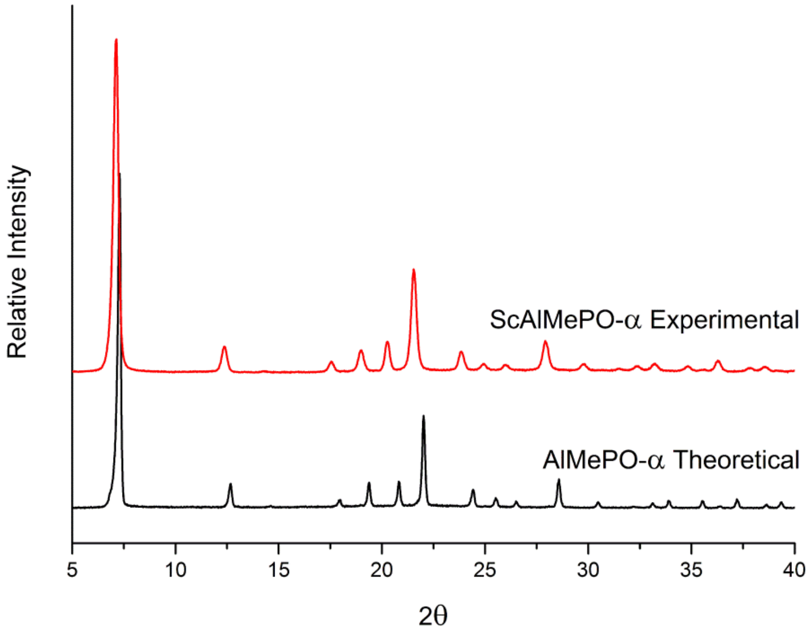

Figure 3.1: Comparison of the as-synthesised ScAlMePO-α sample and the theoretical pattern produced from the published crystal structure.

EDX analysis confirmed the presence of scandium in the product. SEM images of two of the products are shown in Figure 3.2 with example areas used for EDX analysis labelled. The data suggested a ratio of scandium to aluminium of ca. 1 : 3.7 and although this result is not quantitative, it suggested a significant quantity of scandium was incorporated, though further analysis was required to obtain an accurate composition.

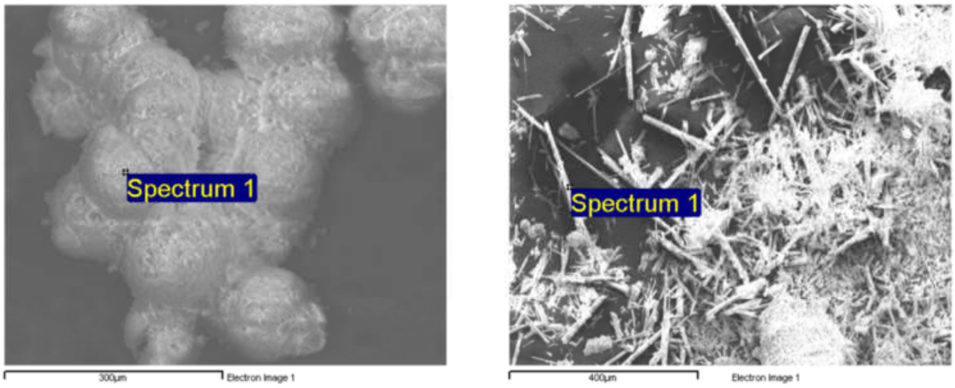

Figure 3.2: SEM images of ScAlMePO-α prepared using methylphosphonic acid (*left*) and using dimethyl methylphosphonate (*right*).

^{27}Al solid-state NMR analysis on the same sample showed that there was in fact a very small quantity of aluminium present in octahedral geometry, this means that although the scandium has been incorporated into the structure, it is not in full occupancy on the octahedral site rather $Sc_{1-x}Al_{3+x}(CH_3PO_3)_6$. The ^{45}Sc MAS NMR shows a single scandium site, consistent with the scandium on the octahedral site (Figure 3.3).

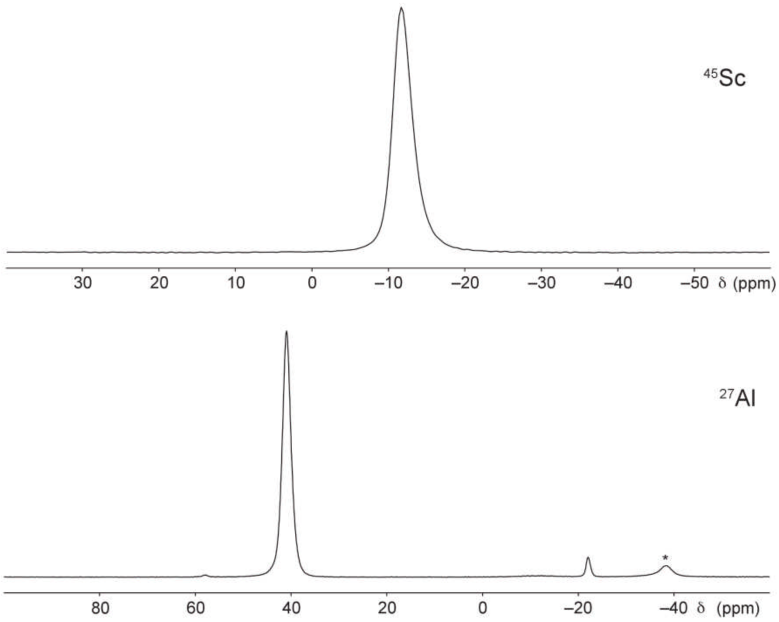

Figure 3.3: ^{45}Sc (*top*) and ^{27}Al (*bottom*) NMR spectra on the ScAlMePO-α. *Spinning sideband

The same sample of ScAlMePO-α was sealed in a 0.7 mm diameter glass capillary and an X-ray diffraction pattern collected for 14 hours. The pattern was indexed to obtain a unit cell of a = 14.280 Å c = 8.766 Å in the trigonal space group $P\ 3_1\ c$. Rietveld refinement was used to obtain unit cell parameters and a composition for the material, with aluminium and scandium disordered over the octahedral site. The fractional occupancy of the two metals were allowed to vary, with the condition that the sum of the two occupancies was equal to 1. The overall R_{wp} converged at 6 % indicating a 97.25 % : 2.75 % Sc : Al ratio (see Figure 3.4 for the Rietveld plot).

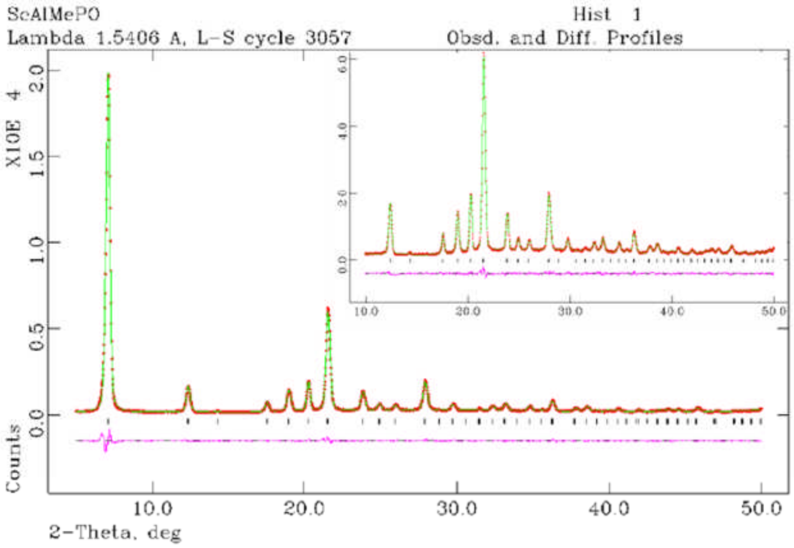

Figure 3.4: Rietveld refinement plot for AlMePO-α.

From Table 3.1 it was observed that both phase pure AlMePO-β and also mixed phase products were produced despite having suitable quantities of scandium in the reaction gel in each case. When the β phase did form (as part of a mixture with ScAlMePO-α or as the main product), the phase contained no scandium (Figure 3.5) despite having scandium available in the reaction. The mixtures were identified to be ScAlMePO-α and the (aluminium only) AlMePO-β.

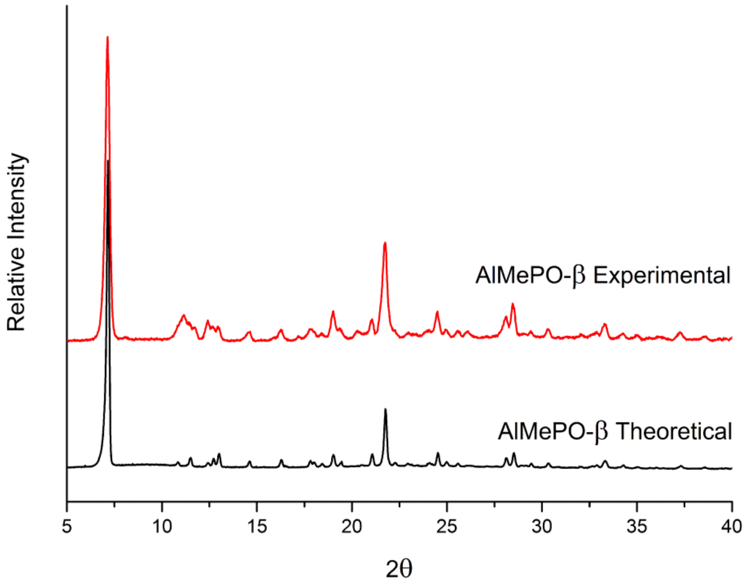

Figure 3.5: Comparison of the AlMePO-β phase and the theoretical pattern produced from the published crystal structure.

This unit cell expansion in ScAlMePO-α is accompanied by an increase (~2 %) in the pore diameter on scandium incorporation which might be significant when considering size selective separation processes. Initial adsorption studies on the ScAlMePO-α material, however, (prepared using methylphosphonic acid) indicated that the sample was not porous. It was also reported in the literature that when the α polymorph of the pure aluminium solid was prepared directly (rather than via topotactic transformation of the β form) there was limited porosity. One hypothesis for this observation is that intergrowth of crystal planes occurs more readily in the α polymorph which would block access to the channels, as evident in the SEM images above (Figure 3.2). When the DMMP ester was used in the synthesis of ScAlMePO-α, products were highly crystalline and yielded some evidence of permanent microporosity (Figure 3.6). The accessible porosity is lower than that observed for the best samples of AlMePO-α (~1/3 of the expected capacity) but represents a significant improvement over the non-porous materials prepared with the acid precursor.

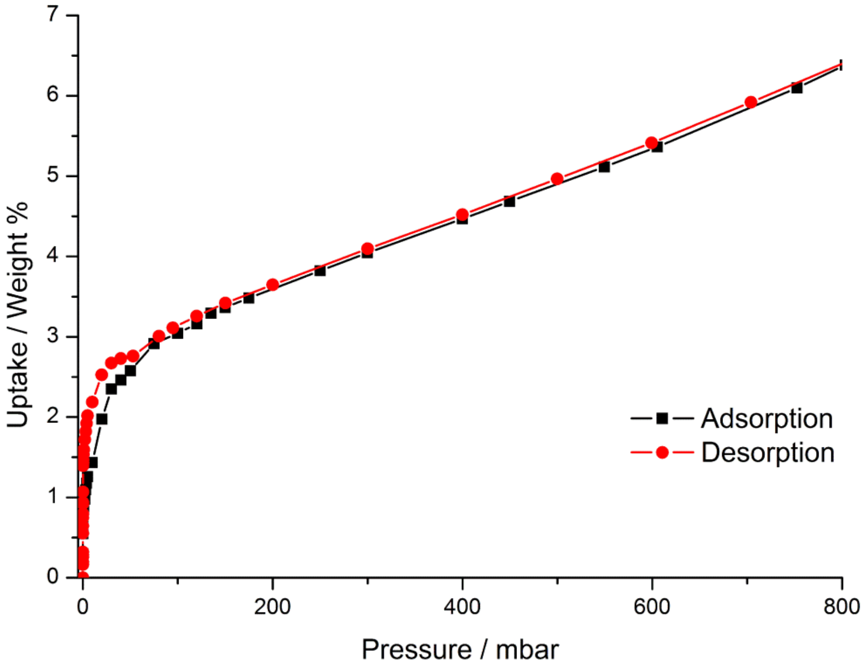

Figure 3.6: Nitrogen adsorption isotherm for ScAlMePO-α measured at 77 K.

3.2 Lanthanide Bisphosphonates

Recent studies have shown that it is possible to produce framework materials with the lanthanide metals and N,N'-piperazinebis(methylenephosphonic acid) herein referred to as H_4L (ligand **1**) and also the 2-methylpiperazine derivative H_4L' (ligand **2**) and the 2,5-dimethyl derivative (ligand **3**) and shown in Figure 3.7.[100]

Synthetic work on the lanthanide phosphonates along with preliminary work on structure type-I, discussed in this section, was performed by J. A. Groves and J. P. S. Mowat and discussed in the MChem thesis of J. P. S. Mowat.[101] This work focuses on the structural characterization of the synthesised products to understand the structure in the bulk phase and the effects of dehydration.

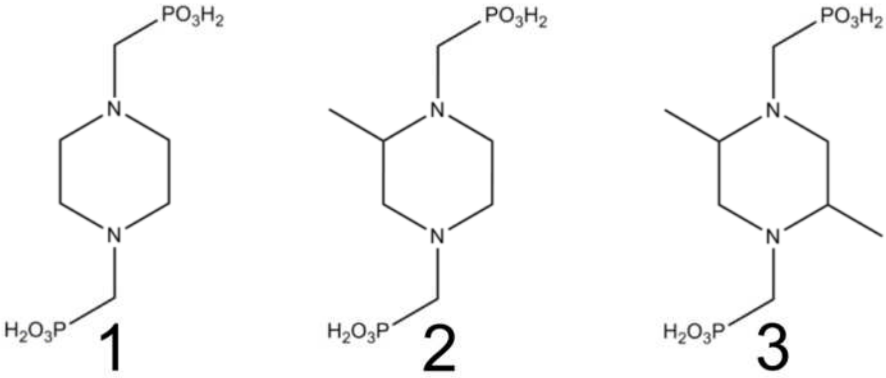

Figure 3.7: Piperazine-bis(methylenephosphonic acid) linker (H_4**1**) *(left)*, the 2-methyl-piperazine derivative (H_4**2**) *(middle)* and the 2,5-dimethyl- derivative (H_4**3**) *(right)*.

In this work, the hydrothermal chemistry of the lighter (and larger) lanthanides was investigated with the three piperazine-based bisphosphonic acid linkers with resulting structures characterized by single crystal and powder diffraction and elemental analysis. The bisphosphonic acid ligands used were prepared in-house using a modified form of the Mannich reaction. Updated synthesis and characterisation work on the ligands by M. T. Wharmby[102] - a colleague in the Wright group - is reported in the supplementary information reported alongside this work on the lanthanide bisphosphonates, Mowat *et al.*[103] and will not be discussed here.

3.2.1 Synthesis conditions

A series of hydrothermal crystallisations were performed using a solution of lanthanide oxide or salt and bisphosphonate ligand in water with the pH was adjusted to the desired value by addition of an alkali metal hydroxide solution. Three novel phases were prepared and characterized, denoted by the Roman numerals I II and III. Product phases in this section are described by [(Cation),(Framework metal)-Phase-**Ligand**] for example K,Ce-I-**1**.

Table 3.2 and Table 3.3 show the range of synthetic conditions used in the preparations and the resulting products. In a typical synthesis of the cerium type I phase, K,Ce-I-**1**, $Ce(NO_3)_3$ and ligand **1** in the ratio 2 : 3 were stirred in water (approximately 1000 equivalents) and base was added until the pH of the resultant aqueous solution was pH 7. Reaction mixture was transferred to a PTFE lined autoclave and heated for 150 hours. The resulting product was filtered and washed with water.

Metal Source /Phosphonic acid	Millimoles metal	Millimoles ligand	Temp. / °C	Time / h	Initial pH / added cation	Product phase
La_2O_3 / **1**	1.00	1.50	190	150	6.5 / Na^+	Na,La-I-**1**
$LaAc_3$ / **1**	0.67	1.00	190	200	6.5 / Na^+	Na,La-I-**1**
La_2O_3 / **1**	0.67	1.00	190	150	4.0 / none	La-II-**1**
$LaBr_3$ / **1**	1.00	1.50	190	150	5.0 / none	La-II-**1**
$La(Ac)_3$ / **1**	0.67	1.00	190	200	5.0 / none	La-II-**1**
$Ce(NO_3)_3$ / **1**	0.67	1.00	190	150	8.0 / K^+	K,Ce-I-**1**
$CeCl_3$ / **1**	0.67	1.00	190	300	7.5 / K^+	K,Ce-I-**1**
$Ce(NO_3)_3$ **1**	0.33	1.00	190	300	5.0 / none	K,Ce-II-**1**
$NdAc_3$ / **1**	0.67	1.00	160	150	7.0 / K^+	K,Nd-I-**1**
$NdAc_3$ / **1**	1.00	1.00	190	100	5.0 / Na^+	Nd-I-**1**
$NdAc_3$ / **1**	0.67	1.00	190	100	5.0 / Na^+	Nd-I-**1**
$NdAc_3$ / **1**	1.00	1.00	190/160	100	<5 / none	amorphous

Table 3.2: Synthesis condition for the lanthanide bisphosphonate with ligand **1**

From the synthesis conditions explored, it was clear structure type I and II were formed with phosphonic acid **1**. Phase I was prepared above pH 6.5 for La^{3+} and Ce^{3+} and above pH 5 for Nd^{3+}.

Metal Source / Phosphonic acid	Millimoles metal	Millimoles ligand	Temperature / °C	Time / h	Initial pH / added cation	Product phase(s)
$LaAc_3$ / **2**	0.33	1.00	160	150	7.5 / Na^+	Na,La-I-**2**
$LaAc_3$ / **2**	0.33	1.00	160	150	8.0 / Na^+	Na,La-I-**2**
$LaAc_3$ / **2**	0.66	1.00	160/190	100	5.0 / Na^+	Na,La-I-**2**
$LaAc_3$ / **2**	0.66	1.00	160/190	100	<5 / -	none
$Ce(NO_3)_3$ / **2**	0.67	1.00	190	150	8.0 / K^+	K,Ce-I-**2**
$Ce(NO_3)_3$ / **2**	0.67	1.00	160	150	7.5 / K^+	K,Ce-I-**2**
$Ce(NO_3)_3$ / **2**	0.33	1.00	190	300	5.5	Ce-III-**2**
$Ce(NO_3)_3$ / **3**	1.00	0.67	190	120	7 / Na^+	Na,Ce-I-**3**
$Ce(NO_3)_3$ / **3**	1.00	0.67	190	120	7 / Cs^+	Cs,Ce-I-**3**
$Ce(NO_3)_3$ / **3**	1.00	0.67	190	120	6 / Cs^+	Ce-I-**3** + Ce-III-**3**
$Ce(NO_3)_3$ / **3**	1.00	0.67	190	120	5 / Cs^+	Ce-III-**3**
$NdAc_3$ / **2**	0.67	1.00	140	150	8.0 / Na^+	Nd-I-**2**
$NdAc_3$ / **2**	0.33	1.00	160	150	7.5 / Na^+	Nd-I-**2**
$Nd_2(CO_3)_3$ / **2**	0.67	1.00	190	125	3.5 / none	Nd-III-**2**
$Nd_2(CO_3)_3$ / **3**	0.67	1.00	160/190	150	7 / Na+	Na,Nd-I-**3**
$Nd_2(CO_3)_3$ / **3**	0.67	1.00	160/190	150	6 / Na+	Na,Nd-I-**3**
$Nd_2(CO_3)_3$ / **3**	0.67	1.00	160/190	150	5 / Na+	Nd-III-**3**
$Nd_2(CO_3)_3$ / **3**	0.67	1.00	160/190	150	3 / none	Nd-III-**3**

Table 3.3: Synthesis condition for the lanthanide bisphosphonates with ligands **2** and **3**

3.2.2 Structural characterisation

Cerium Type I displays one dimensional channels and on initial observation of the structure (Figure 3.8), looks like a suitable candidate for adsorption study, however measurements suggested there was no permanent porosity. The structure shows charge balancing cations within the pore system, which may have limited the porosity, although a sample of the material prepared in the absence of alkali metal hydroxide - using triethylamine to alter the pH of the initial solution - displayed a similar lack of porosity.

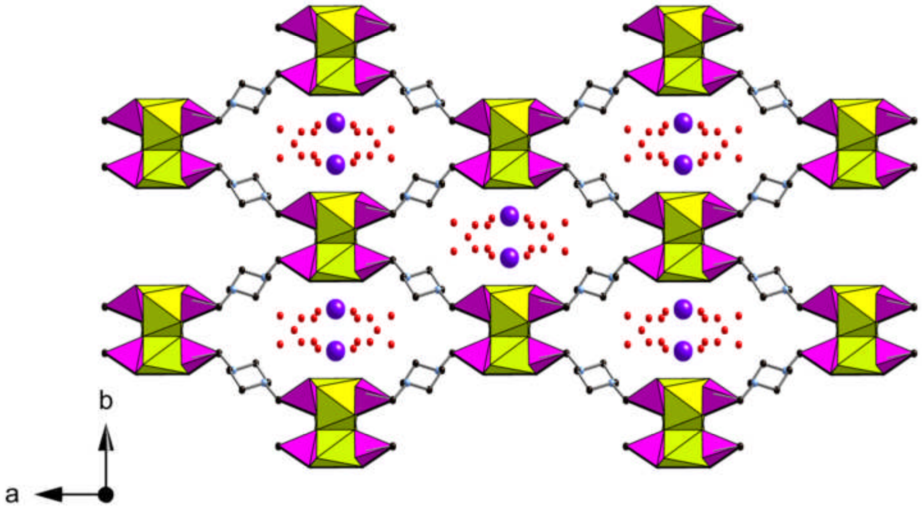

Figure 3.8: Cerium Type I phase, K,Ce-I-**1**, viewed down the channel parallel to the c-axis. Cerium coordination polyhedra are shown in yellow and the phosphonate tetrahedra in purple. Carbon and nitrogen atoms of the piperazine ring are shown as black and blue spheres respectively, larger purple spheres depict the potassium cations and red spheres represent the oxygen atoms of physisorbed water molecules.

K,Ce-I-**1** consists of edge sharing CeO_8 chains with each Ce in a distorted square anti-prism geometry. The oxygen atoms surrounding the cerium are phosphonate oxygen atoms of the bisphosphonate linker where all oxygen atoms of the linker are involved in the metal coordination. Each chain is connected to four adjacent parallel chains by the bridging bisphosphonate linker.

To investigate the activated material, a portion of the sample was dehydrated under vacuum at 150°C and PXRD indicated a change of symmetry between the as-prepared and the dehydrated form of the material (Figure 3.9).

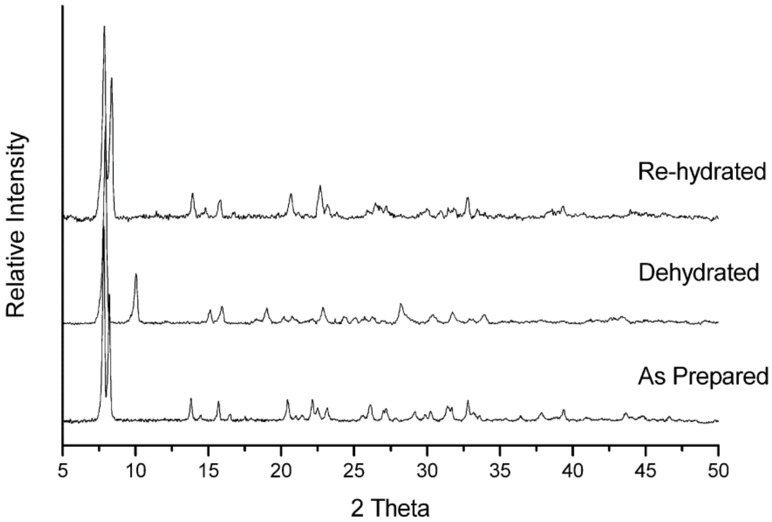

Figure 3.9: Synchrotron X-ray powder diffraction patterns of the K,Ce-I-1 material showing the reversible dehydration effect indicative of a change in the symmetry.

Synchrotron XRD data, collected on the two samples at Diamond Light Source I-11, was of sufficient quality to enable structure solution of the two phases. A structural model from single-crystal data obtained from another example of the Ce-I-**1** structure was used as a starting model in the refinement of the as-prepared K,Ce-I-**1** phase (Figure 3.10). After initial refinement of the unit cell and instrumental parameters, a series of restraints were applied to the framework to ensure that the model retained chemically reasonable bond lengths and angles and least squares refinement of the atomic positions was performed. Fourier mapping of the cell containing just the framework was used to determine the location of residual electron density in the channels attributed to alkali metal cations and the oxygen atoms of water molecules present in the structure. The overall R_{wp} converged at [≈8 %] which confirmed that the bulk phase sample under study was consistent with the model obtained from the single crystal data.

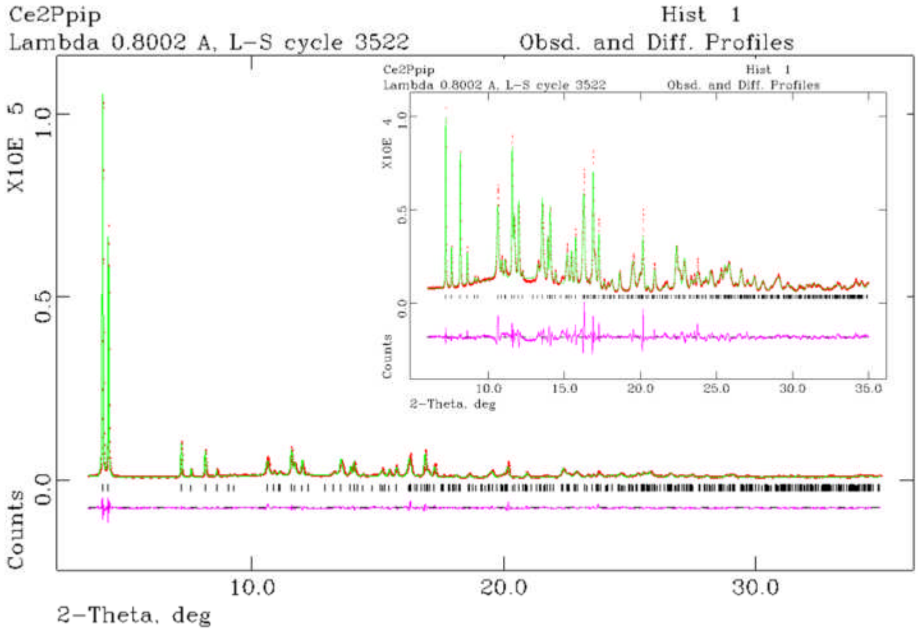

Figure 3.10: Rietveld refinement of the as-prepared (hydrated) form of the K, Ce-I-**1** structure from synchrotron X-ray diffraction data, expansion shown excludes the first two peaks.

Indexing the peaks in the dehydrated form of the sample, K,Ce-I-**1**-deh, showed a change in the unit cell volume from *a* = 22.5864(2) Å, *b* = 12.1186(2) Å, *c* = 5.6613(2) Å, β = 93.040(2)° in the hydrated from to *a* = 21.8 Å, *b* = 9.35 Å, *c* = 5.56 Å, β = 96.6°. From further analysis and consideration of systematic absences, the space group was found to have changed from monoclinic *C* 2/*c* in the as-prepared material to monoclinic *P* $2_1/n$ in the dehydrated form. Along with this change in symmetry was a doubling of the required asymmetric unit. A model was produced using the fractional coordinates from the material in the hydrated form as the starting point and Rietveld refinement was carried out.

The same restraints on bond lengths and angles were applied as in the hydrated form and refinement of the cell dimensions and subsequently the atomic coordinates was performed. From observation of the resultant structure with a low overall residual value, R_{wp} converged at [≈5 %] (Figure 3.11) it was clear that the structure had undergone a large reduction in volume from 1547.42(5) Å^3 to 1128.56(11) Å^3, and the piperazine ring had adopted a boat-like conformation rather than the more common chair configuration, indicative of a large amount of strain imposed by the framework.

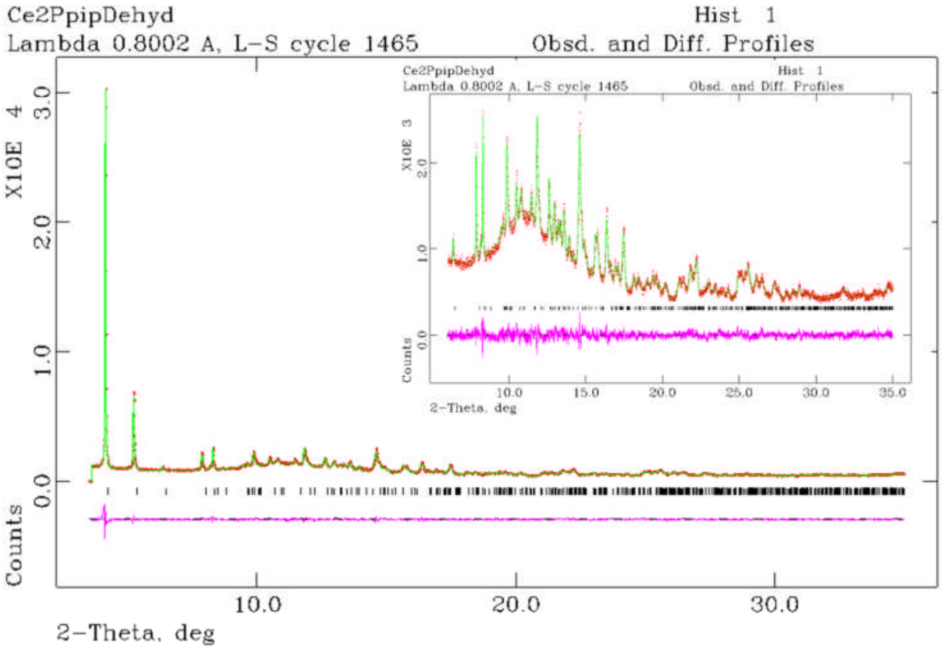

Figure 3.11: Rietveld refinement of K, Ce-I-**1**-deh from synchrotron X-ray diffraction data, expansion shown excludes the first two peaks.

This contraction effect observed upon dehydration means that the materials is not able to retain the open pore structure upon dehydration and is therefore not a suitable candidate for use as an adsorbent (Figure 3.12).

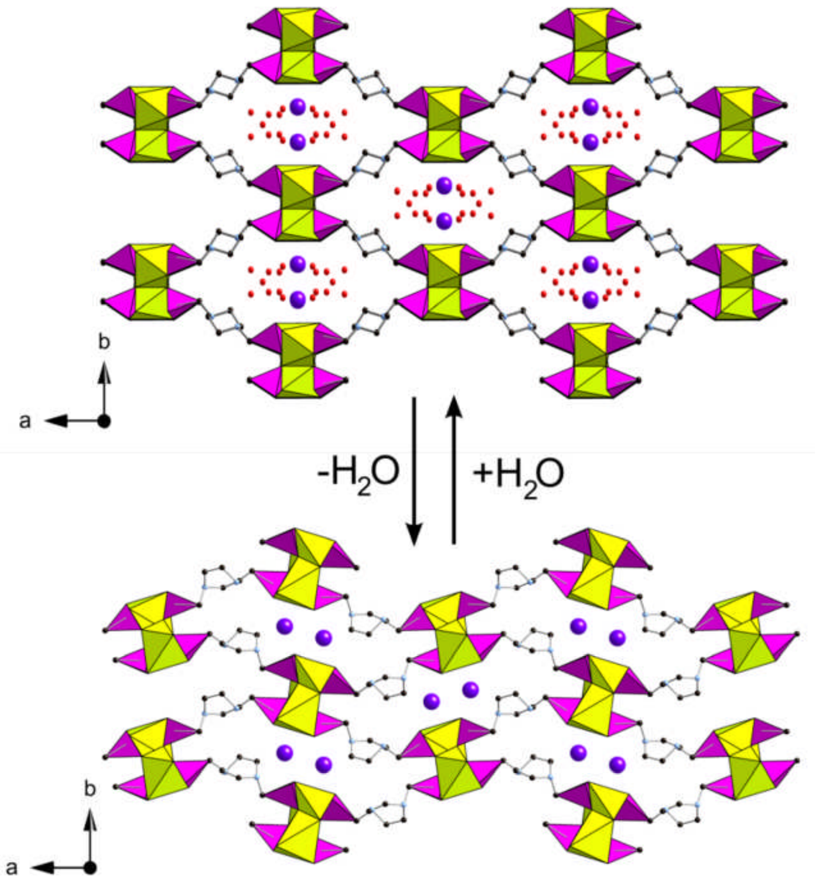

Figure 3.12: Structure of cerium Type I, K,Ce-I-**1**, and the dehydrated form, K,Ce-I-**1**-deh both viewed down the one dimensional channel parallel to the c-axis showing the reduction in channel cross-section and distortion of the piperazine ring. Cerium coordination polyhedra are shown in yellow and the phosphonate tetrahedra in purple. Carbon and nitrogen atoms of the piperazine ring are shown as black and blue spheres respectively, larger purple spheres depict the potassium cations and red spheres represent the oxygen atoms of physisorbed water molecules.

Preparation of the same (Phase I) framework topology was observed with ligands **2** and **3** at the higher pH (>6) but with modified unit cell parameters (Table 3.4).

	K,La-I-**1**	K,Ce-I-**1**	K,Nd-I-**1**	K,Ce-I-**1**	K,Ce-I-**2**	Na,Ce-I-**3**	KCe-I-**1**(dehydrated)
Formula	KLa(**1**)·4H_2O	KLa(**1**)·4H_2O	KNd(**1**)·4H_2O	KCe(**1**)·3.8H_2O	$K_{0.5}H_{0.5}$Ce(**2**)·4H_2O	NaCe(**3**)·3.6H_2O	KCe(**1**)
diffractometer	Stoe	Stoe	Stoe	Synchrotron, ID-31	Synchrotron, ID-31	Synchrotron, I-11	Synchrotron, ID-31
λ of X-rays (Å)	1.54056	1.54056	1.54056	0.800200	0.800200	0.826019	0.800200
Temperature	298 K	298 K	298 K	100 K	100 K	100 K	100 K
crystal system	monoclinic	monoclinic	monoclinic	monoclinic	monoclinic	monoclinic	monoclinic
space group	*C*2/*c*	*C*2/*c*	*C*2/*c*	*C*2/*c*	*C*2/*c*	*C*2/*c*	$P2_1/n$
a (Å)	22.439(13)	22.560(16)	22.445(16)	22.5864(2)	23.0899(10)	22.9150(5)	21.8361(12)
b (Å)	11.942(9)	12.216(8)	12.165(12)	12.1186(2)	13.9954(8)	14.2802(3)	9.3519(4)
c (Å)	5.739(3)	5.648(5)	5.588(5)	5.6613(2)	5.6406(5)	5.6451(1)	5.5629(3)
β(°)	91.76(3)	93.3(4)	92.88(5)	93.040(2)	102.5546(10)	102.8006(10)	96.560(4)
V($Å^3$)	1537(2)	1554(3)	1524(4)	1547.42(5)	1780.06(7)	1801.36(5)	1128.56(11)

Table 3.4: Structural data for the lanthanide bisphosphonates from Rietveld refinement on X-ray powder diffraction data.

Single crystals of K,Ce-I-**2** were analysed by X-ray diffraction and the structure is shown in Figure 3.13.

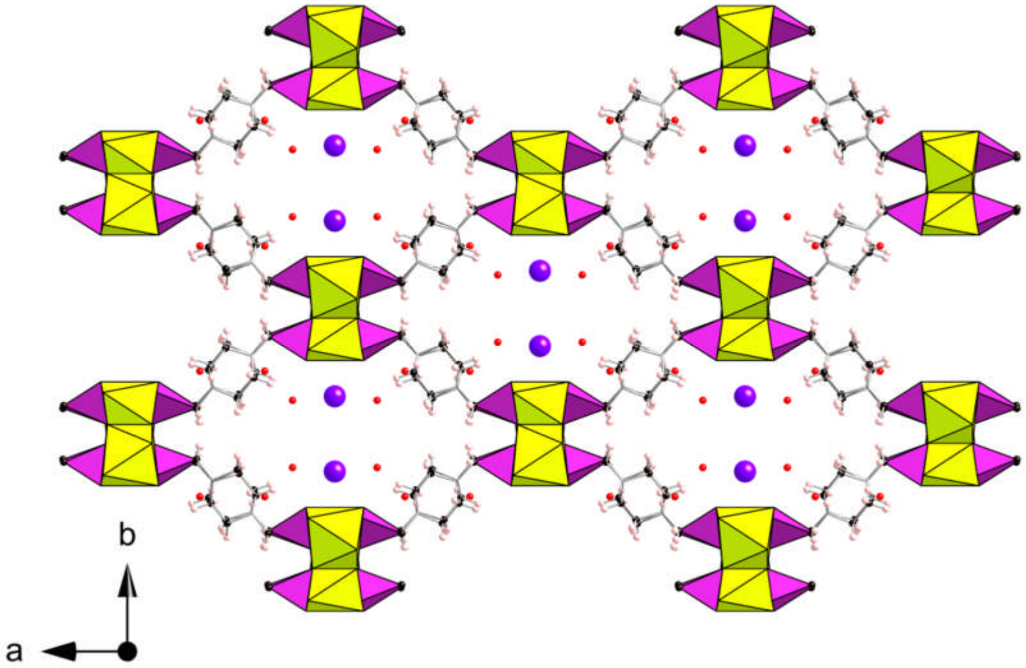

Figure 3.13: K,Ce-I-**2** viewed down the channels parallel to the c-axis. Cerium coordination polyhedra are shown in yellow and the phosphonate tetrahedra in purple. Carbon and nitrogen atoms of the piperazine ring are shown as black and blue spheres respectively, larger purple spheres depict the potassium cations and red spheres represent the oxygen atoms of physisorbed water molecules. Smaller pink spheres represent hydrogen positions on the piperazine ring.

The piperazine ring was observed to be disordered over two positions in the final model, with 50 % occupancy in each position (Figure 3.14). It was not possible to locate the $–CH_3$ groups of the ring by diffraction (there was no evidence of strong peaks in the difference Fourier maps), these are thought to be equatorial due to steric effects and as a result of the disorder in the ring position, assumed to be disordered over the 8 possible geometric positions.

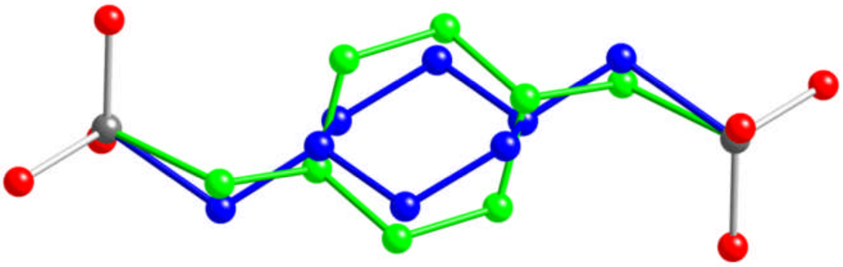

Figure 3.14: Two positions identified for the piperazine-core of linker (coloured blue and green respectively) in K,Ce-I-**2** (proton positions, positioned geometrically in the refinement, were removed for clarity), ordered phosphorus and oxygen positions are shown as the grey and red spheres respectively.

Alkali metal cations were found to lie on the two fold axes with the cation (in this case potassium) coordinating to the phosphonate oxygen in the chain and water molecules distributed through the rest of the channel. Additional electron density (between the stacks of piperazine rings and in the surrounding channel) was attributed to additional water molecule in the structure in lower occupancy. The presence of the alkali metal cations in the final structure was also verified by EDX analysis. One example of Nd-I-**2** showed no evidence of any extra-framework cations and in this case the charge balance in the framework was assumed to be stabilized by protonation of the nitrogen in the piperazine ring of the linker.

Addition of the second –CH_3 group in ligand **3** still produces the same framework topology as ligand **1** but with a further modification of the cell parameters. The structure of the Na,Ce-I-**3** material (Figure 3.15) was refined from synchrotron X-ray powder diffraction, using the atomic coordinates of K,Ce-I-**1** as the starting model. The overall R_{wp} converged to 8.57 %.

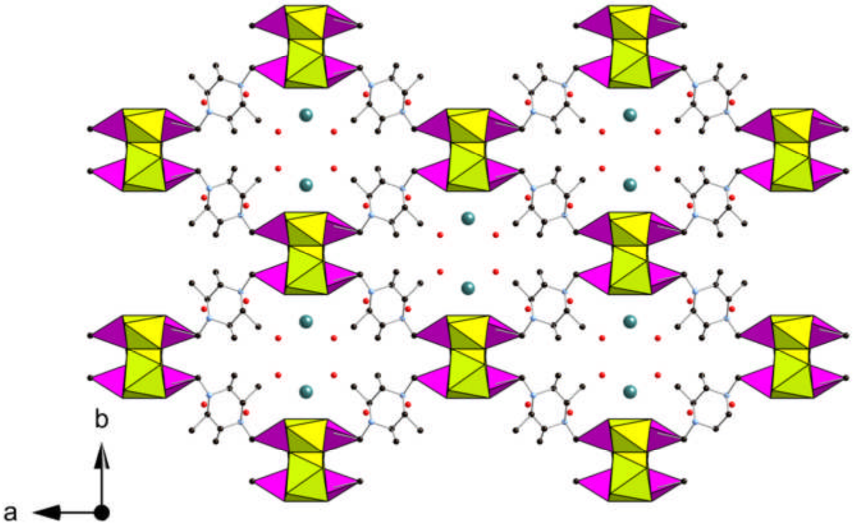

Figure 3.15: Structure of the Na,Ce-I-**3** viewed down the channels (c-axis). Cerium coordination polyhedra are shown in yellow and the phosphonate tetrahedra in purple. Carbon and nitrogen atoms of the piperazine ring are shown as black and blue spheres respectively, larger blue spheres depict the sodium cations and red spheres represent the oxygen atoms of physisorbed water molecules.

Due to the increased steric effects of the two $-CH_3$ groups, the chair conformation is more favourable and would reduce the likelihood of the same dehydrated phase forming as observed with ligand **1**. Comparison of the two type I materials showed that the orientation of the piperazine rings in the respective structures (with ligand **1** and ligand **3)** were different. The plane through the atoms of the ring in the 2,5-dimethyl material is almost perpendicular to the c-axis whereas in the piperazine structure the plane is almost parallel to the axis (Figure 3.16). This change in the configuration of the ring is due to the position of the methyl group with respect to the nearest oxygen atoms of the inorganic chains. Rather than project towards the chain, the ring rotates such that the $-CH_3$ groups project into the more open part of the channel.

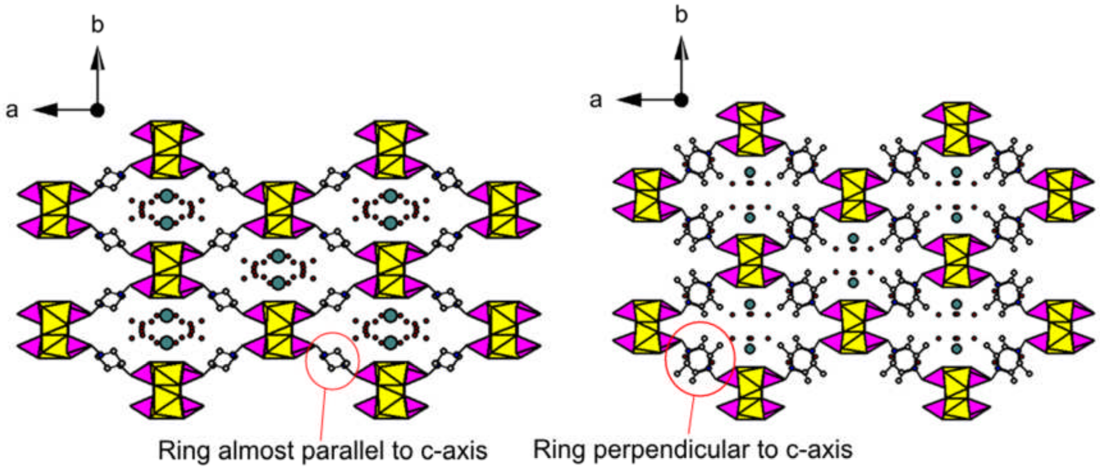

Figure 3.16: Comparison of the Na,Ce-I-**1** and K,Ce-I-**3** structures. The –CH_3 groups result in a rotation of the piperazine ring plane towards perpendicular to the channels. Cerium coordination polyhedra are shown in yellow and the phosphonate tetrahedra in purple. Carbon and nitrogen atoms of the piperazine ring are shown as black and blue spheres respectively, larger blue spheres depict the sodium cations and red spheres represent the oxygen atoms of physisorbed water molecules.

This rotation of the ring results in a significant increase in the length of the b-axis (17.8 %) and arises from torsion around the methylene carbon to piperazine nitrogen bond (Figure 3.17: C2-N1-C1-P2).

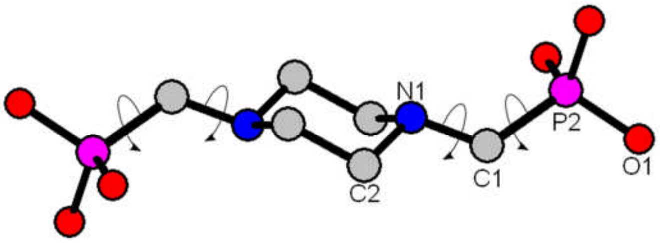

Figure 3.17: Torsion angles measured for ligand **1**.

Structure Type II was observed in the lower pH range without addition of the alkali metal hydroxide for lanthanum and cerium. The structure of Type II is again a chain of edge-sharing 8-fold coordinated lanthanide polyhedra but, unlike Type I, the nitrogen of the piperazine ring is involved in the chain (Figure 3.18). The coordination shell around the metal contains the nitrogen along with 7 phosphonate oxygen atoms. The structure also contains two distinct bisphosphonate linkers. The first ligand binds to the lanthanide through all six of the phosphonate oxygen atoms whereas the second binds through the two ring nitrogen and four phosphonate oxygen atoms. The first ligand is protonated on both nitrogen atoms. The remaining phosphonate oxygen of the second ligand (not involved in coordinating the lanthanide) is assigned to a P=O species (due to shorter bond length of 1.53 Å) and hydrogen bonds to the protonated nitrogen of the first linker.

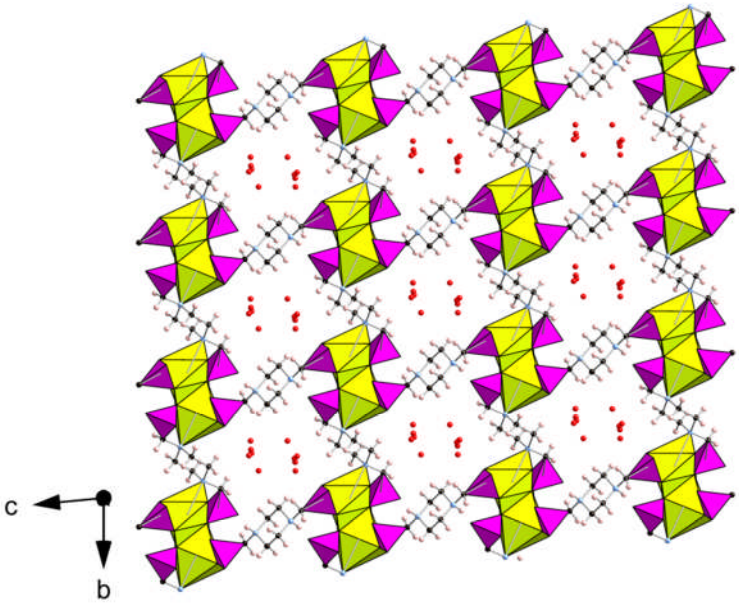

Figure 3.18: La-II-**1** viewed down the channel parallel to the a-axis. Lanthanum coordination polyhedra are shown in yellow and the phosphonate tetrahedra in purple. Carbon and nitrogen atoms of the piperazine ring are shown as black and blue spheres respectively. Pink spheres depict the hydrogen atoms on the piperazine ring and red spheres the oxygen atoms of physisorbed water molecules.

The two phosphonate molecules lead to a difference in the stacking arrangement between the b and c directions. Along c axis, the chains are linked through the ligand with all six oxygen atoms involved in coordination whereas along b, the distance between chains is shorter due to the nitrogen coordinating the lanthanide. Although the structure displays water loss upon heating, reversible on exposure to moist air, there was no measurable porosity for nitrogen at 77 K.

Structure Type III, observed with Ce and Nd at low pH levels with $–CH_3$ group containing ligands (**2** and **3**), is composed of lanthanide phosphonate chains, each linked to four others by the bisphosphonate linker. Each of the three phosphonate oxygens coordinates to a different lanthanide cation along the chain, resulting in a corner sharing arrangement of phosphonate tetrahedra and metal polyhedral. The lanthanide environment in structure Type III is 7-coordinate, LnO_7 polyhedra, with six oxygen atoms from bridging phosphonate and one attributed to a water molecule. Again additional water molecules are present in the framework both in the channels and in a hydrogen bonding arrangement with the protonated nitrogen of the piperazine – half of which are protonated to maintain overall charge balance in the structure.

3.2.3 Summary of lanthanide bisphosphonate studies

The bisphosphonate linkers **1**,**2** and **3** have been shown to produce three framework types with the lighter and larger lanthanides La, Ce and Nd. The metals adopt seven or eight fold coordination with the oxygen and nitrogen of the linker and additional water molecules in all cases producing metal phosphonate chains connected through the bisphosphonate linker. The structure which crystallises from the reaction depends on the pH of the starting gel which influences the protonation state of the organic linker used. The addition of $–CH_3$ groups introduces sufficient steric interactions to direct the formation of different structures. The reversible hydration of structure type I was shown to be accompanied by a significant reduction in unit cell volume and an associated conformational flip from chair to boat configuration in the piperazine ring reversible upon subsequent rehydration. Unfortunately, no permanent porosity was observed from absorption studies using nitrogen and carbon dioxide.

3.3 Column experiments on the nickel bisphosphate, STA-12

The large pore nickel bisphosphonate, STA-12(Ni), was investigated as a candidate material for use as a stationary phase in gas separations. The framework structure of STA-12 is discussed in Chapter 1 above, and shown in Figure 3.19. The pore size and chemistry suggests that the material may be suitable for separating small molecules in a gas chromatography experiment. A range of STA-12(M) materials have been synthesised to date, where M = Mg, Mn, Fe, Co and Ni. Of this series, STA-12(Ni) demonstrates the highest N_2 adsorption capacity and significantly higher uptake of CO_2 over CH_4 at 30°C. Another important consideration is the synthesis conditions. STA-12(Ni) does not have any competitive phases with similar synthesis comditions, nor does it require pH adjustment prior to the hydrothermal crystallisation which is beneficial when increasing the scale of the reaction.

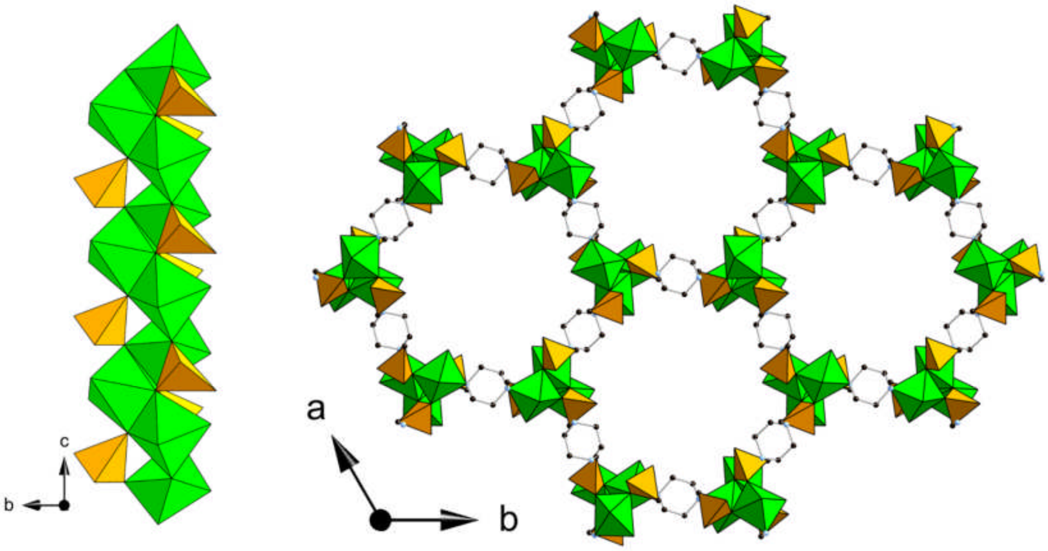

Figure 3.19: Helical nickel phosphonate chains *(left)* and hexagonal channels *(right)* of the STA-12(Ni) framework. Nickel coordination polyhedra are shown in green and the phosphonate tetrahedra in orange. Carbon and nitrogen atoms of the piperazine ring are shown as black and blue spheres respectively.

3.3.1 Synthesis

In preparation for the selectivity and separation experiments, a large quantity of STA-12(Ni) was required (~10 g). In a typical synthesis of STA-12(Ni), using a 40 mL autoclave, the reaction yields around 250 mg of product. Initially the synthesis of STA-12(Ni) was based on the literature preparation and to increase the quantity produced, a series of reactions were performed varying the dilution to maximize the quantity of product formed without limiting the porosity, detailed in Table 3.5.

Nickel Acetate	$H_4\mathbf{1}$	Water	Temp /°C	Time /h	Product
2	1	500	220	100	STA-12(Ni)
2	1	1000	220	100	STA-12(Ni)
2	1	1500	220	100	STA-12(Ni)
2	1	2000	220	100	STA-12(Ni)

Table 3.5: Reaction conditions for large scale STA-12(Ni) synthesis, reaction scaled using 50 mL of water in a 100 mL volume PARR type autoclave.

The series shows an improvement in the crystallinity with increasing dilution (Figure 3.20). The most concentrated gel mixture (2 : 1 : 500) showed noticeably broader diffraction peaks than the 1000 and 1500 products. The chosen gel composition for the large scale synthesis was 2 : 1 : 1000 ($Ni(OAc)_2{\cdot}4H_2O$: $H_4\mathbf{1}$: H_2O) on a 50 mL scale using a 100 mL Teflon® lined autoclave heated at 220°C for 100 hours. The product yield from a typical reaction of this type was ~85% (based on the nickel).

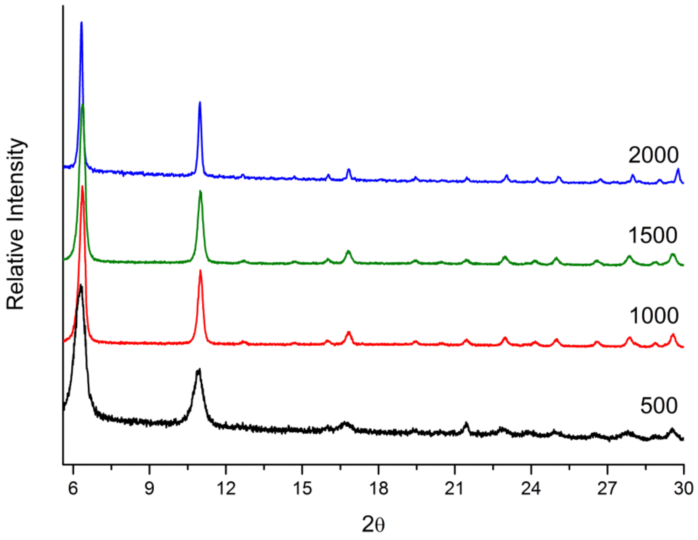

Figure 3.20: STA-12 reaction products labeled by the relative quantities of water used in the synthesis

3.3.2 Breakthrough experiments

Following the successful synthesis of a suitable quantity of STA-12(Ni), breakthrough curves were used to measure the selectivity in the separation of CH_4 and CO_2. The data was collected at 30°C using a packed column of STA-12(Ni) powder. Experiments were performed in Lyon, in collaboration with Gerhard Pirngruber, IFP-Lyon. A schematic representation of the breakthrough experiment is shown in Figure 3.21.

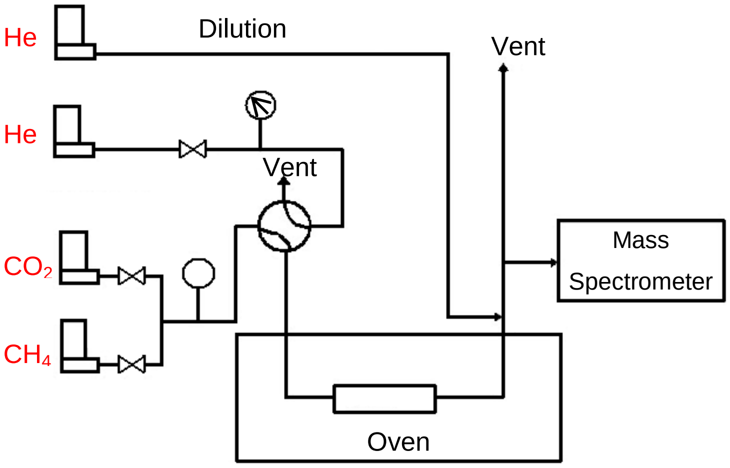

Figure 3.21: Schematic of breakthrough curve equipment

Breakthrough experiments are described in section 2.5.2 above. In the STA-12(Ni) case, a 50:50 binary mixture of CO_2 and CH_4 was used at both 1 bar and 5 bar pressure. At 1 bar pressures, both components are adsorbed initially until saturation of the adsorption sites. At this point, the CH_4 is first to breakthrough followed by a roll-up peak, resulting from the displacement of adsorbed CH_4 by CO_2 (Figure 3.22).

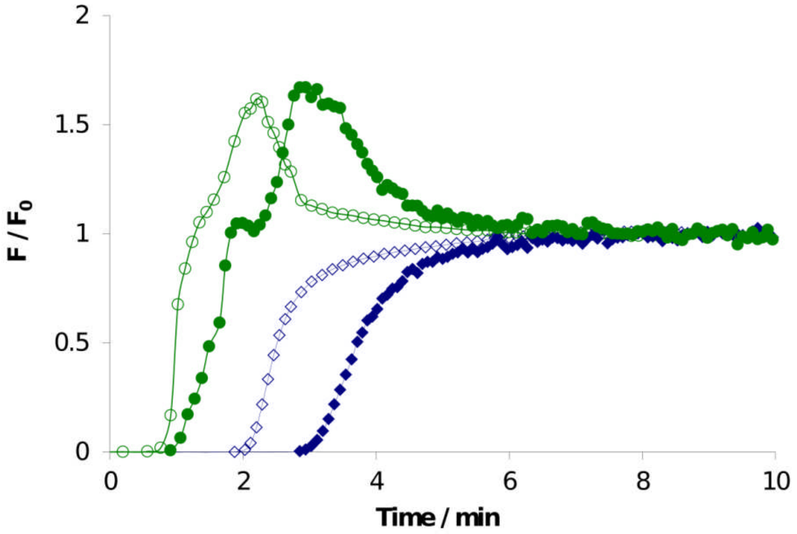

Figure 3.22: Breakthrough curves of a 50/50 mixture of CO_2/CH_4 over STA-12-Ni at 303 K. Full symbols: 1 bar total pressure, open symbols: 5 bar total pressure. CH_4: circles, CO_2: diamonds.

The final step is saturation of the column with CO_2 after which the CO_2 breaks through to the detector. Similar behaviour was observed at the higher pressure (5 bar) with a higher measured selectivity for CO_2 over CH_4. The roll-up effect is a strong indicator of high selectivity as the incoming CO_2 (after initial saturation of the adsorption sites with both components) displaces the adsorbed CH_4 resulting in a column saturated with CO_2 in the presence of a mixture. The values obtained for the selectivity on a 50:50 binary mixture and a 70:15:15 ternary mixture of CO_2:CH_4:CO at 1,5 and 10 bar are shown in Table 3.6.

P (bar)	Gas mix CO_2:CH_4:CO	CO_2 uptake (mmolg^{-1})	CH_4 uptake (mmolg^{-1})	CO uptake (mmolg^{-1})	CO_2/CH_4 selectivity	Min* CO_2/CH_4 selectivity	Max* CO_2/CH_4 selectivity	CO_2/CO selectivity
1	50:50:0	1.19(11)	0.19(7)	n.a.	6.5	4.7	10.1	n.a.
5	50:50:0	3.44(23)	0.14(9)	n.a.	24.3	14.8	44.6	n.a.
10	50:50:0	3.67(27)	0.00(28)	n.a.	∞	44.6	∞	n.a.
1	70:15:15	1.7(3)	0.05(2)	0.07(2)	7.2	5.2	12.0	5.2
5	70:15:15	2.3(4)	0.00(5)	0.00(8)	>11			>6
10	70:15:15	4.4(4)	0.00(12)	0.00(15)	>8			>6

Table 3.6: Selectivity results for STA-12(Ni), calculated from the breakthrough curve data.*Minimum and maximum values determined by taking measurement errors into account.

Single component breakthrough curves, used to measure the adsorption capacity, gave values of 2.51(2), 3.9(3) and 4.4(4) mmolg^{-1} at pressures of 1, 5 and 10 bar respectively (Figure 3.23). These calculated values are around 80 % of the capacity of previously measured STA-12(Ni) at the same temperature, indicating a lower than optimal capacity, possibly due to pore blocking or insufficient activation. If this value is assumed to be correct, it suggests that at 10 bar, all of the open metal sites (4 mmolg^{-1}) are occupied by CO_2.

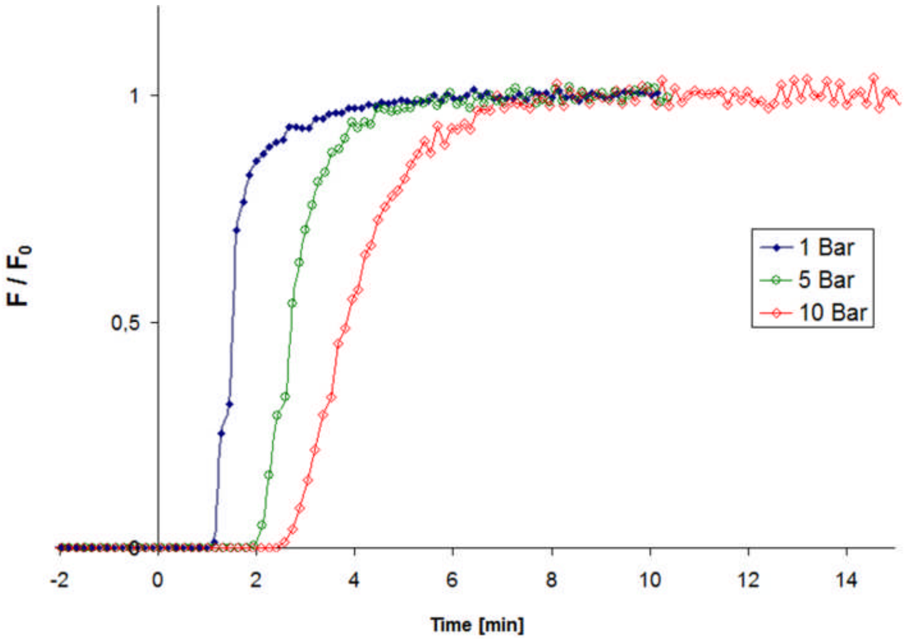

Figure 3.23: Single component breakthrough curves for CO_2 on STA-12(Ni)

The selectivity for the 50:50 binary mixture of CH_4 and CO_2 at 1 bar is calculated to be 6.5 (with a range 4.7 – 10.1 based on the errors on the individual components) within experimental error of that calculated from the single component isotherms (the ratio of uptakes from the single component isotherms is 10). This value is similar to that observed for the Cu^{2+} based HKUST-1 also with coordinatively unsaturated sites in the dehydrated state. Also of interest is that the selectivity is observed to increase with pressure for STA-12(Ni) (to a range of 44.6 - ∞ at 10 bar) whereas it is reported to increase more slowly for HKUST-1 (up to around 10 at 10 bar). A similar trend is observed in the ternary mixture at the higher pressure where the uptake of CH_4 and CO is zero with experimental error. This increase in selectivity is attributed to preferential adsorption of CO_2 on the open metal sites, blocking them from uptake of CH_4 and CO as the CO_2 uptake increases.

Additional breakthrough experiments were performed on the STA-12(Ni) column to support the selectivity values calculated from the binary mixture breakthrough curves. These included testing the column at 1, 5 and 10 bar pressure for CH_4 breakthrough where the column is pre-saturated with CO_2 (Figure 3.24). This, as expected, resulted in very low breakthrough times, approaching 0 at 10 bar indicating almost no CH_4 is adsorbed in the presence of CO_2. The desorption was also studied (Figure 3.24) and again confirmed that the CH_4 was purged very quickly whereas the CO_2 showed a much more gradual release.

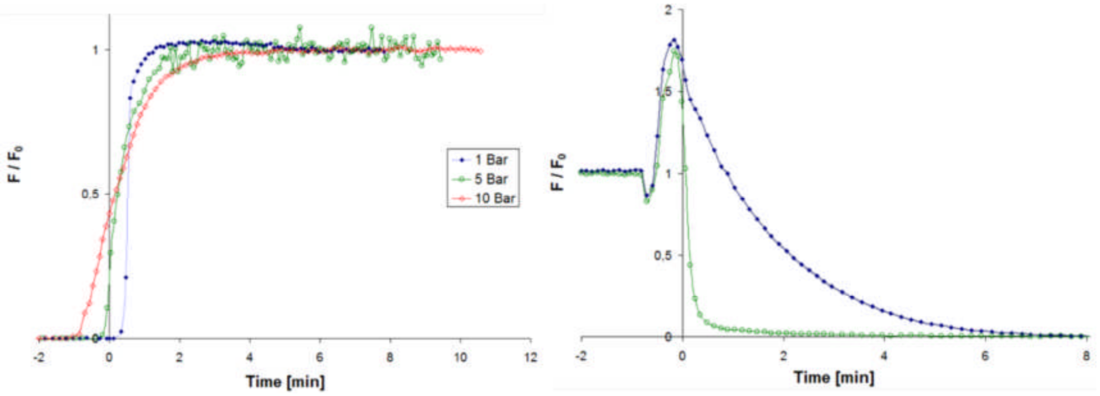

Figure 3.24: Single component breakthrough curves for CH_4 on the STA-12(Ni) column pre-saturated with CO_2 (*left*) and the desorption of the 50/50 binary mixture at 1 bar (*right*).

The selectivities measured for STA-12(Ni) are similar to calculated values for MOFs with accessible Cu^{2+} sites at low pressure and much higher at high pressure and they are much higher than MOFs which do not contain coordinatively unsaturated sites such as MOF-5 and ZIF-8 (both around 2.5).

3.3.3 PLOT column

The high selectivities measured for STA-12(Ni) suggest that the material is suitable for use as a stationary phase in gas chromatography (GC) experiments. STA-12(Ni) precipitates from the reaction gel as a microcrystalline powder, consisting of small needle crystals (0.1 × 0.1 × 1 μm). This suggests the packed column approach would not suitable as there would be minimal inter-particle void space and as such there would likely be problems maintaining a constant pressure and flow through the column. A more suitable method of column preparation is the porous layer open tubular (PLOT) approach. The preparation of this type of column requires small particles, preferably with a uniform particle size distribution, which are dispersed in solvent and deposited on the inner surface of a capillary column. This was performed in collaboration with Agilent Technologies, Inc. where STA-12(Ni) samples, prepared in St. Andrews were sent for preparation of the PLOT column. The resulting PLOT column had a thin, uneven coating of the STA-12(Ni) particles, due to the needle like morphology of the crystals arranging both parallel to the column walls and projecting out into the open capillary. The resulting later was measured to range in thickness from 0.06 – 0.6 μm which, although maximizing the surface area, might lead to reproducibility problems upon preparation of subsequent columns. The retention times and plate numbers for a series of single component alkanes are shown in Table 3.7.

Alkane	Boiling point (K)	Retention time (min)	Plate number
Methane	111.6	0.95	6533
Ethane	184.6	1.05	11,949
Propane	231.1	1.50	16,907
Isobutane	261.5	2.52	18,171
n-Butane	272.7	2.76	15,595
Neopentane	282.7	3.66	26,247
Isopentane	300.9	4.17	34,972
n-Pentane	309.3	4.41	25,070
n-Hexane	342.2	6.08	27,525

Table 3.7: Retention times and plate numbers for a series of low boiling point alkanes on the STA-12(Ni) PLOT column

A gas chromatogram was collected, using a mixture of hydrocarbons present in a natural gas mixture, measured using a flame ionization detector (FID) (Figure 3.25). The chromatogram shows the components to be eluted in order of their respective boiling points, indicating no size selective effects, as expected based on the pore size of dehydrated STA-12(Ni).

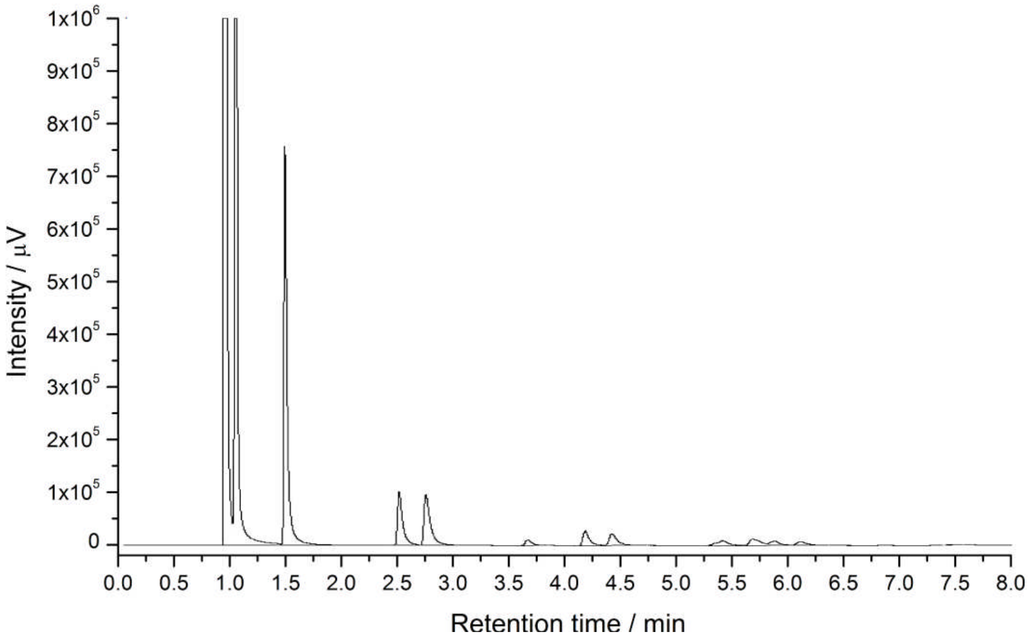

Figure 3.25: Gas chromatogram showing the signals recorded for the components listed in Table 3.7

Following the testing by Agilent Technologies, Inc., the column was tested in a GC oven in St. Andrews. Laboratory grade hexane (mixed isomers) was passed through the column using an isothermal temperature of 150°C showed four reasonably well resolved peaks (Figure 3.26). A second mixture of 50:50 *n*-hexane and the mixed hexane isomers indicated that the linear *n*-hexane eluting last (Figure 3.26).

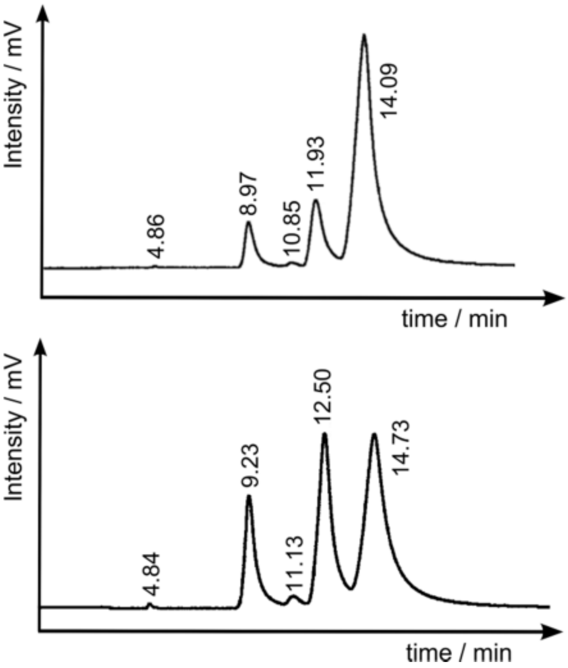

Figure 3.26: Gas chromatograms collected on a PLOT column containing STA-12(Ni)

Further work is required to improve the uniformity of the coating and explore further the separation behaviour and selectivity to specific applications. However, the initial results are encouraging and confirm that a PLOT column method is a feasible approach to prepare MOF based columns.

3.4 Summary of metal phosphonate studies

It was shown that by varying the metal source and the methylphosphonate precursor it was possible to control the particle morphology and porosity in the mixed metal ScAlMePO-α. A series of hydrothermal reaction conditions were used to understand the effects of modifying parameters such as the use of methylphosphonic acid or the dimethyl ester derivative and the solubility of the scandium precursor. The final product was characterized by means of laboratory X-ray powder diffraction, solid state NMR and elemental analysis confirming that the product was the mixed metal ScAlMePO-α with the occupancy of the octahedral site calculated to be 97.5% scandium and 2.5% aluminium from Rietveld refinement against the powder X-ray diffraction data.

The bisphosphonate linkers **1**, **2** and **3** have been shown to produce three framework types with the lighter and larger lanthanides La, Ce and Nd. The metals adopt seven or eight fold coordination with the oxygen and nitrogen of the linker and additional water molecules, in all cases producing metal phosphonate chains connected through the bisphosphonate linker. The structure which crystallises from the reaction depends on the pH of the starting gel which influences the protonation state of the organic linker used. The addition of $–CH_3$ groups introduces sufficient steric interactions to direct the formation of different structures. The reversible hydration of structure type I was shown to be accompanied by a significant reduction in unit cell volume and an associated conformational flip from chair to boat configuration in the piperazine ring, reversible upon subsequent rehydration.

Testing of the permanently porous STA-12(Ni) as a stationary phase for gas chromatography yielded some promising results. Selectivity values, measured using breakthrough curves with pure components and mixtures, indicated that STA-12(Ni) was a suitable material for further study in chromatography experiments, with high selectivity for the adsorption of carbon dioxide over methane. STA-12(Ni) samples were used to prepare a PLOT column, in collaboration with Agilent Technologies, Inc. and tested for a series of low boiling point hydrocarbons. The column showed effective baseline separation of the mixture, despite the poorly optimized coating arising from the long, needle-like particle morphology of STA-12(Ni). Higher molecular weight liquid C_6 mixtures were tested ion the same column in a capillary GC oven in St. Andrews, again showing some interesting preliminary results which indicate that STA-12(Ni) could have applications in this area.

4 Synthesis of Scandium Carboxylate MOFs

4.1 Overview

As discussed in the introduction, scandium has been shown to be a promising candidate for MOF synthesis. With this in mind, and considering the wide range of structures which have been reported in the literature with trivalent metals and simple carboxylate linkers, a series of carboxylate linkers will be investigated with different scandium sources to further explore the crystal chemistry. This work expands on an initial exploratory hydrothermal study on scandium carboxylates reported in the PhD thesis of Dr. Stuart Miller. The work yielded, among other examples, the first permanently porous scandium based MOF, Sc_2BDC_3.[27,83] Also of interest was another phase, observed as a minor product in a preparation of Sc_2BDC_3, identified to be isostructural with the MIL-53(Cr) framework in the as-synthesised form.[104] The structure was solved from a single crystal, taken from the mixture with Sc_2BDC_3, however, the MIL-53(Sc) phase was not observed to form as the pure product. The preparation of this material as well as evidence for the scandium trimer based MIL-88(Sc) framework, reported by Dietzel and co-workers,[84] suggests that there is a number of scandium based MOFs which should be chemically stable.

During the course of this thesis there has been an increased interest in scandium based MOF materials resulting in the discovery of other novel framework types to those discussed here. The first of these materials was a scandium squarate, reported by Gandata *et al.*[105] and shown in (Figure 4.1).

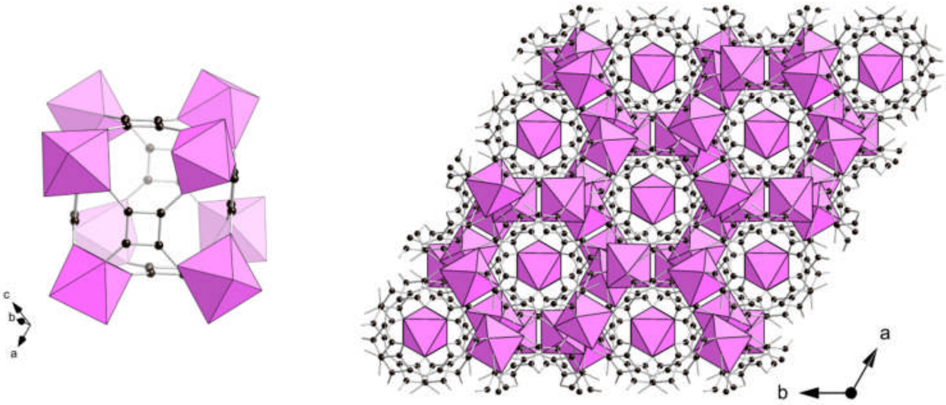

Figure 4.1: Scandium squarate structure showing a single single cage (*left*) and the structure viewed down the c-axis (*right*). Scandium octahedra are shown in pink. Black spheres represent the carbon atoms of the organic linker.

Although the structure possesses cubic cavities, the porosity cannot be accessed by gas molecules due to the small windows between cages.[105] Work in the same research group of Monge *et al.* also yielded a scandium croconate structure (Figure 4.2).[106] In this case the structure is not a 3D framework, rather an arrangement of $[Sc_7(croc)_6(H_2O)(OH)_7O]$ clusters. This structure is interesting as it is an example of a scandium-based cluster that could be incorporated into a MOF framework with a suitable organic linker. Around the same time, the group also published a review of scandium, yttrium and lanthanum carboxylate and sulfonate MOFs including the scandium carboxylates discussed here.[107]

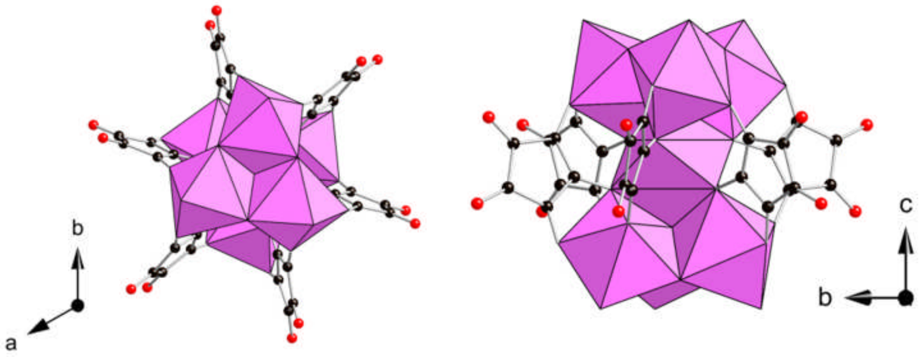

Figure 4.2: View down the c-axis and a-axis showing a single $[Sc_7(croc)_6(H_2O)(OH)_7O]$ cluster. Scandium coordination polyhedra are shown in pink. Black and red spheres represent the carbon and oxygen atoms of the organic linker respectively.

Work by Ibarra *et al.*[108,109] yielded four scandium MOF frameworks. The first of these was the scandium terephthalate MIL-88B(Sc) framework, previously reported by Dietzel *et al.*[84] Published with the MIL-88B(Sc) was a novel scandium carboxylate prepared with the large tri-carboxylate linker 1,3,5-tris(4-carboxyphenyl)benzene commonly referred to in literature as BTB shown in (Figure 4.3).[108]

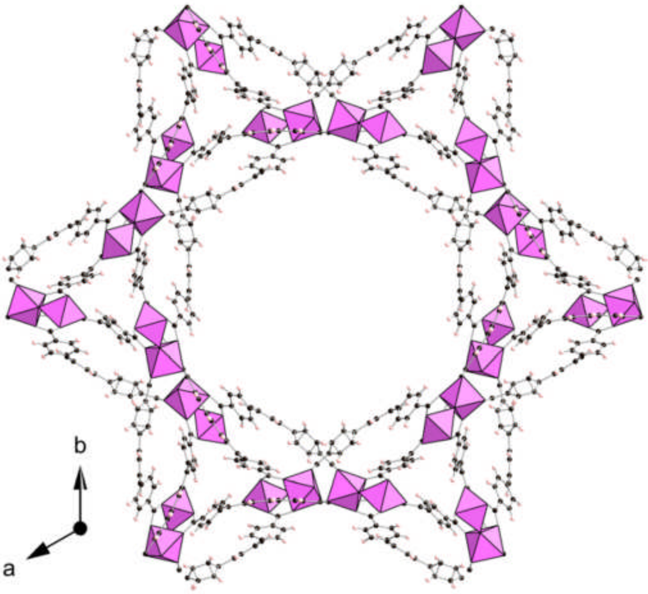

Figure 4.3: Large pore scandium carboxylate MOF, Sc-BTB composed of the trimeric scandium cluster and 1,3,5-tris(4-carboxyphenyl)benzene. Scandium octahedra are shown in pink. Black and pink spheres represent the carbon and hydrogen atoms of the organic linker respectively.

Further work in the same research group of Schröder *et al.* yielded two novel scandium frameworks using the biphenyl-3,3’,5,5’-tetracarboxylate and thiophene-2,5-dicarboxylate linkers shown in (Figure 4.4).[109]

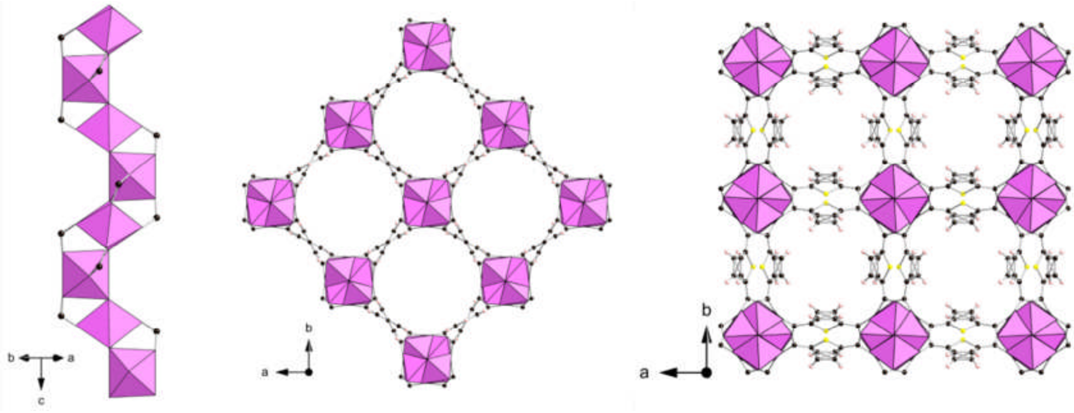

Figure 4.4: Scandium carboxylate MOFs comprised of helical corner-sharing octahedral scandium chains (*left*) and the resulting porous frameworks with the biphenyl-3,3’,5,5’-tetracarboxylate (middle) and thiophene-2,5-dicarboxylate (*right*). Scandium octahedra are shown in pink. Black yellow and pink spheres represent the carbon, sulfur and hydrogen atoms of the organic linker respectively.

This work explores the hydrothermal and solvothermal crystal chemistry of scandium[110-112] with the di, tri and tetra carboxylate linkers show below (Figure 4.5).

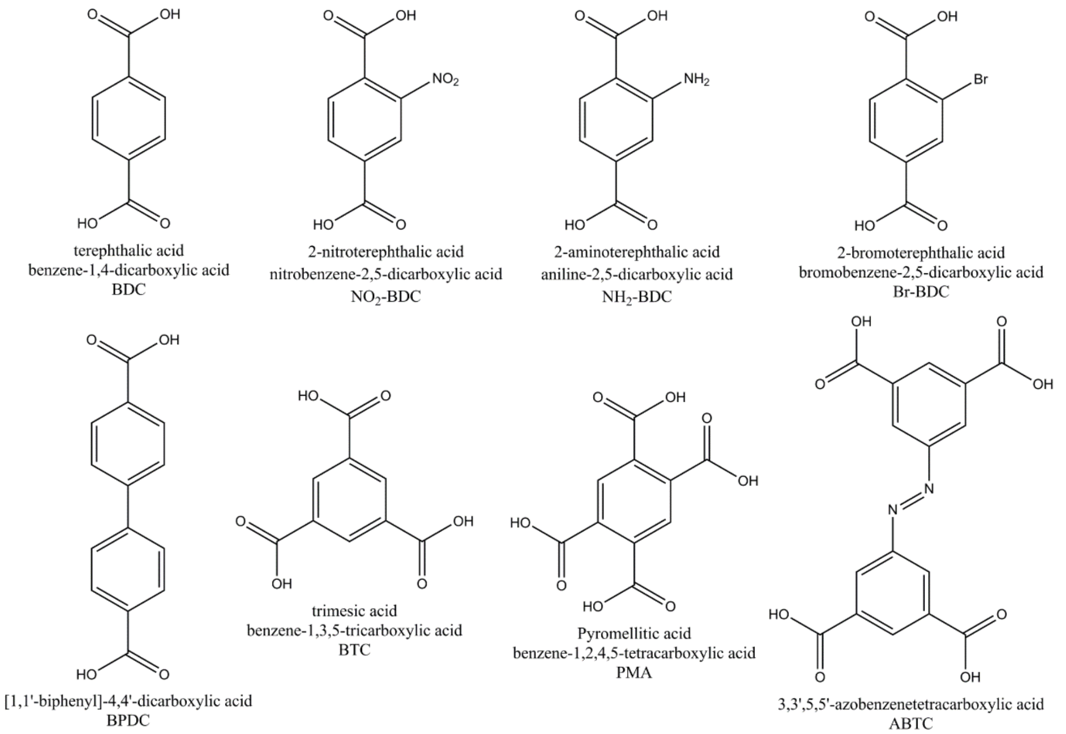
terephthalic acid
benzene-1,4-dicarboxylic acid
BDC

2-nitroterephthalic acid
nitrobenzene-2,5-dicarboxylic acid
NO_2-BDC

2-aminoterephthalic acid
aniline-2,5-dicarboxylic acid
NH_2-BDC

2-bromoterephthalic acid
bromobenzene-2,5-dicarboxylic acid
Br-BDC

[1,1'-biphenyl]-4,4'-dicarboxylic acid
BPDC

trimesic acid
benzene-1,3,5-tricarboxylic acid
BTC

Pyromellitic acid
benzene-1,2,4,5-tetracarboxylic acid
PMA

3,3',5,5'-azobenzenetetracarboxylic acid
ABTC

Figure 4.5: The di-, tri- and tetra-carboxylate linkers used in this work.

4.2 Experimental

The crystal chemistry of the scandium terephthalate system was explored, varying the quantity of scandium, carboxylic acid linker, solvent and temperature with the aim of preparing and characterising novel frameworks. Experiments with terephthalic acid were performed first, using both hydro- and solvothermal syntheses, via conventional heating. Reaction stoichiometries were based on previous work with scandium carboxylates and literature examples of trivalent carboxylates. In a typical preparation, the metal salt or oxide and terephthalic acid were dissolved or thoroughly mixed in solvent (with mechanical stirring), transferred to a Teflon lined stainless steel autoclave and heated in a conventional oven. In a typical synthesis of the scandium terephthalate, Sc_2BDC_3, scandium nitrate (Metall Rare Earth Limited, 0.269 mmol, 0.0768 g) and terephthalic acid (Aldrich, 98%, 0.539 mmol, 0.0895 g) were dissolved in DEF (Alfa Aesar, 98%, 6mL) with continuous stirring, the solution was transferred to a 23 mL Teflon lined stainless steel Parr autoclave and heated for 72 hours at 190°C.

Upon cooling, the reaction was filtered and washed thoroughly with ethanol to remove excess DEF and the product was transferred to a drying oven and left overnight to ensure removal of the ethanol. Products were filtered and washed with the reaction solvent where possible, however, reactions using DMF and DEF as the solvent were filtered in a fume hood and washed with ethanol to minimise release of the potentially toxic solvent upon drying.

Following the successful optimization of syntheses using scandium and terephthalic acid, further study was performed on the longer polycarboxylate linkers using the optimized reaction syntheses. Details of the reaction stoichiometries used are outlined in tables in the relevant sections where the reactions are scaled based on 6 mL volume of solvent, an appropriate volume for the autoclaves used and a suitable level of dilution (if the yield is 50% or greater) to obtain enough product for analysis using powder X-ray diffraction, TGA and adsorption.

Where possible, the structures were solved from single crystal X-ray diffraction using direct methods and Fourier mapping. Bulk phase purity in the products was checked using powder X-ray diffraction, either to compare the experimental pattern with a simulated pattern from the crystal structure or, if the data was of suitable quality, by Rietveld refinement allowing refinement of the atomic positions. In a number of cases discussed below, single crystals were not available and the powder X-ray diffraction data, even when collected for up to 16 hours (to maximise the signal to noise ratio in the diffraction pattern), was not of sufficient quality to enable Rietveld refinement. To identify these low crystallinity products, typical of MOFs with exceptionally large unit cells (up to 76.4 Å), the data was compared to literature examples where the same linker and trivalent metals with similar chemical behavior (such as chromium, iron and indium) were used. This approach was successful in the identification of the remaining crystalline phases observed in this work. The unit cell of these materials was indexed using the Fullprof suite of programs and refined using the Le Bail method to compare the unit cell and symmetry of the scandium analogue to the literature structure.

4.3 Scandium Dicarboxylates

A series of hydrothermal and solvothermal reactions were carried out using scandium oxide or scandium nitrate and terephthalic acid as outlined in Table 4.1. Reactions conditions were also chosen to replicate the synthetic conditions reported for literature materials thought to be possible with scandium, such as those used in the preparation of MIL-53(Fe) reported by Whitfield *et al.*[113] Where literature preparations included mixed solvents or additives, the reactions were performed with and without these additions (such as pyridine in the synthesis of MIL-53(Sc)) to determine whether that all additions were necessary to prepare the observed products.

4.3.1 Higher temperature (160 - 220°C) dicarboxylate syntheses

Temp. /°C	Solvent	Scandium source	Molar ratios in Preparation				Time / h	Product
			Sc	H_2BDC	Solvent	Pyridine		
190 - 220	H_2O	$Sc(NO_3)_3.3H_2O$	1.0	1.5	600	-	24 - 72	Sc_2BDC_3
190 - 220	H_2O	Sc_2O_3	1.0	1.5	600	-	72	Sc_2BDC_3*
190	DMF	Sc_2O_3	1.0	1.5	300	-	72	Recryst. H_2BDC
190	DEF	$Sc(NO_3)_3.3H_2O$	1.0	1.5	200	-	40	Sc_2BDC_3 ‡
190	DEF	$Sc(NO_3)_3.3H_2O$	1.0	1.0	200	15	40	MIL-53(Sc)
190	DMF	$Sc(NO_3)_3.3H_2O$	1.0	1.5	300	-	40	Sc_2BDC_3
190	DMF	$Sc(NO_3)_3.3H_2O$	1.0	1.0	300	-	40	MIL-53(Sc) + Sc_2BDC_3
190	DMF	$Sc(NO_3)_3.3H_2O$	1.0	1.5	300	15	40	MIL-53(Sc)
190	DMF	$Sc(NO_3)_3.3H_2O$	1.0	1.0	300	15	40	MIL-53(Sc) ‡

Table 4.1: Synthetic conditions and products in hydrothermal and solvothermal crystallisations of scandium terephthalates at higher temperatures (190-220°C). *Reaction performed in a 100 ml Parr autoclave using 50mL solvent volume. ‡Reactions reproducibly yield highly crystalline phase pure products

4.3.1.1 Sc_2BDC_3

Higher temperature (160 – 220°C) hydrothermal reactions, using both the scandium oxide and scandium nitrate, were successful in the preparation of Sc_2BDC_3. Samples prepared using the soluble scandium nitrate source were observed to crystallise as large prismatic, single crystals (>100×30×30) µm with no evidence of impurities. The scandium oxide was also successful in the synthesis of Sc_2BDC_3 but the product formed as a microcrystalline powder forming as a dense layer of aggregates at the bottom of the autoclave. These polycrystalline particles range in size from <5 µm to 150 µm with powder X-ray diffraction analysis indicating that some unreacted scandium oxide was also present. Attempts to remove the scandium oxide by sonication were unsuccessful due to the small particle size observed for Sc_2BDC_3 prepared via this route. To prepare pure samples of Sc_2BDC_3 from scandium oxide, the reaction was first performed using the stated conditions, but rather than filtering and washing the product after the reaction, the product was broken up in a pestle and mortar (still under the 'mother liquor'). An additional 10 % of the starting quantity of terephthalic acid was added to the suspension and the reaction heated for a further 72 hours (Figure 4.6). This approach yielded Sc_2BDC_3 with similar crystallinity to the first reaction but with a small quantity of recrystallized terephthalic acid. Unlike the scandium oxide, terephthalic acid is easily removed from the Sc_2BDC_3 product (known to have suitable thermal stability) by heating in a tube furnace under flowing air at 350°C (terephthalic acid sublimes below this temperature). Simply adding a 10% excess of terephthalic acid to the starting mixture was not sufficient to improve the purity of the product as the initial reaction still crystallised as a dense layer of aggregates where the unreacted scandium oxide is inaccessible to the free terephthalic acid in solution yielding a mixture of all three components. This approach was also successful in the preparation of large scale samples for packed column testing.

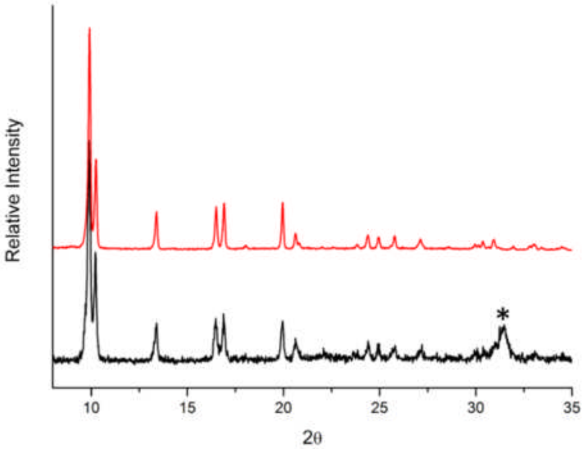

Figure 4.6: Sc_2BDC_3 reaction products using Sc_2O_3. The pattern below (black) shows the first reaction with un-reacted Sc_2O_3 impurities* and the pattern above (red) shows the sample after a second heating cycle with additional terephthalic acid.

The reaction was scaled up to 50 mL of solvent in a 100 mL PARR autoclave and heated at 200°C for 72 hours. Again in this case, to ensure the reaction has gone to completion, the product was ground in a pestle and mortar and heated for a further 72 hours yielding Sc_2BDC_3 and excess terephthalic acid. The final product was washed, dried and calcined at 350°C for 10 hours to remove the unreacted acid.

Solvothermal reactions using DMF and DEF yielded both the highly crystalline Sc_2BDC_3 and a second product, identified to be MIL-53(Sc), the respective frameworks are shown in Figure 4.7.

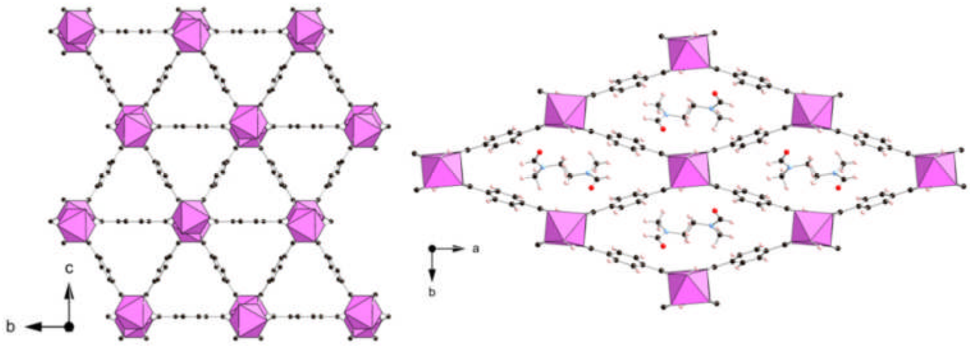

Figure 4.7 : High temperature products Sc_2BDC_3 and MIL-53(Sc). Scandium octahedra are shown in pink. Black, red and blue spheres represent the carbon, oxygen and nitrogen atoms of the organic linker respectively.

The solvothermal syntheses were also more sensitive to the scandium source used. The oxide was unsuccessful under the solvothermal conditions (using DMF and DEF) at the higher temperature (≥190°C). The more soluble scandium sources (nitrate and chloride) yielded crystalline products, often with much larger crystal size than the hydrothermal reactions.

Syntheses were performed using scandium oxide (Sc_2O_3, 99.999%, Stanford Materials Corporation), scandium nitrate ($Sc(NO_3)_3 \cdot 3H_2O$, 99.9%, Metall Rare Earth Limited) and a scandium chloride solution (prepared by dissolving Sc_2O_3 in a stoichiometric amount of HCl to produce $ScCl_{3(aq)}$). Sc_2BDC_3 was prepared according to the ratios reported in Chapter 4. In a typical synthesis of highly crystalline Sc_2BDC_3, terephthalic acid (Aldrich, 98%) and scandium nitrate in the ratio 2:1 were dissolved in diethylformamide, DEF (Alfa Aesar, 98%) and heated at 463K for 72 hours. The resulting solid was washed with ethanol and dried at 333K. For the variable temperature ^2H solid-state NMR experiments it was necessary to prepare Sc_2BDC_3 using d_4-terephthalic acid (Sigma, 98 atom % D), the same solvothermal route as described above was used in the preparation and as no additional species are involved in the framework, deuterated solvents were not required. Hydrothermal syntheses using scandium oxide, successful in the synthesis of the pure terephthalate form of Sc_2BDC_3, were also successful in the preparation of the amino and nitro functionalised derivatives of Sc_2BDC_3 using the functionalised organic linkers, 2-nitroterephthalic acid (Alfa Aesar, 99%) and 2-aminoterephthalic acid (Aldrich, 99%). Subsequent hydrothermal syntheses using scandium nitrate as the scandium source were successful in the preparation of single-crystals of the $Sc_2(NO_2\text{-}BDC)_3$.

By analyzing the products and comparing the results to the synthesis conditions it was found that adjusting the experimental ratio to match the stoichiometry of the products favoured the respective materials. To prepare the highly crystalline Sc_2BDC_3 product, DEF was the preferred choice of solvent as it gave the pure Sc_2BDC_3 reproducibly, the DMF reactions would on occasion give a mixture of Sc_2BDC_3 and small quantities of MIL-53(Sc).

4.3.1.2 Functionalised Sc_2BDC_3

The small pore Sc_2BDC_3 is a particularly interesting candidate for a number of separation experiments. The reasons for this are the small pore cross-section, where guest molecules can interact with more than one face of the pore channel, the naturally hydrophobic pore surface and the high thermal stability. To modify and tune the properties of the material, reactions using NH_2-BDC, NO_2-BDC and Br-BDC as the organic linker were explored with the aim of preparing the functionalised derivatives of the Sc_2BDC_3framework. The reaction conditions used are shown below in Table 4.2.

Temp. /°C	Scandium source	Solvent	Molar ratios in Preparation				Time / h	Product
			Ligand	Sc	Liganc	Solvent		
190	$Sc(NO_3)_3.3H_2O$	H_2O	NH_2-BDC	1.0	1.5	600	72	MIL-88(Sc)-NH_2
190	$Sc(NO_3)_3.3H_2O$	DEF	NH_2-BDC	1.0	1.5	300	72	MIL-88(Sc)-NH_2
190	Sc_2O_3	H_2O	NH_2-BDC	1.0	1.5	600	72	$Sc_2(NH_2\text{-BDC})_3$ + Sc_2O_3
190	$Sc(NO_3)_3.3H_2O$	H_2O	NO_2-BDC	1.0	1.5	600	72	$Sc_2(NO_2\text{-BDC})_3$
190	$Sc(NO_3)_3.3H_2O$	DEF	NO_2-BDC	1.0	1.5	300	72	MIL-53(Sc)-NO_2
190	Sc_2O_3	H_2O	NH_2-BDC	1.0	1.5	600	72	$Sc_2(NO_2\text{-BDC})_3$ + Sc_2O_3
190	$Sc(NO_3)_3.3H_2O$	DEF	Br-BDC	1.0	1.5	300	72	Sc_2BDC_3-?
220	$Sc(NO_3)_3.3H_2O$	H_2O	NO_2-BDC	1.0	1.5	600	72	Amorphous
220	$Sc(NO_3)_3.3H_2O$	H_2O	NH_2-BDC	1.0	1.5	600	72	Amorphous

Table 4.2: Reaction conditions used in the preparation of functionalised Sc_2BDC_3

The sets of reaction conditions used were based on the successful syntheses used to prepare the pure terephthalate form of Sc_2BDC_3 described above. It was clear from the results that the solvothermal reactions were not suitable for the preparation of either $Sc_2(NH_2\text{-}BDC)_3$ or $Sc_2(NO_2\text{-}BDC)_3$. The conditions used to prepare large crystals of Sc_2BDC_3 with the unfunctionalised terephthalate yielded alternative products for these functionalised linkers, MIL-88(Sc)-NH_2 for the NH_2-BDC and MIL-53(Sc)-NO_2 for NO_2-BDC. This is likely to be due to structure directing effects of the NH_2- and NO_2- inclusion which create a preference for the lower density frameworks. The Br-BDC reactions in DEF did yield a structure which looked, from the powder X-ray diffraction pattern, to have the Sc_2BDC_3 framework topology (Figure 4.8). The characterisation on this material however, suggested it was not the fully brominated $Sc_2(Br\text{-}BDC)_3$ product. This will be discussed further in Chapter 5 along with characterisation data on the other functionalised derivatives.

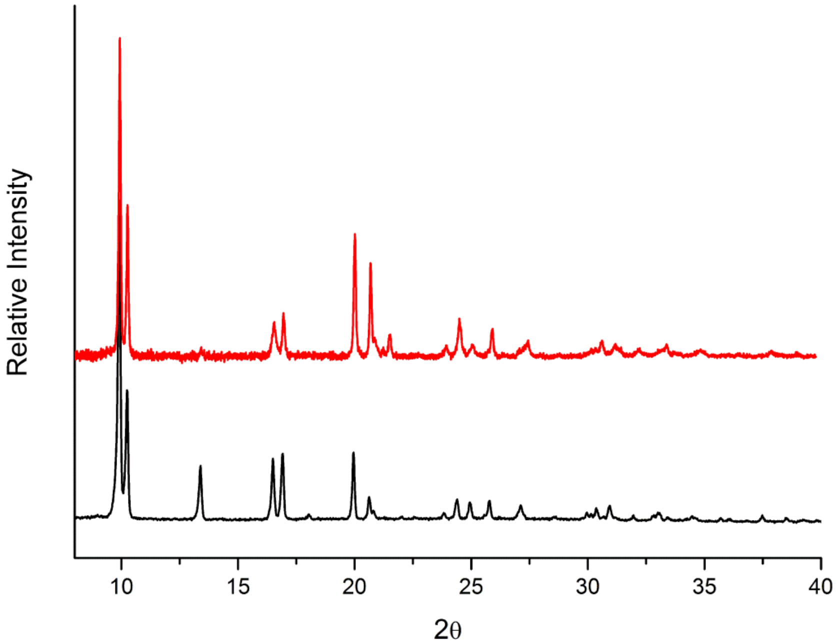

Figure 4.8: As-synthesised Sc_2BDC_3 (*below*) and the product formed using the Br-BDC precursor (*above*)

For further discussion and structural characterization on Sc_2BDC_3 including the structural response to variation in temperature and comparison with the functionalized derivatives please see Chapter 5.

4.3.1.3 MIL-53(Sc)

A typical reaction for the preparation of MIL-53(Sc) is prepared using a solution of scandium nitrate hydrate, terephthalic acid, pyridine and N,N-dimethylformamide in a molar ratio ($Sc(NO_3)_3 . 3H_2O$) : H_2BDC : C_5H_5N : DMF of 1 : 1 : 15 : 200. The solution is then thoroughly mixed by stirring at room temperature and heated at 463 K for 40 hours in a Teflon lined stainless-steel PARR autoclave. Following the reaction, samples were filtered and washed thoroughly with either DMF or ethanol and dried in a drying oven at 323 K.

It was also observed that addition of pyridine to the solvothermal reaction, in the initial synthesis solution, yielded phase pure MIL-53(Sc) (often as large single crystals) more consistently than the same reaction without addition of pyridine. Reactions with an excess of scandium were successful in the preparation of phase pure MIL-53(Sc) but due to the high cost of scandium nitrate, the pyridine route with stoichiometric amounts of the reactants was preferable and used for subsequent batch syntheses. This conditions were adapted from the synthesis of MIL-53(Fe), reported by Whitfield *et al.*[113], and used by Miller *et al.*[83] in the preparation of large crystal of Sc_2BDC_3. Reactions with and without the addition of hydrogen peroxide (used to keep the iron in the 3+ oxidation state) indicated that peroxide was not necessary in the scandium system and it was removed from subsequent preparations.

MIL-53(Sc) was observed to form in competition with the Sc_2BDC_3 in the higher temperature solvothermal reactions. From the table of syntheses the products are simply denoted MIL-53(Sc), the identification of the products from the powder diffraction patterns, however, was not a trivial process (see Chapter 6).

The crystallinity and particle size of products varied greatly from one reaction to the next with very little reproducibility other than forming the MIL-53(Sc) framework. Indeed, repeating the same reaction composition in three different types of autoclave resulted in three different powder diffraction patterns representing different states of solvation (Figure 4.9).

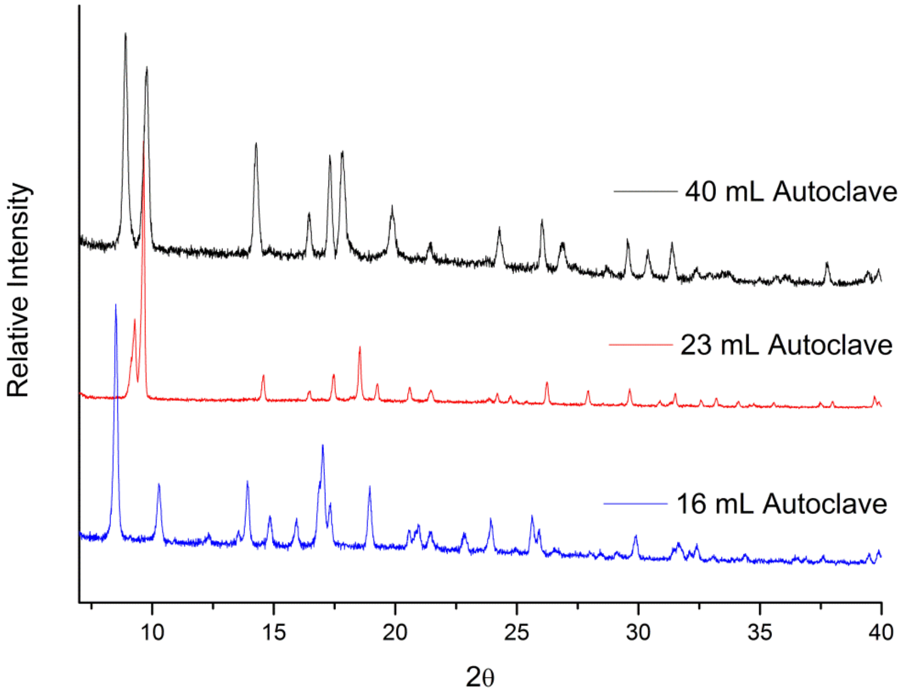

Figure 4.9: Three as-synthesised diffraction patterns for MIL-53(Sc) where the variation is caused by the shape and volume of the autoclave.

4.3.1.4 Functionalised MIL-53(Sc)

Following the successful introduction of functional groups in the small pore Sc_2BDC_3, further reactions were performed to target the synthesis of functionalised MIL-53(Sc) structures. Reactions were performed using NH_2-BDC, NO_2-BDC and Br-BDC as the organic linker. Only scandium nitrate was used as the metal source in these reactions as scandium oxide was unsuccessful in attempts to prepare the pure terephthalate form of MIL-53(Sc). The reaction conditions used are shown below in Table 4.3.

Temp. /°C	Scandium source	Solvent	Molar ratios in Preparation					Time / h	Product
			Ligand	Sc	Ligand	Pyridine	Solvent		
190	$Sc(NO_3)_3.3H_2O$	DEF	NH_2-BDC	1.	1.5	-	200	72	MIL-88(Sc)-NH_2
190	$Sc(NO_3)_3.3H_2O$	DMF	NH_2-BDC	1.	1.5	-	300	72	MIL-88(Sc)-NH_2
190	$Sc(NO_3)_3.3H_2O$	DEF	NH_2-BDC	1.	1.5	15	200	72	MIL-88(Sc)-NH_2
190	$Sc(NO_3)_3.3H_2O$	DMF	NH_2-BDC	1.	1.5	15	300	72	MIL-88(Sc)-NH_2
190	$Sc(NO_3)_3.3H_2O$	DEF	NO_2-BDC	1.	1.5	-	200	72	MIL-53(Sc)-NO_2
190	$Sc(NO_3)_3.3H_2O$	DMF	NO_2-BDC	1.	1.5	-	300	72	MIL-53(Sc)-NO_2
190	$Sc(NO_3)_3.3H_2O$	DEF	NO_2-BDC	1.	1.5	15	200	72	MIL-53(Sc)-NO_2
190	$Sc(NO_3)_3.3H_2O$	DMF	NO_2-BDC	1.	1.5	15	300	72	MIL-53(Sc)-NO_2
190	$Sc(NO_3)_3.3H_2O$	DEF	Br-BDC	1.	1.5		200	72	Sc_2BDC_3-?
190	$Sc(NO_3)_3.3H_2O$	DEF	Br-BDC	1.	1.5	15	300	72	Sc_2BDC_3-?

Table 4.3: Reaction conditions used in attempts to prepare functionalised MIL-53(Sc)

The sets of reaction conditions used were based on the successful syntheses used in the preparation of the pure terephthalate from of MIL-53(Sc) described above (Table 4.1).

As discussed in the Sc_2BDC_3 synthesis section above, reactions using the BrBDC linker yielded a product with the Sc_2BDC_3 framework. This was also true of the same reaction with addition of pyridine found to favour MIL-53(Sc) in the pure terephthalate reactions. Reactions using the NH_2-BDC linker yielded a product identified to be MIL-88B(Sc)-NH_2 (Figure 4.10).

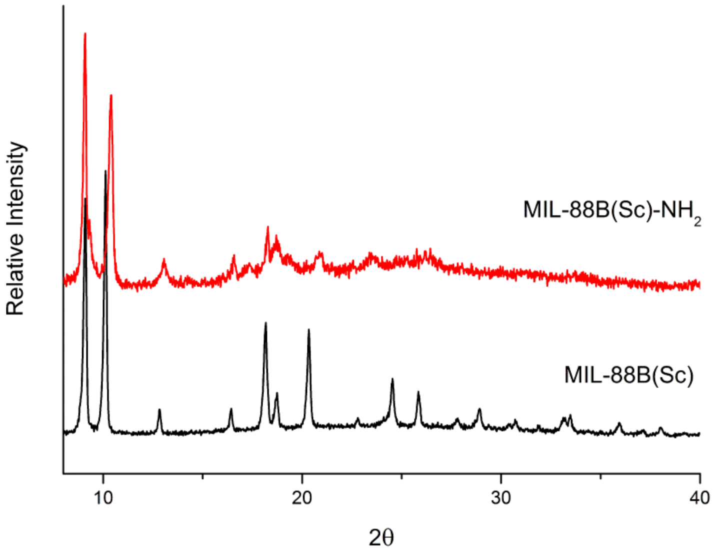

Figure 4.10: As-synthesised X-ray diffraction patterns for MIL-88B(Sc) and the MIL-88B(Sc)-NH_2 products

The results indicated that MIL-53(Sc)-NO_2 formed readily, with and without the addition of pyridine, crystallising as large prism-like single crystals (~50-100 µm in length). For further discussion and structural characterization on both MIL-53(Sc) and MIL-53(Sc)-NO_2 including the structural response to variation in temperature, see Chapter 6.

4.3.2 Lower temperature (80 – 140°C) dicarboxylate syntheses

4.3.2.1 MIL-88B(Sc)

Lower temperature (80-140°C) hydrothermal reactions using the scandium oxide and scandium nitrate were unsuccessful yielding only the recrystallised terephthalic acid (and unreacted oxide when used as the source). Solvothermal reactions over the same temperature range were successful yielding two scandium terephthalate phases, believed to be due to the increased solubility of the terephthalic acid in the DMF or DEF compared to water (Table 4.4).

Temp. /°C	Solvent	Scandium source	Molar ratios in Preparation			Time / h	Product
			Sc	H_2BDC	Solvent		
100	H_2O	Sc_2O_3	1.0	1.0	600	24 - 72	Sc_2O_3 + Recryst. H_2BDC
100	DMF	Sc_2O_3	1.0	1.0	300	24 - 72	Sc_2O_3 + Recryst. H_2BDC
100	H_2O	$Sc(NO_3)_3.3H_2O$	1.0	1.0	600	24 - 72	Recryst. H_2BDC
100	DMF	$Sc(NO_3)_3.3H_2O$	1.0	1.2	300	24 - 48	MIL-88B(Sc)
100	DMF	$Sc(NO_3)_3.3H_2O$	1.2	1.0	300	24 - 48	MIL-88B(Sc)
100	DMF	$Sc(NO_3)_3.3H_2O$	1.2	1.0	300*	24 - 48	MIL-101(Sc) + MIL-88B(Sc)
100	DEF	$Sc(NO_3)_3.3H_2O$	1.0	1.2	200	24 - 48	MIL-88B(Sc)
100	DEF	$Sc(NO_3)_3.3H_2O$	1.2	1.0	200	24 - 48	MIL-88B(Sc)
140	H_2O	$Sc(NO_3)_3.3H_2O$	1.0	1.0	600	24 - 72	Recryst. H_2BDC
140	DMF	$Sc(NO_3)_3.3H_2O$	1.0	1.2	300	24 - 48	MIL-88B(Sc)
140	DMF	$Sc(NO_3)_3.3H_2O$	1.2	1.0	300	24 - 48	MIL-88B(Sc)
140	DEF	$Sc(NO_3)_3.3H_2O$	1.0	1.2	200	24 - 48	MIL-88B(Sc)

Table 4.4: Synthetic conditions and products in hydrothermal and solvothermal crystallisations of scandium terephthalates at lower temperatures (80-140°C). *Reaction performed in a 100 ml PARR type autoclave using 50mL solvent volume.

Reaction products were identified by means of powder X-ray diffraction. In the case of the highly flexible MIL-88B(Sc) structure, this was challenging due to the large variation in the observed diffraction patterns, resulting from variations in the occluded solvent species present in the channels. To improve the consistency in the experimental powder diffraction patterns, samples were washed thoroughly with ethanol after filtration and dried at 50°C. Samples treated in this way were found to have a more reproducible powder diffraction pattern which could be indexed, using the TREOR method in the Fullprof suite of programs, as the hexagonal unit cell (*P*-62*c*, *a* = 11.2190(9) Å, *c* = 19.373(3) Å) similar to that observed for the literature MIL-88B(Cr) (*P*-62*c*, *a* = 11.0282(10) Å, *c* = 18.9717(10) Å) (Figure 4.11).

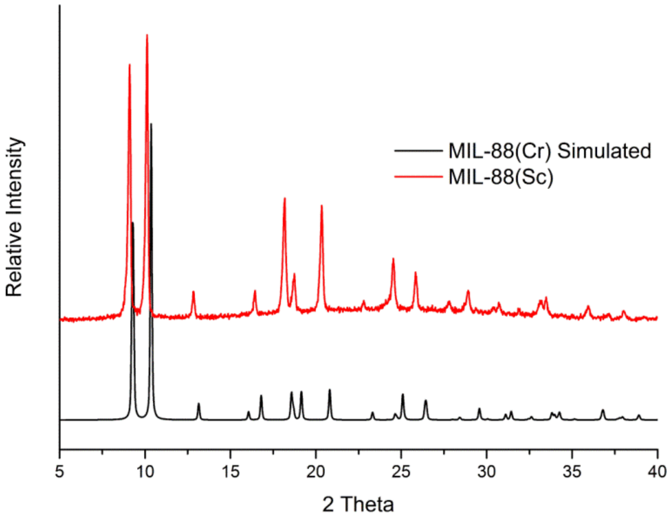

Figure 4.11: Experimental powder diffraction pattern of as-synthesised MIL-88B(Sc) compared to the pattern simulated from the literature structure of MIL-88B(Cr)

Rietveld refinement was used to confirm the structure of the as-synthesised material, denoted MIL-88(Sc)-DMF, using laboratory X-ray powder diffraction data collected at room temperature from 5-70 °2θ over 16h. The starting atomic positions were adapted from the structural model of MIL-88B(Cr), reported by Serre *et al.*[67], using the unit cell values obtained from the indexing software. The additional solvent species were modeled as a mixture of DMF (solvent from the reaction) and H_2O (from reaction or adsorbed from air following drying at 50°C) and were again adapted from those reported for MIL-88B(Cr). Geometric distance constraints were applied to the model to maintain chemical sense in the ligand and the trimetric cluster building unit. The plot from the Rietveld refinement of MIL-88B(Sc)-DMF is shown in Figure 4.12. The final structural formula was determined to be $[Sc_3O(OH)(OH_2)_2(BDC)_3]$ in agreement with the elemental analysis on a calcined sample: C expected. 41.40 wt.%; C measured, 41.13 wt.%, N measured 0.0 wt.%.

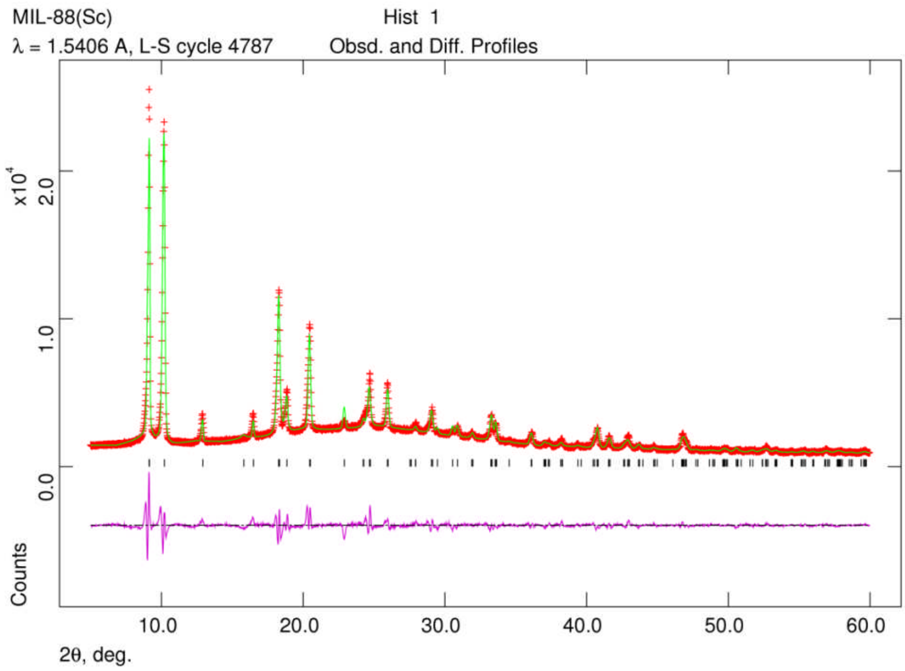

Figure 4.12: Rietveld profile fit for MIL-88B(Sc)-DMF

Thermogravimetric analysis shows the material to be stable to heating (under flowing air) to temperatures >450°C. TGA on an ethanol-washed sample, MIL-88B(Sc)-DMF, shows a weight loss of 19.5% up to 450°C attributed to loss of solvent and adsorbed water (Figure 4.13). Due to the high thermal stability, it is possible to remove the occluded species by heating, so to test this, a sample was calcined at 350°C for 12 hours and the TGA data collected again, showing no significant weight loss up to the final decomposition above 450°C.

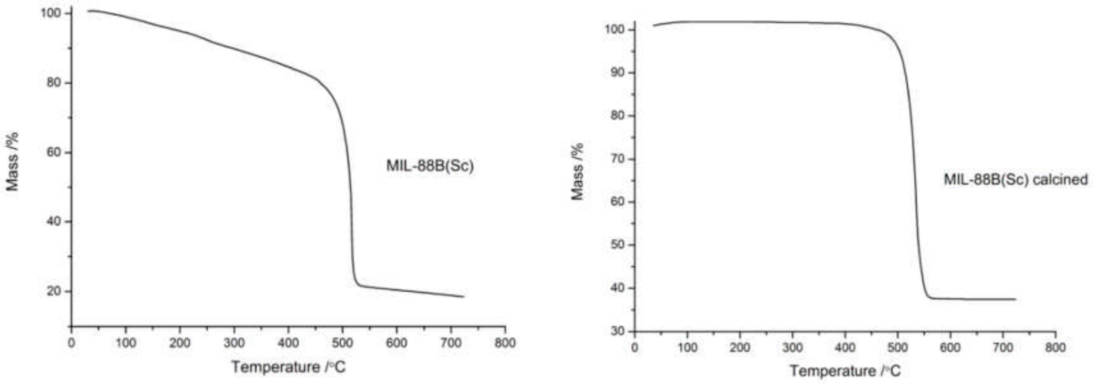

Figure 4.13: Thermogravimetric analysis on MIL-88B(Sc) in the as-prepared form (*left*) and calcined form (*right*).

To investigate the fully desolvated structure, a sample was heated to 350°C to remove all occluded species and sealed in a quartz glass capillary *in vacuo*. The resulting diffraction pattern could not be indexed as a single unit cell, suggesting a mixture of multiple states of closure in the framework. As the literature MIL-88B(Cr) was more responsive to immersion in solvent, a sample of activated MIL-88B(Sc) was immersed in methanol and sealed in a capillary for powder X-ray diffraction analysis. The resulting was a dramatic change to the observed powder X-ray diffraction pattern (Figure 4.14), the unit cell for MIL-88(Sc)-MeOH was indexed as hexagonal, *P*-62*c*, a = 15.62 Å, c = 15.96 Å, volume = 3372 $Å^3$ showing a solvent induced increase in cell volume of 60%, a response similar to that of MIL-88B(Cr) (cell volume under methanol = 3375 $Å^3$)[67].

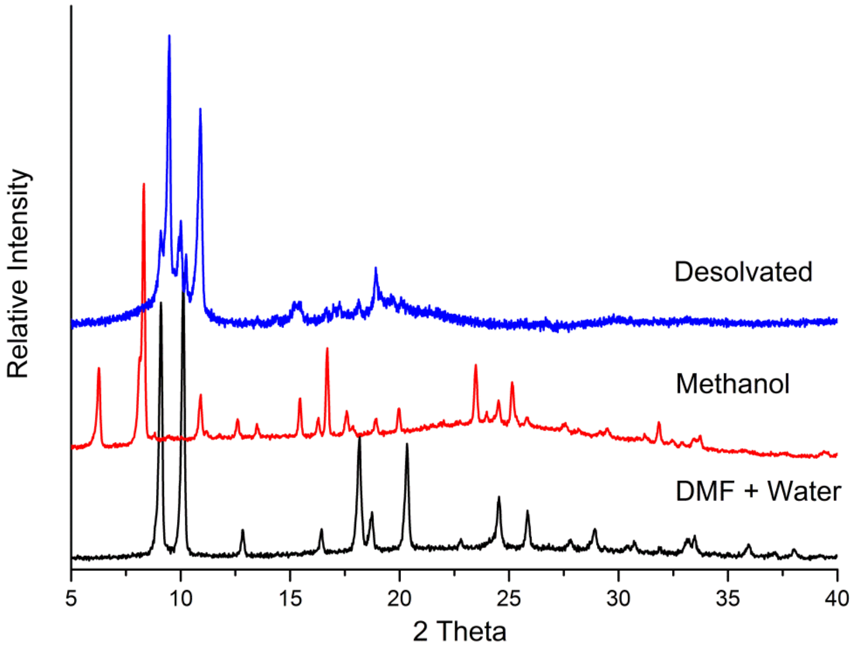

Figure 4.14: As-synthesised (black), methanol solvated (red) and desolvated (blue) diffraction patterns for MIL-88B(Sc).

The MIL-88 framework is composed of trimeric clusters, where three metals share a μ_3-O and are bridged to the adjacent metals with 6 carboxylate groups. This leaves two coordinatively unsaturated metal sites and one negatively charged species (to maintain charge balance) on the cluster. From the synthesis conditions this negatively charged species is assumed to be a hydroxide, the only alternative being the nitrate counter ion, but elemental analysis indicated there was no nitrogen present in the calcined sample. The other two species on the trimeric unit could be exchanged solvent species or water for the pre and post-calcination materials respectively. The framework consists of the trimeric clusters, each linked to 6 adjacent trimers through the bridging terephthalates creating both one dimensional channels, and trigonal bipyramidal cages through the structure (Figure 4.15 and Figure 4.16).

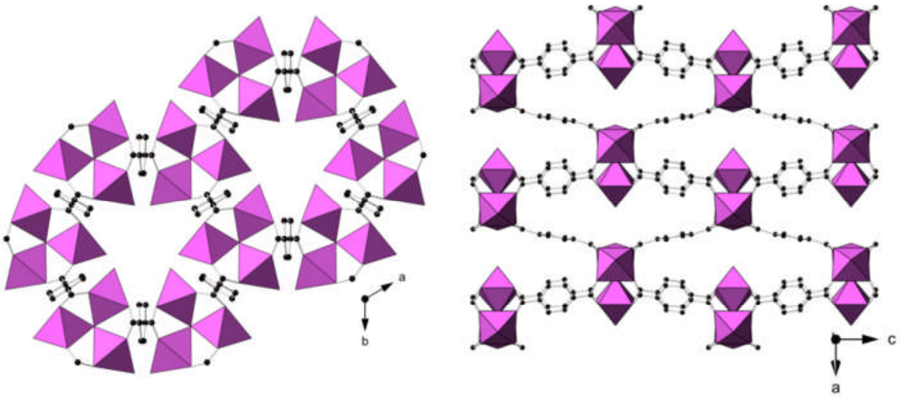

Figure 4.15: View down the channels parallel to the c-axis (*left*) and perpendicular to the channels, showing the cage-like structure of MIL-88B(Sc). Scandium octahedra are shown in pink. Black spheres represent the carbon atoms of the organic linker.

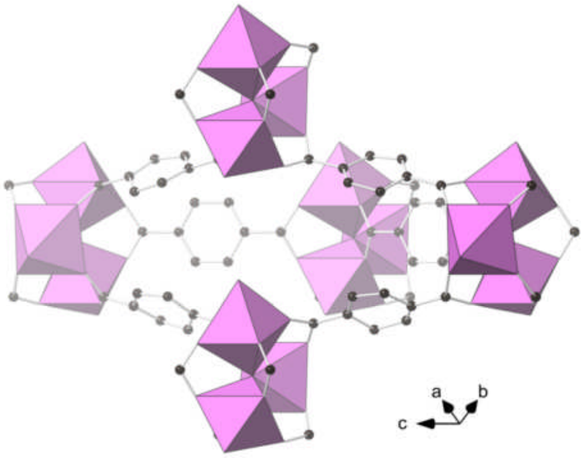

Figure 4.16: Single trigonal bipyrimidal cage in the MIL-88B(Sc) structure, Scandium octahedra are shown in pink. Black spheres represent the carbon atoms of the organic linker.

^{45}Sc solid state NMR on MIL-88(Sc)-DMF showed a single broad signal characteristic of a disordered distribution of the scandium environment likely a result of the trimeric units containing a random distribution of a single hydroxide and two water molecules per unit (Figure 4.17).

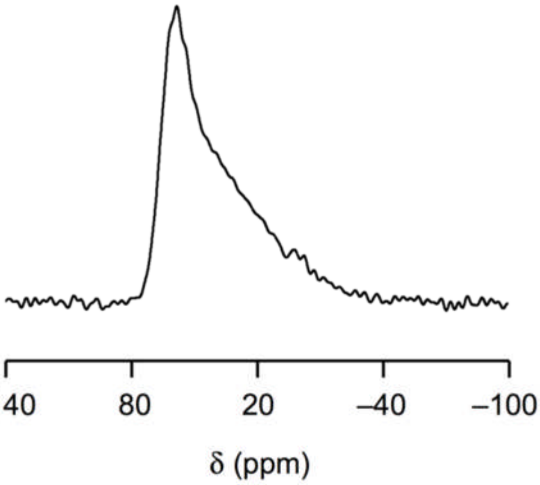

Figure 4.17: Solid state ^{45}Sc NMR on MIL-88B(Sc)

^{1}H and ^{13}C confirm the presence of the terephthalate with the ^{1}H spectra showing an additional signal arising from the bound hydroxide species (Figure 4.18). The broader signals suggest a more disordered environment than observed for the highly crystalline Sc_2BDC_3 framework which displays much narrower lineshapes, resulting from the flexibility of the MIL-88B(Sc) framework.

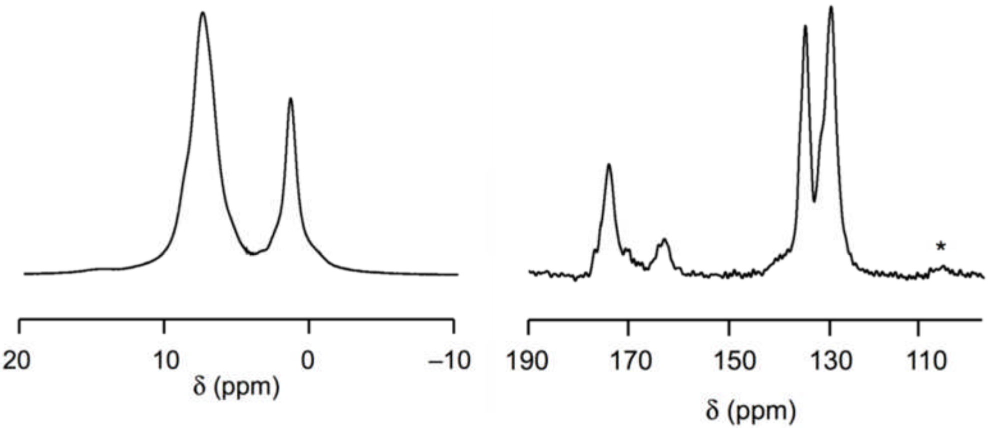

Figure 4.18: ^{1}H (*left*) and ^{13}C (right) MAS NMR spectra of MIL-88B(Sc).

Gas adsorption studies on MIL-88B(Sc) activated at high temperature (350°C, 12 hours) indicated the material had no permanent porosity to either nitrogen or carbon dioxide. During this study, a paper was published by Ibarra *et al.*[108] on the synthesis of MIL-88B(Sc). They reported an activation using acetone exchange followed by activation at 170°C was successful in accessing the porosity of the material. This method ensures the framework is in an open configuration before removal of the solvent at much lower temperatures, possible insufficient energy to allow the framework to close.

4.3.2.2 MIL-88D(Sc)

As the terephthalate based MIL-88B(Sc) was observed to form readily, similar reactions were performed with the longer dicarboxylate linker, 4,4'-biphenyldicarboxylic acid (BPDC).

These reactions yielded a single novel phase identified to be MIL-88D(Sc). In contrast to MIL-88B(Sc), there was very little variation in the diffraction patterns between the different syntheses. To compare the flexibility of the MIL-88D(Sc) to that of MIL-88B(Sc), the sample was activated, immersed in solvent and sealed in a capillary. Powder X-ray diffraction showed no significant changes to the unit cell upon immersion in solvent (Figure 4.19) suggesting the structure is much more rigid than that of the smaller terephthalate based derivative.

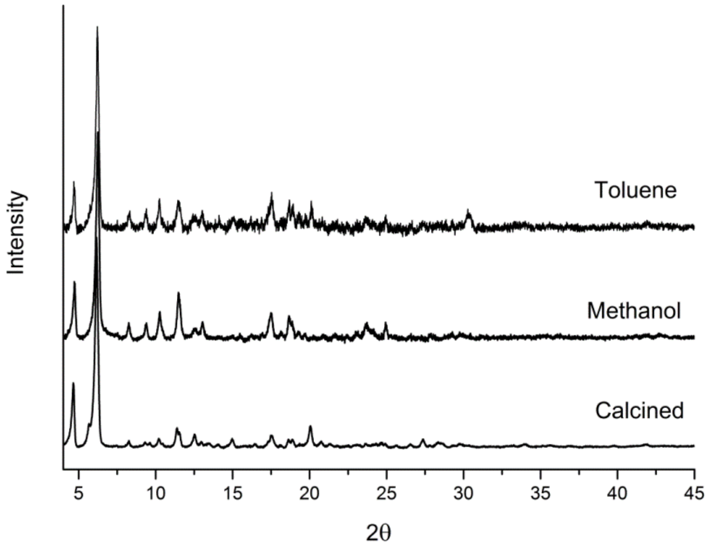

Figure 4.19: Calcined, methanol solvated and toluene solvated X-ray diffraction patterns for MIL-88D(Sc)

It was possible to index the measured diffraction patterns and obtain a unit cell for the MIL-88D(Sc)-MeOH yielding a hexagonal unit cell, *P*-62*c*, a = 21.476(11) Å, c = 21.836(18) Å, volume = 8722(10) Å^3. Rietveld analysis was attempted using a model constructed from the MIL-88B(Sc). To prepare the model, a full trimer unit, incliding the attached carboxylate groups were transposed into the new, larger unit cell with the same distances and angles as MIL-88B(Sc) and the linker molecules were positioned geometrically to connect the trimers (Figure 4.20). The data were not of sufficient quality to enable reliable refinement of the atomic positions, probably due to the large quantities of disordered extra-framework solvent molecules present in the structure. To enable approximate estimations of pore channel diameter and cage size, the model was allowed some freedom to refine using heavily weighted geometric constraints producing a framework model in reasonable agreement with the experimental diffraction data.

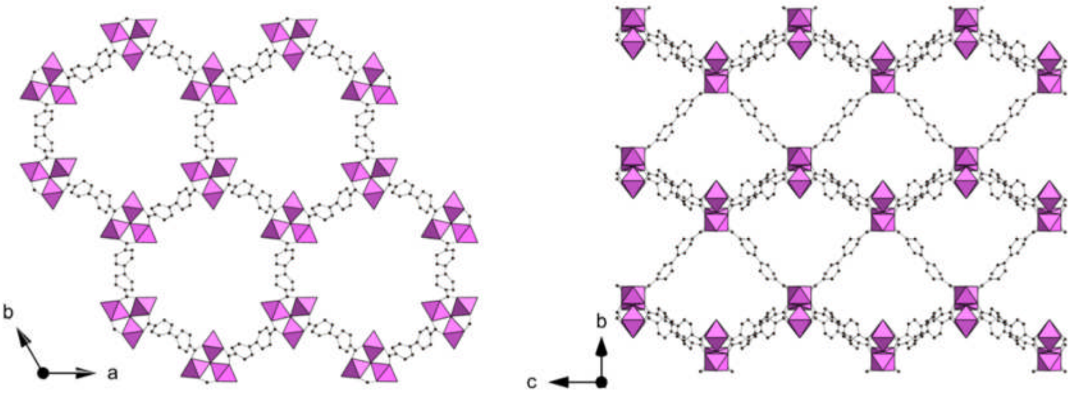

Figure 4.20: View down the channels parallel to the c-axis (*left*) and perpendicular to the channels, showing the cages in MIL-88D(Sc). Scandium octahedra are shown in pink. Black spheres represent the carbon atoms of the organic linker.

The structural model has the same framework topology and connectivity as MIL-88B(Sc) with direct replacement of terephthalic acid with the longer biphenyldicarboxylate linker. From the unit cell and structural data, it is clear that MIL-88D(Sc) adopts an open geometry with channels of ~12 Å and windows into the trigonal bypyrimidal cages of ~10 Å (Figure 4.21).

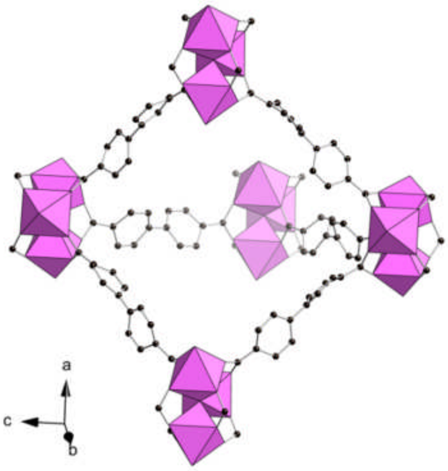

Figure 4.21: Single trigonal bipyrimidal cage in the MIL-88B(Sc) structure. Scandium octahedra are shown in pink. Black spheres represent the carbon atoms of the organic linker.

The X-ray diffraction pattern, simulated from the structural model (Figure 4.22), showed good agreement with the experimental diffraction pattern from the methanol solvated sample. This is despite the lack of guest molecules in the model which, in the case of MIL-88B(Sc), have a significant influence on the relative intensities observed in the experimental pattern.

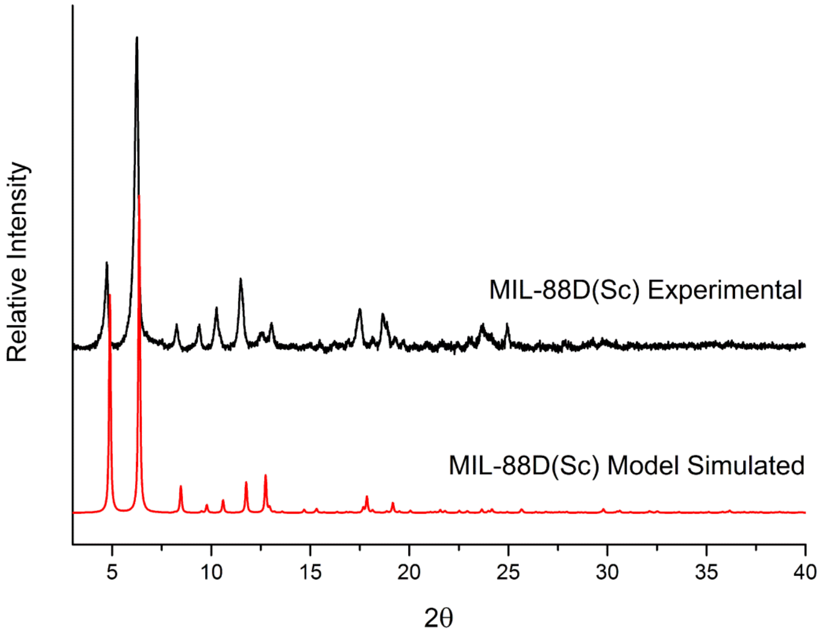

Figure 4.22: Simulated X-ray diffraction pattern for the MIL-88D(Sc) model compared to the experimental pattern of the methanol solvated MIL-88D(Sc).

TGA shows a gradual weight loss up to 300°C of 18% characteristic of adsorbed water and solvent removal before complete decomposition of the material to Sc_2O_3 at 450°C (Figure 4.23).

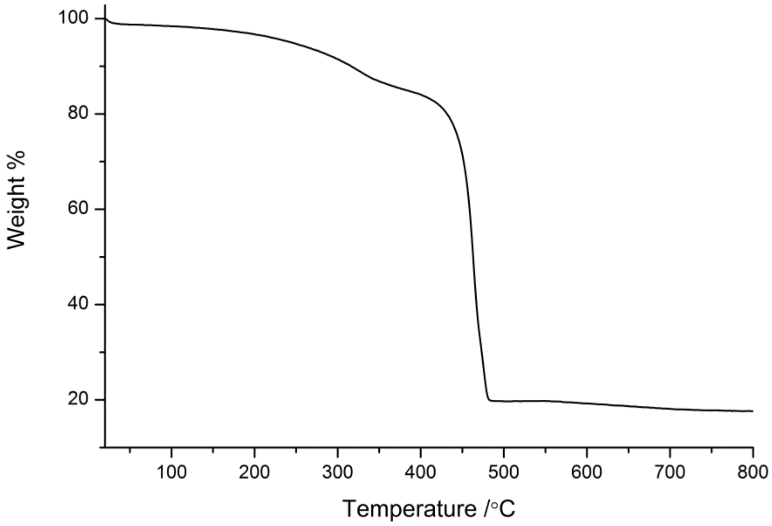

Figure 4.23: Thermogravimetric analysis data on MIL-88D(Sc)

To ensure the sample was still crystalline after heating, a sample was sealed in a quartz glass capillary after heating for 6 hours at 200°C at 1 × 10^{-5} torr. Although there were some changes in the relative intensities due to the removal of solvent, the main reflections were consistent with the X-ray diffraction pattern and therefore unit cell of the solvated material. From the splitting in some of the reflections in the pattern, it is possible that there is a minor component or fraction of the bulk sample that is undergoing some structural distortion (significantly less that that observed for MIL-88B(Sc), however, the majority of the bulk phase remains rigid (Figure 4.19).

The adsorption properties of the activated material were explored using nitrogen and carbon dioxide adsorption. The nitrogen adsorption at 77 K shows a type I isotherm with an uptake of 7.8 mmolg^{-1} at 500 mbar, indicating permanent porosity but less that that predicted for a low density open framework such as MIL-88D(Sc) (Figure 4.24). Carbon dioxide adsorption at 196 K shows a much higher uptake (Figure 4.24), to around 16 mmol g^{-1}, but with what appears to be a weak interaction. This difference in behavior between the two gases is unusual and although the powder diffraction data for the samples is in good agreement, the two isotherms were collected on two different samples which may help to explain the behavior. Further analysis is underway to reproduce and understand this behavior.

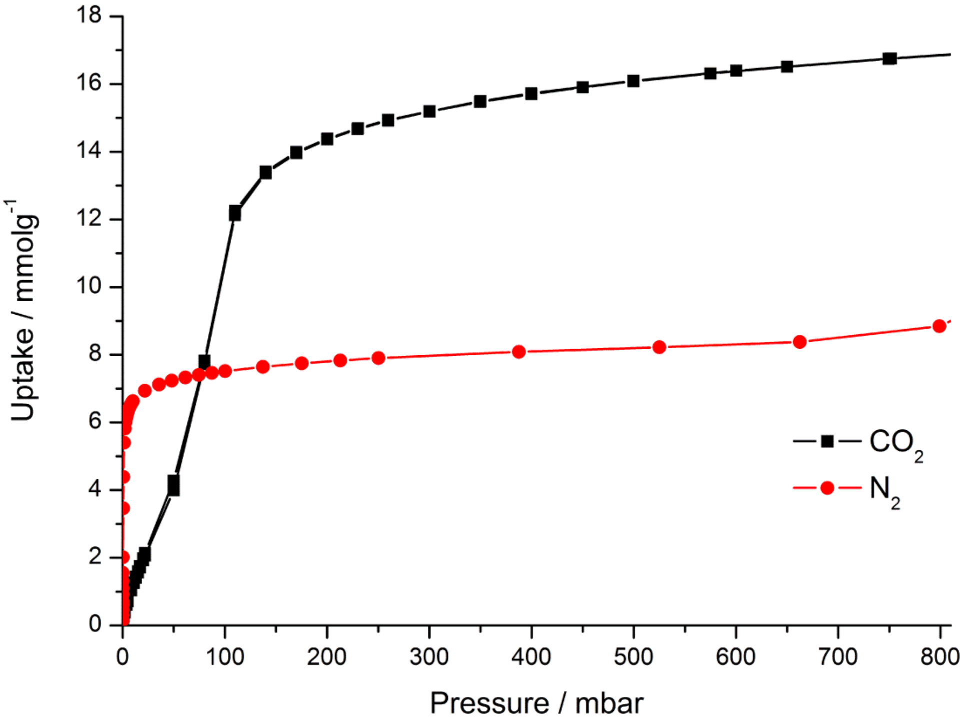

Figure 4.24: N_2 and CO_2 adsorption isotherms collected on MIL-88D(Sc)

4.3.2.3 MIL-101(Sc)

It was expected, based on the successful synthesis of MIL-88B(Sc) (a polymorph of the MIL-101 framework) with the trimeric scandium cluster building unit, under the appropriate conditions the MIL-101(Sc) framework should be possible. Initial synthetic attempts, using a range of conditions including reproducing literature preparations for both MIL-101(Cr) and the amino-terephthalate from of MIL-101(Fe) with scandium proved unsuccessful. MIL-101(Sc) was eventually prepared in a scale-up synthesis using the same molar ratios as used in the synthesis of MIL-88B(Sc), where the reaction yielded a mixture of MIL-101(Sc) and MIL-88B(Sc) (Figure 4.25).

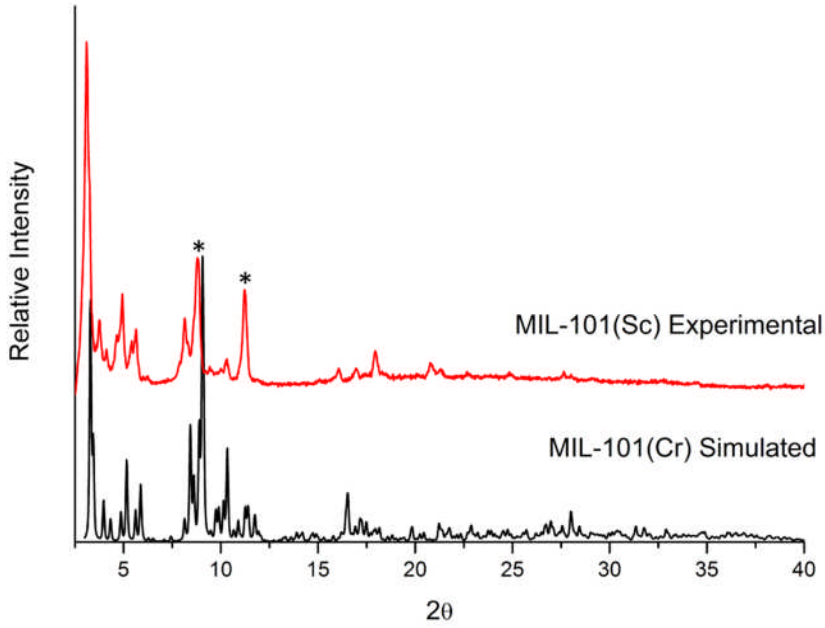

Figure 4.25: Experimental X-ray diffraction pattern of a mixed phase product containing MIL-101(Sc) and MIL-88B(Sc) compared to the simulated pattern for MIL-101(Cr). *Peaks related to the MIL-88B(Sc) impurity

From comparison of the diffraction pattern with other samples of MIL-88B(Sc), there was clear evidence for the sample containing a quantity of MIL-88B(Sc) (Figure 4.26). The large pore structure of MIL-101(Cr) is discussed in detail in Chapter 1.

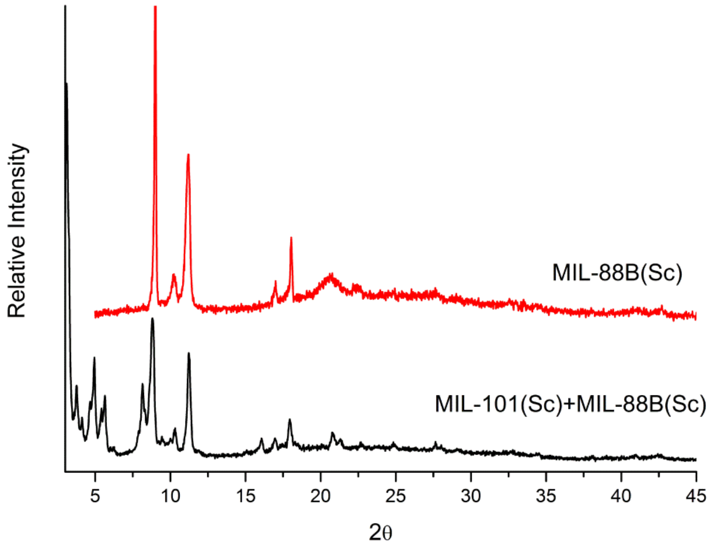

Figure 4.26: Experimental X-ray diffraction pattern of a mixed phase product containing MIL-101(Sc) and MIL-88B(Sc) compared to an example of an as-synthesised diffraction pattern for MIL-88B(Sc)

Due to the low crystallinity of the sample, the X-ray powder diffraction data were not of suitable quality to permit Rietveld refinement. The unit cell was refined using the Le Bail method and the pattern compared to that of the literature MIL-101(Cr).

The nitrogen adsorption capacity of MIL-101(Sc) was predicted to be slightly higher than MIL-101(Cr) due to the larger ionic radius of the scandium cation relative to chromium and the unit cell dimensions determined from powder diffraction studies. There are a large number of literature studies on the activation of MIL-101(Cr) detailing a number of different approaches. These include: solvothermal heating, solvent exchange, heating and sonication to fully remove guest species from the large cages. Activation of MIL-101(Sc) proved difficult as a number of the reported methods, including sonication and heating in DMF or EtOH at 100°C resulted in the recrystallization of the framework to the higher density MIL-88B(Sc) polymorph. The most successful activation involved soaking the sample in MeOH for 72 hours, drying at room temperature and outgassing at 120°C for 8 hours prior to analysis. The accessible porosity, however, was still significantly less than predicted, probably due to a combination of incomplete activation and the presence of the non-porous MIL-88B(Sc) impurity. The porosity of MIL-101(Sc), using nitrogen adsorption (Figure 4.27), was measured at only 0.16 cm^3g^{-1} (assuming the adsorbed nitrogen has the density of liquid nitrogen at that temperature), a capacity significantly less than that of the MIL-101(Cr) at ~2.0 cm^3g^{-1} after activation.

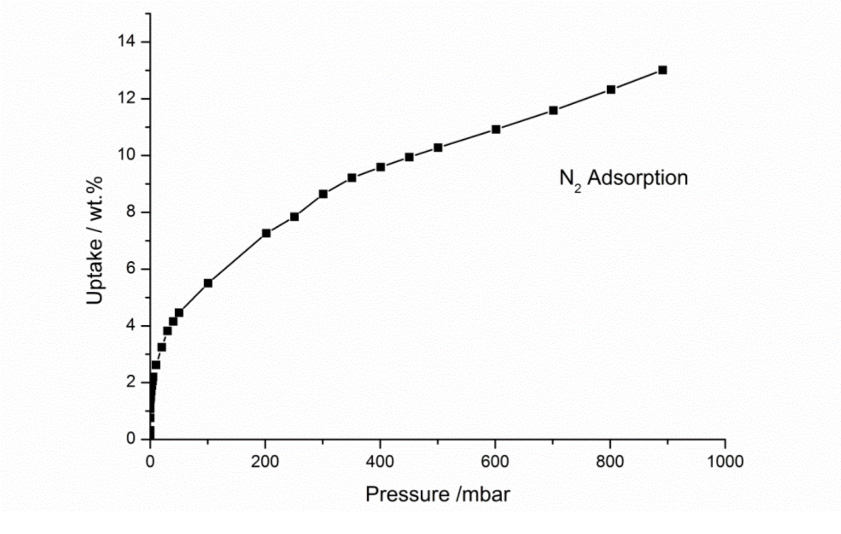

Figure 4.27: Nitrogen adsorption isotherm collected on MIL-101(Sc) at 77 K.

TGA showed that MIL-101(Sc) has a lower thermal stability than that of the MIL-88B(Sc) polymorph with decomposition starting at around 300°C (Figure 4.28).

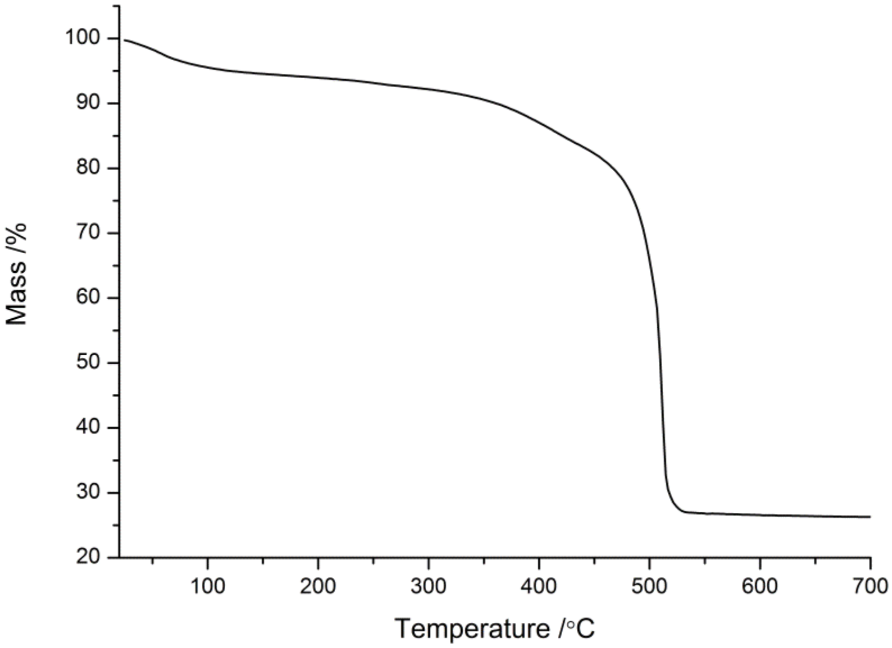

Figure 4.28: Thermogravimetric analysis on MIL-101(Sc)

More recent synthesis studies by colleagues in the Wright group have improved the purity of the MIL-101(Sc) synthesis working at shorter reaction times and lower temperatures yet the activation still proves to be a problem and requires further investigation.

4.4 Scandium trimesates

Attempts to prepare metal organic framework materials with scandium oxide and trimesic acid (benzene-1,3,5-tricarboxylic acid), both hydrothermally and solvothermally were unsuccessful. There was no evidence for any crystalline products other than the recovered starting materials. Solvothermal preparations however, using scandium nitrate over a range of temperatures (100 - 150°C) were successful yielding a novel structure with the MIL-100 framework topology.

The structure was identified by comparison with literature examples of trivalent trimesates with the measured powder X-ray diffraction pattern showing good agreement to the simulated pattern (Figure 4.29).

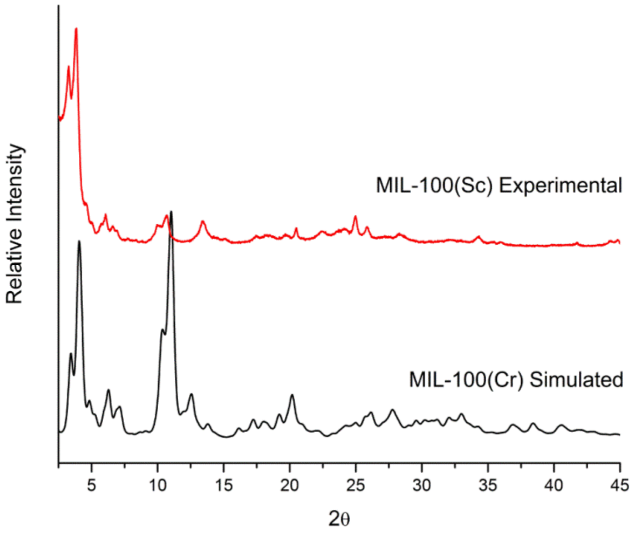

Figure 4.29: Experimental X-ray diffraction pattern of MIL-100(Sc) compared to the simulated pattern for MIL-100(Cr).

Due to the large unit cell and low crystallinity, the experimental patterns were not of sufficient quality to perform structural refinement. Refinement of the unit cell parameters was possible using the Le Bail method, the unit cell and symmetry used in the refinement was taken to be the same as for MIL-100(Cr), giving the refined cell in *F d*-3*m* with *a* = 75.436(8) Å.

The unit cell of MIL-100(Sc) is slightly larger than that measured for MIL-100(Cr) due to the larger ionic radius of the scandium ion (88.5 pm for Sc^{III} and 75.5 pm for Cr^{III}).

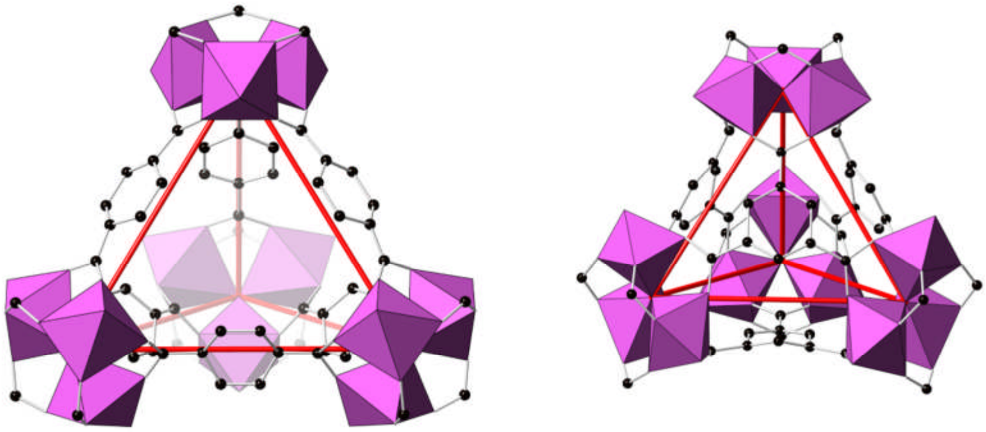

Figure 4.30: Comparison of the ‘super-tetrahedral’ units of the MIL-101(Cr) and MIL-100(Cr) respectively. Scandium octahedra are shown in pink. Black spheres represent the carbon atoms of the organic linker.

The trimeric units are the same as those in MIL-101 but in this case the trimesates units are on the face of the tetrahedra (Figure 4.30), each connecting to three trimer units. As a result, the pore size is slightly smaller than MIL-101. The structure contains two types of cage with porosity into the mesoporous region. The internal diameter of the cages in MIL-100(Cr) are 25 Å for the smaller cage and 29 Å for the larger (Figure 4.31 and Figure 4.32). The smaller cage is accessible through microporous pentagonal windows with a cross-sectional diameter of 5.5 Å, and the larger cage through both the pentagonal windows and larger hexagonal windows of diameter 8.6 Å.[4]

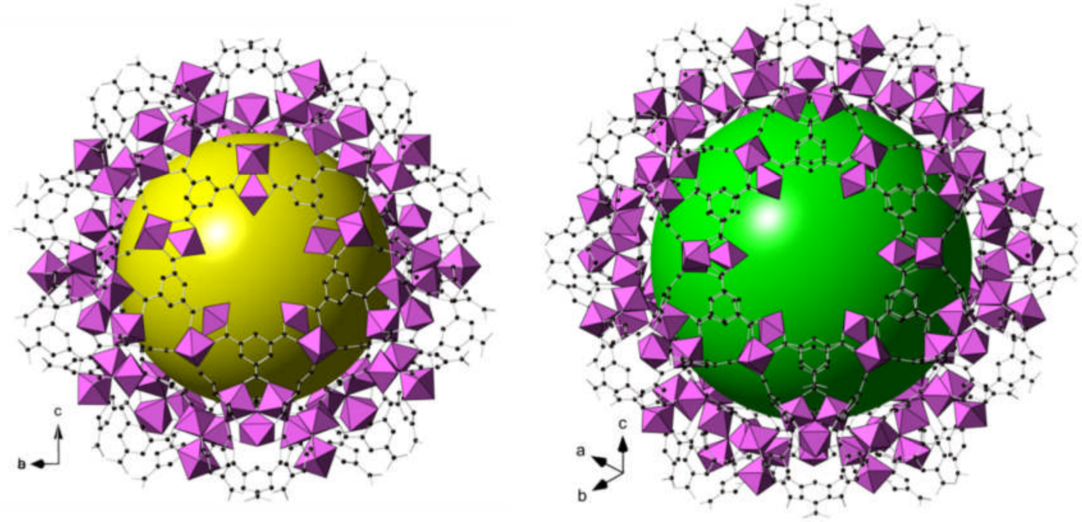

Figure 4.31: Two types of mesoporous cage from the MIL-100(Cr) structure showing the accessibility of the structure and trimer-lined pore surface. Coloured spheres used to identify the location of the pore cavity. Scandium octahedra are shown in pink. Black spheres represent the carbon atoms of the organic linker.

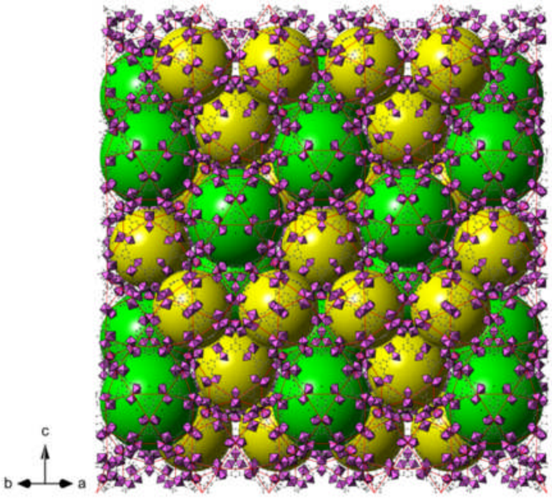

Figure 4.32: MIL-100 structure viewed down the 110 direction. Coloured spheres used to identify the location of the two types of pore cavity (Coloured as in Figure 4.31). Scandium octahedra are shown in pink. Black spheres represent the carbon atoms of the organic linker.

The large open cavities of MIL-100(Sc) are lined with the scandium based clusters, and the associated coordinatively unsaturated Lewis acidic sites. This suggests that MIL-100(Sc) is an interesting candidate for use as a heterogeneous Lewis acid catalyst and is currently under investigation in this area by colleagues in the Wright group.

Thermogravimetric analysis on MIL-100(Sc) shows a gradual weight loss of 16% up to ~300°C attributed to loss of solvent and adsorbed species. Above 300°C the structure decomposed to give Sc_2O_3 (Figure 4.33).

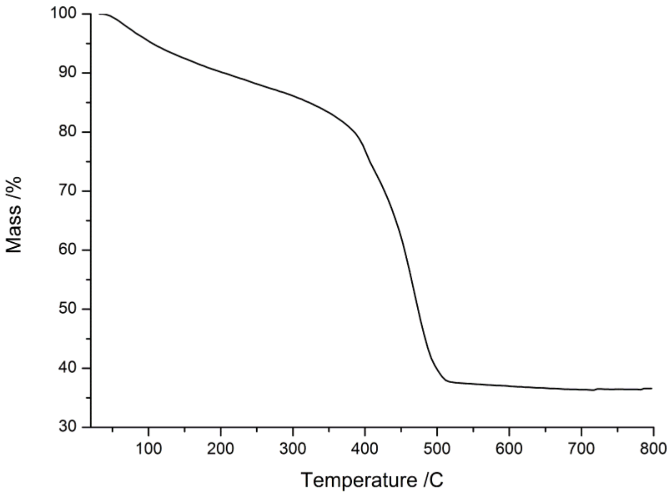

Figure 4.33: Thermogravimetric analysis on MIL-100(Sc)

Solid state ^{45}Sc MAS NMR on MIL-100(Sc) was similar to the spectrum for MIL-88B(Sc), showing a broad lineshape characteristic of disorder (Figure 4.34). This is thought to be characteristic of the trimer based frameworks, arising from the statistical disorder of species influencing the scandium environment. ^{1}H and ^{13}C MAS NMR were in agreement with the proposed model (Figure 4.34). The ^{1}H spectrum displays resonances from the aromatic protons, hydroxyl/water protons and lower intensity signals from adsorbed DMF. The presence of DMF is clearly visible in the ^{13}C spectrum with resonances observed in the alkyl region along with evidence for the carbonyl (from DMF), carboxylate and aromatic (from trimesate linkers) carbon resonances.

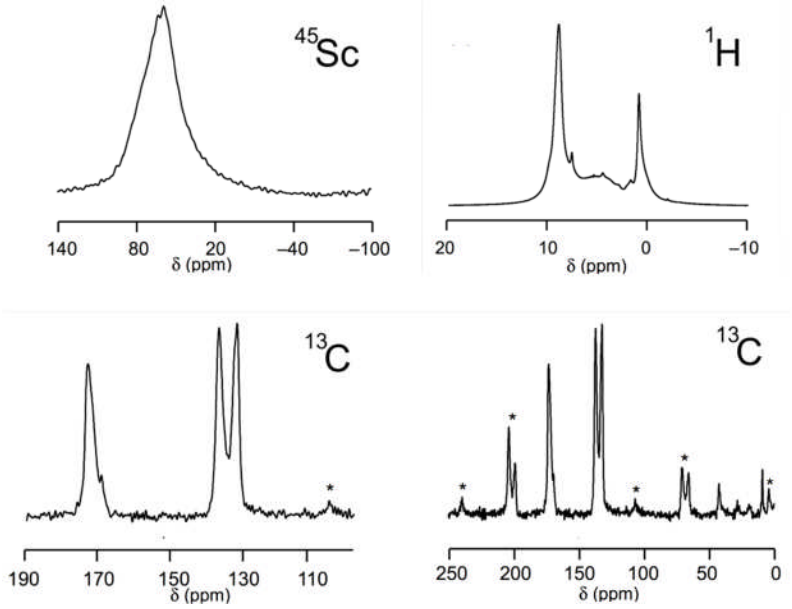

Figure 4.34: Solid state ^{45}Sc NMR on MIL-100(Sc) (*top left*) ^{1}H (top right) and ^{13}C (bottom) MAS NMR spectra of MIL-100(Sc)

Nitrogen adsorption on a sample of MIL-100(Sc) stirred in methanol for 72h and evacuated at 180°C shows an isotherm typical of a structure with mesoporous cavities (Figure 4.35). The measured pore volume is 0.72 $cm^3 g^{-1}$ which, although high, is lower than that measured for MIL-100(Cr) (1.10 $cm^3 g^{-1}$)

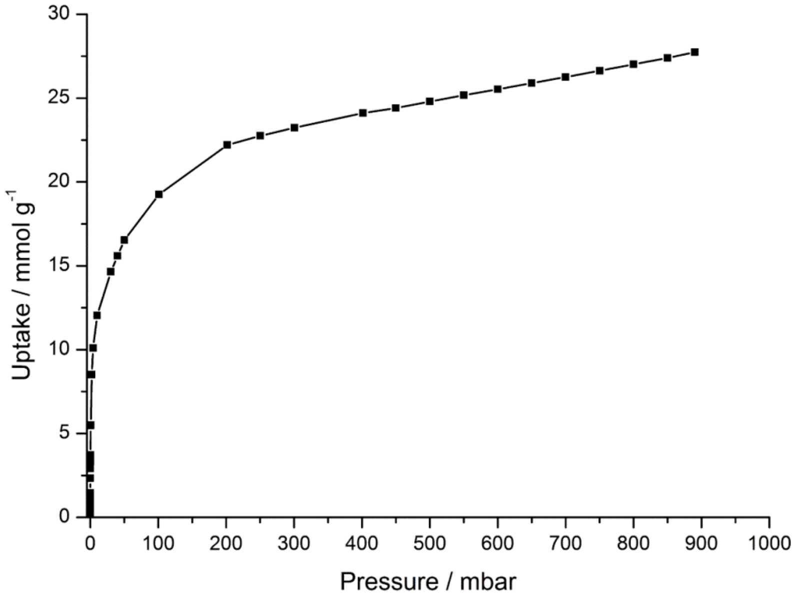

Figure 4.35: Nitrogen adsorption isotherm collected on MIL-100(Sc) at 77 K.

Carbon dioxide adsorption on the same sample of MIL-100(Sc) showed a maximum uptake of ~ 21 mmol g^{-1}, a similar value to that measured for MIL-100(Cr) (19.5 mmol g^{-1}, 8 MPa at 303 K) (Figure 4.36).

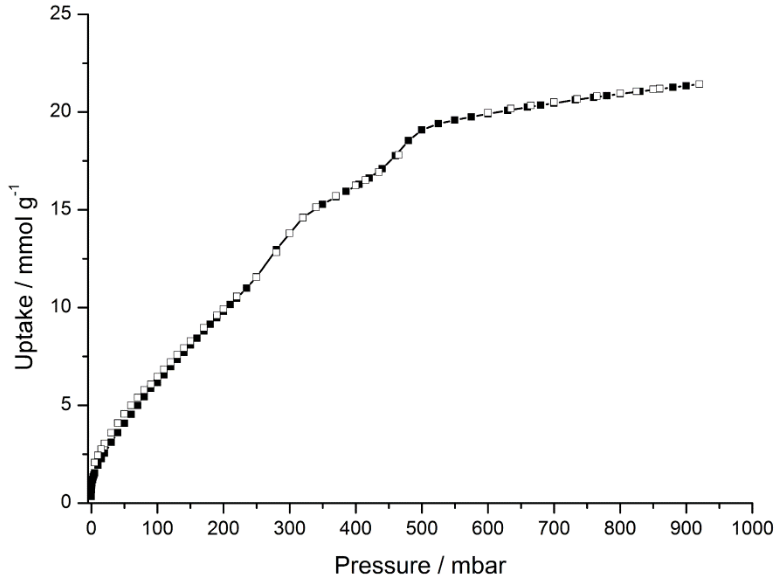

Figure 4.36: Carbon dioxide adsorption isotherm collected on MIL-100(Sc) measured at 196 K.

4.5 Scandium Tetracarboxylates

A series of reactions using the tetracarboxylate linkers, 3,3’,5,5’-azobenzenetetracarboxylic acid (ABTC) and pyromellitic acid (PMA) were carried out, to prepare novel metal organic framework materials again using scandium oxide and scandium nitrate.

4.5.1 Sc-PMA

Reactions of scandium oxide and nitrate with the PMA linker yielded a novel structure under hydrothermal conditions, details of the synthetic conditions are listed in Table 4.5.

Temp. /°C	Solvent	Scandium source	Sc	H_4PMA	Solvent	Time / h	Product
220	H_2O	Sc_3O_3	1.0	1.0	600	72	Sc_4PMA_3
150	H_2O	$Sc(NO_3)_3.3H_2O$	1.0	1.0	600	72	Sc_4PMA_3
190 - 220	DMF	$Sc(NO_3)_3.3H_2O$	1.0	1.0	300	72	Unknown
190	DEF	$Sc(NO_3)_3.3H_2O$	1.0	1.0	200	72	Unknown

Table 4.5: Reaction conditions for scandium and the pyromellitic acid linker

Sc_4PMA_3 contains isolated ScO_6 octahedra, fully coordinated by the pyromellitate counter ions creating a highly interconnected structure. As the PMA linker has 4 carboxylate groups, on two pairs of adjacent carbons, the steric interaction force two to sit in a geometry parallel to the ring plane and two to sit perpendicular (Figure 4.37).

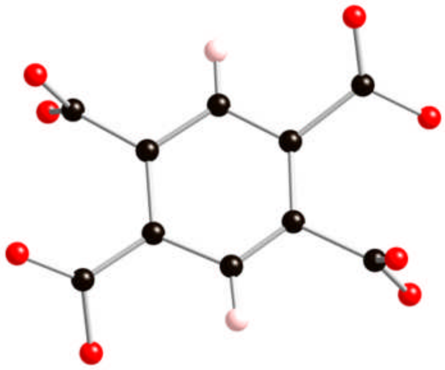

Figure 4.37: Single molecule of pyromellitic acid showing the geometry of the carboxylate groups with respect to the phenyl ring. Black, red and pink spheres represent the carbon, oxygen and hydrogen atoms of the organic linker respectively.

The structure was solved using direct methods from single crystal X-ray diffraction data in the rhombohedral space group *R* -3 with unit cell *a* = 15.934(9) Å, *c* = 10.762(4) Å. The structure consists of scandium octahedra fully coordinated by the tetra-carboxylate linker with no additional species present, with a formula unit of Sc_4PMA_3. Powder diffraction data shows good agreement between the crystal structure and the bulk phase with evidence for a small amount of an unknown impurity (Figure 4.38).

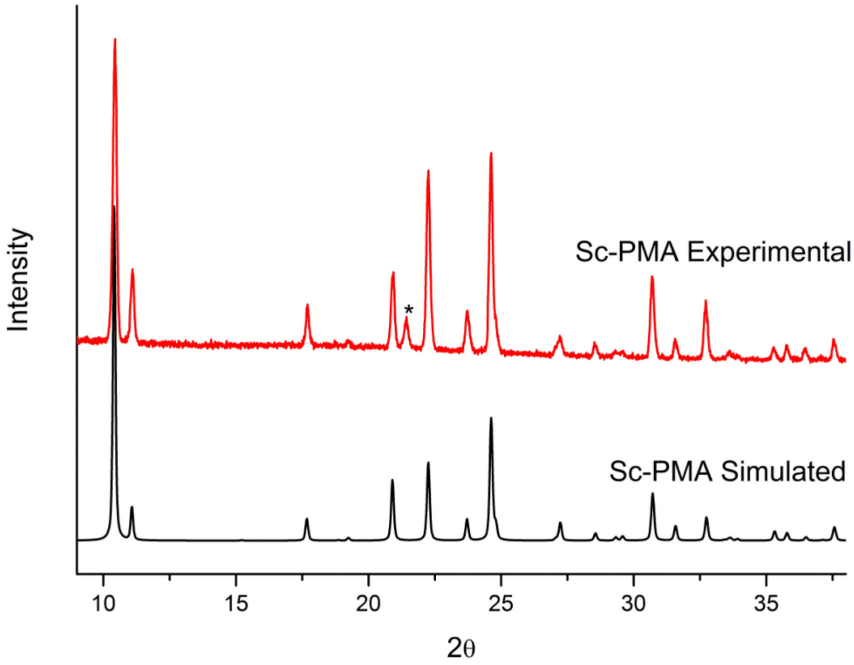

Figure 4.38: Experimental powder diffraction pattern of Sc_3PMA_4 compared to the pattern simulated from the single crystal model.

As the linker molecule in the Sc_3PMA_4 structure is fully coordinated by the scandium, each PMA linker connects 8 different ScO_6 octahedra creating a dense arrangement of scandium octahedra as shown in Figure 4.39.

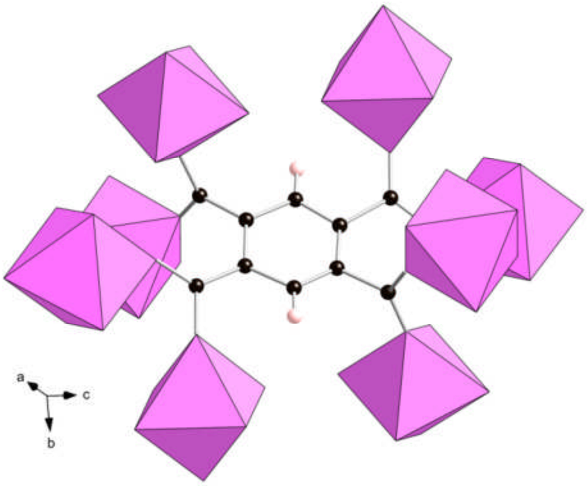

Figure 4.39: Pyromellitate molecule in the Sc_3PMA_4 structure showing the connectivity to the 8 different scandium octahedra. Scandium octahedra are shown in pink. Black and pink spheres represent the carbon and hydrogen atoms of the organic linker respectively.

There are some cavities between the phenyl rings in the structure (Figure 4.40), with an internal diameter of ~6.5 Å, but due to the arrangement of the scandium octahedra, there are no windows or channels through which they can be accessed (Figure 4.41). This was confirmed by nitrogen adsorption which showed no significant uptake indicating no permanent accessible porosity.

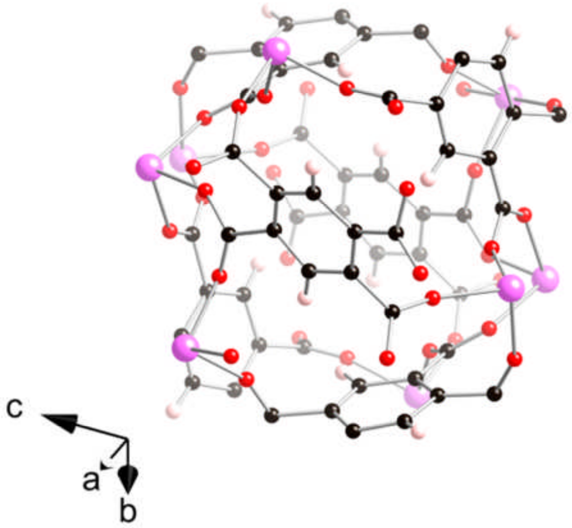

Figure 4.40: Cavity present in the Sc_3PMA_4 structure. Large pink spheres represent the scandium positions. Black, red and smaller pink spheres represent the carbon, oxygen and hydrogen atoms of the organic linker respectively.

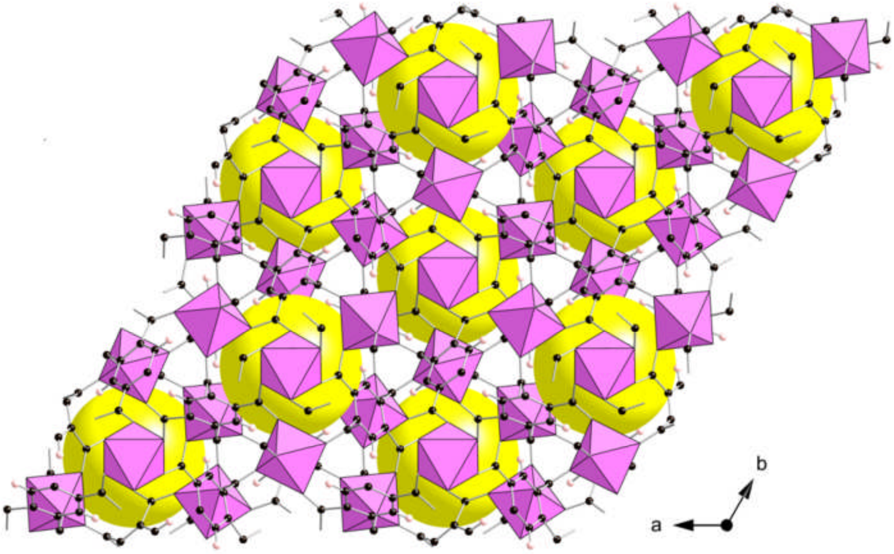

Figure 4.41: Sc_3PMA_4 structure viewed down the c-axis. Yellow spheres indicate the location of the cavities. Scandium octahedra are shown in pink. Black spheres represent the carbon atoms of the organic linker.

TGA shows the material to have a high thermal stability (Figure 4.42), with negligible weight loss up to the framework decomposition temperature of >500°C to give Sc_2O_3. This was similar to that observed for Sc_2BDC_3 and further evidence that the scandium carboxylate based frameworks show exceptionally high thermal stability when there are no additional coordinating species present as part of the framework.

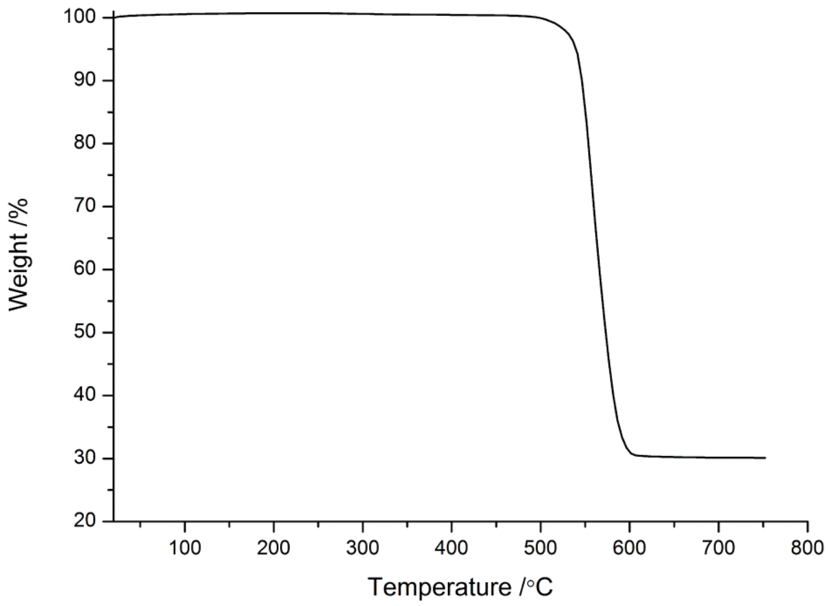

Figure 4.42: Thermogravimetric analysis on Sc_3PMA_4

4.5.2 Sc-ABTC

The 3,3’,5,5’-azobenzenetetracarboxylic acid linker (Figure 4.43) was prepared via the literature preparation reported by Wang *et al.*[114]

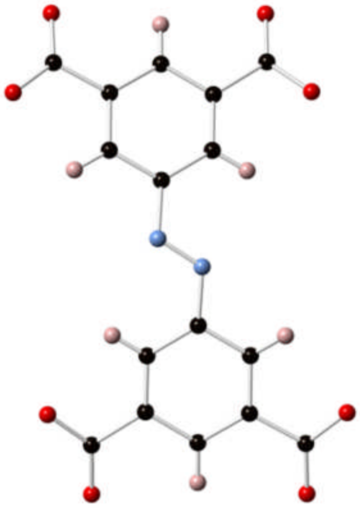

Figure 4.43: 3,3’,5,5’-azobenzenetetracarboxylic acid linker

The *trans*-azobenzene core of the molecule creates a slightly staggered arrangement in the phenyl rings and is reported to undergo photo-isomerization between the *cis* and *trans* isomers with the *trans* isomer the more energetically favourable.

Temp. /°C	Solvent	Scandium source	Sc	H_4ABTC	Solvent	Time / h	Product
120	H_2O	$Sc(NO_3)_3.3H_2O$	3.0	2.0	1800	48	H_4ABTC
120	EtOH	$Sc(NO_3)_3.3H_2O$	3.0	2.0	900	48	H_4ABTC
120 - 220	DMF	$Sc(NO_3)_3.3H_2O$	3.0	2.0	450	48	Sc-ABTC
120 - 220	H_2O	Sc_3O_3	3.0	2.0	1800	72	H_4ABTC + Sc_2O_3

Table 4.6: Reaction conditions for scandium and the 3,3’,5,5’-azobenzenetetracarboxylic acid linker

Synthetic hydrothermally preparations (Table 4.6) using scandium oxide and the ABTC linker proved unsuccessful, however, solvothermally there was evidence for a novel product. Solvothermal crystallisations, using scandium nitrate over a wide range of temperatures (120 - 220°C), yielded the same product. Comparison of the measured diffraction pattern with the literature trivalent structures again proved successful (Figure 4.44) with the material (denoted as Sc-ABTC) identified to be isostructural with that reported for the indium based *soc*MOF of Eddaoudi *et. al.*[115]

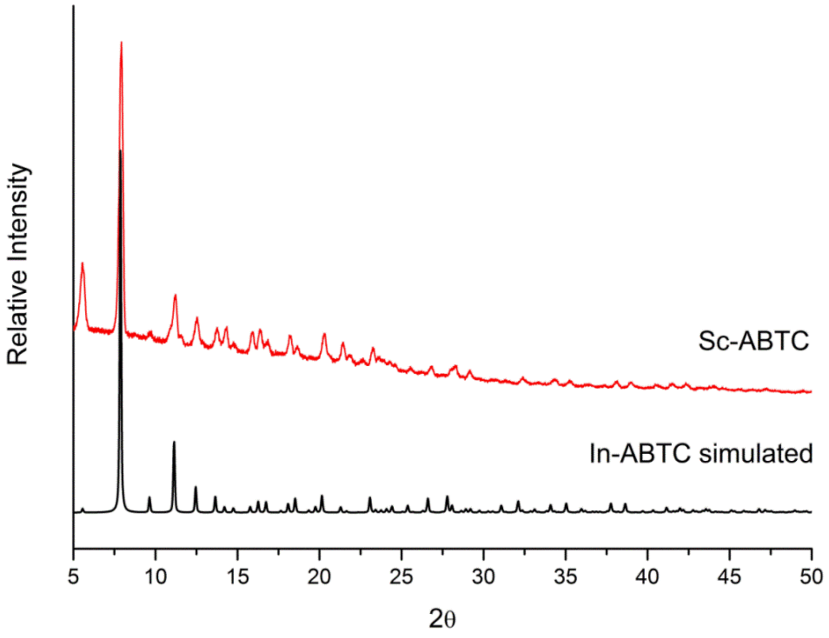

Figure 4.44: Comparison of the Sc-ABTC experimental pattern with the simulated pattern from the literature structure of socMOF(In).[115]

The Le Bail method was used to obtain the unit cell parameters for the scandium model, in the same symmetry as the reported indium structure, refined to be cubic *P*-43*n*, *a* = 22.4567(11) Å (Figure 4.45). The laboratory powder diffraction data was not of sufficient quality to permit full Rietveld refinement of the atomic positions.

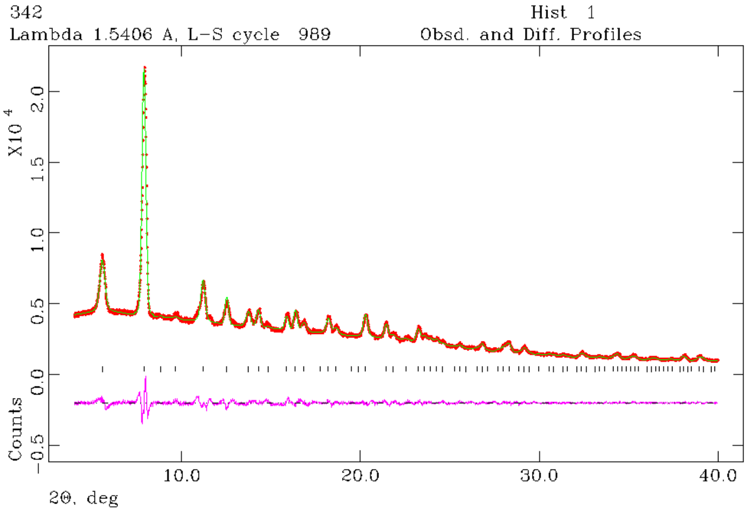

Figure 4.45: Le Bail plot for the unit cell refinement on Sc-ABTC

The structure of In-ABTC is best described as stacks of corner sharing cubes (Figure 4.46), in the form of cages with a full ligand molecule on each face and a trimer on the vertex, which connect to adjacent cubes through the trimeric cluster (Figure 4.47).

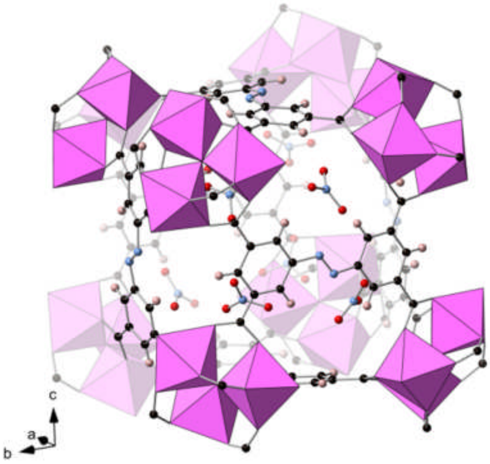

Figure 4.46: Single cubic cage from the socMOF(In) structure with charge-balancing nitrate counter-ions. Scandium octahedra are shown in pink. Black, red and blue spheres represent the carbon, oxygen and nitrogen atoms of the organic linker respectively.

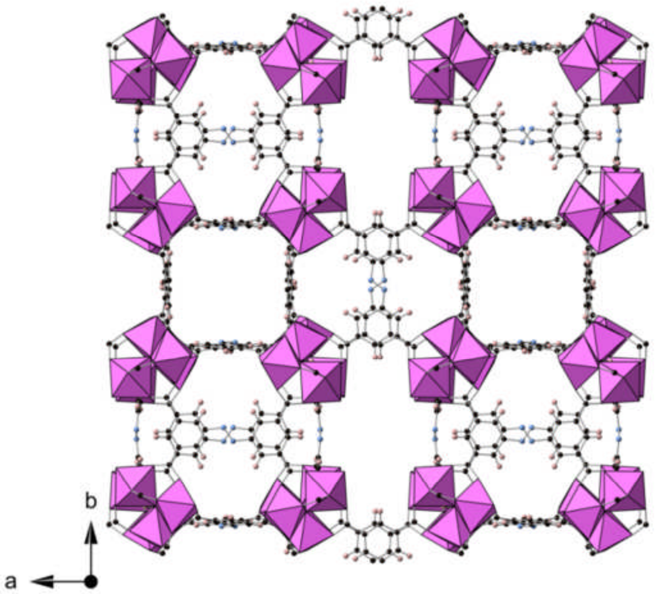

Figure 4.47: socMOF(In) structure viewed down the c-axis. Scandium octahedra are shown in pink. Black, red and blue spheres represent the carbon, oxygen and nitrogen atoms of the organic linker respectively.

TGA analysis on Sc-ABTC shows an initial 10 % weight loss up to 473 K attributed to loss of solvent (Figure 4.48). Above 523 K, the data displays a complex five step weight loss attributed to decomposition of the ligand as the decomposition occurs at a lower temperature than the other scandium trimer based frameworks.

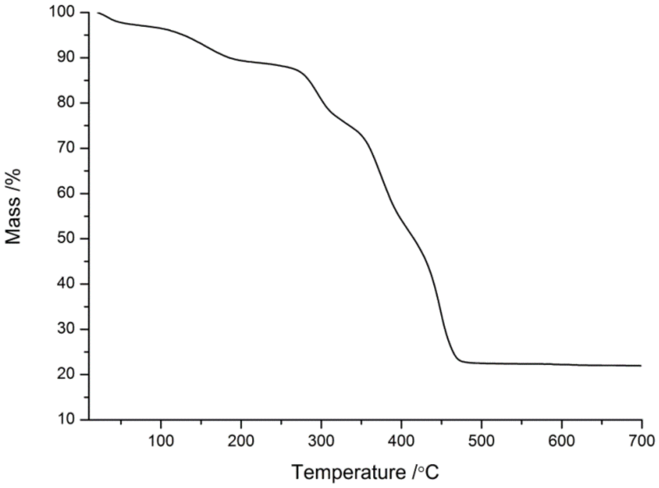

Figure 4.48: Thermogravimetric analysis on Sc-ABTC

To investigate if the steps in the TGA were reversible, a sample was calcined at 200°C, a temperature above the first two weight loss events attributed to solvent molecules in the channels. PXRD of the calcined sample showed no significant change to the peak positions (Figure 4.49) indicating the unit cell remained unchanged upon heating at this temperature. Calcination at higher temperature, 220°C and above, yielded an amorphous product indicating that the remaining weight loss events were irreversible and attributed to decomposition of the organic linker.

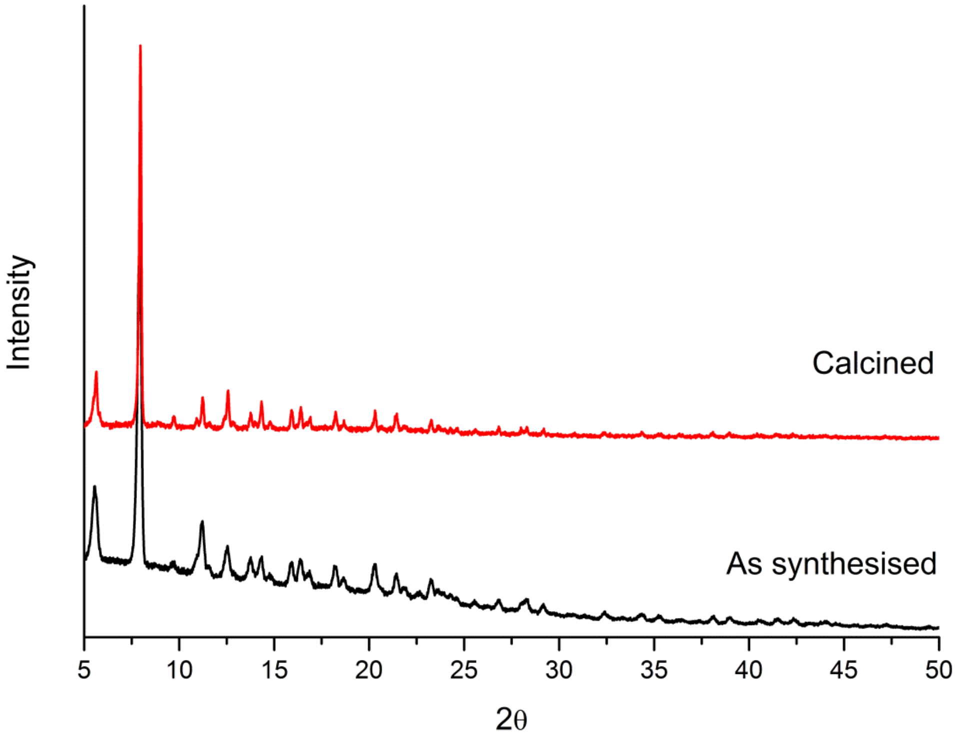

Figure 4.49: Comparison of the Sc-ABTC diffraction patterns in the as-synthesised and calcined form.

Solid state ^{45}Sc MAS NMR again shows the broad signal characteristic of the trimeric scandium unit (Figure 4.50). The ^{1}H MAS NMR, however, was not as expected for a trimer unit with evidence for only the aromatic protons and some residual DMF. The ^{13}C MAS NMR is consistent with that of the linker molecule, with a large chemical shift (to ~151.9 ppm) of the aromatic carbon attached to the azo- nitrogen (Figure 4.50).

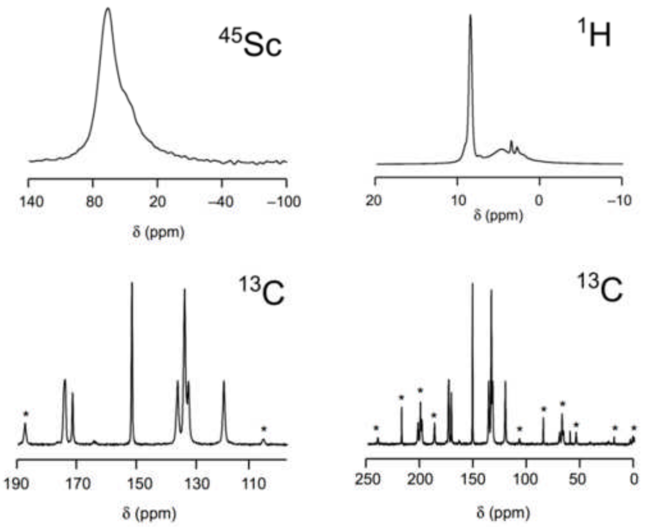

Figure 4.50: Solid state ^{45}Sc NMR on MIL-100(Sc) (*top left*) ^{1}H (top right) and ^{13}C (bottom) MAS NMR spectra of MIL-100(Sc)

The ^{1}H spectrum suggests that the framework charge is not balanced by hydroxide on the trimer itself but rather by nitrate counter ions as observed crystallographically within cages of the indium *soc*MOF in the reported structure (Figure 4.51).

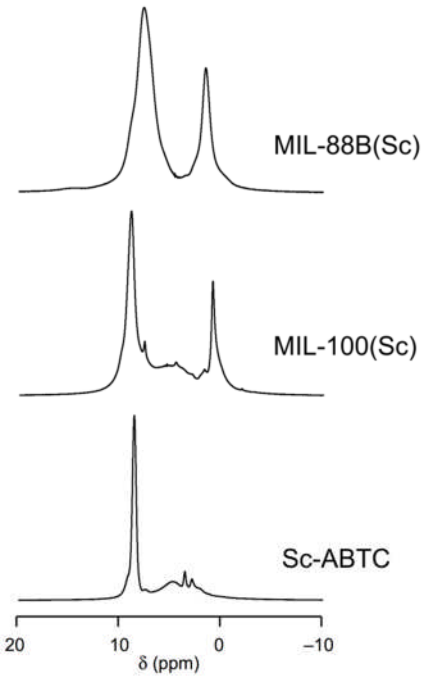

Figure 4.51: Solid state ^{1}H NMR on the three trimer-based frameworks MIL-88B(Sc), MIL-100(Sc) and Sc-ABTC

Nitrogen adsorption on Sc-ABTC at 77 K showed the structure to have permanent microporosity with a type 1 isotherm and a total uptake of 15 mmolg^{-1} (Figure 4.52). This value equates to a pore volume of 0.57 cm^{3}g^{-1}, slightly larger than that reported for *soc*MOF(In) at 0.54 cm^{3}g^{-1}. Carbon dioxide adsorption at 196 K showed a maximum uptake of over 13 mmolg^{-1} (Figure 4.53).

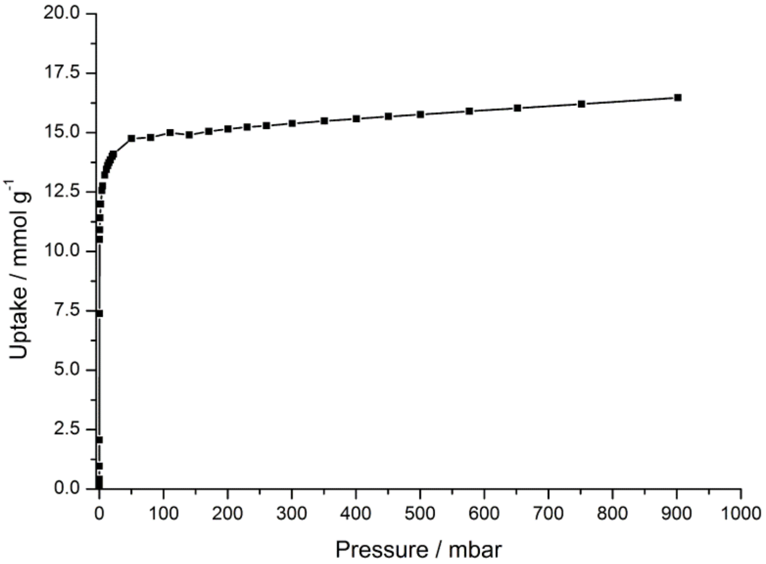

Figure 4.52: Nitrogen adsorption isotherm on Sc-ABTC at 77 K

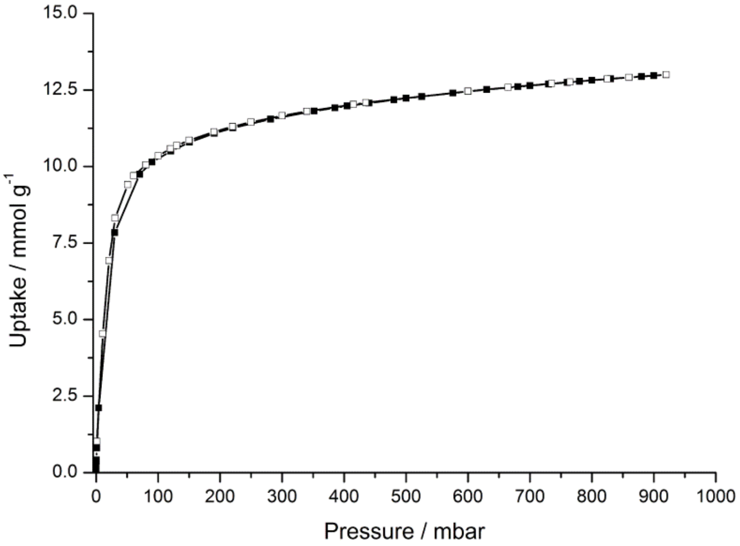

Figure 4.53: Carbon dioxide adsorption isotherm on Sc-ABTC at 196 K

To understand the adsorption behavior of the Sc-ABTC, simulation work on Sc-ABTC was carried out, in collaboration with Ana-Marie Banu and Tina Düren at the University of Edinburgh.

Pore size distributions (PSD) were calculated using the method developed by Gelb and Gubbins (Figure 4.54). The technique calculates the largest diameter for a sphere that can fit into the cavities without overlap with framework atoms. The calculated distribution suggests three distinct pore sizes of around 3.2 Å, 4.3 Å and 4.9 Å, created by the stacking arrangement of the cube shaped cages.

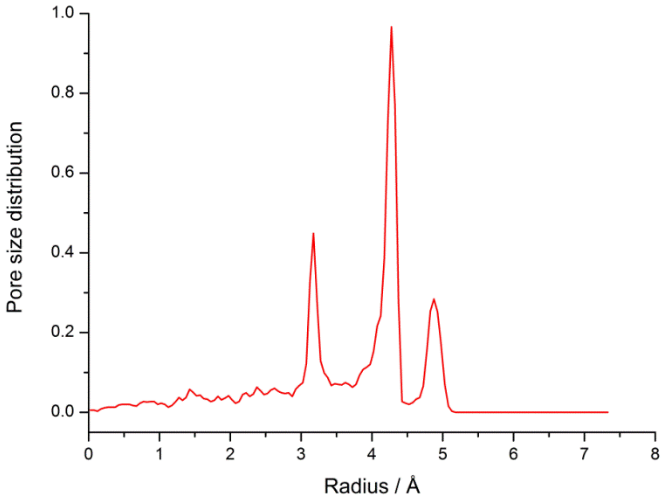

Figure 4.54: Pore size distribution calculated for the Sc-ABTC

Simulations were also used to predict the adsorption isotherm for a fully activated form of the Sc-ABTC structure. As the atomic positions could not be refined from the powder diffraction data, the structure of the isostructural socMOF(In) was used to simulate the adsorption isotherms for nitrogen and carbon dioxide. One important consideration in the simulation was whether or not the cubic cages in the structure were accessible. Measuring distances in the socMOF(In) structure, it was determined that there are 'windows' that could allow access to the cages but the aperture of the opening, at around 2.6 Å (Figure 4.55) (measurements include the van der Waals radius of the atoms around the opening), is too small and would not allow N_2 or CO_2 molecules to access the cage.

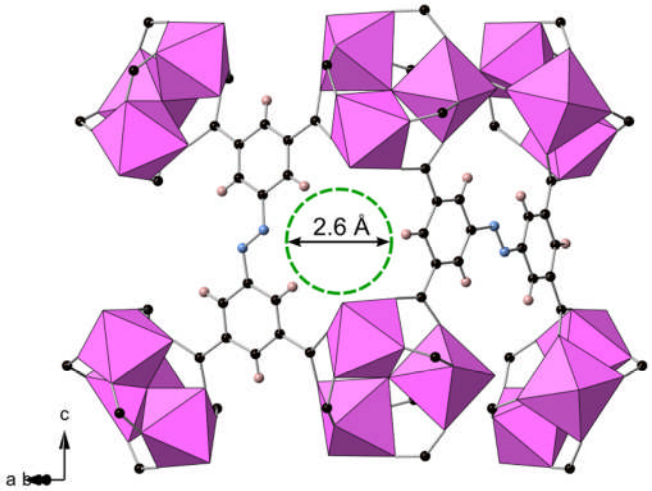

Figure 4.55: Possible window into the cubic cage with a cross-sectional diameter of 2.6 Å (allowing for the van der Waals radius of the surrounding atoms). Scandium octahedra are shown in pink. Black, blue and pink spheres represent the carbon, nitrogen and hydrogen atoms of the organic linker respectively.

To support the prediction that the cages are not accessible, simulations were performed where the full structure was accessible and repeated with the area inside the cages defined by the simulations to be inaccessible (denoted 'full structure' and 'blocked cages' respectively in Figure 4.56 and Figure 4.57 below).

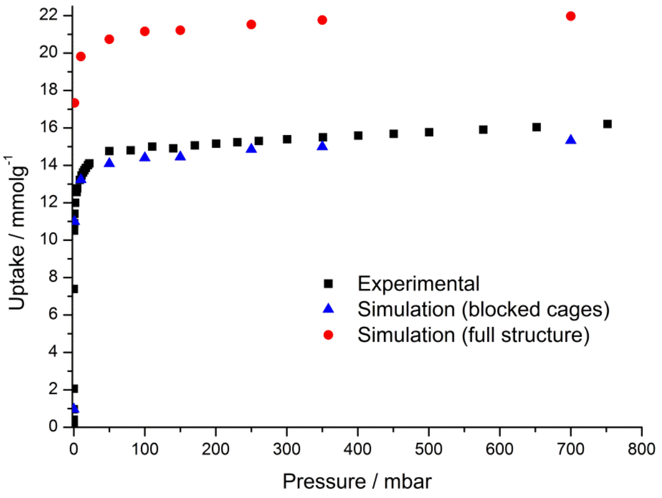

Figure 4.56: Simulated and experimental nitrogen adsorption isotherms for Sc-ABTC

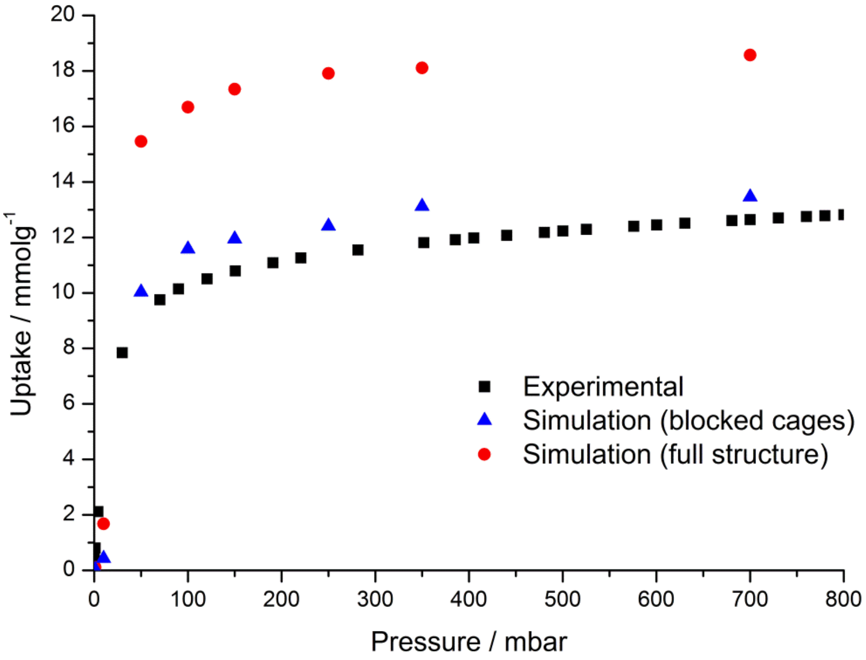

Figure 4.57: Simulated and experimental carbon dioxide adsorption isotherms for Sc-ABTC

The data shows good agreement between the simulated isotherms (with inaccessible cages) and the experimental data for both the CO_2 and N_2 data. The advantage of having simulations in good agreement with experimental data on MOF structures such as this are that the models can be used to simulate other gases and mixtures to predict behavior in separation applications which would be impractical to measure experimentally.

4.6 Summary of scandium carboxylate syntheses

Solvothermal investigation of syntheses using scandium sources and terephthalic acid identified four framework topologies. Two of these products, Sc_2BDC_3 and MIL-53(Sc), were observed at the higher end of the temperature range studied (160 – 220°C), and in these preparations the reaction stoichiometry favoured that of the final product, 1:1 for MIL-53(Sc) and 2:3 for Sc_2BDC_3. It was also found that the addition of pyridine to the reaction favoured the formation of MIL-53(Sc) and was preferable to adding an excess of scandium. At the lower end of the temperature range studied (80 – 140°C), solvothermal reactions yielded the two polymorphic structures MIL-88B(Sc) and MIL-101(Sc), the latter produced as the major component in mixtures with MIL-88B(Sc). By extending the length of the dicarboxylate linker (using 4,4'-biphenyldicarboxylic acid) it was also possible to prepare the isoreticular form of MIL-88B(Sc), denoted MIL-88D(Sc), which suggests that the other members of the MIL-88 series should also be possible, i.e. the fumarate-based MIL-88A and the naphthalate-based MIL-88C.

Reactions with scandium and trimesic acid yielded the large pore MIL-100(Sc), with the same framework topology as MIL-101(Sc), but with no impurity phases present. This was the only product observed for scandium and trimesic acid with the structure confirmed by powder X-ray diffraction, solid state NMR and elemental analysis.

Solvothermal reactions with the tetra-carboxylate linkers, 3,3',5,5'-azobenzene-tetracarboxylic acid and pyromellitic acid, under similar conditions to the terephthalate reactions, yielded the Sc-ABTC and Sc_4PMA_3 frameworks respectively. Sc_4PMA_3 is a fully coordinated scandium carboxylate with high thermal stability solved from single crystal X-ray diffraction. Although the structure possesses cavities of ~6.5 Å, there are no windows of sufficient size for gas molecules to access the porosity. The Sc-ABTC, isostructural with socMOF(In), was prepared and characterized by powder X-ray diffraction, solid state NMR and elemental analysis.

5 Synthesis, Characterisation and Functionalisation of Sc_2BDC_3

5.1 Introduction

As stated in the introduction, the first reporting of a permanently porous scandium based MOF was the scandium terephthalate, Sc_2BDC_3.

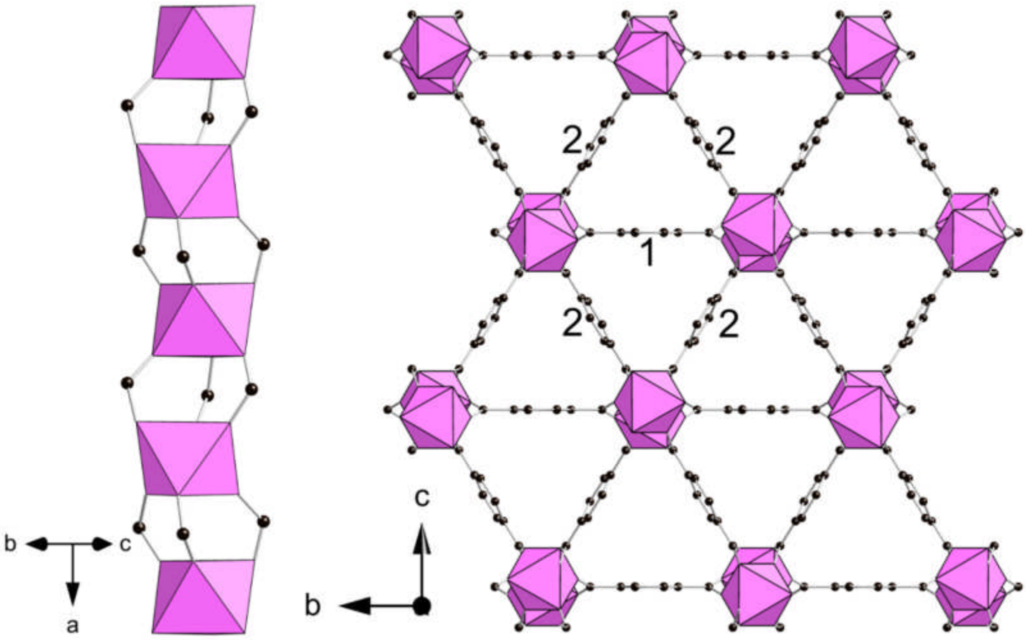

Figure 5.1: Single scandium carboxylate chain and view down the narrow triangular channels in Sc_2BDC_3. Scandium octahedra are shown in pink. Black spheres represent the carbon atoms of the organic linker.

Sc_2BDC_3, first reported by Miller *et al.*[27], is a small pore scandium terephthalate framework where the scandium is fully coordinated by terephthalate counter ions resulting in an array of triangular phenyl ring lined pore channels. Reported in the orthorhombic *Fddd* symmetry, the chains are made up of isolated ScO_6 octahedra along the a-axis where each ScO_6 octahedra is linked to two others by three carboxylate units in each direction as shown in Figure 5.1. The chains are each linked to six adjacent chains through the terephthalate linkers creating the triangular channels. Due to the angles required to connect to all six adjacent chains, there are two crystallographic terephthalate positions which represent the framework. The first terephthalate molecule is at an angle to the chains whereas the second is perpendicular (Figure 5.2).

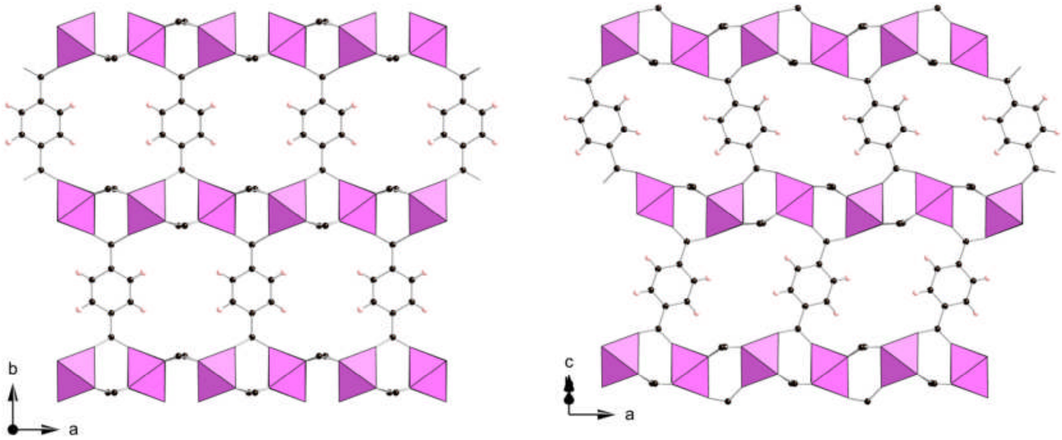

Figure 5.2: Layers of ‘Group 1’(*left*) and ‘Group 2’(*right*) terephthalates. Scandium octahedra are shown in pink. Black and pink spheres represent the carbon and hydrogen atoms of the organic linker respectively.

Due to the angle of the group 1 terephthalates and because they connect to chains on different levels, it is believed that the structure cannot demonstrate the same isoreticular expansion observed for the cluster-based MOFs such as MOF-5, by simply extending the length of the dicarboxylate linker. Sc_2BDC_3 was shown to have a remarkably high thermal stability, over 550°C under flowing air.[27] *In situ* powder X-ray diffraction shows that the structure remains crystalline up to 400°C in air with thermal decomposition, by loss of the framework terephthalates, above 500°C. Nitrogen adsorption experiments on the activated solid show an adsorption capacity of around 21 wt%, or a pore volume of 0.26 cm^3, higher than expected, considering the crystallographic cross-section of the channels (~4Å) (Figure 5.3).

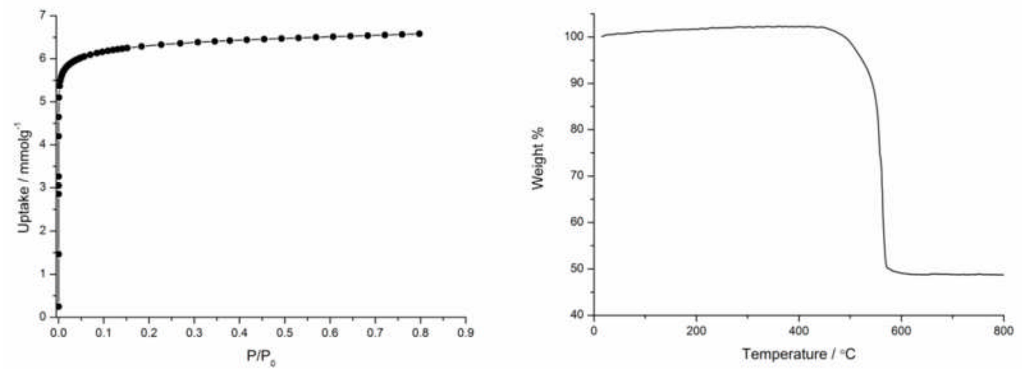

Figure 5.3: Nitrogen adsorption at 77 K and thermogravimetric analysis on Sc_2BDC_3.

The Sc_2BDC_3 framework is a particularly interesting candidate for adsorption and separation experiments due to the small pores and hydrophobic nature of the framework. The small channel cross section means that the adsorbed species can interact with two or more channel walls simultaneously. A follow up study on Sc_2BDC_3 also reported by Miller *et. al*, shows the crystallographic response of the framework to the adsorption of fuel-related gases. Experimental adsorption isotherms, measured on Sc_2BDC_3, show the material has permanent porosity to a number of fuel-related small gas molecules (CO_2, CH_4, O_2, CO, N_2, H_2) and identifies the single crystal studies identified crystallographic positions for the adsorbed species.[83]

Single crystals of Sc_2BDC_3, prepared solvothermally, were glued into a 0.3 mm quartz capillary mounted on a goniometer head with a vacuum/gas pressure controller attached. Following activation, known pressures of adsorbate were dosed onto the crystal at low temperatures and pressures to ensure ordering of the adsorbed species. Single crystal data collected at a constant pressure of adsorbed species were of sufficient quality to locate the adsorption sites for all species investigated apart from H_2 which, due to the low electron density, could not be identified unambiguously. The crystallographic data for the series of adsorbed species is shown in Table 5.1.[83]

	As-prepared	CO_2	H_2	CH_4	C_2H_4
Formula unit	Sc_2BDC_3	$Sc_2BDC_3 \cdot 2CO_2$	$Sc_2BDC_3 \cdot xH_2$	$Sc_2BDC_3 \cdot CH_4$	$Sc_2BDC_3 \cdot 2C_2H_4$
Pressure	-	1 bar	0.25 bar	9 bar	5 bar
Temperature /K	93	235	80	230	230
Space group	*Fddd*	*C2/c*	*C2/c*	*Fddd*	*Fddd*
Unit cell	orthorhombic	monoclinic	monoclinic	orthorhombic	orthorhombic
a (Å)	8.776(6)	8.747(2)	8.769(13)	8.8001(3)	8.8650(4)
B (Å)	20.795(13)	34.464(8)	34.4517(16)	20.7921(5)	20.7000(7)
C (Å)	34.41(2)	11.092(2)	11.1373(12)	34.3972(6)	34.3750(12)
β °	90	110.95(3)	111.14(1)	90	90

Table 5.1: Structural data from *in situ* gas adsorption studies on Sc_2BDC_3[83]

Of particular interest is the change in the symmetry observed on the adsorption of CO_2 from the orthorhombic *Fddd* to monoclinic *C2/c*. This symmetry change results in the presence of two different channels in alternating layers represented by three unique terephthalate environments. This change was proposed to be a result of the CO_2 adsorption where the molecules of CO_2 were observed to occupy different sites within the two channels. In the first channel, the CO_2 occupies a position where all three atoms are in the ac-plane (Figure 5.4) and the axis of the molecule is aligned so the C=O oxygen points towards a framework (Group 2a) phenyl C-H with a distance of 2.87 and 2.89 Å. Channel B has two symmetry related sites for CO_2, with the axis of the molecules in this channel parallel to the plane of the phenyl ring in the (Group 2b) terephthalate. Due to the close contact (~2.2 Å) between the two symmetry related CO_2 positions, the two sites cannot be occupied simultaneously with this orientation. Another consequence of this reorientation of the terephthalates, in the monoclinic form, is that channel B becomes more of a cavity arrangement (phenyl ring plane tilted further from the channel direction (a-axis)) while channel A becomes more accessible (phenyl ring plane almost parallel to the channel direction (a-axis)).

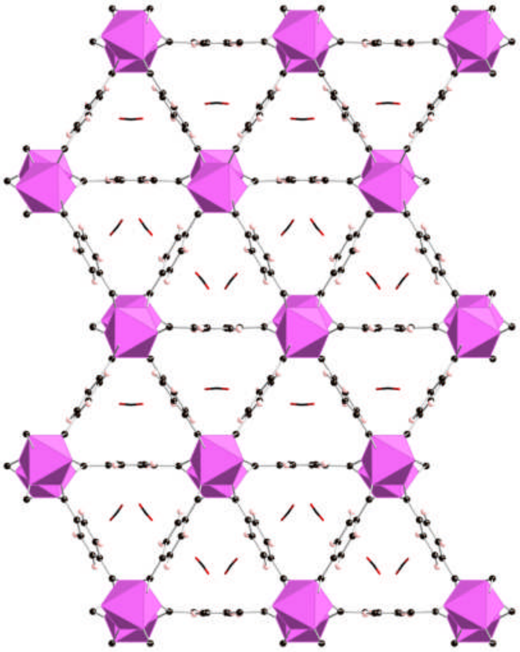

Figure 5.4: Crystallographic positions for CO_2 molecules adsorbed in Sc_2BDC_3 determined from *in situ* single-crystal gas adsorption experiments. Scandium octahedra are shown in pink. Black spheres represent the carbon atoms of the organic linker. The black and red stick represents the position of the adsorbed CO_2.

5.2 Aims

Initial work on Sc_2BDC_3 suggests the material is a suitable candidate for the separation of small gas molecules. In this work the selectivity and separation properties of Sc_2BDC_3 are investigated and also if the material can be modified for specific applications by means of functionalising the internal surface by using functionalised organic linkers.

5.3 Experimental

Hydrothermal and solvothermal conditions have been used to prepare Sc_2BDC_3 as reported by Miller *et al.*[27,83] From the synthetic studies, reported in Chapter 3, Sc_2BDC_3 was observed to form at the high end of the temperature range studied, between 190 – 220°C. Sc_2BDC_3 is strongly favoured by hydrothermal conditions, and produced by all three scandium sources used in this work (scandium oxide, chloride and nitrate) and the terephthalic acid linker. The solvothermal route, reported to produce large crystals of Sc_2BDC_3, was also successful but more sensitive control of the conditions was required due to the presence of a competitive phase (MIL-53(Sc)). One major difference in the two higher temperature phases is the ratio of scandium to terephthalate in the final products. As the name suggests, the ratio of Sc : terephthalate in Sc_2BDC_3 is 2:3 (compared to 1:1 in the MIL-53(Sc)) framework and, as expected, a higher ratio of terephthalic acid in the synthesis (greater than the stoichiometric amount for Sc_2BDC_3) was found to favour the pure Sc_2BDC_3 product.

Synthesised materials were identified by laboratory powder X-ray diffraction, elemental analysis and thermogravimetric analysis (TGA). Laboratory X-ray diffraction patterns were obtained in Debye-Scherrer geometry within sealed 0.7 mm quartz capillaries on a Stoe STADI/P diffractometer with monochromated Cu $K_{\alpha 1}$ X-rays (λ = 1.54056Å). Experimental powder diffraction patterns were used as the primary technique to access the purity of the products and where necessary, unreacted terephthalic acid was removed by calcination in a tube furnace under flowing air at 350°C for 12 hours. Some products from the hydrothermal reactions using scandium oxide as the metal source contained traces of the unreacted scandium oxide which proved difficult to remove, the presence of this impurity was minimised by addition of an excess of terephthalic acid in the reaction mixture which, if present in the product, could easily be removed by calcination.

TGA was performed at 5 K min^{-1} up to 1172 K under flowing air. Elemental analysis (carbon, hydrogen, nitrogen) was performed on pure samples using a Carlo Erba instruments EA 1110 CHNS analyser.

Solid-state NMR experiments were performed using Bruker Avance III spectrometers operating at magnetic field strengths of 9.4 and 14.1 T. Experiments at both magnetic fields were carried out using Bruker 4-mm MAS probes. Chemical shifts are given relative to TMS for ^{13}C and ^{2}H, and 0.2 M $ScCl_3$ (aq) for ^{45}Sc. ^{13}C transverse magnetisation was obtained by ramped cross polarisation (CP) from ^{1}H. Two-pulse phase modulation (TPPM) ^{1}H decoupling was applied during acquisition. ^{13}C CP MAS NMR spectra were acquired with between 4400 and 6144 transients separated by a recycle interval of 3 seconds. ^{45}Sc MAS NMR spectra were obtained by direct polarisation of ^{45}Sc, using between 256 and 1024 transients separated by a recycle interval of 3 s. Variable-temperature ^{2}H wideline NMR spectra were acquired for a static sample in the range 298 – 383 K using using the quadrupolar echo pulse sequence $(90^\circ_{\phi}–\tau–90^\circ_{\phi'}– \tau)$. Spectra were recorded using an echo duration, τ, of 40 µs and a 16-step phase cycle designed to refocus both linear and quadratic spin interactions.[13] Spectra were obtained using between 2206 and 14336 transients separated by a recycle interval of 5 s.

Adsorption isotherms of N_2 on all samples were measured at 77K using a Micromeritics Tristar II 3020. Adsorption of CO_2 was measured on Sc_2BDC_3 prepared solvothermally and on functionalised samples prepared hydrothermally using scandium oxide as the scandium source. Isotherms were collected up to 900 mbar at 196 K (ethanol/dry ice mixture) and 273 K (Grant GR150 thermostatic refrigerated bath) using a Hiden IGA automatic gravimetric porosimeter. Prior to adsorption of N_2 or CO_2, the samples were heated at 443 K under a vacuum of 3×10^{-7} mbar for 8 hours. In addition, laboratory powder X-ray diffraction was performed on samples in quartz glass capillaries that had been activated at 443 K and allowed to adsorb CO_2 at 298 K and 1 bar before being sealed (by glue).

5.4 Results

To investigate Sc_2BDC_3 as a candidate material for use in adsorption and separation experiments, it was necessary to understand how the material behaves under the conditions used in such experiments. Typically, separations are carried out above room temperature and as such the material may have different properties to those identified in low temperature adsorption studies. In this work, the thermal response of Sc_2BDC_3 is investigated between 100 K and 523 K by synchrotron powder X-ray diffraction and in the range 25 – 110°C by ^2H wideline NMR.

5.4.1 Synchrotron Powder X-ray Diffraction studies

5.4.1.1 Sc_2BDC_3

To understand the temperature dependence of the Sc_2BDC_3 structural behaviour, a highly crystalline sample (prepared solvothermally as described in Chapter 3) was ground to a fine powder, to avoid preferential orientation, activated and flame sealed in a quartz glass capillary for analysis. This treatment was important to ensure that any observed behaviour was independent of adsorbed guest molecules in the framework. *In situ* synchrotron powder X-ray diffraction data – collected at beamline I-11 of the Diamond Light Source (DLS) – over the temperature range of 100 K to 623 K was used to explore the thermal response of the activated framework. The temperature was controlled by means of a Cryostream 700 Series between 100 K and 293 K and using a hot air blower in the region above room temperature 293 K – 523 K. In each case the diffraction pattern was collected from 0-140° 2θ by constant velocity scanning in Debye-Scherrer geometry using the beamline's multianalyser crystal system, with the measured intensities binned to a 2θ interval of 0.001 degrees (Figure 5.5).

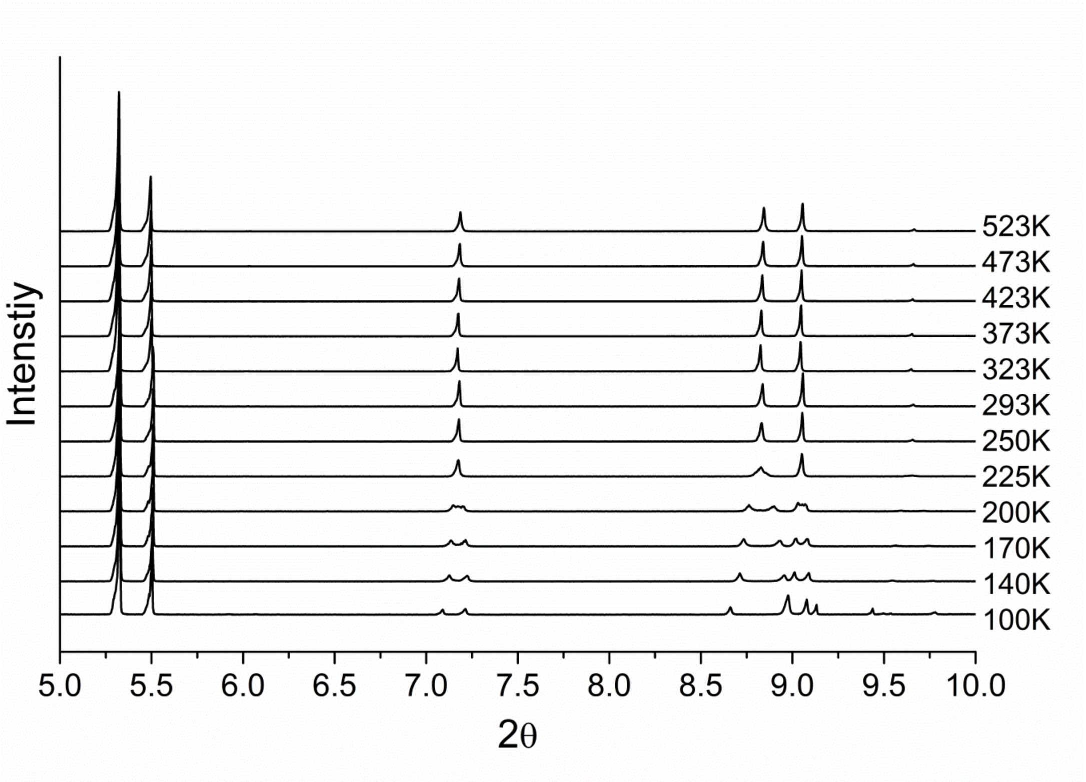

Figure 5.5: Expansion of the low angle region of variable temperature synchrotron X-ray diffraction patterns collected on an evacuated capillary of Sc_2BDC_3

On initial observation of the measured diffraction patterns, a symmetry change was observed occurring at around 200 K. Indexing the patterns and fitting the unit cell using the Le Bail method showed good agreement between the measured patterns, above and below the phase transition, with the literature structural models of Sc_2BDC_3 in the orthorhombic *Fddd* (above 200 K) and monoclinic *C2/c* symmetry (below 200 K). Rietveld analysis was used to obtain final atomic positions using the framework models using the literature examples of orthorhombic and monoclinic Sc_2BDC_3 as the starting model. Bond restraints were applied to maintain chemical sense in the ligands, the following values were applied: Sc-O, 2.09(2) Å; O-O, 2.97(2) Å; O-C, 1.27(2) Å; C-C(aromatic), 1.39(2); C-C (aromatic-carboxylate), 1.49(2) Å. Crystallographic data for the series of structures are shown in Table 5.2.

Structure	Sc2BDC3 – 140 K	Sc2BDC3 – 170 K	Sc2BDC3 – 250 K	Sc2BDC3 – 293 K	Sc2BDC3 – 323 K	Sc2BDC3 – 373 K	Sc2BDC3 – 423 K	Sc2BDC3 – 473 K	Sc2BDC3 – 523 K
Formula unit	$Sc_2(C_8H_4O_4)_3$	$Sc_2(C_8H_4O_4)_3$	$Sc_2(C_8H_4O_4)_3$	$Sc_2(C_8H_4O_4)_3$	$Sc_2(C_8H_4O_4)_3$	$Sc_2(C_8H_4O_4)_3$	$Sc_2(C_8H_4O_4)_3$	$Sc_2(C_8H_4O_4)_3$	$Sc_2(C_8H_4O_4)_3$
Formula weight	582.26	582.26	582.26	582.26	582.26	582.26	582.26	582.26	582.26
Temperature/K	140	170	250	293	323	373	423	473	523
Space group	*C2/c*	*C2/c*	*Fddd*	*Fddd*	*Fddd*	*Fddd*	*Fddd*	*Fddd*	*Fddd*
X-ray source	Synchrotron	Synchrotron	Synchrotron	Synchrotron	Synchrotron	Synchrotron	Synchrotron	Synchrotron	Synchrotron
Diffractometer	Beamline i11	Beamline i11	Beamline i11	Beamline i11	Beamline i11	Beamline i11	Beamline i11	Beamline i11	Beamline i11
Wavelength (Å)	0.826019	0.826019	0.826019	0.825028	0.825028	0.825028	0.825028	0.825028	0.825028
Unit cell (Å)									
a/Å	8.75434(14)	8.75468(15)	8.75292(4)	8.745851(13)	8.742107(14)	8.73461(15)	8.72548(2)	8.71576(2)	8.704711(3)
b/Å	34.38536(13)	34.37449(16)	20.7551(5)	20.74388(3)	20.739628(3)	20.733114(3)	20.728004(2)	20.722986(3)	20.71887(3)
c/Å	11.14542(8)	11.16967(1)	34.35779(8)	34.34896(4)	34.34945(4)	34.35274(4)	34.35838(4)	34.36496(4)	34.37361(6)
β/°	111.4791(8)	111.7476(1)	90	90	90	90	90	90	90
Volume/Å^3	3122.00(5)	3122.13(6)	6241.70(4)	6231.68(2)	6227.83(2)	6221.131(14)	6214.124(15)	6206.88(2)	6199.34(3)
No. Reflections	404	630	471	665	665	663	661	659	657
No. Atoms (Non-H)	20	20	11	11	11	11	11	11	11
No. Restraints	39	39	22	22	30	30	22	22	22
R	0.0823	0.0864	0.0751	0.046	0.0479	0.0436	0.0434	0.045	0.0488
wR	0.1102	0.1146	0.0969	0.0644	0.0659	0.0607	0.0594	0.0635	0.0693
Max. and min. residual e^- density (e/Å^3)	0.188, -0.254	0.809, -0.528	0.582, -0.641	0.532, -0.425	0.523, -0.554	0.497, -0.498	0.602, -0.516	0.627, -0.447	0.464, -0.439

Table 5.2: Structural data from Rietveld refinements on the variable temperature series collected on Sc_2BDC_3.

At room temperature, Rietveld refinement gives the structure as orthorhombic *Fddd* (a = 8.74585(1) Å, b = 20.74387(2) Å, c = 34.34896(4) Å) (Figure 5.6).

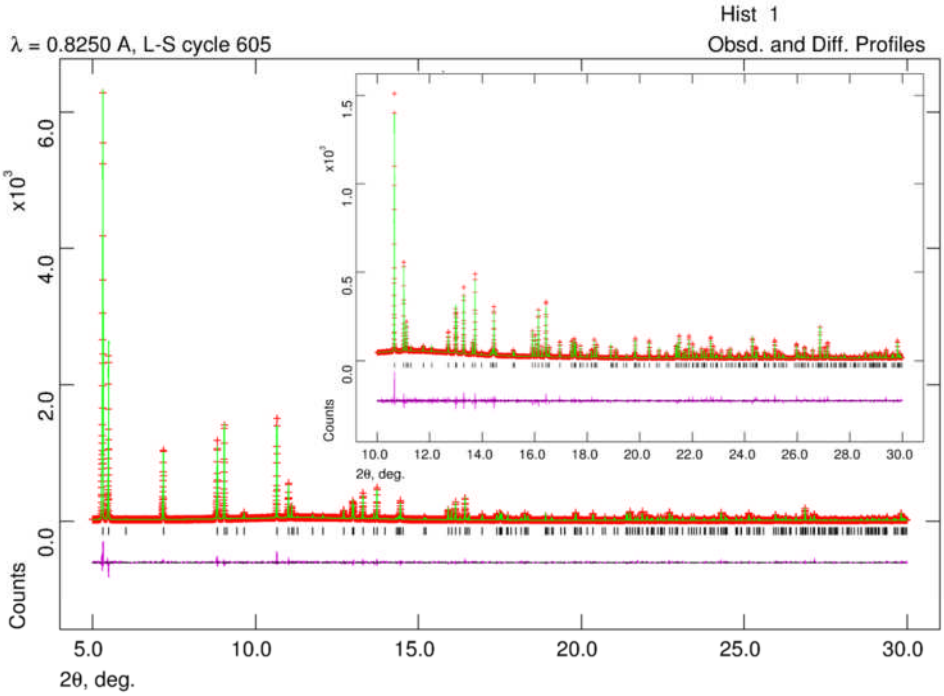

Figure 5.6: Rietveld profile fit for the orthorhombic *Fddd* structure at 373 K

Upon cooling to 100 K, the structure shows a reversible change to a monoclinic structure in *C2/c*, (a = 8.7543(1) Å, b = 34.3853(1) Å, c = 11.14542(8) Å, β = 111.4791(8)°). The observed change in symmetry under these conditions was unexpected as the structure solved from single crystal data, measured at 100 K in a N_2 stream, gave the orthorhombic *Fddd* structural model. Rietveld profile fit for the refinement of the monoclinic structure in *C2/c* is shown in Figure 5.7. This inconsistency is attributed to the presence of guest species (adsorbed from the air) in the single-crystal studies, and there was no activation or treatment prior to the data collection.

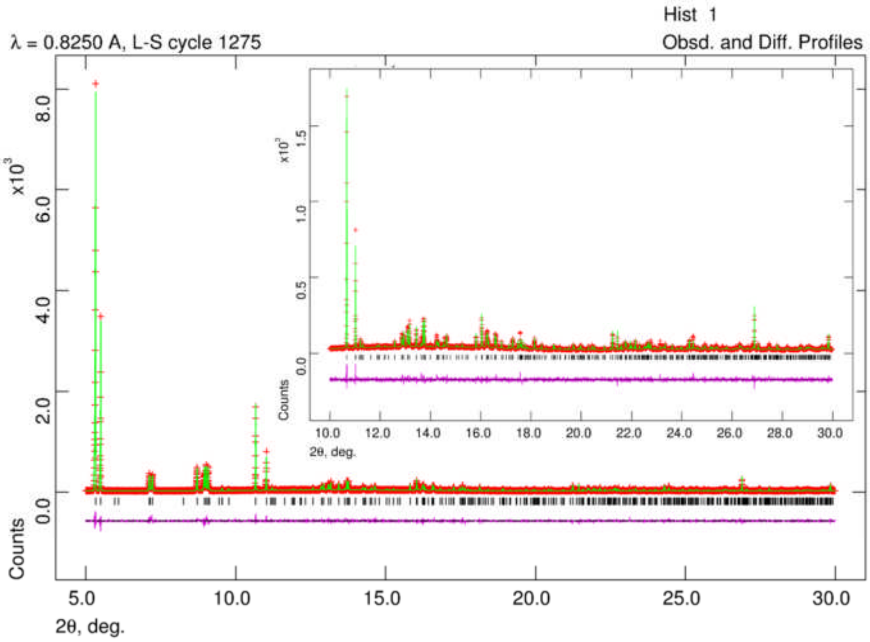

Figure 5.7: Rietveld profile fit for the monoclinic *C2/c structure* at 140 K

The change to monoclinic is a result of a rotation of the ScO_6 octahedra, accompanied by a shift in the orientation of the group 1 terephthalate away from 90° to the chain direction, and two types of unidirectional channel with three nonequivalent terephthalate environments. A similar reorientation is observed in the single-crystal studies of CO_2 adsorption but in this case the change is observed in the absence of guest species. Above the transition temperature, the structure appears to remain orthorhombic up to the highest temperature (523 K). Plotting the unit cell parameters and cell volume as a function of temperature it was observed that over the temperature range where the structure changed symmetry to monoclinic (100 K – 200 K) there was little change in the overall cell volume. In the orthorhombic region, however, the cell volume displays a significant negative thermal expansion (NTE). The trends in the unit cell parameters and cell volume, measured from the final models after Rietveld refinement, are shown in Figure 5.8.

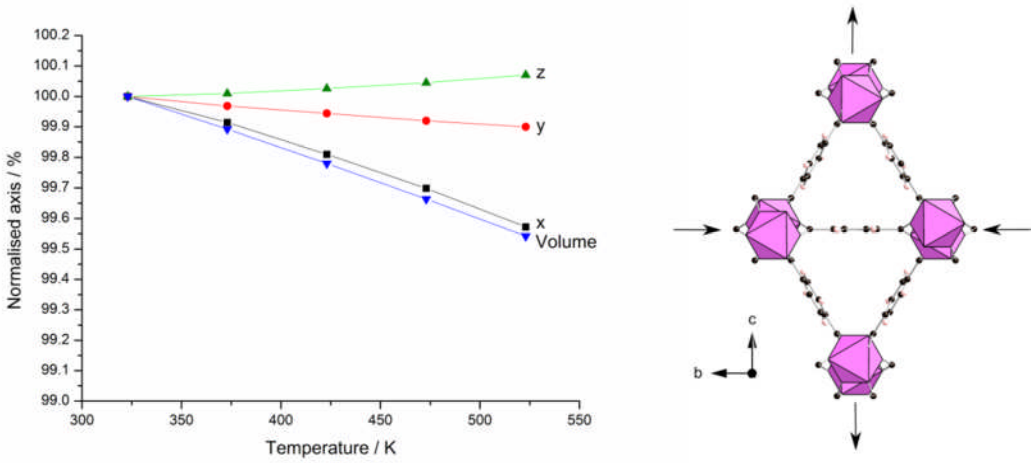

Figure 5.8: Plot of the trends in the normalized cell parameters (normalized over the orthorhombicregion from 323 - 523 K) (*left*) and the direction of the distortion with respect to the channel direction

This negative thermal expansion is consistent with values reported by Keppert *et al.*[116] on the metal-organic framework MOF-5. The cubic MOF-5 structure displays an isotropic linear thermal expansivity in the cell volume of 4.0 × 10^{-5} K^{-1} over a similar range of temperatures. Single crystal studies on the material shows the contraction is caused by twisting and vibration in the carboxylate group and out-of-phase twisting and vibration in the phenyl rings. For Sc_2BDC_3 the expansion is anisotropic, in the orthorhombic form the NTE is linear but upon symmetry change to monoclinic and further cooling, the cell volume remains constant. The plot of the cell parameters as a function of temperature shows that the trends in the cell volume mirror that of the short axis of the cell (a-axis, along the chain). This change is consistent with similar twisting and vibration of the carboxylate as observed in the MOF-5 structure. In this case of Sc_2BDC_3, the structure is composed of unidirectional chains, rather than the octahedral clusters in MOF-5, resulting in more anisotropic volume changes. In the monoclinic region (140 K – 225 K) there is almost no change in the measured cell volume possibly due to the symmetry change counteracting the NTE effects of translation and vibration which, by extrapolation of the linear behavior at higher temperature, would also be expected on further cooling. A representation of the chain showing the observed contraction is shown in Figure 5.9.

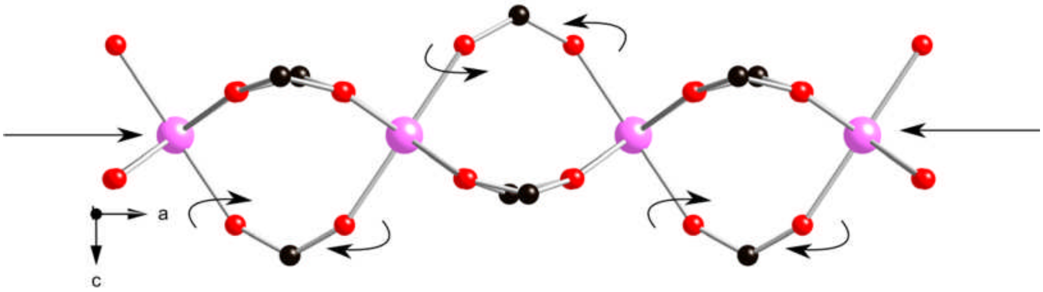

Figure 5.9: Chain rotation responsible for the negative thermal expansivity of Sc_2BDC_3. Pink, red and black spheres represent the scandium, oxygen and carbon atoms respectively.

High-resolution synchrotron powder diffraction data was also collected on the amino- and nitro- functionalised derivatives $Sc_2(NH_2\text{-}BDC)_3$ and $Sc_2(NO_2\text{-}BDC)_3$. Initial unit cell determination on the measured diffraction patterns, using the Fullprof suite of programs,[117] was used to determine if the literature structural models (orthorhombic *Fddd* or monoclinic *C*2*/c* were appropriate starting points for Rietveld refinement. Following this, it was determined that $Sc_2(NH_2\text{-}BDC)_3$ was in good agreement with the orthorhombic *Fddd* model while $Sc_2(NO_2\text{-}BDC)_3$ was consistent with the monoclinic *C*2*/*c model.

Structure	$Sc_2(NO_2\text{-}BDC)_3$ 100 K	$Sc_2(NO_2\text{-}BDC)_3$ 293 K	$Sc_2(NO_2\text{-}BDC)_3$ 373 K	$Sc_2(NO_2\text{-}BDC)_3$ 473 K	$Sc_2(NH_2\text{-}BDC)_3$ 100 K	$Sc_2(NH_2\text{-}BDC)_3$ 293 K
Formula unit	$Sc_2(C_8H_3NO_6)_3$	$Sc_2(C_8H_3NO_6)_3$	$Sc_2(C_8H_3NO_6)_3$	$Sc_2(C_8H_3NO_6)_3$	$Sc_2(C_8H_5NO_4)_3$	$Sc_2(C_8H_5NO_4)_3$
Formula weight	717.26	717.26	717.26	717.26	627.31	627.31
Temperature/K	100	293	373	473	100	293
Space group	C 2/c	C 2/c	C 2/c	C 2/c	F ddd	F ddd
X-ray source	Synchrotron	Synchrotron	Synchrotron	Synchrotron	Synchrotron	Cu Kα
Diffractometer	Beamline i11	Beamline i11	Beamline i11	Beamline i11	Beamline i11	STOE STADI P
Wavelength (Å)	0.826019	0.825028	0.825028	0.825028	0.826019	1.54056
Unit cell (Å)						
a/Å	8.6674(2)	8.66399(7)	8.6614(7)	8.65457(8)	8.72068(16)	8.6995(4)
b/Å	34.3485(3)	34.42204(13)	34.42917(12)	34.43651(13)	20.82072(17)	20.8176(8)
c/Å	11.42264(15)	11.42526(6)	11.42032(6)	11.41078(6)	34.3857(3)	34.3571(12)
β/°	115.2333(12)	114.9321(5)	114.8277(4)	114.6647(5)	90	90
Volume/$Å^3$	3076.19(8)	3089.83(3)	3090.83(3)	3090.52(3)	6243.44(13)	6222.2(4)
No. Reflections	625	406	407	407	518	701
No. Atoms (Non-H)	29	29	29	29	13	13
No. Restraints	85	67	71	70	39	29
R	0.0552	0.0484	0.0469	0.0471	0.05	0.046
wR	0.072	0.0667	0.0647	0.0672	0.0681	0.0606
Max. and min. residual e^- density (e/$Å^3$)	0.436, -0.453	0.293, -0.441	0.353, -0.435	0.336, -0.420	0.718, -0.761	0.854, -0.61

Table 5.3: Structural data from Rietveld refinements on the functionalised Sc_2BDC_3

5.4.1.2 $Sc_2(NH_2\text{-}BDC)_3$

To begin structure solution of $Sc_2(NH_2\text{-}BDC)_3$ at 100 K, an orthorhombic framework model, taken from single crystal studies on the unfunctionalised Sc_2BDC_3, was selected and used as the starting atomic positions in the Rietveld refinement. In this case there was evidence of a second phase in the Rietveld refinement, consistent with some unreacted scandium oxide which was fitted and refined as a separate phase. To identify the location of the $–NH_2$ group, the framework was first refined with distance constraints applied to maintain chemical sense in the model, the same as those used for the pure terephthalate described above: Sc-O, 2.09(2) Å; O-O, 2.97(2) Å; O-C, 1.27(2) Å; C-C(aromatic), 1.39(2); C-C (aromatic-carboxylate), 1.49(2) Å. Following convergence of the refinement with only the framework model, difference Fourier mapping was used to locate possible positions for the $–NH_2$ group nitrogen (Figure 5.10).

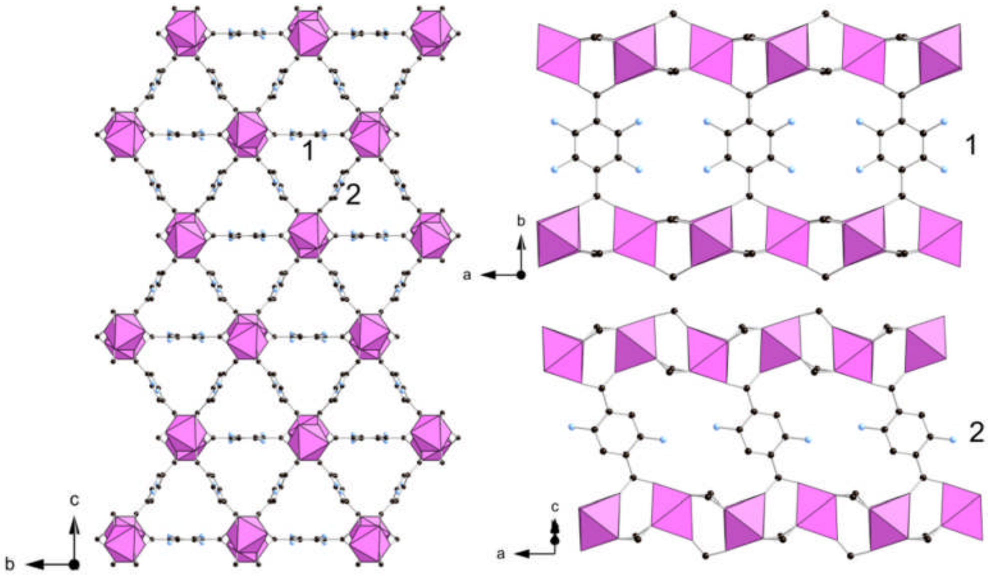

Figure 5.10: View down the channels and the two types of terephthalate layers Group 1(*top*) and Group 2(bottom) in $Sc_2(NH_2BDC)_3$. Scandium octahedra are shown in pink. Black and blue spheres represent the carbon and nitrogen atoms of the organic linker respectively.

As the sample was evacuated prior to analysis, there was assumed to be no guest species present in the framework, and the main differences in the electron density maps should therefore be the amino groups. In the orthorhombic model, there are three crystallographic carbon positions to which the $–NH_2$ group could be, one on the group 1 and two on the group 2 terephthalate. Atomic positions, identified by the difference Fourier mapping, suggested there was some ordering of the $–NH_2$ position on the group 2 linker with statistical disorder on the single atomic position on the group 1 terephthalate. This was confirmed by geometrically positioning atoms in all the possible crystallographic sites, allowing the occupancy to vary (with the sum of the two sites constrained to a maximum value of one group per phenyl ring). The two approaches both suggested ordering of the $–NH_2$ on the group 2 terephthalate, which, due to the tilt of the group 2 ligand, positions the $–NH_2$ group pointing away from the chains of scandium octahedra. This model was also used as for refinement of the structure at 298 K, which remained orthorhombic. The Rietveld plots for $Sc_2(NH_2\text{-BDC})_3$ and the crystallographic data are given in Figure 5.11 and Table 5.3 respectively.

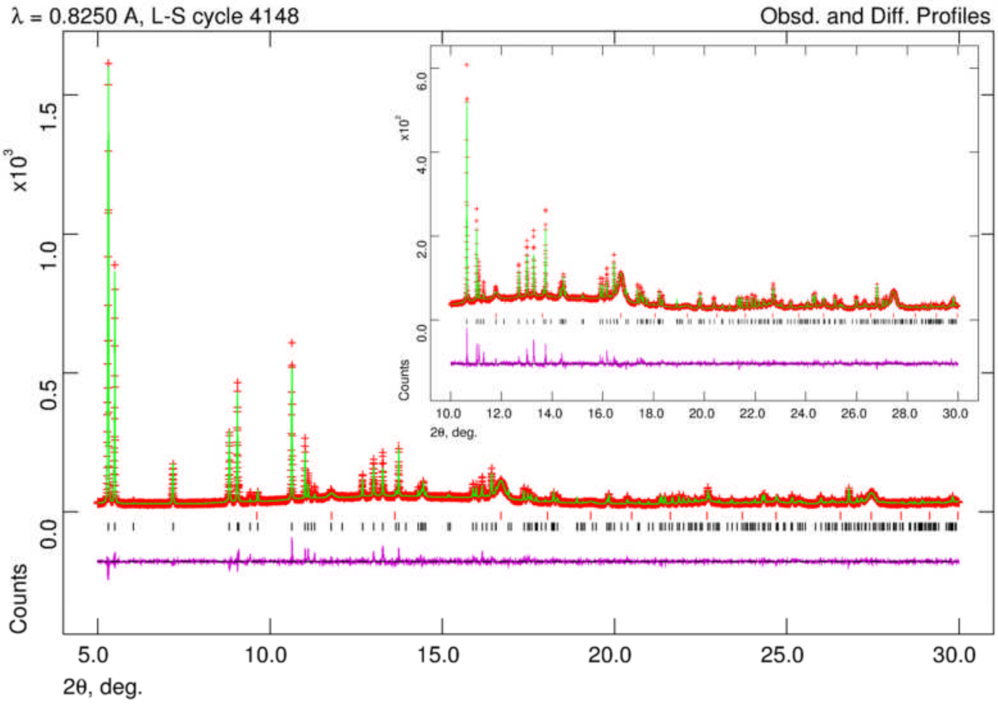

Figure 5.11: Rietveld profile fit for $Sc_2(NH_2\text{-BDC})_3$ including a small amount of Sc_2O_3 impurity fitted as a second phase in the refinement

5.4.1.3 $Sc_2(NO_2\text{-}BDC)_3$

As stated above, indexing the diffraction data at 100 K suggested $Sc_2(NO_2\text{-}BDC)_3$ was in good agreement with the monoclinic model from the previous single-crystal studies. In this model there are three unique terephthalates and six crystallographically-distinct carbon sites where the $-NO_2$ groups could be located. Again, distance constraints were applied to the framework model and the structure was refined to convergence, more difficult in this case due to the larger difference in electron density from the absent $-NO_2$ group. A combined approach of constrained-occupancy refinement and geometric positioning was again used to determine the $-NO_2$ group positions with the final atomic positions constrained and allowed to refine (Figure 5.12).

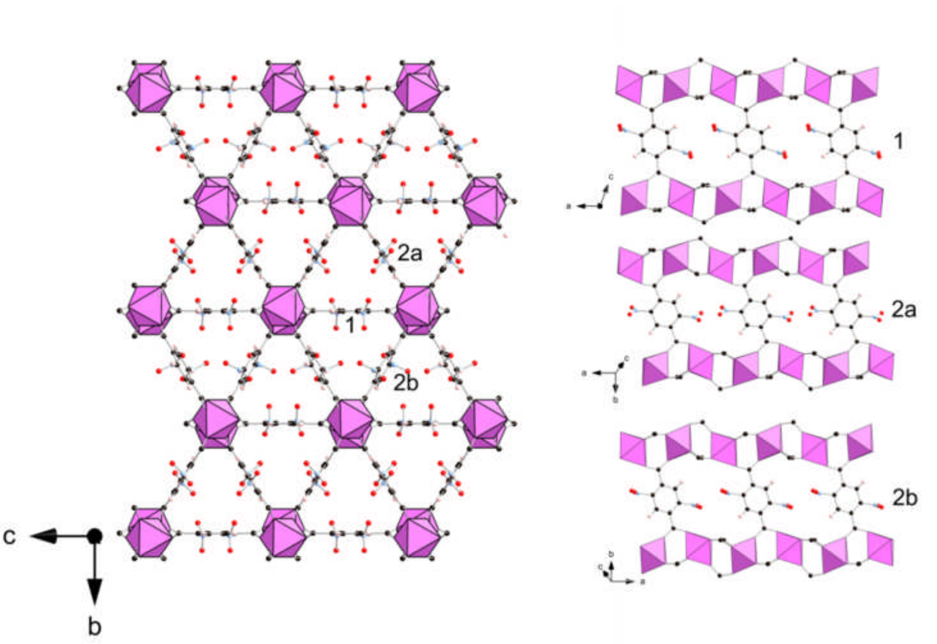

Figure 5.12: View down the channels and perpendicular to the three types of terephthalate layers (Group 1(*top*), Group 2a (*middle*) and Group 2b (*bottom*) in Sc_2BDC_3. Scandium octahedra are shown in pink. Black, blue and red spheres represent the carbon, nitrogen and oxygen atoms of the organic linker respectively.

Upon heating to 473 K, the structure remained monoclinic and the low temperature structure was used as a starting point for the Rietveld refinement. The Rietveld plots for $Sc_2(NO_2\text{-}BDC)_3$ and the crystallographic data are given in Figure 5.13 and Table 5.3 respectively.

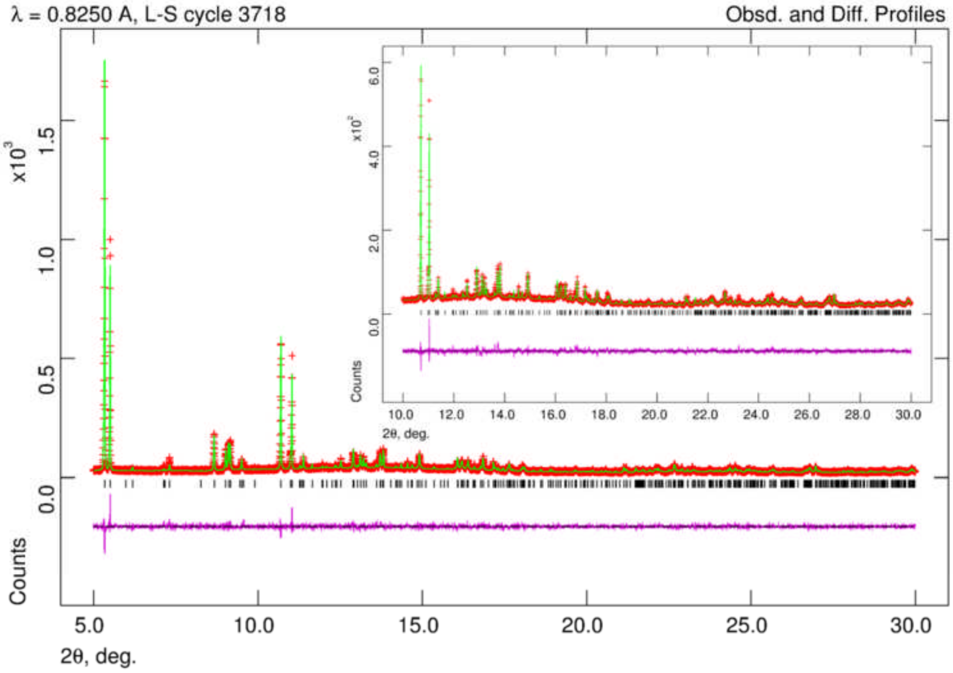

Figure 5.13: Rietveld profile fit for $Sc_2(NO_2\text{-}BDC)_3$

Subsequent single-crystal diffraction data collected at room temperature on a sample of $Sc_2(NO_2\text{-}BDC)_3$ (prepared hydrothermally using scandium nitrate) gave further evidence for the position of the $-NO_2$ group. Data were collected using a Rigaku Mo MM007 high brilliance generator and Saturn 70 CCD detector, at least a full hemisphere of data was collected using ω scans and intensities were corrected for Lorentz-polarisation and for absorption. The structure was solved using direct methods with hydrogen atoms fixed in idealised positions. The data was refined using the SHELX suite of programs to give a final structural model in monoclinic *C*2/*c*, in good agreement with that obtained from Rietveld analysis of the synchrotron powder X-ray data (Table 5.4).

Structure	$Sc_2(NO_2\text{-}BDC)_3$ 273 K
Formula unit	$Sc_2(C_8H_3NO_6)_3$
Temperature/K	273
Space group	*C2/c*
X-ray source	Cu Kα
Diffractometer	Rigaku MM007
Wavelength (Å)	0.71073
Unit cell (Å)	
a/Å	8.669(4)
b/Å	34.370(15)
c/Å	11.053(6)
β/°	110.486(6)
R_1	0.157

Table 5.4: Crystallographic data for $Sc_2(NO_2\text{-}BDC)_3$ from single crystal diffraction data

5.4.1.4 $Sc_2(Br\text{-}BDC)_3$

From the synthetic studies discussed in Chapter 3, it was clear that reactions using the Br-BDC linker were successful in the preparation of a product with the Sc_2BDC_3 framework (Figure 4.8). Comparison of the X-ray diffraction pattern to the pure terephthalate form of Sc_2BDC_3 indicated the cell was similar to the monoclinic *C2/c* model observed for Sc_2BDC_3 at low temperature. Rietveld refinement was used, starting with the monoclinic model, to try and solve the structure and obtain positions for the –Br on the phenyl ring. Geometrically positioned –Br were placed on all suitable carbon positions and the occupancy fixed to total one Br per terephthalate unit disordered over all possible positions. The refinement converged at wR = 6.6% (Figure 5.14) but with large thermal parameters on all -Br positions. The refinement showed that the product did have the monoclinic Sc_2BDC_3 framework but the position and occupancy of the –Br could not be identified unambiguously. The crystallographic details are given in Table 5.5.

Structure	$Sc_2(Br\text{-}BDC)_3$ 100 K
Formula unit	$Sc_2(C_8H_3O_4Br)_3$
Temperature/K	100
Space group	*C2/c*
X-ray source	Cu Kα
Diffractometer	STOE STADI P
Wavelength (Å)	1.54056
Unit cell (Å)	
a/Å	8.7307(7)
b/Å	34.2210(8)
c/Å	11.2829(5)
β/°	113.755(5)
Volume/Å^3	3085.5(3)
R	0.0492
wR	0.0661

Table 5.5: Crystallographic data for Sc_2BDC_3 prepared with 2-bromoterephthalic acid

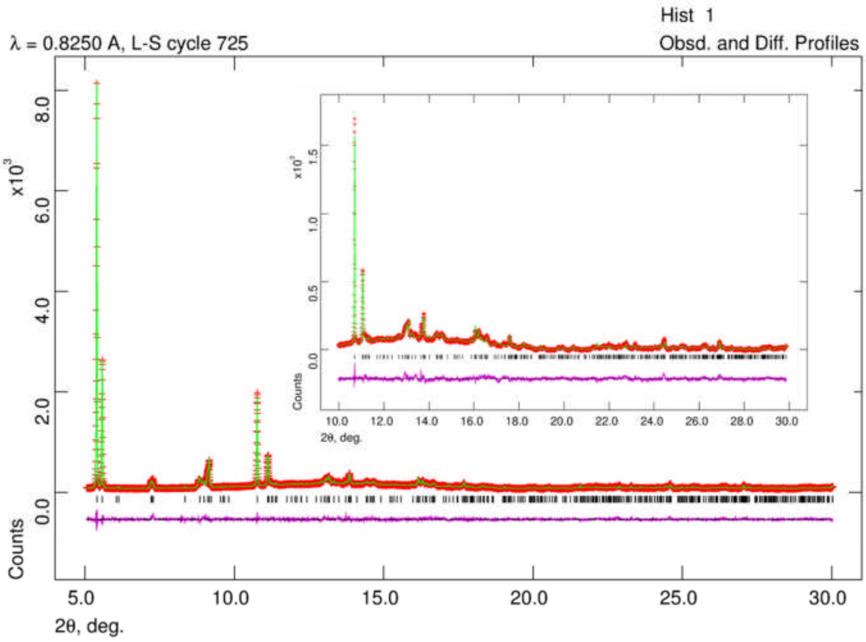

Figure 5.14: Rietveld profile fit for Sc_2BDC_3 prepared with 2-bromoterephthalic acid

EDX analysis suggested there was some bromine present in the sample but it was not possible to get an accurate Sc : Br ratio. Elemental analysis on the sample suggested there was also nitrogen present in the sample which could only arise from the DEF used in the solvent. The cross-sectional diameter of the triangular channels in Sc_2BDC_3 are not large enough to accommodate a DEF molecule suggesting that the nitrogen content is not a result of adsorbed solvent. Comparing ^{13}C Solid-state NMR on the –Br sample (Figure 5.15) with the other functionalised Sc_2BDC_3 structures showed some agreement albeit with broadening of the signals indicative of greater disorder. The position of the carbon identified to be attached to the $–NH_2$ and $–NO_2$ groups in the respective structures is shown to have a similar chemical shift to a signal in the Br-BDC structure. There is also evidence for alkyl carbon chains at lower ppm. At this point, the hypothesis is that the scandium nitrate is catalysing a reaction of the 2-bromoterephthalic acid with the DEF during the synthesis, resulting in 2-diethylamino-terephthalic acid which is incorporated into the Sc_2BDC_3 framework as well as the 2-bromoterephthalic acid. Further study is required to confirm this and identify the relative quantities of each linker present in the final solid.

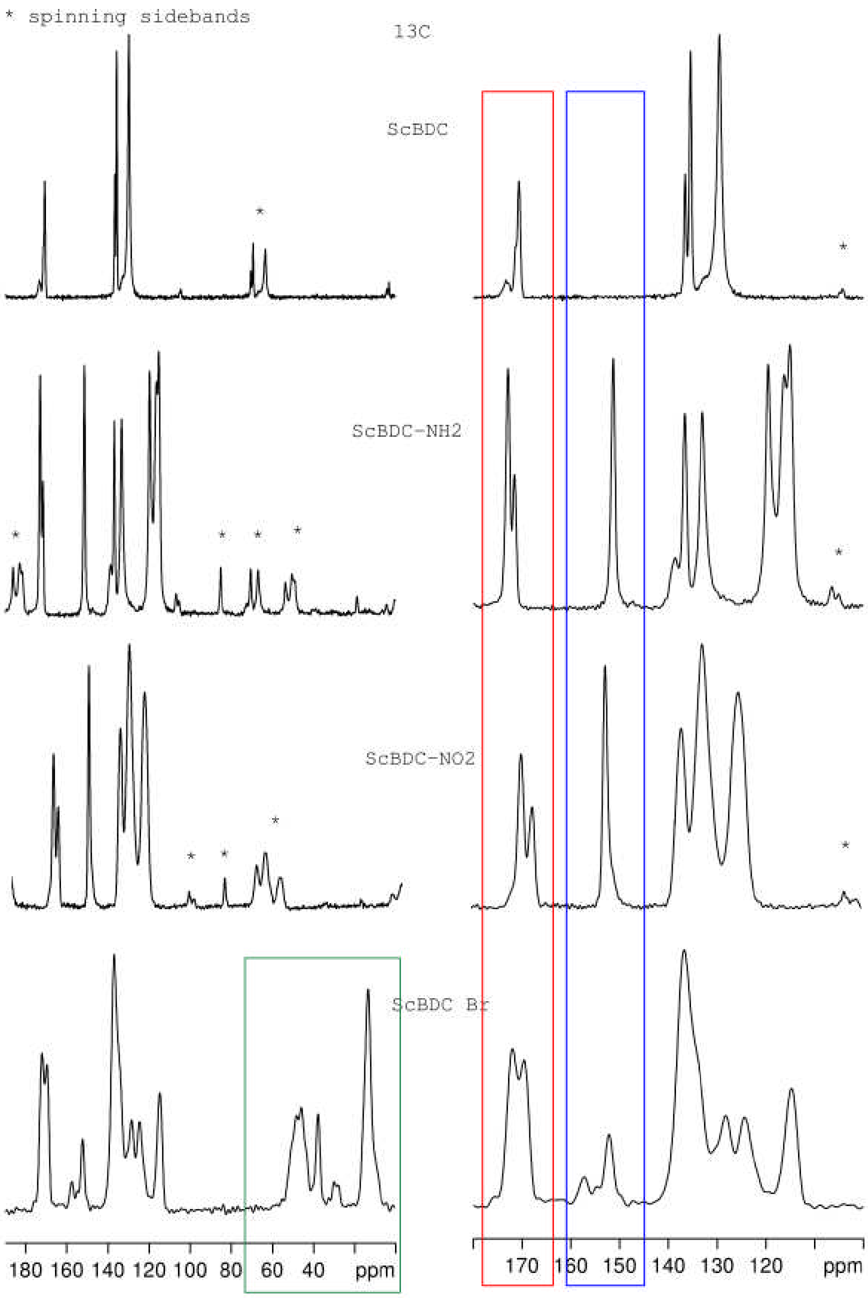

Figure 5.15: Comparison of ^{13}C NMR on the functionalised Sc_2BDC_3 frameworks. Alkyl carbon signals are identified in the green box, carboxylate carbon signals in red and carbon position for the functional group in blue.

5.4.2 Solid-State NMR

5.4.2.1 Variable-Temperature ^{2}H Solid-State NMR

To understand the dynamics in the Sc_2BDC_3 framework, ^{2}H solid-state NMR, a method for probing motion on the microsecond timescale, was measured on a deuterated sample of Sc_2BDC_3. This approach has been used on the literature materials MIL-47(V) and MIL-53(Cr), to observe ring flipping of the phenyl rings.[118] To understand the behavior of Sc_2BDC_3, static ^{2}H NMR experiments, carried out in collaboration with Dr. Sharon Ashbrook and coworkers were recorded in the temperature range 298 – 383 K, shown in Figure 5.16.

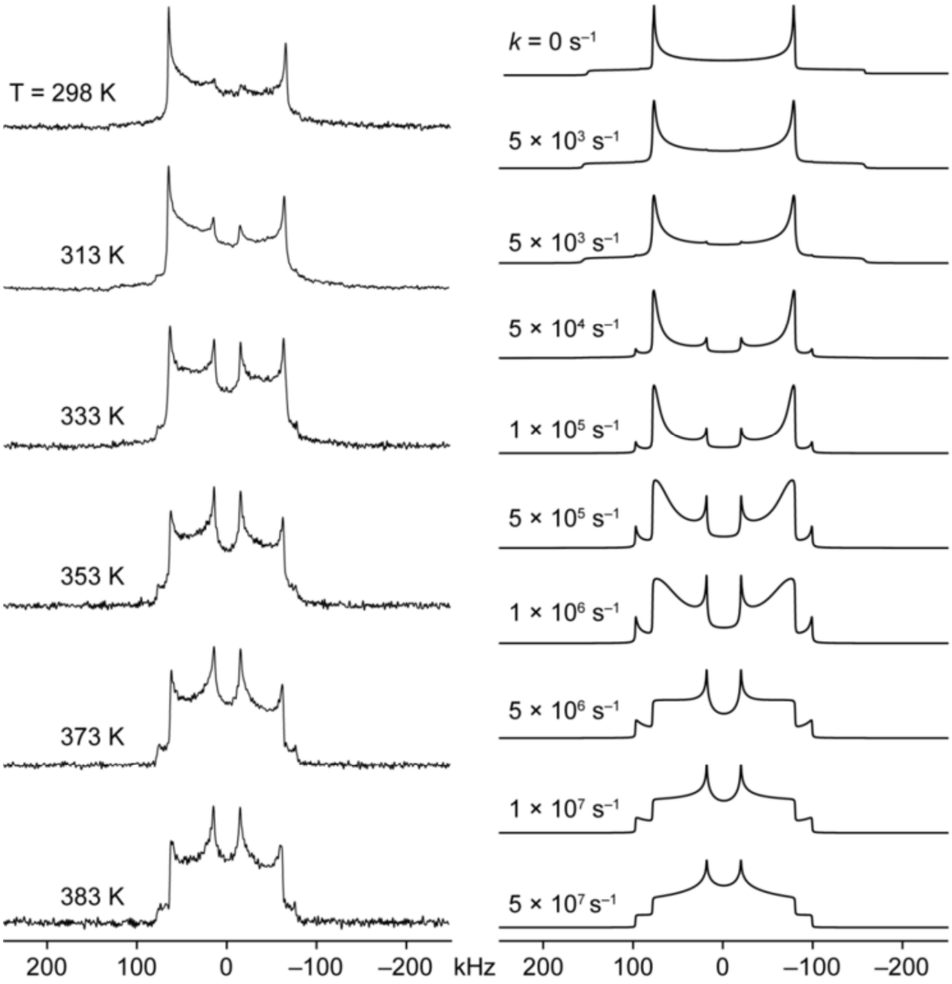

Figure 5.16: Experimental ^{2}H wide-line NMR spectra of fully deuterated Sc_2BDC_3 recorded at temperatures from 298 – 383 K compared with simulated spectra using the EXPRESS[119] simulation program

The spectrum at room temperature is predominantly a Pake doublet powder lineshape, with a broad pair of singularities, or 'horns', separated by ~130 kHz. However there is evidence for a second, narrower pair of lower intensity horns, separated by approximately 30 kHz, observed near the centre of the spectrum. Upon increasing the temperature, the lineshape changes dramatically as the narrower pair of horns increases greatly in intensity relative to the broader pair. To aid in the interpretation of these results, simulations were performed using the EXPRESS software package.[119] ^{2}H wideline NMR spectra were simulated assuming a 180° flip around the C_2 axis of a deuterated benzene ring with deuterium C_Qs of 210 kHz and η_Q of 0. Simulations were performed for a range of rate constants between 0 and 5×10^7 s^{-1}. The changes in the lineshape in the simulated spectra, shown in Figure 5.16, resemble those observed in the experimental spectra. However, at temperatures greater than 353 K, smaller changes in the experimental lineshape are observed, and the spectra do not appear to exactly follow the changes in lineshape predicted by the simulation. A possible explanation for the observed behaviour is that one portion of the rings undergo ring flipping while another portion remains immobile or flips with a different rate constant. In this case, the observed spectrum would comprise a superposition of two powder patterns with different degrees of partial averaging, resulting in more complex changes in lineshape with temperature. Indeed, given the presence of two crystallographically-distinct linkers it is possible that they may each exhibit different motional behaviours. Attempts to characterize the two types of linker separately by ^{2}H MAS NMR were unsuccessful owing to the crystallographically-distinct deuterium sites in the structure having the same chemical shift.

5.4.2.2 ^{45}Sc and ^{13}C Solid-State NMR

Room temperature ^{45}Sc (9.4 T) MAS NMR spectra for unfunctionalised and functionalised Sc_2BDC_3 are shown in Figure 5.17.

The spectrum for $Sc_2(BDC)_3$, shown in Figure 5.17(a), exhibits a second-order quadrupolar-broadened MAS lineshape corresponding to a single site with a quadrupolar coupling constant, C_Q, of 4.5 MHz and asymmetry parameter, η_Q, of 0.2. This is consistent with the single Sc site in the crystal structure and is in good agreement with previous data reported for the same material.

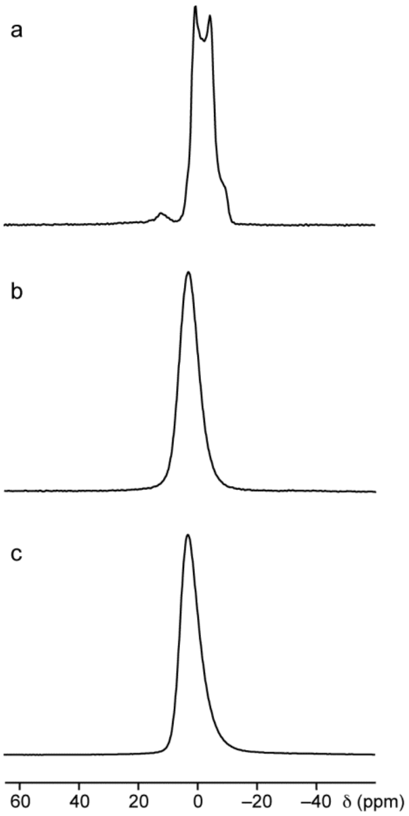

Figure 5.17: ^{45}Sc (9.4 T) MAS NMR spectra of Sc_2BDC_3(a), $Sc_2(NH_2\text{-}BDC)_3$(b) and $Sc_2(NO_2\text{-}BDC)_3$(c)

In contrast to Sc_2BDC_3, the ^{45}Sc MAS NMR spectra for the functionalised solids, shown in Figure 5.17(b) and Figure 5.17(c), show smooth featureless lineshapes with characteristic ‘tails’ at low frequency, indicating disorder. This can be attributed to statistical disorder of the orientations of the functional groups resulting in a distribution of Sc quadrupolar coupling constants. Despite the disorder, the linewidths for $Sc_2(NH_2\text{-}BDC)_3$ and $Sc_2(NO_2\text{-}BDC)_3$ appear slightly reduced compared with that of $Sc_2(BDC)_3$, indicating a smaller average C_Q for the Sc species in the functionalised Sc_2BDC_3. Additionally, the peaks in the spectra for the $Sc_2(NH_2\text{-}BDC)_3$ and $Sc_2(NO_2\text{-}BDC)_3$ are shifted downfield relative to the unfunctionalised material, consistent with a smaller quadrupolar interaction.

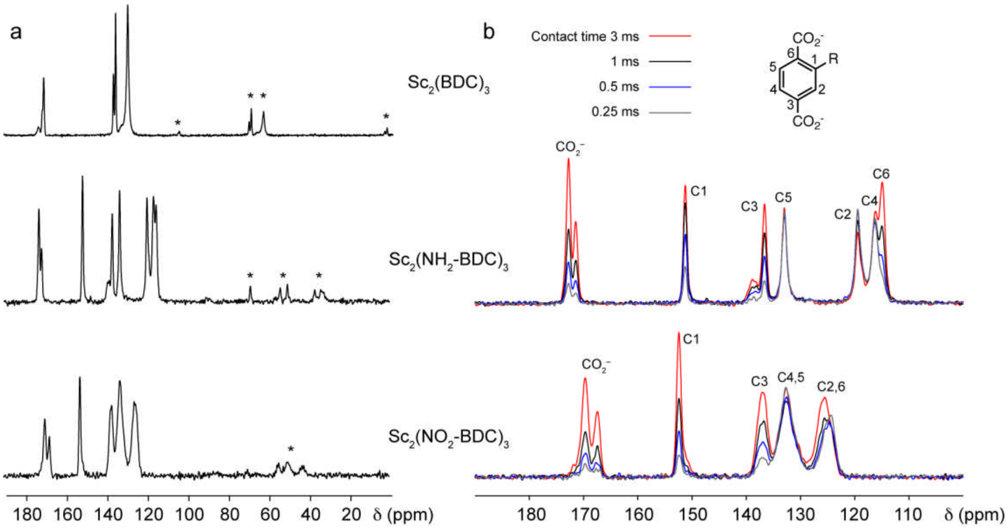

Figure 5.18: (a)^{13}C (14.1 T) CP MAS NMR spectra of unfunctionalized and functionalized Sc$_2$BDC$_3$ MOFs recorded at a MAS rates of between 10 and 12.5 kHz and at room temperature. (b) Expanded carboxylate and aromatic regions of variable-contact time ^{13}C CP MAS NMR of functionalized Sc$_2$BDC$_3$ MOFs. Spinning sidebands are indicated by an asterisk *

Room temperature ^{13}C (14.1 T) CP MAS NMR spectra for Sc$_2$BDC$_3$ and the functionalised analogues are shown in Figure 5.18. For the two functionalised frameworks, ^{13}C CP MAS NMR spectra were recorded with a range of cross-polarisation contact times between 0.25 – 3 ms (as shown in Figure 5b) in order to distinguish aromatic CH and quaternary carbons. The spectrum for Sc$_2$BDC$_3$ has been assigned previously using DFT calculations. Resonances are observed in two main groups, with aromatic carbons between 120 and 140 ppm and carboxylate carbons between 170 and 180 ppm. Within the aromatic region, protonated carbons are observed at lower chemical shift, while quaternary carbons are found at higher chemical shift. Considering the carboxylate region of the spectrum, the 2:1 doublet-like appearance of the resonance is consistent with the two different terephthalate linkers (and their populations) in the structure.

Addition of the functional groups lowers the symmetry of the terephthalate linker, resulting in more complex ^{13}C CP MAS NMR spectra for Sc$_2$(NH$_2$-BDC)$_3$ and Sc$_2$(NO$_2$-BDC)$_3$. In the spectrum for Sc$_2$(NH$_2$-BDC)$_3$, shown in Figure 5.18(a), the resonance corresponding to the C1 site is shifted downfield owing to the electron withdrawing effect of the directly-bonded nitrogen. In the variable-contact time ^{13}C CP MAS NMR spectra, shown in Figure 5b, the quaternary carbons C1, C3 and C6 exhibit much slower CP build-up rates than the CH carbons C2, C4 and C5 owing to the absence of directly-bonded protons. The assignment of the aromatic carbon sites is supported by DFT calculations performed on an isolated 1-aminoterephthalate molecule.

In the ^{13}C CP MAS NMR spectrum of $Sc_2(NO_2\text{-}BDC)_3$, shown in Figure 5.18, the C1 carbon is again shifted downfield owing to the electron withdrawing effect of the directly-bonded $-NO_2$ group. Aromatic CH and quaternary carbons are distinguished in variable-contact time ^{13}C CP MAS NMR spectra, shown in Figure 5.18(b). The quaternary C3 resonance at 137.1 ppm exhibits a relatively slow CP build-up rate, while the unresolved resonances corresponding to CH carbons C4 and C5 at 132.6 ppm show almost constant intensity over the range of contact times used. The overlap of the quaternary C6 and CH C2 carbons at 125.3 ppm results in a more complex build-up profile. This assignment is again supported by DFT calculations on an isolated 2-nitroterephthalate molecule.

5.4.3 Adsorption Studies

5.4.3.1 Nitrogen adsorption

Nitrogen adsorption data Adsorption of N_2 at 77 K gives a pore volume of 0.26 cm^3g^{-1} at $P/P_0 = 0.1$ for Sc_2BDC_3. The inclusion of $-NH_2$ groups reduces porosity to 0.148 cm^3g^{-1} (reduced by 43 %) and inclusion of $-NO_2$ groups renders the material non-porous to N_2 (Figure 5.19). This can be understood from the structures: the amino groups do not project into the channels (although they do take up some space in gaps in the channel walls) whereas the O atoms of the nitro groups project significantly into the channels, reducing the size of the constrictions below the diameter of N_2 molecules (2 centre L-J diameter 3.26 Å). In addition, at 77 K these groups are not likely to undergo rapid re-orientational motion to permit diffusion of gas molecules.

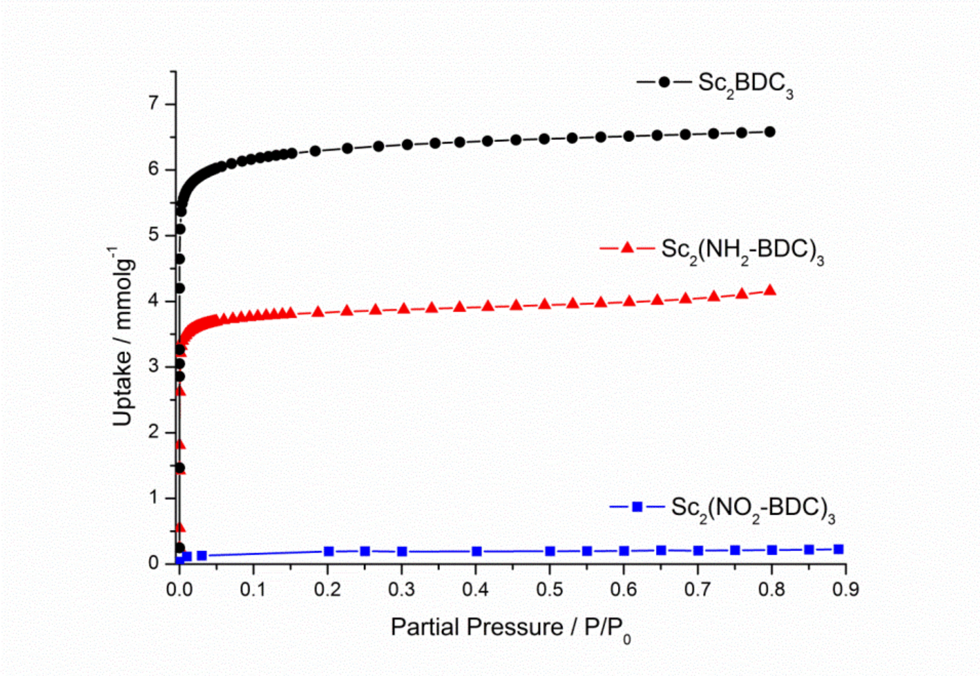

Figure 5.19: Nitrogen adsorption data on Sc_2BDC_3, $Sc_2(NH_2\text{-}BDC)_3$ and $Sc_2(NO_2\text{-}BDC)_3$ at 77 K

5.4.3.2 Carbon dioxide adsorption

Adsorption isotherm data at 196 K and 273 K up to 1 bar of CO_2 on Sc_2BDC_3 and its functionalised variants are shown in Figure 5.20 and Figure 5.21.

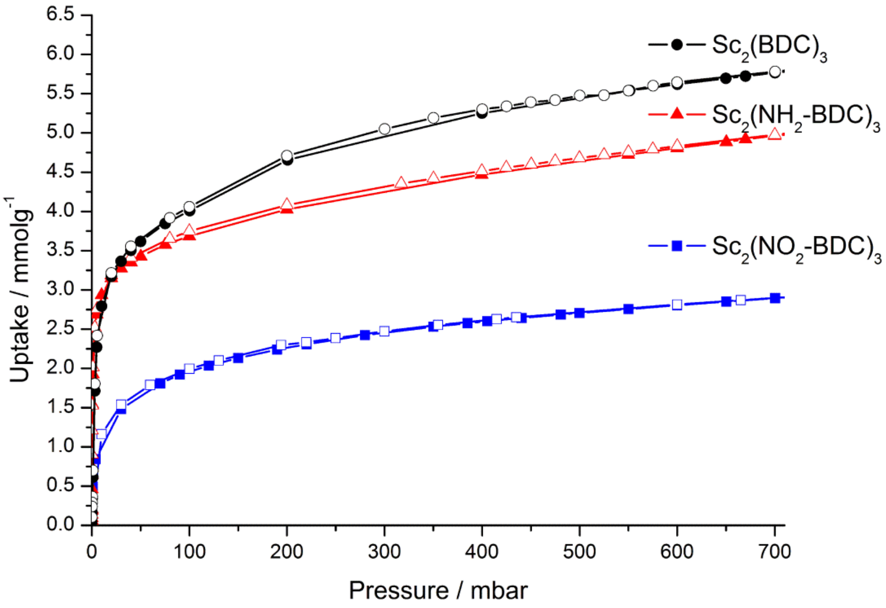

Figure 5.20: Carbon dioxide adsorption data on Sc_2BDC_3, $Sc_2(NH_2\text{-}BDC)_3$ and $Sc_2(NO_2\text{-}BDC)_3$ at 196 K

Low temperature adsorption data (195 K) for CO_2 show that the addition of $-NH_2$ and $-NO_2$ groups to the Sc_2BDC_3 results in a decrease in the maximum adsorption capacity of the material (which for the unfunctionalised solid is 6 $mmolg^{-1}$). The decrease in capacity is relatively small (-13 %) for the amino-functionalised form, especially when the increased mass of the functionalised solid (+8%) is taken into account. That the CO_2 capacity (196 K) is reduced less by amino-functionalisation than the N_2 capacity (77 K) could be due to differences in stacking of the two types of differently sized molecules. It may be that the longer CO_2 molecules stack predominantly along the channels and are less affected by the presence of the functional groups between the rings. In addition, pore blocking by $-NH_2$ groups could reduce the uptake of the larger N_2 molecules in the functionalised solid.

Analysis of the low pressure region shows that there is a higher uptake at low P (<30 mbar at 195 K) for the aminoterephthalate form (Figure 5.21). The reduction in CO_2 adsorption capacity of the NO_2-functionalised solid (-50%) is much greater than the change in mass (+24%). The decrease arises from the occupation of space in the channels by the nitro group O atoms. That 3 $mmolg^{-1}$ can still be taken up is remarkable, given the narrow bottlenecks in the triangular channels measured crystallographically. These openings are smaller than the L-J diameter (across the molecule) of CO_2, 2.98 Å, so that the ability of $Sc_2(NO_2\text{-}BDC)_3$ to take up CO_2 must be attributed to the ability of $-NO_2$ groups to rotate to allow CO_2 molecules to pass.

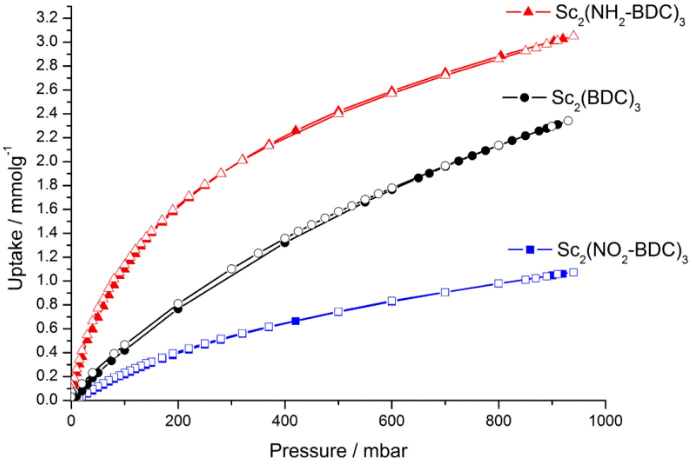

Figure 5.21: Carbon dioxide adsorption data on Sc_2BDC_3, $Sc_2(NH_2\text{-}BDC)_3$ and $Sc_2(NO_2\text{-}BDC)_3$ at 273 K

Adsorption of CO_2 at 273 K up to 0.9 bar (Figure 5.21) is able to distinguish between the solids on the basis of their strengths of adsorption. Notably, samples of each solid loaded at 293 K with 1 bar of CO_2 showed that under these similar conditions they did not change symmetry from the empty structures. While the uptake of $Sc_2(NO_2\text{-}BDC)_3$ is lower than that of Sc_2BDC_3 as expected from the available porosity measured at 195 K, the $Sc_2(NH_2\text{-}BDC)_3$ shows an increased uptake which is particularly marked at lower pressures. This derives from a higher heat of interaction of CO_2 with the amine groups. Similar effects have been predicted theoretically.[120] Combining these effects of functionalisation may be of use in tuning the adsorption and selectivity of the material for specific applications in gas storage and separation.

5.4.4 Adsorption Simulation

The single crystal structure at 230 K and 5 bar CO_2 was determined as monoclinic, with a maximum uptake of CO_2 in this structure of 3.5 mmol g^{-1}. Since the empty structure at 230 K is expected from the current work to be orthorhombic, it appears that the adsorption of CO_2 stabilises the monoclinic structure via sorbate-sorbent interactions. In order to investigate this further, GCMC simulations were performed in collaboration with David Fairen-Jimenez and Tina Düren at the University of Edinburgh. The monoclinic and orthorhombic models for the scandium terephthalate framework were used in the modeling, assuming a temperature of 196 K, at which experimental data has been collected. Two monoclinic structures were taken, one refined against the X-ray powder diffraction data at 170 K from this work (mono-170) and the other from a structure solved from single crystal X-ray diffraction experiments of CO_2 adsorbed on Sc_2BDC_3 at 230 K and 5 bar (mono-CO_2).[83] The orthorhombic structure was that measured previously at 298 K. Figure 5.22 shows the simulated locations of 3.5 mmol g^{-1} of CO_2 in the three different simulated structures, compared with the structure measured experimentally at this uptake (at 230 K, 5 bar). Experimentally, this uptake is achieved at 3 kPa.

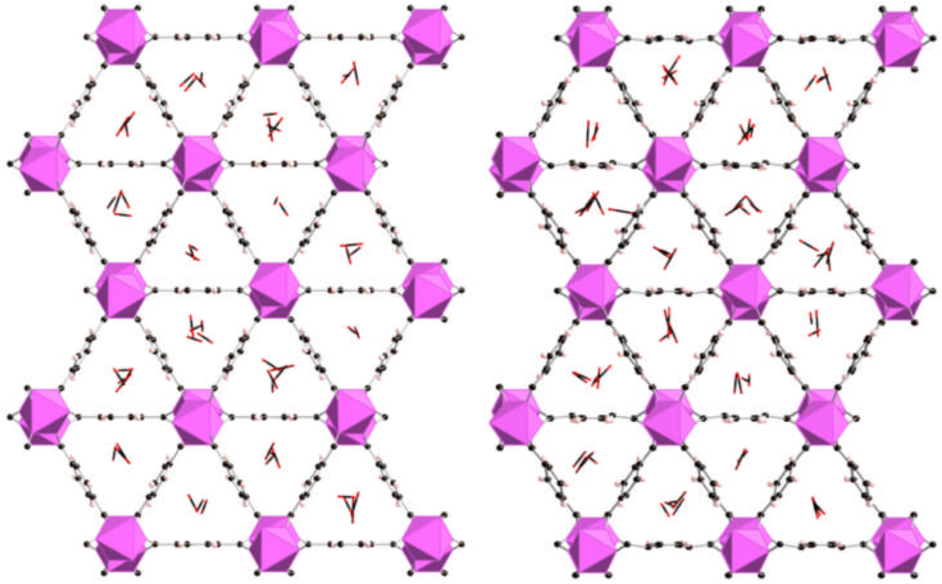

Orthorhombic @ 250 K Monoclinic @ 170 K

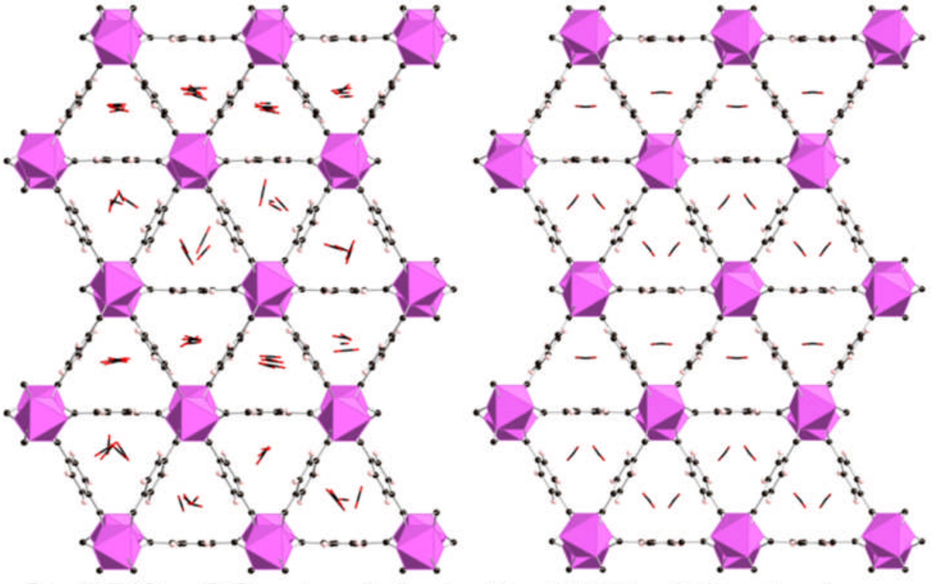

Sc_2BDC_3_CO_2 simulated Sc_2BDC_3_CO_2 single-crystal

Figure 5.22: Snapshots of simulated CO2 adsorption at 235 K and a loading of 3.5 mmol g^{-1} inside Sc_2BDC_3 orthorhombic model (*top left*), Sc_2BDC_3 monoclinic model (*top right*) from temperature series at 170 K, Sc_2BDC_3 _CO_2 single crystal structure (*bottom left*) compared to the positions identified by single crystal (*bottom right*). CO_2 positions are indicated by the red/black stick representation in the framework model.

CO_2 adsorption on three forms of the Sc_2BDC_3 structure observed experimentally was investigated using grand canonical Monte Carlo (GCMC) simulation[19] implemented in the multipurpose simulation code Music.[20] In the grand canonical ensemble, the chemical potential, the volume and the temperature are kept fixed as in adsorption experiments. Atomistic models were used for the Sc_2BDC_3 structures, with the atoms frozen at the crystallographic positions. In the simulations, CO_2 molecules were randomly moved, rotated, inserted and deleted, allowing the number of molecules in the framework to fluctuate. The chemical potential was related to the system pressure by the Peng-Robinson equation of state.[21]

The standard 12-6 Lennard-Jones (LJ) potential was used to model the interatomic interactions. The parameters for the framework atoms were obtained from the Dreiding force field,[22] while CO_2 was modeled by the TraPPE three-center model[23] (Table 4). The Lorentz-Berthelot mixing rules were employed to calculate the mixed parameters. Interactions beyond 15 Å were neglected for the simulations. Mulliken partial charges for the framework atoms were calculated using CASTEP and are given in the Supporting Information. A total number of 5×10^7 Monte Carlo steps were performed. The first 40% were used for system equilibration, carefully ensuring that thermodynamic equilibrium was reached, while the remaining steps were used to calculate the ensemble averages. After equilibration, snapshots were obtained, which represent the position of all CO_2 molecules from a single configuration during the simulation process. Snapshots (Figure 5.22) provide a visual impression about the degree of pore filling and organization of the CO_2 molecules inside the framework, and are reported here for simulations at 230 K (at which temperature the position of CO_2 has been observed experimentally) and a pore filling of 3.5 mmol g^{-1}.

All channels in the orthorhombic structure are identical, whereas there are two different types in the monoclinic structures. In each of the orthorhombic and mono-170 structures, there is considerable disorder in the orientation of the CO_2 molecules, but in the mono-CO_2 structure the molecules show a much higher degree of order in both sets of channels, which is consistent with the structure observed experimentally. The ordering would be expected to stabilise the guest-host assembly enthalpically. This indicates that the structure of Sc_2BDC_3 adapts to 'fit' the CO_2 adsorbate. This is manifested, for example, by a change in the tilt of terephthalate groups 2a and b with respect to the channel axis, and by a change in the monoclinic angle. Previous work shows that adsorption at 230 K of larger molecules, such as methane and ethane, is achieved in Sc_2BDC_3 that remains orthorhombic. This indicates that Sc_2BDC_3 is a flexible structure, which can distort from orthorhombic to monoclinic above the phase transition temperature in response to sorption of molecules of appropriate size, and that the degree of that distortion is variable, according to the size and shape of the adsorbate molecules. The adsorption data at 195 K (Figure 5.23) shows a slight step at an uptake of ca. 4 mmolg^{-1}.

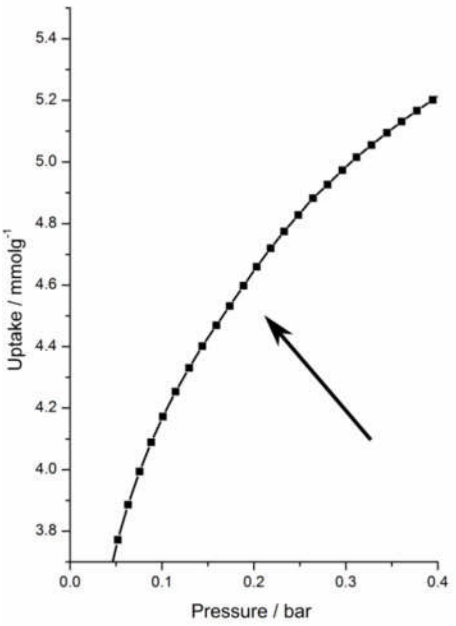

Figure 5.23: carbon dioxide adsorption data on Sc_2BDC_3 at 195 K. Position of the observed step in the adsorption data is indicated by the arrow.

This type of step in the isotherm might be explained either by a change in the arrangement of CO_2 molecules in the monoclinic form, or as seems more likely from preliminary modelling, a change in the symmetry to orthorhombic, with larger cell volume, that could accommodate more molecules. A similar effect has been observed for ZIF-8 in the uptake of N_2, where the imidazolate groups rotate to give a new structure that allows greater uptake. Modelling and experimental studies are ongoing to resolve the cause of this observed effect.

5.4.5 Breakthrough curves and Column testing on Sc_2BDC_3

The small pore, hydrophobic Sc_2BDC_3 is thought to be a suitable candidate for gas separation experiments. To measure the selectivity and understand the properties of Sc_2BDC_3, breakthrough curves were used to measure the selectivity in the separation of CH_4 and CO_2. The data was collected at 30°C using a packed column of Sc_2BDC_3 powder. Experiments were performed in collaboration with Gerhard Pirngruber, IFP.

Breakthrough curves using pure CO_2 showed good reproducibility (Figure 5.24) and with the adsorbed quantity calculated to be 0.75(4) mmol g^{-1} at 1 bar and 30°C, slightly lower than the quantity expected from gravimetric adsorption under the same conditions (0.9 mmol g^{-1})[121]. This was likely due to a small amount of the non-porous Sc_2O_3 impurity present in the scaled-up syntheses. Based on the ratio of the quantities adsorbed at room temperature, the selectivity is calculated at 0.75/0.14 = 5.4. From the breakthrough curves, the quantities adsorbed under these conditions (using a 50:50 mix of CH_4 and CO_2), were 0.37 mmol g^{-1} and 0.00(1) mmol g^{-1} (Table 5.6). These values indicate a very high selectivity for CO_2 over CH_4 and considering that Sc_2BDC_3 was observed to preferentially adopt a monoclinic structure in response to CO_2 adsorption, it is thought that even as part of a mixture, the CO_2 adsorbs strongly causing this adjustment in the structure and prevents the uptake of CH_4. The Sc_2BDC_3 column showed evidence for displacement of adsorbed CH_4 to preferentially adsorb more CO_2 as evidenced by the roll-up effect observed in the CH_4 breakthrough (Figure 5.25).

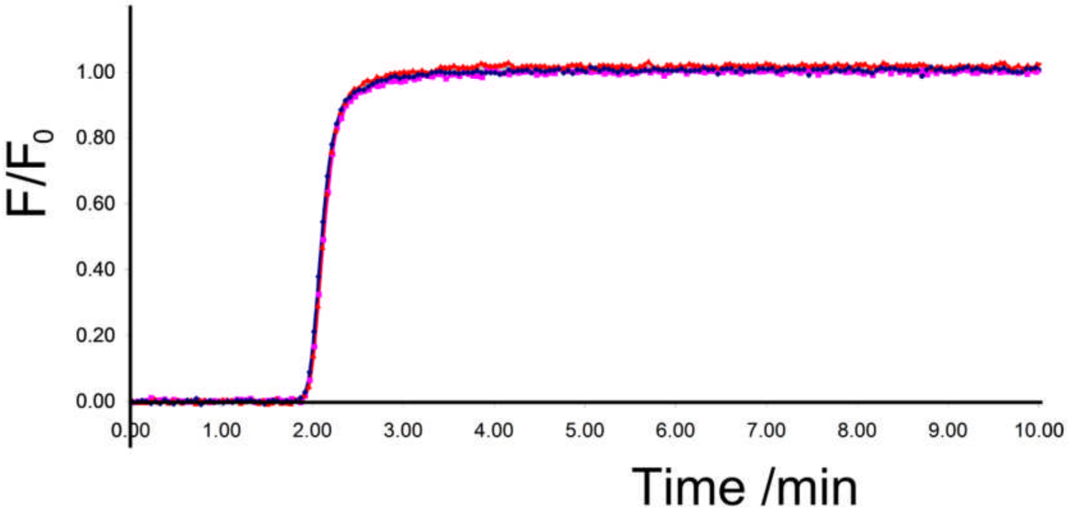

Figure 5.24: Breakthrough curves for CO_2 on a packed column of Sc_2BDC_3

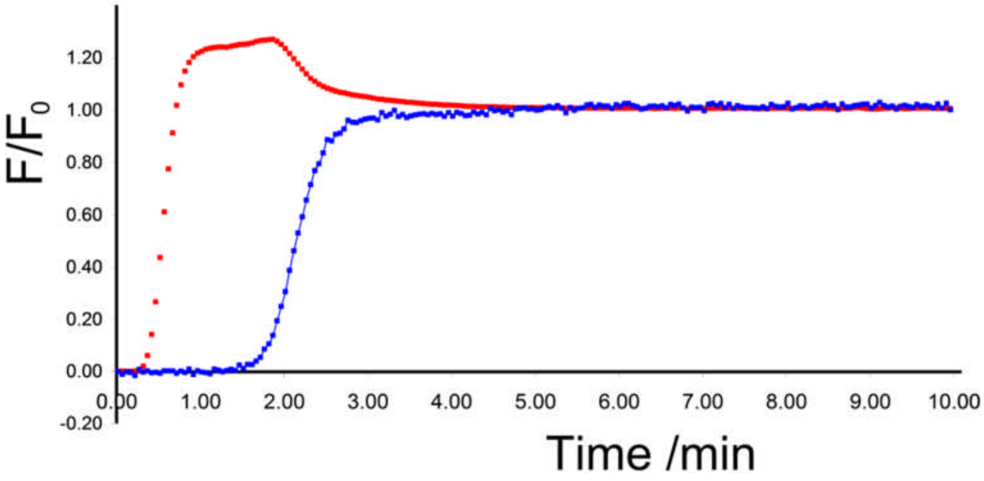

Figure 5.25: Breakthrough curves for a 50:50 binary mixture of CH_4 and CO_2 on a packed column of Sc_2BDC_3

Gas mixture	p CO_2 (bar)	p CH_4 (bar)	q_{ads} CO_2 (mmol g^{-1})	q_{ads} CH_4 (mmol g^{-1})
CO_2	1.05		0.75*	-
CH_4		1.05	-	0.14*
CO_2/CH_4	0.53	0.53	0.37‡	0.00(1)‡

Table 5.6: Adsorbed quantities for CO_2, CH_4 and a 50:50 binary mixture of CH_4 and CO_2. *Calculated from adsorption. ‡Calculated from breakthrough curves.

To test the Sc_2BDC_3 as a possible stationary phase for gas chromatography, a packed column of Sc_2BDC_3 was prepared using ~5 g of product in a U-shaped column with an internal diameter of 5mm (Figure 5.26).

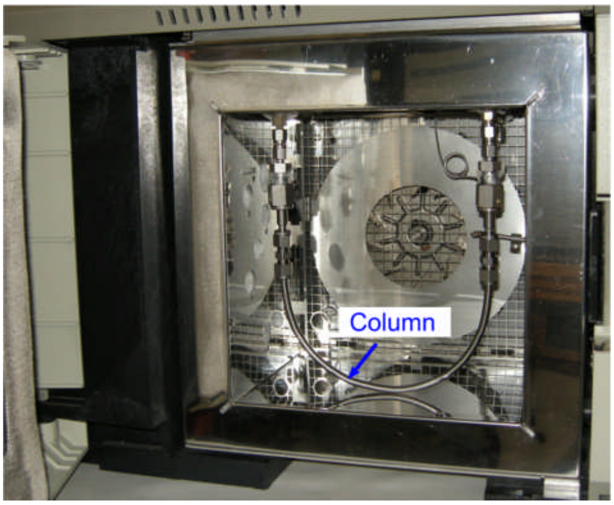

Figure 5.26: GC oven containing the packed column of Sc_2BDC_3

The column was tested using range of different C_6 and C_7 hydrocarbon mixtures and individual components separately to measure the retention times. Results showed that the Sc_2BDC_3 column could separate the components based on the shape of the molecules rather than the boiling points (Figure 5.27).

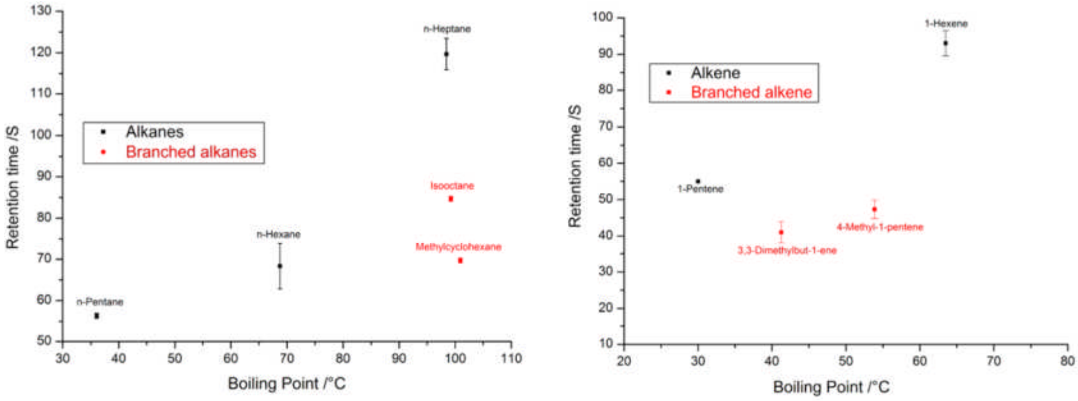

Figure 5.27: Plots of retention time against boiling point for a series of branched and straight chain hydrocarbons. The retention times are an average of 5 runs on the individual components

The retention times were taken as the peak maxima from the individual components injected onto the column. Although the retention times suggested that the column was performing well, there was significant tailing in the GC trace that meant there was rarely full baseline separations when mixtures were used and the last components to elute were extremely broad. An example of two GC traces from mixed component runs are shown in Figure 5.28.

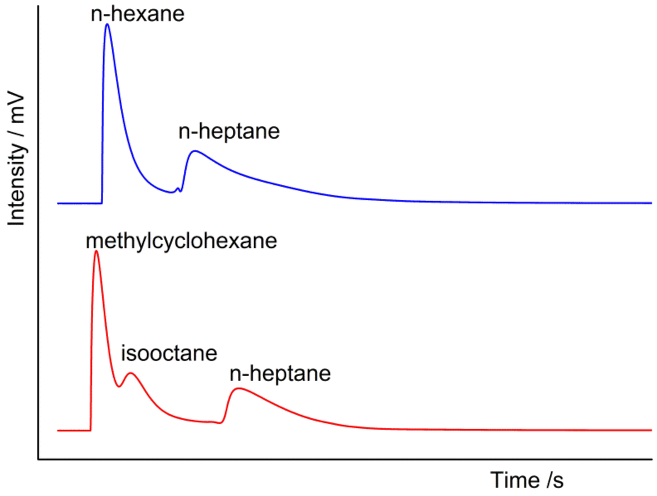

Figure 5.28: GC traces from a C7 and a linear alkane mixture injected onto the Sc_2BDC_3 column

The reason for the poor peak shape in the Sc_2BDC_3 column is thought to be the range of particle size typical for a large scale synthesis of Sc_2BDC_3. The average sample ranges from 2 – 100 µm particles which likely cause diffusional problems in the packed column. Attempts to prepare a PLOT column via the same route as STA-12(Ni), were also unsuccessful due to the particle size. Sc_2BDC_3 is a promising candidate for use in gas chromatography, however, further testing is required to optimise the synthesis for a monodisperse product, comprised of small particles.

5.5 Summary

The 2-amino- and 2-nitroterephthalate forms of the scandium terephthalate MOF, Sc_2BDC_3 have been synthesised for the first time by means of hydrothermal synthesis, using Sc_2O_3 (or $Sc(NO_3)_3$ for $Sc_2(NO_2\text{-}BDC)_3$) as the scandium source. The crystal structure of these and the unmodified Sc_2BDC_3 have been measured by Rietveld refinement against X-ray powder diffraction data at 100 K. Whereas Sc_2BDC_3 and the -NO_2 forms adopt monoclinic *C*2/*c* symmetry at this temperature, the amino form has orthorhombic *Fddd* symmetry. Strong partial ordering effects are observed in the location of functional groups: in the orthorhombic -NH_2 form the groups are ordered over one of two sites on one linker, and disordered over C atoms on the second linker, whereas in the monoclinic -NO_2 form the groups are ordered over one in two possible carbons on each of the crystallographically-distinct terephthalate groups. Statistical disorder over symmetrically equivalent C atoms remains, although within rows of at least some of the terephthalate groups it is likely for steric reasons that the functional groups will take up the same orientation in adjacent linkers.

As the temperature of Sc_2BDC_3 is raised, it undergoes a phase transition to orthorhombic at 200 K, characterised by synchrotron X-ray diffraction on a powder sample. The orthorhombic form demonstrates negative thermal expansivity over the range 200 – 533 K, which can be attributed to libration and translation of the aromatic rings. In addition, at least one of two crystallographically distinct phenyl groups shows π flips as shown by ^2H wideline NMR spectroscopy over the measured temperature range 333 – 383 K. Upon raising the temperature from 100 K to 293 K, the -NH_2 form remains orthorhombic and the NO_2-form remains monoclinic even if the temperature is raised to 473 K. That the -NH_2 form remains orthorhombic is attributed to stabilisation via interaction of the amine group H atom with a carboxylate oxygen, whereas the steric effect of the -NO_2 group acts to prevent the monoclinic structure becoming orthorhombic at room temperature or above. The structural changes that are observed in this series of compounds therefore demonstrate the flexibility possible even in MOFs that do not exhibit the extreme breathing effects shown by MIL-53 or MIL-88. This flexibility arises from the rotation of carboxylate groups with respect to the aromatic rings of the terephthalate linkers and the hinge-like motion of the carboxylate groups where they are coordinated to the metal cations.

The CO_2 adsorption behaviour of Sc_2BDC_3, reported previously, can be interpreted in terms of favoured uptake of CO_2 by the monoclinic rather than the orthorhombic form, at least for uptakes less than *ca*. 4 mmol g^{-1}. Molecular modelling indicates ordering in the monoclinic form (as observed experimentally) whereas CO_2 would not occupy such well-defined sites in the orthorhombic structure. The CO_2 adsorption on Sc_2BDC_3 is strongly affected by functionalization. Amino groups reduce the adsorption capacity but increase the uptake at low pressures, due to stronger interactions with the CO_2. Remarkably, while -NO_2 groups reduce CO_2 uptake, as expected from their steric bulk and the reduction in cell volume that results from the change in symmetry to monoclinic that their inclusion induces, they do not block off the porosity as might be expected from the crystal structure. It is likely that that the -NO_2 groups can rotate and the framework structure adjusts to enable CO_2 molecules to diffuse through the channels and gain access to the cage-like porosity located between the O atoms of the -NO_2 groups that project into the channels.

Although at first glance a relatively simple and rigid structure, close examination of Sc_2BDC_3 and its functionalised analogues reveals a wealth of structural adaptation is possible, with flexibility and re-orientation mechanisms that operate over a range of different temperatures and timescales and which have important consequences for determining its adsorption behaviour. A scheme summarising the structural response to adsorption and functionalization is shown in Figure 5.29.

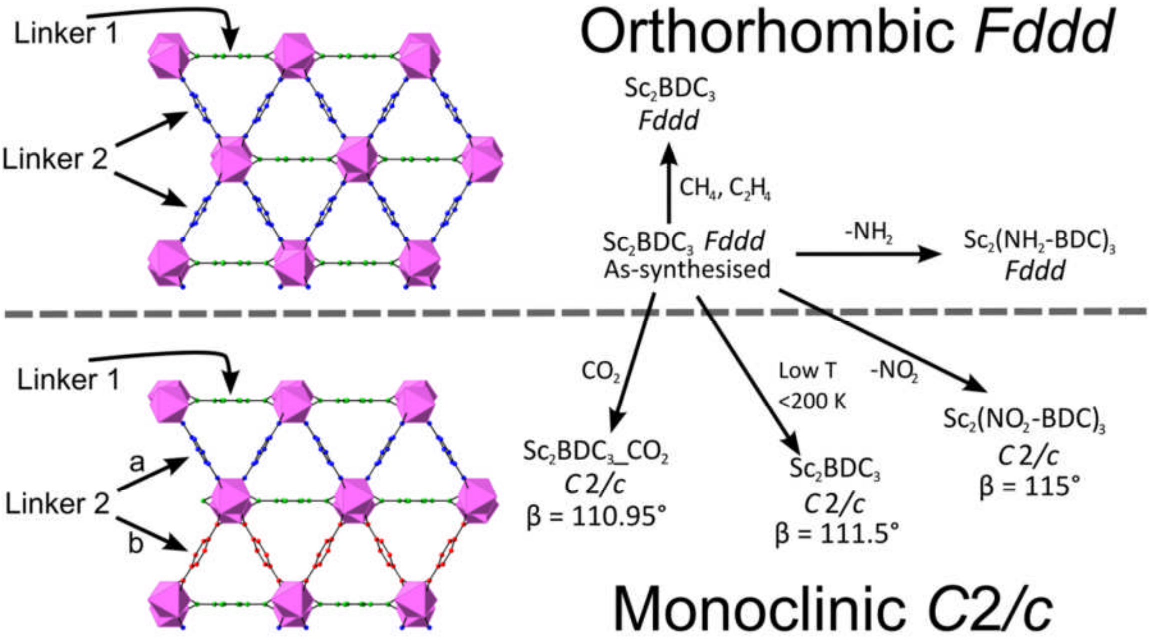

Figure 5.29: Scheme summarising the structural response of Sc_2BDC_3. Scandium octahedra are shown in pink. Coloured spheres represent the different crystallographic environments for the organic linker.

The amino-terephthalate, $Sc_2(NH_2\text{-}BDC)_3$, was found to be orthorhombic (*Fddd*) symmetry at both 100 K and 298 K. The structure, as shown in Figure 5.10, shows the positions of the amino groups located by a combination of geometric positioning, difference Fourier and occupancy refinement using Rietveld refinement. On the Group 1 terephthalate, perpendicular to the scandium carboxylate chains, the symmetry dictates that there is only one crystallographic site that the $-NH_2$ group can occupy and it is therefore disordered over the four symmetry related positions. The Group 2 terephthalates, however, are positioned at an angle (69.4°) to the chain (c-axis) and in this case there are two distinct sites the $-NH_2$ group can occupy. As a result of the tilt, there are two pairs of crystallographic positions for the $-NH_2$ group, one of which is too close to the carboxylate oxygen of the adjacent metal octahedra (N---O = 2.70Å) and is found to be unoccupied. The $-NH_2$ is therefore found to be statistically disorder over the remaining pairs of less sterically hindered sites. Considering the flipping motion of phenyl rings observed in the pure terephthalate Sc_2BDC_3, it is thought that a 180° flip in the phenyl ring (of the Group 2 terephthalate) in $Sc_2(NH_2\text{-}BDC)_3$ would be highly unfavourable as it would result in the $-NH_2$ group flipping to the sterically hindered unoccupied site.

Powder diffraction data at room temperature was also indexed as orthorhombic *Fddd.* Notable, there is no symmetry change to monoclinic observed for $Sc_2(NH_2\text{-}BDC)_3$, indicating that the $–NH_2$ group is involved in stabilising the structure in the orthorhombic symmetry. This is believed to be due to the favourable interaction between the $–NH_2$ group H-atoms and carboxylate group O-atoms in the orthorhombic structure. It is not believed to be a steric effect that causes the $-NH_2$ functionalised Sc_2BDC_3 to favour the orthorhombic symmetry as the larger $–NO_2$ group adopts only the monoclinic symmetry.

In contrast to $Sc_2(NH_2\text{-}BDC)_3$, the nitro-functionalised $Sc_2(NO_2\text{-}BDC)_3$ structure was indexed as monoclinic at low temperature (100 K), room temperature (293 K) and upon heating (473 K). The high temperature diffraction data shows the monoclinic symmetry is still observed at 473 K suggesting that the material crystallises directly in the monoclinic symmetry (463 K synthesis temperature). Structure solution from synchrotron powder and single crystal diffraction show a degree of ordering of nitro groups on the Group 1, 2a and 2b linkers (Figure 5.12). As observed in molecular crystal structures where a nitro and a carboxylate group are present, on adjacent carbons of a phenyl ring, the nitro group is rotated ~90° from the plane of the ring.[122,123] This is a result of the steric interactions between the $–NO_2$ O-atoms and the O-atoms of nearby carboxylate groups.

Due to steric constraints arising from the bulky $-NO_2$ group, the monoclinic symmetry is observed over the temperature range studied (100 K to 473 K). The reason the monoclinic structure is favoured for $Sc_2(NO_2\text{-}BDC)_3$ is because the Group 1 terephthalate can tilt away from the scandium carboxylate chains, measured to be an angle of (96.12°) meaning that the nitro group oxygen atoms are further from the nearest carboxylate oxygens along the chain. This subtle tilt, accompanied by a translation of the scandium carboxylate chains leading to two crystallographic scandium sites, allows for a nitro – carboxylate oxygen – oxygen distance of 3.12 Å, compared with 2.8 Å if it were perpendicular to the chains, as observed in the orthorhombic form. At room temperature and above, where the pure terephthalate Sc_2BDC_3 is observed in the orthorhombic symmetry, the steric bulk of the $–NO_2$ group prevents $Sc_2(NO_2\text{-}BDC)_3$ from going orthorhombic favouring the lower symmetry monoclinic form. To measure and compare these distances and angles, measurements were taken from the single crystal structural data for $Sc_2(NO_2\text{-}BDC)_3$ and compared to a hypothetical orthorhombic model where a $–NO_2$ group was geometrically positioned (with the same geometry to the ring as the $Sc_2(NO_2\text{-}BDC)_3$ crystal structure) to measure the theoretical nitro – carboxylate oxygen – oxygen distance of 2.8 Å. Along each chain of Group 1, 2a and 2b linkers in $Sc_2(NO_2\text{-}BDC)_{3,}$ the close oxygen – oxygen distances, on the occupied pairs of crystallographic sites, indicate there is likely to be further ordering in each individual chain. There is no evidence from the powder or single crystal diffraction of a larger unit cell or further reduction in symmetry suggesting that over the bulk structure, the $–NO_2$ groups on each linker are evenly distributed over the two symmetry related sites represented by one crystallographic position, but each chain (or even the complete layer for the Group 2a and 2b linkers) may show ordering.

The rotated geometry of the $-NO_2$ groups, with respect to the phenyl rings, means that the narrow pore space is further constricted by oxygen atoms projecting into the channels. The $–NO_2$ groups also leads to a more segmented series of cavities rather than a channel. The free diameters of the restricted channel openings are 1.95 and 2.40 Å although there are larger cavities between the bottlenecks, the shape of which would depend on the location of $-NO_2$ groups disordered over symmetrically equivalent sites on the phenyl groups.

The extent to which the $Sc_2(NO_2\text{-}BDC)_3$ deviates from the orthorhombic at 100 K (i.e. the monoclinicity), which can be measured by the degree of tilt in the group 1 terephthalate (from 90° in the orthorhombic structure), is larger in $Sc_2(NO_2\text{-}BDC)_3$ (83.9°) than the pure terephthalate monoclinic Sc_2BDC_3 (86.2°), indicating a significant steric effect resulting from the inclusion of the $-NO_2$ group. This results in a reduction of the unit cell volume from 3122 to 3076 $Å^3$, a decrease of 1.5%, despite the inclusion of the bulky $-NO_2$ group.

In conclusion, powder X-ray diffraction of the parent Sc_2BDC_3 indicates that at between 200 and 225 K the structure distorts from orthorhombic to monoclinic, the mechanism of which is a concerted rotation of carboxylate groups. This phase transition is prevented in $Sc_2(NH_2\text{-}BDC)_3$ by the interactions between the $-NH_2$ group and adjacent carboxylate O atoms, but in $Sc_2(NO_2\text{-}BDC)_3$ the presence of bulky nitro groups stops the framework adopting the orthorhombic structure even at 473 K, and strong partial ordering of nitro groups is observed over all terephthalate linkers. Comparison of different monoclinic variants show the scandium terephthalate framework is itself flexible, and varies with temperature and the nature of substituents.

6 Synthesis, Characterisation and Functionalisation of MIL-53(Sc)

6.1 Introduction to MIL-53

The trivalent metal terephthalate MIL-53, with the chemical formula MOH(BDC) (M = Al, Cr, Fe, Ga, In), is one of the most studied metal-organic frameworks.[29,63,113,124-128] The response of this highly flexible framework to changes in temperature, gas adsorption and solvent exchange has been studied both experimentally and computationally to understand and predict the behavior of this and other flexible MOF materials.[63,127-131] The structural transitions observed for the MIL-53(M) family are reversible on subsequent heating cooling cycles and the nature of the breathing behaviour is sensitive to the metal involved in the framework.[127,128,132] MIL-53(Al) is currently one of the few metal-organic framework materials that is available to purchase from chemical suppliers, it is produced by BASF and sold under the name Basolite® A100.

Initial synthetic studies on the chromium and aluminium terephthalate system yielded the structure for MIL-53(Cr) in the as-synthesised (MIL-53as), the open (MIL-53ht) and the hydrated (MIL-53lt) form.[29] The structure was solved from powder X-ray diffraction data on the aluminium analogue, synthesised at a similar time, using direct methods in the Expo software. The atomic positions from this structure solution were taken as a starting model and refined against the diffraction data for the chromium material. In the as-synthesised state, MIL-53(Cr)as, the channels in the structure are filled with unreacted terephthalic acid guest molecules from the synthesis.[29] Calcination of the MIL-53(Cr)as at 573 K under air atmosphere results in removal of the free terephthalic acid molecules in the channels which, upon cooling to room temperature, adsorbs water to give MIL-53lt. In-situ diffraction experiments on the MIL-53(Cr) show that upon heating, the structure loses the adsorbed water to give the open from of the framework MIL-53(Cr)ht at around 523 K. The open and hydrated forms of the MIL-53(Cr) are often referred to in the literature as the large pore (-*lp*) and narrow pore (-*np*) forms respectively, referring to the accessible pore cavity in the individual structures (Figure 6.1).

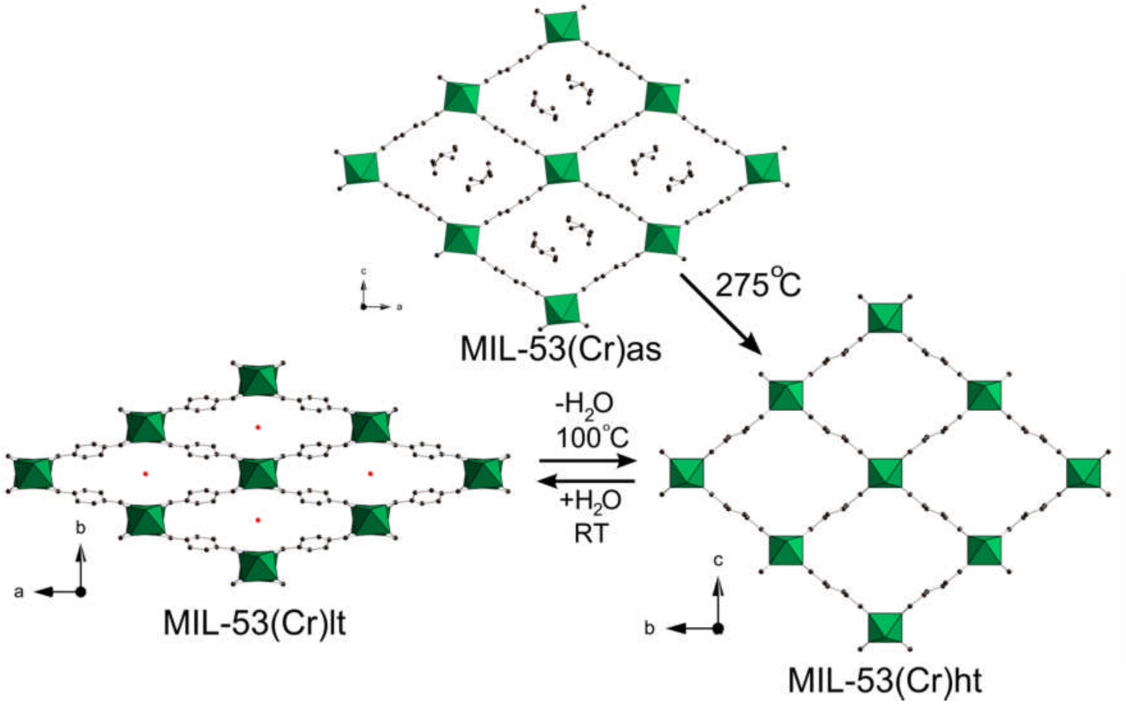

Figure 6.1: Chromium terephthalate MIL-53(Cr) in the as-synthesised (*top*), hydrated (*bottom left*) and the fully open state (*bottom right*). Chromium octahedra are shown in green. Black spheres represent the carbon atoms of the organic linker.

Studies on the aluminium analogue of MIL-53, probing the hydration and dehydration behavior with solid-state NMR and in-situ powder X-ray diffraction gave a rationale for the observed flexibility.[63] They proposed that the bridging hydroxyl groups along the chains in the structure were involved in a hydrogen bonding network with the adsorbed water molecules. This favourable interaction is thought to stabilize the narrow pore MIL-53(Cr)lt form which is reversible upon removal of the adsorbed water (by heating) to obtain the large pore form MIL-53(Cr)ht.

Adsorption studies on the aluminium and chromium analogues of MIL-53 showed that a structural response in the material could be induced by a suitable pressure of carbon dioxide.[126] The CO_2 adsorption isotherms measured at 304 K display a significant step (at 6 bar) from an initial adsorption of ~3 mmol g^{-1} to around 8 mmol g^{-1}. As the sample is activated by heating to 373 K, the sample is in the dehydrated (large pore) state prior to the adsorption experiment. Upon adsorption of the quadrupolar CO_2 molecule at the lowest pressure point, it was proposed that the interactions between the gas and the framework resulted in the shrinkage of the framework to the narrow pore form which is present up to the step at ~6 bar.[126] Above the threshold pressure, the framework is thought to open to the large pore form allowing for total pore filling (Figure 6.2). The adsorption of methane was studied in parallel and the non-polar methane does not have the same influence on the structure with a classic type I isotherm (Figure 6.2). It was assumed that as the metal is fully coordinated by oxygen in an octahedral geometry, the metal sites would not contribute strongly to the adsorption behaviour.[126]

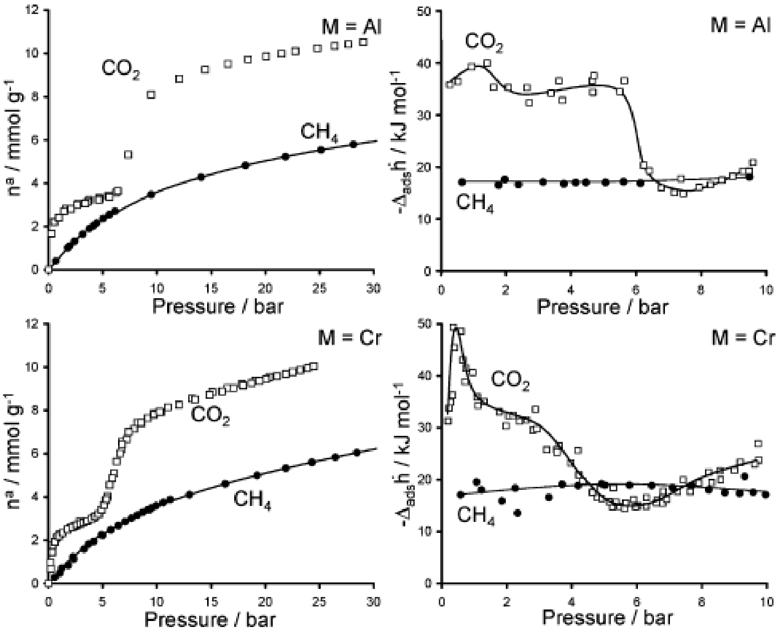

Figure 6.2: MIL-53(Cr) carbon dioxide and methane adsorption isotherms (*left*) and differential enthalpies (*right*) for MIL-53(Al) (*top*) and MIL-53(Cr) (*bottom*)[126]

Comparison of the adsorption isotherms with MIL-47(V) (same network topology with μ_2-O^{2-} ions rather than the hydroxyl groups on the chains see Chapter 1), which does not display the flexibility observed for MIL-53, suggests that in MIL-53 the CO_2 molecules initially sorb to the hydroxyl groups on the chains until filling of the narrow pore form occurs. At the higher pressures (>6 bar), the framework opens to the maximum pore capacity with a different adsorption mechanism with a noticeably lower measured enthalpy of adsorption.

To obtain further evidence for this hypothesis, in-situ powder X-ray diffraction data[129] was collected under various pressures of CO_2 at beamline MPW6.2 Daresbury, UK. The data supported the hypothesis that the activated structure was of the open channel type - MIL-53ht - which, at the low pressures of CO_2, closes to the MIL-53lt narrow pore form. Above ~2 bar (at 293 K), the diffraction shows evidence of a change to a different unit cell, indexed as that of the open MIL-53ht. Cycling this pressure change multiple times showed the change to be reversible and reproducible on subsequent adsorption and desorption cycles (Figure 6.3).

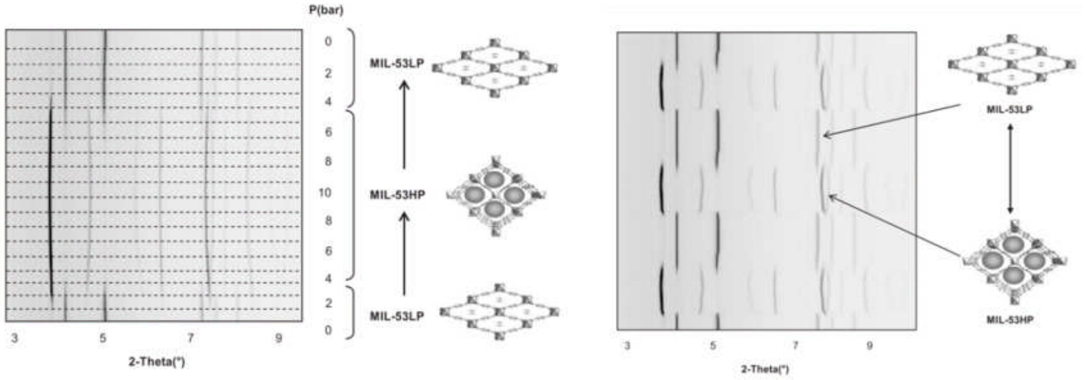

Figure 6.3: Powder X-ray diffraction patterns of MIL-53(Cr) under various pressures of CO_2 at 293 K[129]

Computational studies on the MIL-47 and MIL-53 frameworks using density functional theory (DFT) calculations, with adsorbed CO_2 molecules introduced, add further support to the theory that the initial adsorption is a result of the interaction between the oxygen of the CO_2 and two μ_2-OH from the metal chains on opposite sides of the channels (Figure 6.4).[131] The calculations report an enthalpy of adsorption of between -41 kJ mol^{-1} and -45 kJ mol^{-1} for the CO_2 molecule between the two chains in the narrow pore structure. These values compared to between -16 kJ mol^{-1} and -18 kJ mol^{-1} for the interaction with one chain and the phenyl rings of the open channel where the chains are too far apart for the CO_2 molecule to interact strongly with both hydroxyl protons.

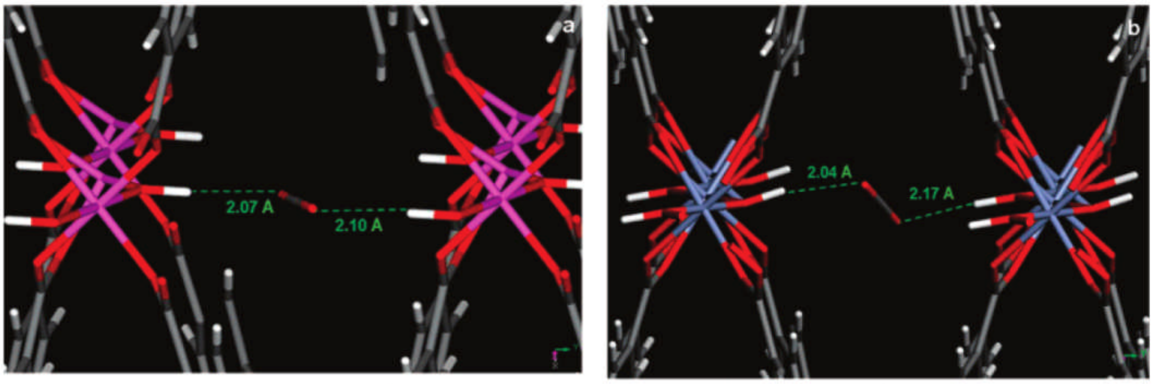

$\Delta H = -41\ kJ.mol^{-1}$ $\Delta H = -45\ kJ.mol^{-1}$

Figure 6.4: Calculated carbon dioxide positions in the MIL-53(Al) (*left*) and MIL-53(Cr) (*right*) structures

More recent synthetic studies on other trivalent metals have extended the range of structures with the MIL-53 framework to include indium,[125] gallium[128] and iron.[113]

MIL-53(In) was reported by Anokhina *et al.*[125] as a hybrid inorganic – organic vernier structure with hydrogen bonded chains of extra-framework terephthalic acid molecules present within the channels (Figure 6.5). Thermogravimetric analysis on the material indicated that the framework was not stable to removal of the terephthalic acid molecules and as such, the flexibility and structural response of the framework could not be studied.

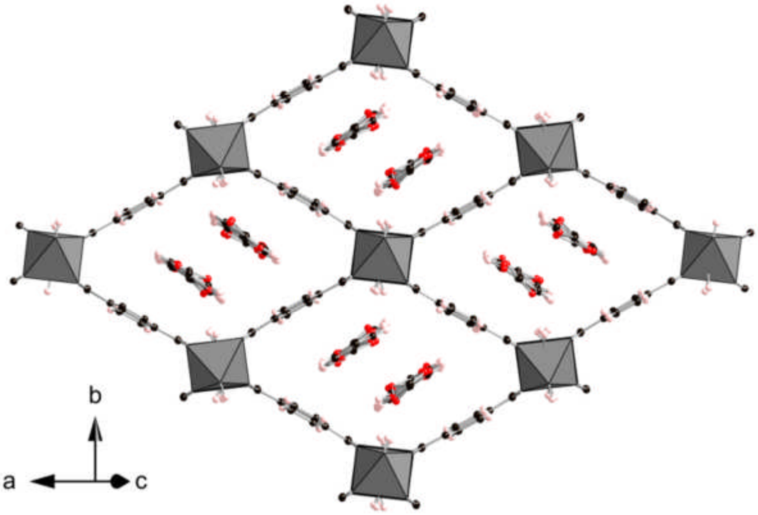

Figure 6.5: MIL-53(In) viewed down the channels. Indium octahedra are shown in grey. Black, red and pink spheres represent the carbon, oxygen and hydrogen atoms of the organic linker respectively.

MIL-53(Fe), reported by Whitfield *et al.,* was synthesised with pyridine molecules in the channels hydrogen bonded to the hydroxyl group on the inorganic chain (Figure 6.6).[113]

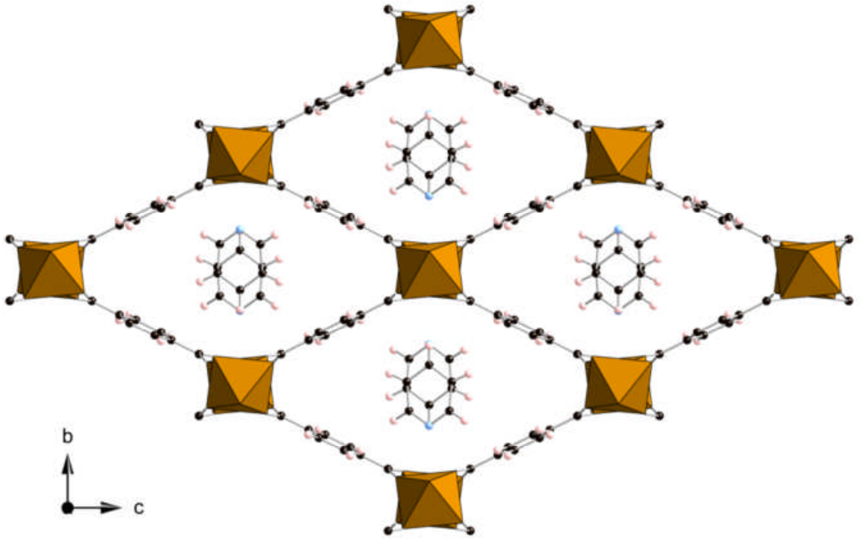

Figure 6.6: MIL-53(Fe) in an open configuration with ordered pyridine molecules present in the channels parallel to the a-axis. Iron octahedra are shown in orange. Black, blue and pink spheres represent the carbon, nitrogen and hydrogen atoms of the organic linker respectively.

The dehydration and structural flexibility of the MIL-53(Fe), subsequently reported by Millange *et al.*[127], shows a more complex evolution of the structure on heating than that observed in the chromium and aluminium case (Figure 6.7). The initial dehydration step results in a decrease in the unit cell volume to a triclinic unit cell with two types of channel present in the material. Upon further increase in temperature, the structure changes again to a high temperature phase with a smaller channel opening than the narrow pore hydrated MIL-53lt referred to in literature as the very narrow pore from or MIL-53-*vnp*.[127]

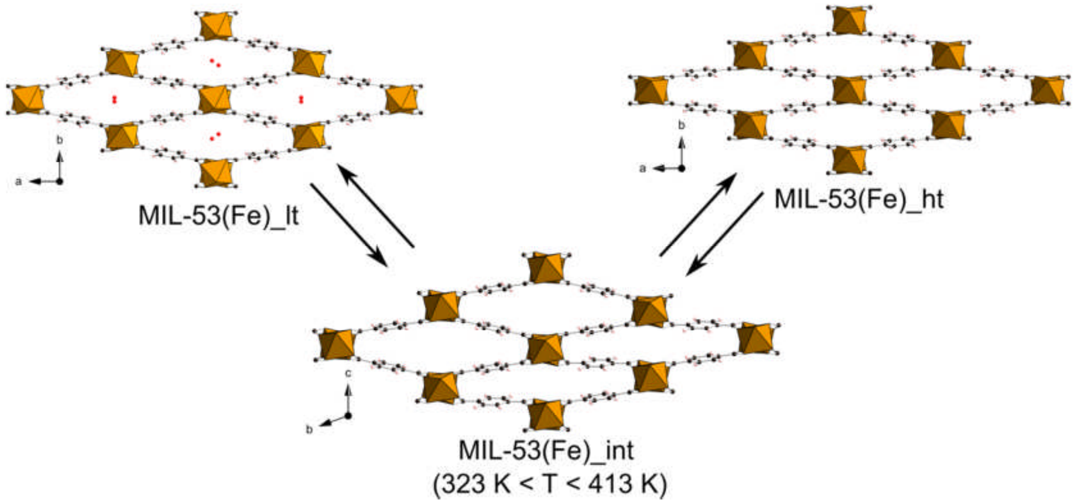

Figure 6.7: Structural evolution of MIL-53(Fe) from the hydrated (*left*) through the dehydrated structure at low temperature (*middle*) to the high temperature form (right). Iron octahedra are shown in orange. Black and red spheres represent the carbon and oxygen atoms of the organic linker respectively.

No rational was given for the markedly different dehydration behavior of the MIL-53(Fe), the ionic radii, electronegativity and bonding distances are similar between the MIL-53(Cr) and MIL-53(Fe) yet the response to the adsorption and desorption of water differs greatly.

The final MIL-53 derivative where the desolvation and structural flexibility has been studied in detail is the MIL-53(Ga) synthesised by Vougo-Zanda and co-workers[133] with the structural analysis reported by Volkringer et. al.[128] The structure of the hydrated MIL-53(Ga) is isostructural with that of the MIL-53-*lt* observed for iron, chromium and aluminium. Upon heating, the structure initially closes to the MIL-53-*vnp* structure observed at high temperature for MIL-53(Fe).[128] Above 473 K there is evidence for the structure progressively opening to the large pore MIL-53(Ga)-*lp*. A figure comparing the structural evolution of the aluminium, gallium and iron MIL-53 derivatives, reported with the structural analysis of MIL-53(Ga) is shown in Figure 6.8.[128]

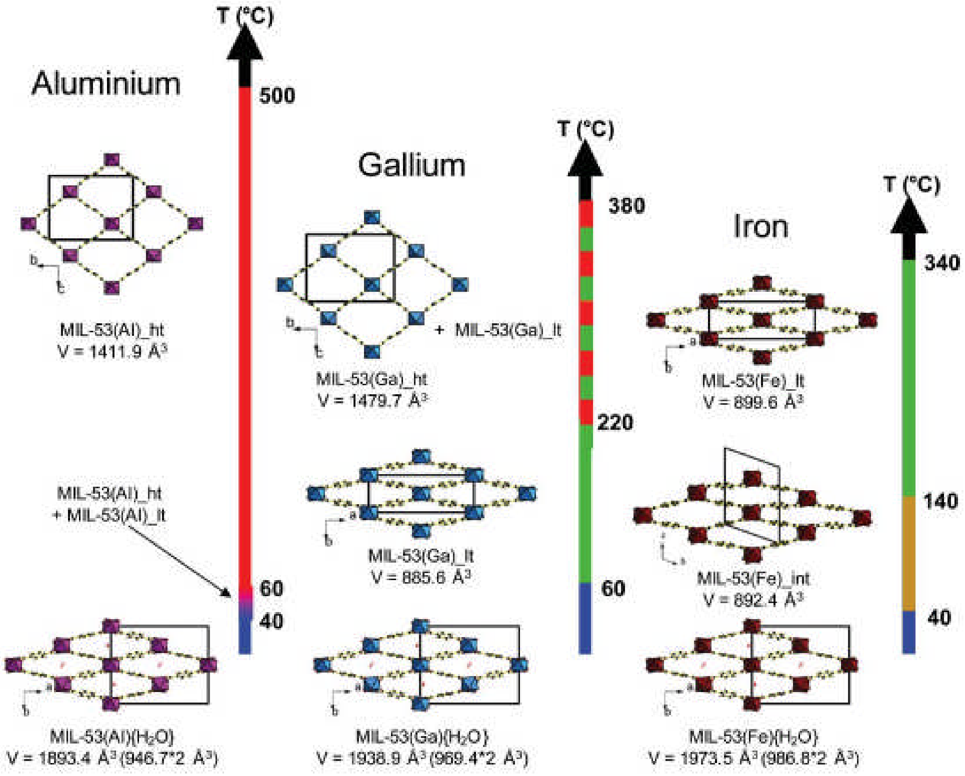

Figure 6.8: Comparison of the structural evolution, as a function of temperature, for MIL-53(Al), MIL-53(Ga) and MIL-53(Fe)

The difference in the dehydration response by subtle modification of the metal present in the MIL-53 series suggests it may be possible to control or tailor the properties of the material for practical applications in adsorption and separation.

The work presented in this chapter on the synthesis and characterisation of MIL-53(Sc) is reported in the RSC journal Dalton Transactions.[112] Details of the solid-state NMR characterization of MIL-53(Sc) including data and figures, carried out in collaboration with Dr. Sharon Ashbrook and co-workers, are reproduced by permission of The Royal Society of Chemistry. DOI: 10.1039/C1DT11729G

6.2 Structure Characterisation

Some preparations in this system crystallised as large, needle like, single crystals. When viewed under the microscope, the crystals visibly deformed and fractured upon drying. To prevent this undesirable loss of crystallinity, a selection of single crystals were kept under the mother-liquor of the reaction and transferred directly to a poly-fluorinated oil for mounting on the diffractometer. This coating helped to prevent the solvent loss and the data was sufficient to obtain a structural model in orthorhombic, $Pna2_1$ with unit cell: a = 19.344(2) Å, b = 9.1802(14) Å, c = 7.3013(11) Å, $\alpha = \beta = \gamma = 90°$. The structure is shown in Figure 6.9 with crystallographic details in Table 6.1.

	MIL-53(Sc)-DMF
Formula unit	Sc(OH)BDC·DMF
Formula weight	299.18
T	173 K
Space group	$Pna2_1$
X-ray source	Cu Kα radiation
wavelength(Å)	1.54178
Unit cell(Å)	a = 19.344(2)
	b = 9.1802(14)
	c = 7.3013(11)
Z	4
RI(all data)	0.0804
RI(I 2σI)	0.0556
max and min residual e^- density (e/Å^3)	0.425, -0.444

Table 6.1: Crystallographic data for MIL-53(Sc)-DMF solved from single crystal X-ray diffraction data .

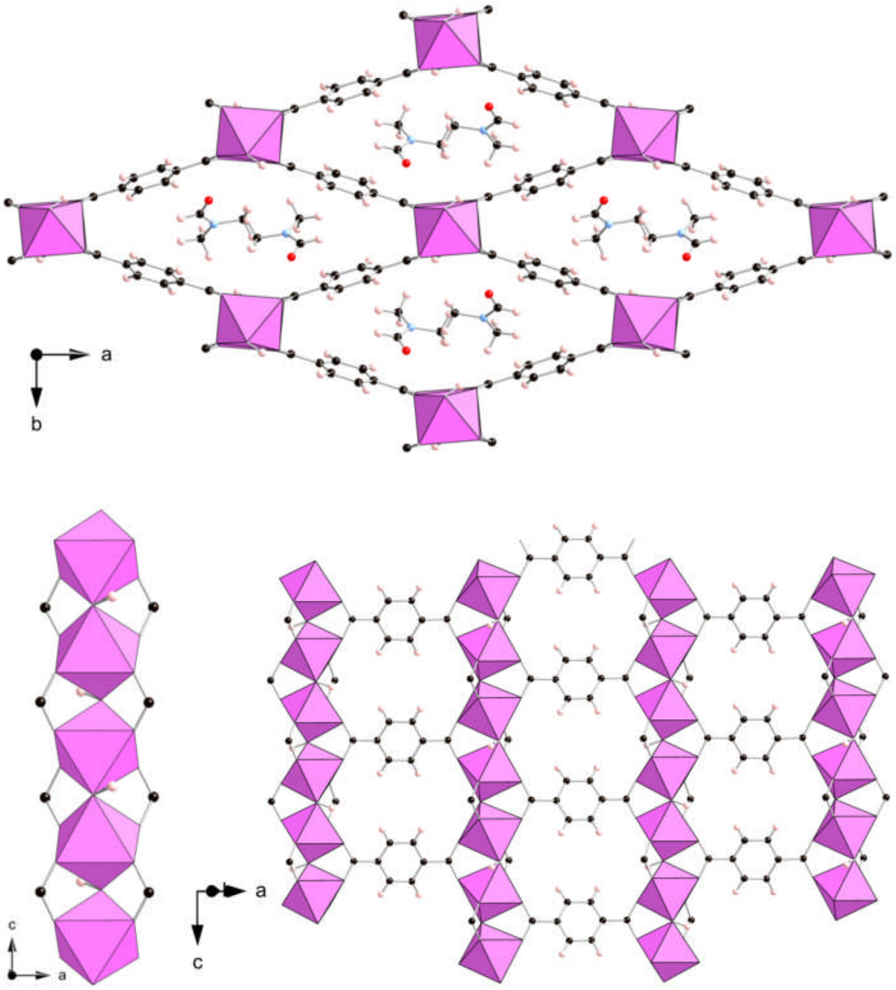

Figure 6.9: Structure of MIL-53(Sc)-DMF viewed down the channels parallel to the c-axis (*top*) a single corner sharing chain (bottom *left*) and the layers of terephthalates connecting the chains (*bottom right).* Scandium octahedra are shown in pink. Black and pink spheres represent the carbon and hydrogen atoms of the organic linker respectively.

The structure was solved from direct methods with hydrogen atoms positioned geometrically on the extra-framework DMF solvent molecule and the aromatic ring. The framework of MIL-53(DMF) is isostructural with that of the literature examples of the MIL-53(M) series discussed above. The framework is composed of infinite, corner sharing, $ScO_4(OH)_2$ chains with the bridging through the μ-2 hydroxyl groups. The coordination around the metal is filled by the 2 bridging hydroxyl groups and four oxygen atoms of four terephthalate groups, connecting each chain to 4 adjacent chains resulting in the diamond like channel arrangement. Although the framework connectivity is isostructural with MIL-53, this is the first example of ordered extra-framework DMF solvent molecules within the channels. Also of interest in the model is the position of the proton on the bridging hydroxyl group. Difference Fourier calculations on the model suggested a fixed position for the proton which was accepted and refined to give the final position. The position of the proton (Figure 6.10) indicates a hydrogen bonding arrangement with the carboxylate oxygen of the adjacent metal in the chain not, a similar position to that observed in the computational analysis of the 'empty' MIL-53(Fe) reported by Devic *et al.*[134]

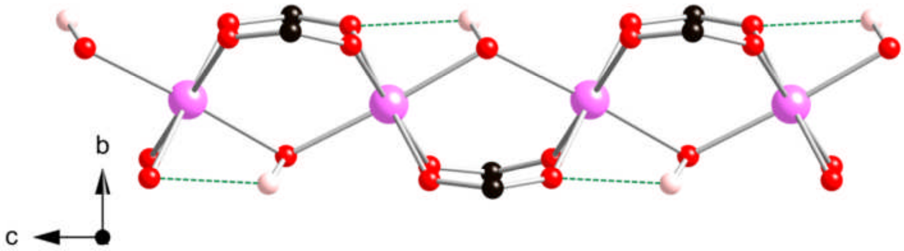

Figure 6.10: Scandium hydroxide chain in MIL-53(Sc)-DMF showing the close contact between hydroxide proton and carboxylate oxygen. Large pink spheres represent the scandium positions. Black, red and smaller pink spheres represent the carbon, oxygen and hydrogen atoms of the organic linker respectively.

Thermogravimetric analysis on MIL-53(Sc)-DMF shows a progressive weight loss of 10 % up to 673 K with complete decomposition of the framework to Sc_2O_3 at 723 K under flowing air. The decomposition temperature, like that observed for Sc_2BDC_3, is representative of the strong Sc-O bonds and is the highest in the MIL-53 system. Heating MIL-53 in a tube furnace to 623 K for 12 hours resulted in a desolvated material which TGA showed to have minimal weight loss up to the same decomposition temperature of 723 K (Figure 6.11). Powder X-ray diffraction on the material, post calcination, showed the material was still crystalline although with a markedly different diffraction to that observed for the MIL-53(Sc)-DMF.

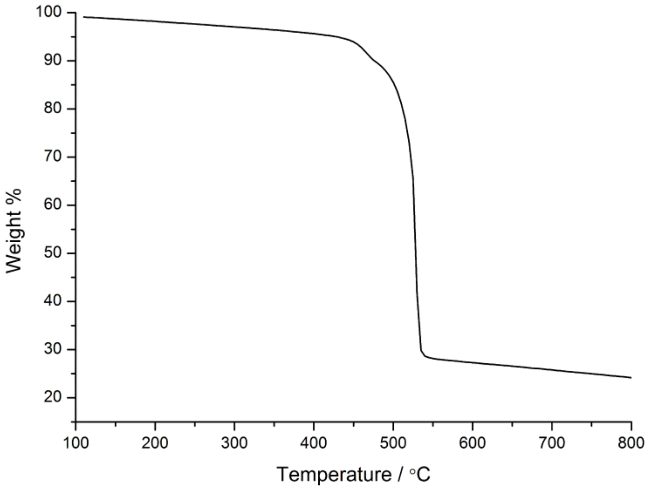

Figure 6.11: Thermogravimetric analysis on MIL-53(Sc)

To further understand the desolvation of MIL-53(Sc), a portion of sample (already heated to 623 K in a tube furnace) was ground lightly to prevent preferred orientation, transferred to a quartz capillary and heated to 625 K for 12 hours *in vacuo*. The dehydrated capillary was flame sealed and the X-ray diffraction data collected on the capillary in Debye-Scherrer geometry. To collect the re-hydrated diffraction pattern, the same capillary was broken open and left in a moisture rich environment for 72 hours to ensure full hydration and the pattern collected again. Comparison of the powder diffraction patterns of the materials (Figure 6.12), post filtration, showed that the samples washed thoroughly with ethanol showed more consistency in the observed product and were similar to the pattern observed for the fully hydrated material. Subsequent sample samples were treated first with thorough washing in ethanol and calcination in the tube furnace at 623 K prior to analysis.

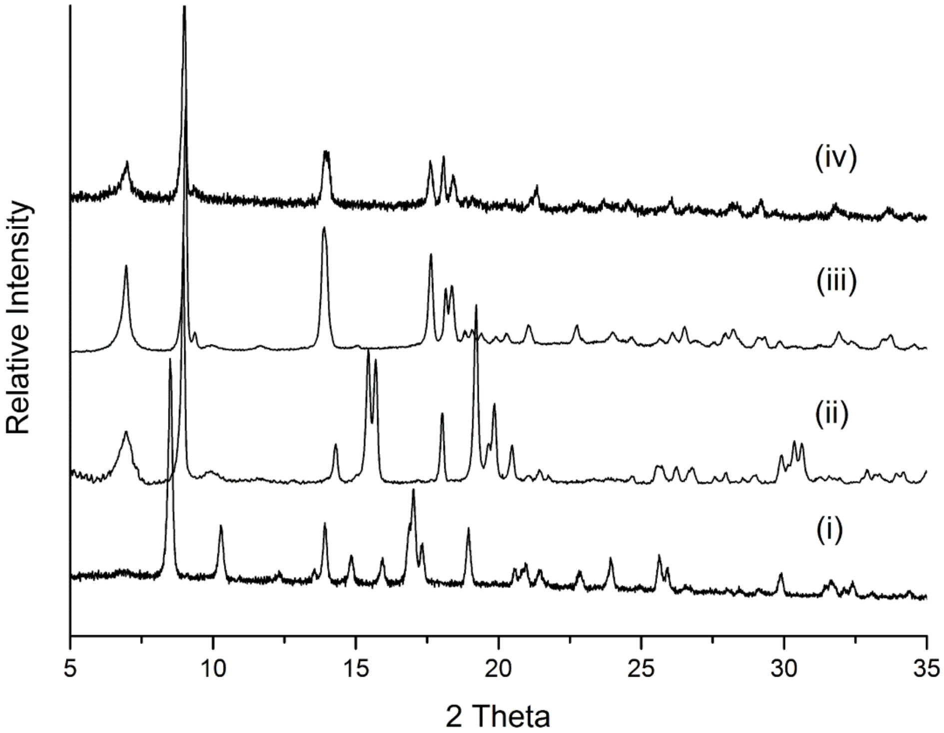

Figure 6.12: X-ray diffraction patterns for MIL-53(Sc) in the as-synthesised state (i), after calcination (ii), calcined and re-hydrated (iii) and ethanol washed, dried and allowed to re-hydrate (iv).

To identify the calcined and rehydrated phases denoted MIL-53(Sc)-CAL and MIL-53(Sc)-H_2O respectively, powder diffraction patterns were compared against the simulated diffraction patterns of the literature MIL-53 examples. The hydrated material (and the ethanol washed products) showed some agreement with the literature material MIL-53(Fe)-INT but indexing the patterns gave the unit cell parameters in *P*-1 of *a* = 7.27 Å, *b* = 13.45 Å, *c* = 20.68 Å, *α* = 71.57°, *β* = 84.21°, *γ* = 87.73° (compared to *P*-1, *a* = 6.887 Å, *b* = 10.558 Å, *c* = 13.466 Å, *α* = 109.9° , *β* = 88.06°, *γ* = 104.0°, for the MIL-53(Fe)). Initial attempts to produce a suitable starting model for Rietveld refinement were made using the atomic coordinates of the MIL-53(Fe)-INT but were unsuccessful. To get a suitable model for MIL-53(H_2O), single crystals of the as-prepared materials were first dried overnight at 323 K then for a further 12 hours at 623 K with a slow heating ramp to reduce the degradation of the crystals due to the loss of solvent. The crystals were cooled to room temperature and allowed to re-hydrate gradually in a moisture rich environment. The crystals were then checked under optical microscope and mounted on a glass fibre for the data collection. Despite the high residual values, (Rint = 0.4669) the data obtained was sufficient to attempt structure solution using the SHELX suite of programs. The structural model obtained was the triclinic model, (*P*-1, *a* = 7.260(6) Å, *b* = 13.071(9) Å, *c* = 20.583(13) Å, α = 72.54(4)° , β = 82.95(3)°, γ = 86.57(4)°, RI = 0.4650) which was used as the starting model in the Rietveld refinement of the powder diffraction data (Figure 6.13).

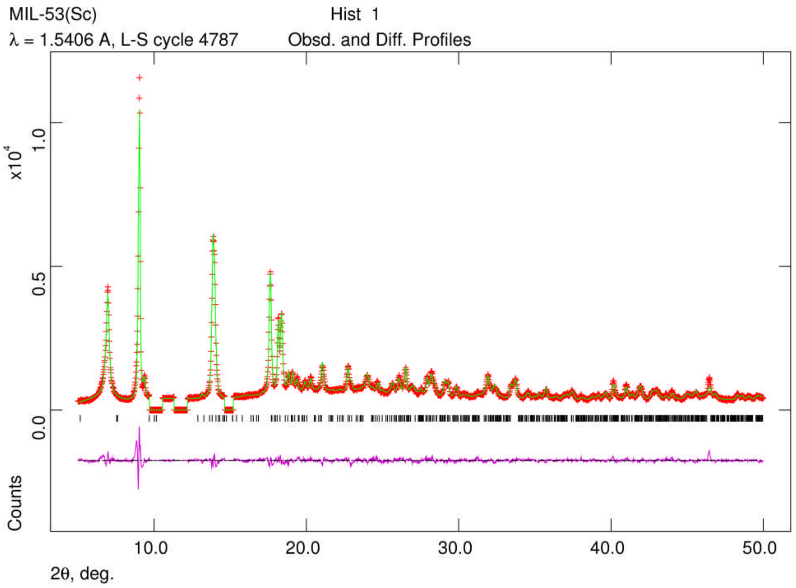

Figure 6.13: Rietveld profile fit for MIL-53(Sc)-H_2O. Excluded regions were determined to be trace amounts of an unknown impurity not present in all samples and were excluded from the refinement.

Distance restraints were applied to the starting model including direct bonding and through space restraints to maintain chemical sense in the framework while allowing for refinement of the atomic positions. Around the scandium site Sc-O bonds were restrained to 2.09(2) Å and O-O distances around the octahedral metal to 2.97(2) Å. Restraints in the terephthalate were fixed at, C-O, 1.27(2) Å, C-C (aromatic carbon) 1.37(2) Å, C-C (aromatic-carboxylate) 1.45(2) with cross-ring restraints of 2.78(4) to help maintain the planar geometry of the phenyl ring. Due to the low symmetry and large unit cell, there is a high number of unique atoms in the system with four scandium sites and six distinct terephthalate units. This resulted in a total of 169 distance restraints required to allow the framework atoms to move while preserving the chemically sensible bonding distances and angles (Figure 6.14).

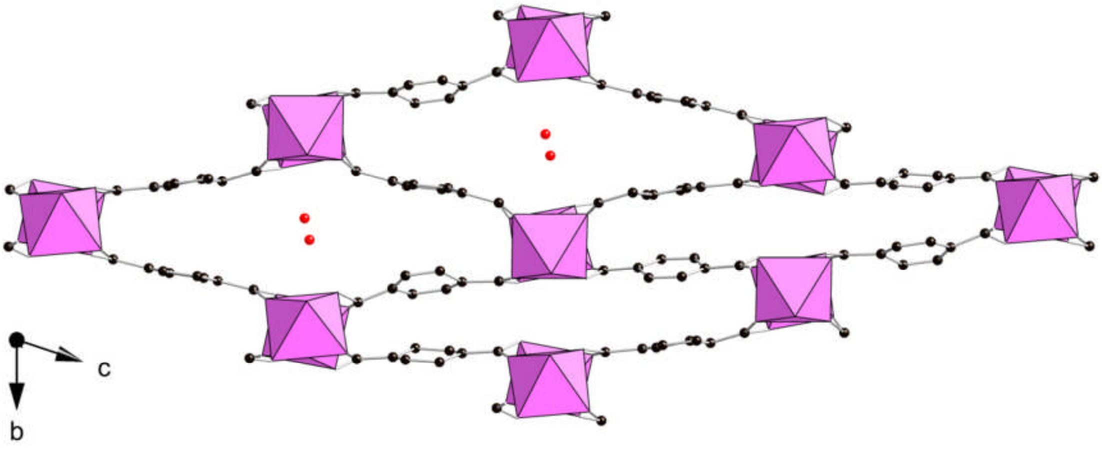

Figure 6.14: MIL-53(Sc)-H_2O viewed down the channel parallel to the a-axis. Scandium octahedra are shown in pink. Black and red spheres represent the carbon and oxygen atoms of the organic linker respectively.

To determine the structure of the fully desolvated structure after calcination MIL-53(Sc)-CAL, the unit cell was indexed from the powder diffraction pattern collected on the in-house diffractometer. Indexing gave a unit cell of a = 20.30 Å, b = 7.33 Å, c = 11.70 Å, β = 105.0°and together with Le Bail fit suggested suitable space groups to be *P*2, *P*2/*c*, $P2_1$ and $P2_1/c$. Using the literature model from the MIL-53(Fe)-*vnp* as a starting point, a model was constructed that was used to produce a starting model for Rietveld refinement. This model, although showing good agreement with the powder X-ray diffraction data (Rwp = ~7%), proved to have some problems with the bond distances and angles and was unstable when the atomic positions were allowed to refine. As the single crystals of MIL-53(Sc)-H_2O maintained crystallinity, to allow single crystal data collection on MIL-53(Sc)-H_2O, it was assumed that the calcined intermediate, MIL-53(Sc)-CAL, must also be crystalline. To prepare these crystals for the X-ray data collection, the crystals were first heated in a tube furnace for 12 hours then transferred to a dry Schlenk tube, evacuated and heated again to 473 K and the tube backfilled with dry N_2 gas. The crystals were subsequently treated as an air sensitive compound and directly coated in perfluorinated oil to avoid exposure to atmospheric water immediately prior to the single crystal data collection. This data also had high residual values (wRp = 0.387), likely due to loss of crystallinity on heating, but was again suitable to obtain a starting model for the Rietveld refinement (Figure

6.15).

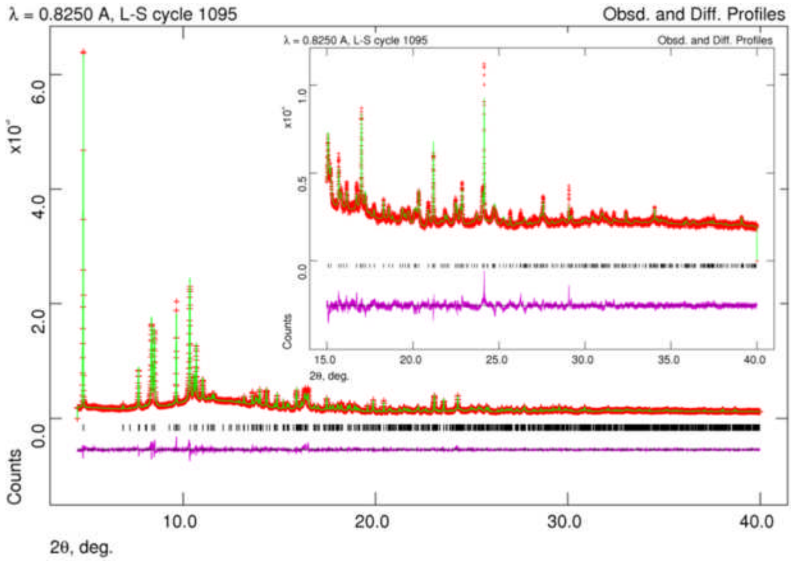

Figure 6.15: Rietveld profile fit for MIL-53(Sc)-CAL

The framework of MIL-53(Sc)-CAL (Figure 6.16) represents the narrowest channel cross-section reported to date for the family of MIL-53 materials, believed to be permitted by the larger radius scandium cation (radius 0.745 Å) compared to Al^{3+},Cr^{3+} or Fe^{3+}. What is particularly apparent, and the reason that the initial structural model adapted from MIL-53(Fe)-*vnp* was not suitable, is the large tilt (~18° from parallel to the c-direction) in the orientation of the plane through the metal hydroxide chains.

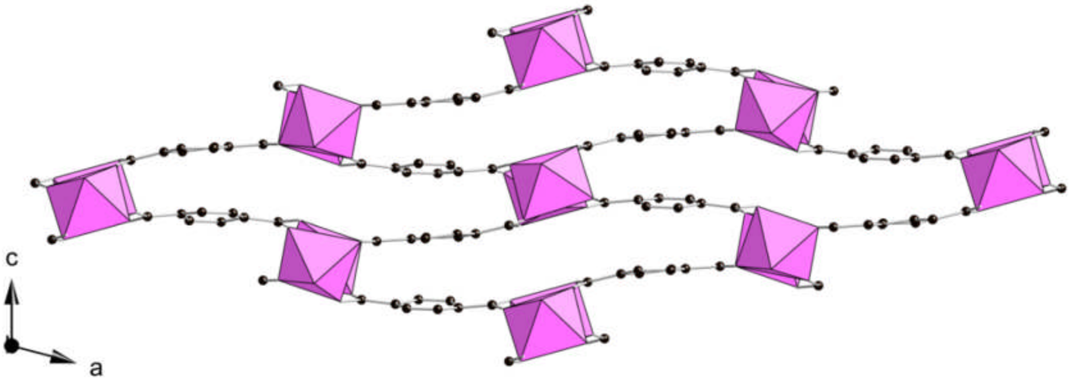

Figure 6.16: MIL-53(Sc)-CAL structure viewed down the channels parallel to the b-axis. Scandium coordination polyhedra are shown in pink, black spheres represent the carbon atoms of the organic linker.

6.2.1 Variable temperature studies

As discussed earlier, the MIL-53(M) family of materials is reported to demonstrate a high degree of flexibility both in response to guest molecules and as a function of temperature. To understand the temperature response of MIL-53, a sample of MIL-53(CAL) was prepared and activated as per the conditions in Chapter 4 and flame sealed in a quartz capillary *in vacuo*. X-ray diffraction data, collected at the high resolution X-ray powder diffraction beamline, I-11, of the Diamond Light Source, was used to look *in-situ* at the structural response to varying the temperature from 100 K through to 623 K (Figure 6.17).

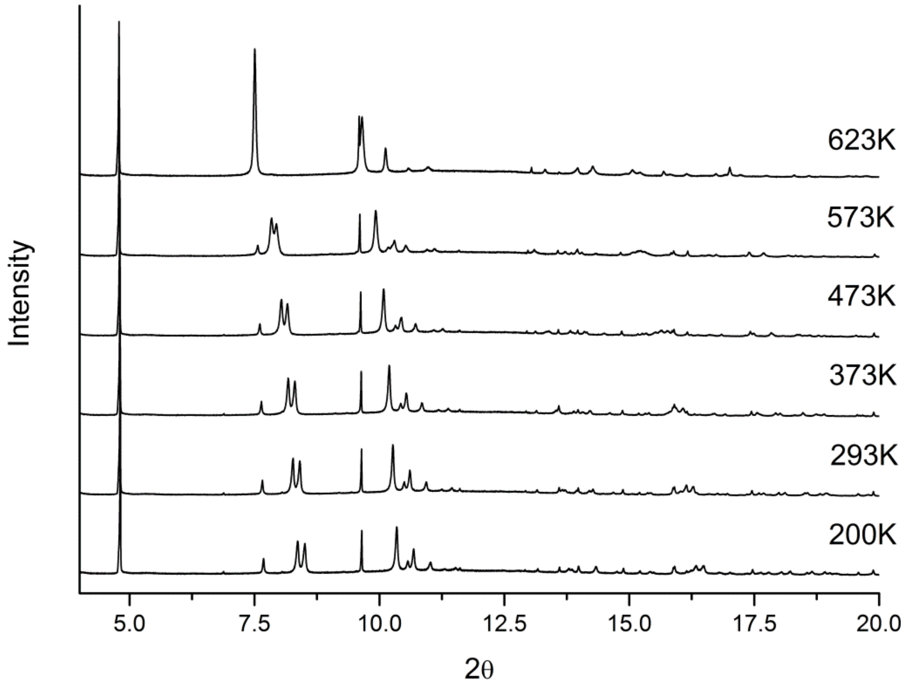

Figure 6.17: Temperature series of synchrotron X-ray powder diffraction patterns on a fully evacuated capillary of MIL-53(Sc)

For each pattern in the series, the data was collected from 0-140° 2θ by constant velocity scanning in Debye-Scherrer geometry using the multi-analyser crystal system available at beamline I11, the measured intensities were binned to a 2θ interval of 0.001°. The series shows a progressive change in the diffraction pattern in the range 100 K – 573 K indexed in the same $P2_1/c$ symmetry as the MIL-53(Sc)-CAL. Rietveld refinement on the 100 K pattern using the starting model of MIL-53(Sc)-CAL showed good agreement with only minimal refinement of the atomic positions required.

Rietveld refinement was also used to obtain a structural model for all the patterns in the series from 100 K through to the 573 K pattern, the crystallographic parameters of these structures are displayed in Table 6.2. The highest temperature pattern in the series, collected at 623 K, shows a clear change in the symmetry to a higher symmetry from. Indexing the pattern gave a monoclinic unit cell with a = 21.5 Å, b = 7.27 Å, c = 6.63 Å, β = 113.5°, from systematic absences the symmetry was determined to be $C2/c$, which on comparison with the literature MIL-53, showed excellent agreement with the literature MIL-53(Fe)-*vnp*. To verify this observation, the MIL-53(Fe)-*vnp* model was used as a starting point in the Rietveld refinement, resulting in the final Rwp of 5.38 %.

	100K	298 K	373K	473K	573K	623K
Formula Unit	$ScOH(C_8H_4O_4)$	$ScOH(C_8H_4O_4)$	$ScOH(C_8H_4O_4)$	$ScOH(C_8H_4O_4)$	$ScOH(C_8H_4O_4)$	$ScOH(C_8H_4O_4)$
Formula Weight	202.05	202.05	202.05	202.05	202.05	202.05
Temperature/K	100	293	373	473	573	623
Space Group	$P2_1/c$	$P2_1/c$	$P2_1/c$	$P2_1/c$	$P2_1/c$	$C2/c$
X-ray Source	Synchrotron	Synchrotron	Synchrotron	Synchrotron	Synchrotron	Synchrotron
Wavelength/Å	0.825028	0.825028	0.825028	0.825028	0.825028	0.825028
Unit Cell: a/Å	20.29839(17)	20.3297(2)	20.36637(2)	20.4289(2)	20.53821(3)	21.5050(3)
b/Å	7.33083(8)	7.32576(8)	7.3192(9)	7.3117(1)	7.2992(1)	7.2743(2)
c/Å	11.6912(1)	11.8382(2)	11.9856(2)	12.2158(2)	12.5604(3)	6.63(8)
β/°	104.9584(12)	105.2058(12)	105.4664(12)	105.8726(14)	106.5514(17)	113.5427(15)
Volume/ Å^3	1680.75(3)	1701.36(3)	1721.95(4)	1755.14(4)	1804.95(5)	950.838(3)
Z	4	4	4	4	4	2
R_p	0.0347	0.0347	0.0338	0.034	0.0315	0.0409
R_{wp}	0.047	0.0449	0.0435	0.0439	0.0413	0.0538
Restraints	35	42	41	41	42	28
Max and min e$^-$ density (e/Å^3)	0.393, -0.488	0.263, -0.229	0.273, -0.307	0.419, -0.322	0.244, -0.245	0.578, -0.366

Table 6.2: Crystallographic data for the variable temperature PXRD series

The observed trends in the unit cell parameters show a progressive 'opening' of the structure on heating from 100 K – 573 K. The mechanism by which the structure opens is as a result of the rotation of the chains from 18° to the *c*-axis in the 100 K to 10° to the *c*-axis in the 523 K model. The chains in the low temperature model, at an angle of +18° and -18° to the c-axis along the long cross-section, combined with the rigid terephthalates give the structure the appearance of an undulating array of channels.

As the chains rotate towards parallel to the axis, the channels become more diamond like in shape up to the symmetry change by 623 K to the more symmetrical channels of the MIL-53(HT) model (Figure 6.18).

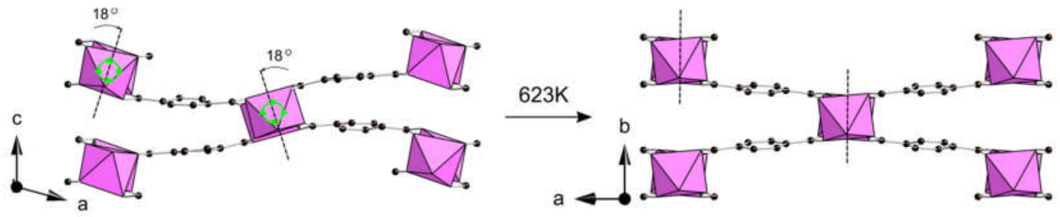

Figure 6.18: MIL-53(Sc)-CAL (*left*) and MIL-53(Sc)-HT (*right*). Chain rotation lead to an opening of the structure upon heating. Scandium coordination polyhedra are shown in pink, black spheres represent the carbon atoms of the organic linker.

The high resolution diffraction patterns were also collected on cooling the sample back down to room temperature, the data shows the symmetry change to be completely reversible with the same $P2_1/c$ symmetry and unit cells observed on the cooling (Figure 6.19).

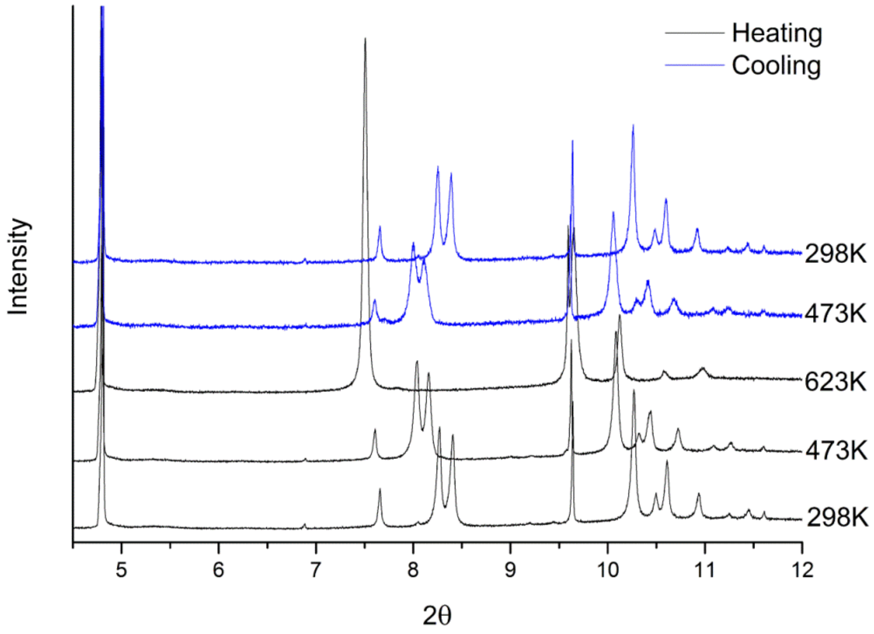

Figure 6.19: Reversibility of the MIL-53(Sc)-CAL ↔ MIL-53(Sc)-HT phase transition

6.2.2 Solid state NMR

To help support the proposed structural models for MIL-53 obtained from the diffraction data, solid-state NMR data was collected on both MIL-53(H_2O) and MIL-53(CAL) in collaboration with Dr Sharon Ashbrook and Valerie Seymour at St Andrews (Figure 6.20). The ^{45}Sc MAS NMR spectra on MIL-53(Sc)-CAL displayed a composite resonance due to the overlap of powder-pattern lineshapes with quadrupolar broadening. To help resolve the different scandium environments, 2D high-resolution multiple-quantum MQ-MAS spectra were measured at high field (20.0 T at the national facility in Warwick), where the high field strength helps to reduce the quadrupolar broadening. The 2D specta showed two clearly resolved ^{45}Sc sites with δ_1 values of 14.6 and 15.2 ppm with an intensity ratio of 1:1. This result for MIL-53(Sc)-CAL was in good agreement with that expected for the model of the dehydrated structure as there are two crystallographically unique scandium sites. The ^{45}Sc MQ-MAS NMR spectra of the hydrated model showed a noticeable shift relative to that of the MIL-53(Sc)-CAL. Again two resonances are observed but in this case with δ_1 values of 15.7 and 16.7 ppm and a relative intensity ratio of 1:3. This was also in good agreement with the model from diffraction as the symmetry suggests the presence of four unique scandium sites. Due to the complex overlapping signals it proved difficult to extract accurate NMR parameters from the spectra however, it was clear that there was a shift to higher C_Q values and higher isotropic chemical shifts in MIL-53(H_2O).

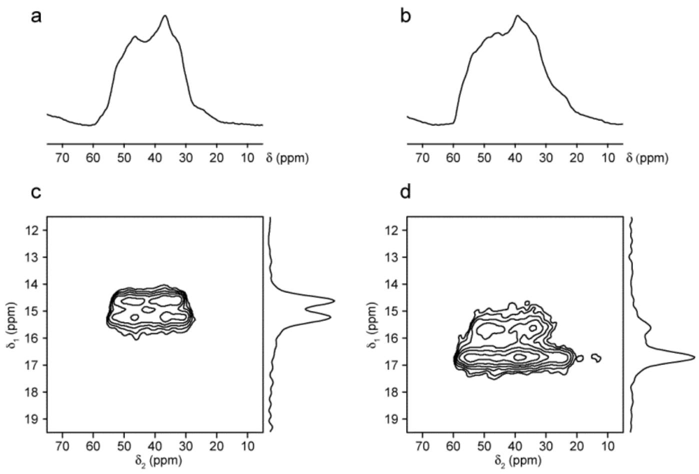

Figure 6.20: 2D MQ-MAS solid state NMR spectra on the MIL-53(Sc)-H_2O (*left*) and MIL-53(Sc)-CAL (*right*)

To interpret the MAS spectra further, the diffraction models for MIL-53(Sc)-H_2O and MIL-53(Sc)-CAL were first geometry optimized then the NMR parameters calculated using the periodic planewave DFT code CASTEP. Calculations on MIL-53(CAL) were in good agreement with the recorded spectra. Calculated values of C_Q (15.9 MHz and 14.7MHz) showed a difference in the two sites although the isotropic chemical shifts of the sites were slightly overestimated (~4 ppm vs 1 ppm recorded). Simulated values of the hydrated model were in broad agreement with the observed spectra, indicated by the higher C_Q values (16.5 and 17.3 MHz)and higher isotropic chemical shifts. Predictions for this model based on the calculations were expected to be challenging as the extra-framework water molecules are distributed over a number of crystallographic sites each not full occupied. In the NMR calculations, full occupancy of water sites was assumed. ^{13}C NMR was also collected on both the hydrated and dehydrated structures. The number resonances observed for MIL-53(Sc)-CAL shows good agreement to the calculated values from the model. Deconvolution of the overlapping signals in the aromatic proved too difficult but where 4 carboxyl carbons are predicted from the model, calculations suggest two pairs of sites, in line with the observed spectra. Due to the drop in symmetry and the large asymmetric unit in the MIL-53(H_2O) 6 independent terephthalates are present in the model leading to a large number of overlapping resonances, again in line with the observed spectra.

6.2.3 Functionalised MIL-53(Sc)

Following the successful synthesis of MIL-53(Sc) and characterisation of the structural derivatives, a series of reactions were carried out to prepare functionalised analogues of the framework. Reactions conditions using the functionalised terephthalic acid precursors are discussed in Chapter 4.

The results from the synthesis suggested that the nitro derivative, denoted MIL-53(Sc)-NO_2, formed readily without the addition of the pyridine required for the synthesis of MIL-53. Samples of MIL-53(Sc)-NO_2, when viewed under optical microscope, were visible as a long prismatic crystals, suitable for single crystal X-ray diffraction. To determine the structure, crystals were chosen, thoroughly washed with ethanol, dried at 313 K and allowed to hydrate under air. Single crystal diffraction yielded the structural model for MIL-53(Sc)-NO_2, shown in Figure 6.21.

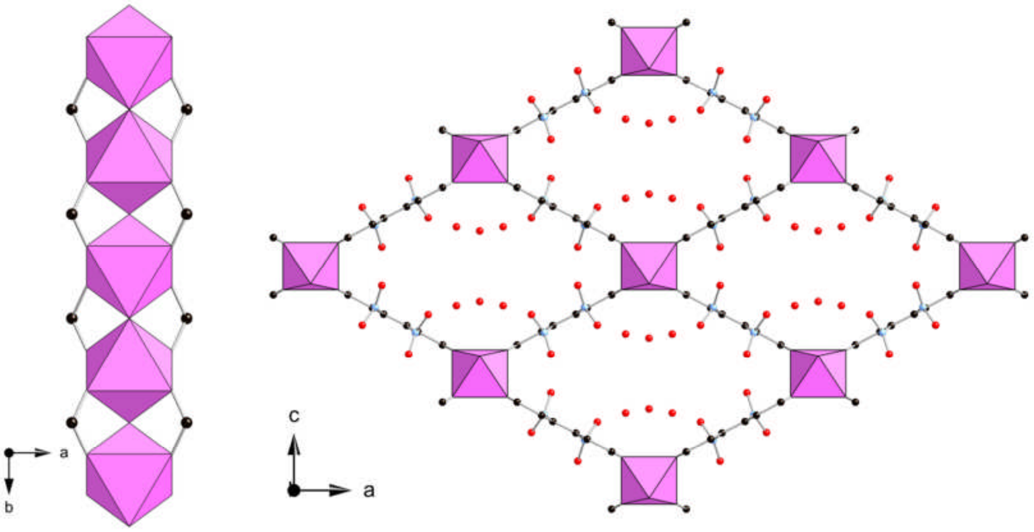

Figure 6.21: MIL-53(Sc)-NO_2, scandium hydroxide chain (*left*) and structure viewed down the channels parallel to the b-axis (*right*). Scandium octahedra are shown in pink. Black, red and blue spheres represent the carbon, oxygen and nitrogen atoms of the organic linker respectively.

The structure of MIL-53(Sc)-NO_2 was solved using direct methods. Structural refinement was performed using a full-matrix least-squares refinement based on F^2 using the ShelX[86] programs integrated into to the WinGX software. Due to the high symmetry, the asymmetric unit contained only one carbon atom to which the –NO_2 group could be attached with the other three ring positions symmetry related. The occupancy of the –NO_2 group positions were set to 0.25 to represent the fact that on each phenyl ring there is only one nitro species, there was no evidence of a larger unit cell or lower symmetry suggesting that the group is fully disordered throughout the framework. Due to the steric hindrance between the -NO_2 group and the carboxylate –CO_2 on the adjacent ring carbon, the –NO_2 group adopts a geometry perpendicular to that of the plane through the 6 phenyl ring carbons and the carboxylate –CO_2. This unfavourable geometry for the –NO_2 group (planar with respect to the phenyl ring in the isolated compound) is known for species where the nitro species is adjacent to a bulky group.[122,123] There is some positional disorder in the model for the –NO_2 group represented by larger displacement parameters as the –NO_2 may not be exactly 90° to the ring plane. Additional electron density in the channels was fitted by partially occupied extra framework water positions.

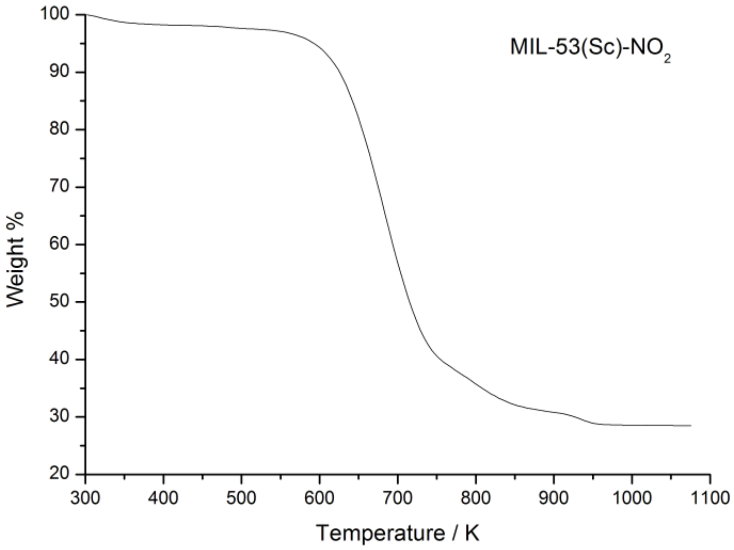

Figure 6.22: Thermogravimetric analysis on MIL-53(Sc)-NO_2

TGA analysis showed a much lower thermal decomposition temperature than that of the parent material, MIL-53. In this case the material, dehydrated prior to the analysis, showed structural decomposition over the range 575 – 700 K under flowing air (Figure 6.22). To verify the presence of the -NO_2 species, elemental analysis was obtained and showed reasonable analysis with the calculated values for MIL-53(NO_2), C expected 35.40 wt.%; C measured, 37.62 wt.%, N expected, 5.17 wt.%; N measured, 5.09 wt.% and H expected 1.5 wt.%; measured, 2.3 wt.%. The higher H contents and C:N ratio over the predicted model suggests the presence of some residual extra-framework water or solvent within the channels.

^{13}C and ^{45}Sc spectra of NO_2-functionalised MIL-53(Sc) are shown in Figure 6.23. The ^{13}C spectrum confirms the presence of a NO_2 group on the aromatic ring, with a peak observed at δ = 151.7 ppm, corresponding to an aromatic carbon attached to N. The increase in the number of resonances (and their frequency spread) indicates a disorder in the exact position of substitution and lowering of the symmetry. The presence of disorder can also be observed in the ^{45}Sc MAS NMR spectrum, where the features of the quadrupolar lineshape appear somewhat broadened

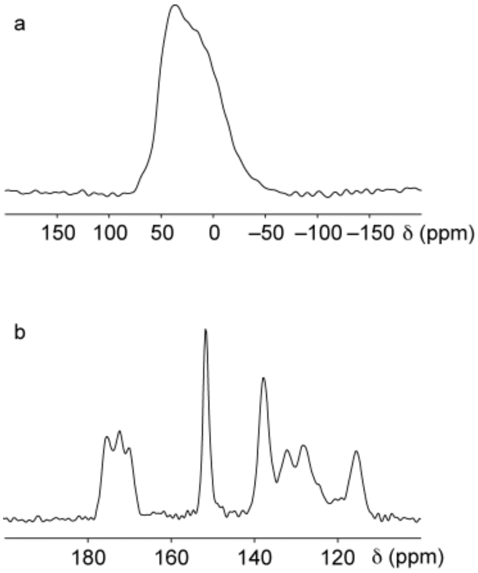

Figure 6.23: (a) ^{45}Sc MAS NMR and (b) ^{13}C CPMAS NMR spectra of NO_2-functionalised MIL-53(Sc) recorded at magnetic field strengths of (a) 14.1 T and (b) 9.4 T, and MAS rates of (a) 60 kHz and (b) 12.5 kHz. Spectra are the result of co-adding (a) 384 and (b) 6144 transients, separated by recycle intervals of (a) 1 s and (b) 3 s.

6.2.4 Adsorption studies

Nitrogen adsorption experiments on the activated MIL-53 show almost no uptake at 77 K. This result was rather surprising at first, the MIL-53(Al) and MIL-53(Cr) materials have a large permanent porosity for nitrogen, with a characteristic step in the adsorption isotherm attributed to the opening or breathing to a larger channel cross-section. This was later understood as the fully activated MIL-53(Sc)-CAL has a narrower channel that any other reported MIL-53 structure and as such has no micropores large enough to accommodate the nitrogen molecules. With carbon dioxide on the other hand, MIL-53(Sc) has a rather unusual two step adsorption isotherm (Figure 6.24).

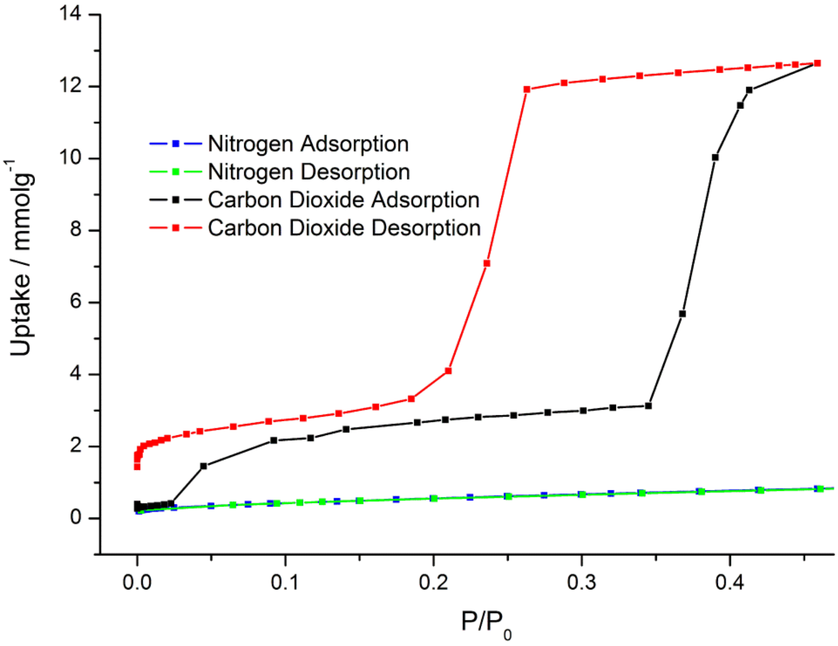

Figure 6.24: Adsorption of Nitrogen (77 K) and CO_2 (196K) of MIL-53(Sc)

Adsorption experiments at 196 K (the temperature of a solid-CO_2/ethanol bath) showed an initial plateau in the isotherm, up to ~0.025 P/P_0, where there is almost no uptake. Above this pressure there is a step in the uptake to around 2-3 mmol g^{-1}, with another plateau, indicating a breathing or opening of the structure to accommodate more of the adsorbate. A final step occurs around 0.35 P/P_0, with a dramatic increase in the uptake to around 13 mmol g^{-1}, representing a step to a significantly more open from of the material. On the desorption branch of the isotherm, the open form of the structure appears to be retained to as low as 0.25 P/P_0, resulting in a large hysteresis before dropping back to a similar plateau as the intermediate on the adsorption branch. There is also hysteresis on the initial step, the desorption branch shows the plateau at around 2 mmol g^{-1} persist to the lowest pressure point. The material required heating to revert to the activated form. The first opening step is also observed in the low pressure isotherm (up to 1 bar) at 268 K. Again the isotherm resembles a non-porous material with an initial plateau up to 600 mbar followed by a step to around 2 mmol g^{-1}. To determine if it is possible to see the second stage of opening closer to room temperature, adsorption isotherms on MIL-53(Sc)-CAL were collected at pressures up to 20 bar in collaboration with Dr. Stuart Miller working in Versailles. The isotherm data shows that the structure at 233 K displays a similar shape of isotherm to that collected at 196 K but with the opening occurring at a much higher pressure. Data collected at 310 K however shows something resembling only the first step at around 2 bar, with a linear slope up to the pressure limit of the equipment at 20 bar (Figure 6.25).

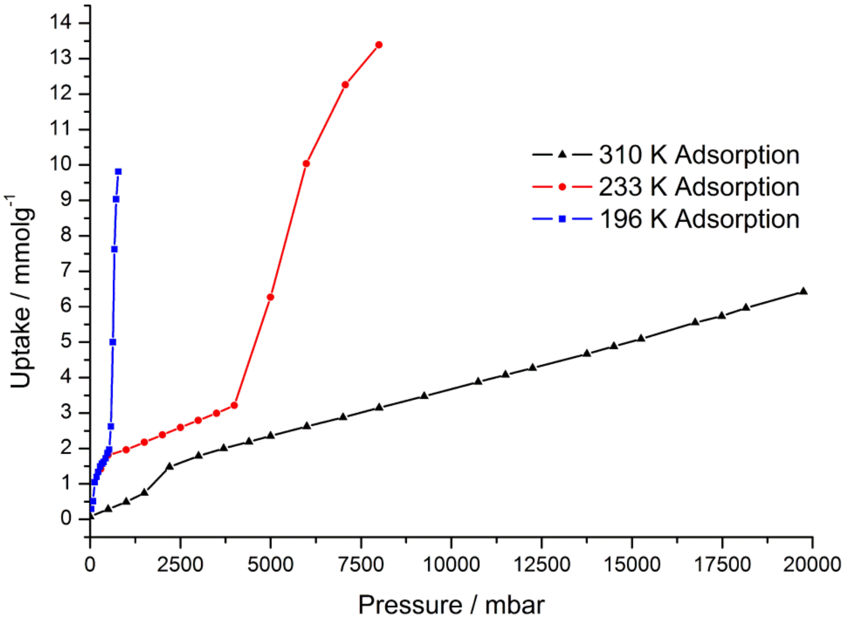

Figure 6.25: High Pressure CO_2 adsorption on MIL-53(Sc)

To understand the response of MIL-53(Sc) to the adsorption of carbon dioxide, a series of structural models, both from the structural characterisation of MIL-53(Sc) and literature examples from the MIL-53(M) series, were used to simulate adsorption isotherms. As there is no software currently available to represent the flexibility of the framework during the adsorption simulation, the models were treated as rigid bodies and the adsorption isotherms calculated. The CO_2 isotherms were calculated using the grand canonical Monte Carlo (GCMC) code implemented in the simulation code MUSIC. Structures were selected to cover a range of the possible structures from the non-porous fully activated model, through to a fully open form derived from the literature MIL-53(Cr). Where necessary, structures were otpimised to better represent the scandium coordination environment, using the CASTEP code, with initial coordinated from a literature model of MIL-53. The are two main advantages of using the geometry optimization, prior to adsorption calculations. The first is the improvement in the geometry particularly in the organic components, the second is that Mulliken partial charges are calculated as part of the optimization process which tend to better represent MOF frameworks in the Music calculations.

The following five structures were chosen with the simulation results are shown in Figure 6.26:

1) MIL-53(CAL) – H atoms added to the model and the structure optimized using CASTEP with a fixed unit cell obtained from the synchrotron powder refinement.
2) MIL-53(HT) – H atoms added to the model and the structure optimized using CASTEP with a fixed unit cell obtained from the synchrotron powder refinement.
3) MIL-53(H_2O) – Extra framework water removed and H atoms added to the structure geometrically, model from powder refinement used directly.
4) MIL-53(DMF) – DMF solvent molecules removed and the and the model used directly from single crystal refinement.
5) MIL-53(LP) model created from literature MIL-53(Cr)-lp with Cr^{3+} replaced with Sc^{3+} and the model optimized using CASTEP with a variable unit cell.

In the simulation, the volume, temperature and chemical potential are kept fixed and the CO_2 molecules randomly inserted, rotated, translated and deleted, with the total number of molecules allowed to vary. The chemical potential in this case is related to the partial pressure of gas in the system and is modeled on the Peng-Robinson equation of state. To effectively simulate the adsorption, 5×10^7 Monte Carlo steps were performed, the first 40 % of which were used for system equilibration and the remaining steps used to calculate the ensemble averages. The interatomic interactions were modeled by the standard 12-6 Lennard Jones (LJ) potential. The parameters for the scandium was obtained from the UFF force fields while the rest of the framework atoms were obtained from the Dreiding force field together with Mulliken partial charges from CASTEP calculations. The CO_2 molecules were modeled by the TraPPE three center model and the Lorentz-Berthelot mixing rules used to calculate the mixed parameters.

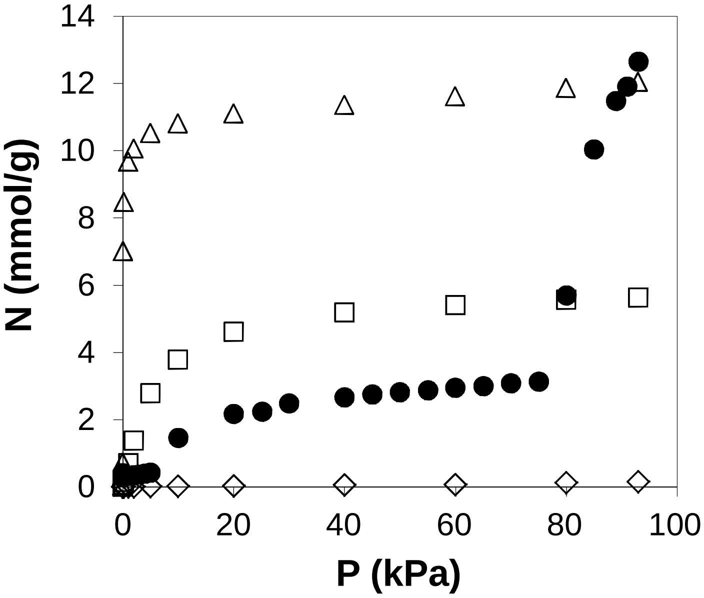

Figure 6.26: Experimental adsorption isotherms on MIL-53(Sc) with predicted isotherms from the various structural forms. Simulated data on as-prepared structure, MIL-53(Sc)-DMF, open squares; intermediate structure, MIL-53(Sc)-INT, open rhombus; and large-pore structure, MIL-53(Sc)-OPEN, open triangles. No adsorption was predicted for the very narrow pore structure

Following the adsorption simulations, it was possible to gain more insight into the structural changes observed as steps in the adsorption isotherms. From diffraction experiments, it is known that the initial structure is of the type MIL-53(Sc)-CAL. To interpret the structure after the first step in the isotherm, adsorption was calculated in the models MIL-53(Sc)-H_2O,-HT,-CAL and -DMF and the capacity compared to that of the experimental isotherm (Figure 6.26). Of the four models, only the MIL-53(Sc)-DMF showed porosity to the CO_2 molecule and the uptake was greater than that observed in the experimental isotherm. Comparison to literature isotherms however, suggests that the structure is of the form MIL-53(Cr)-*np* which reports an uptake similar to that observed for MIL-53(Sc). The second step in the isotherm, to the maximum uptake of

13.5 mmol g^{-1}, is consistent with the structural model for MIL-53(Sc)-OPEN and represents the structure opened to the maximum capacity. To verify the presence of the open structure, *in-situ* powder X-ray diffraction data was collected on a sample of MIL-53(Sc) under pressure of CO_2 at 298 K at Diamond Light Source beamline i11. The data showed that at low pressures of CO_2 (0 – 0.03 Bar), there was little change in the structure from the MIL-53(Sc)-CAL form, consistent with the plateau in the early part of the isotherm (Figure 6.27).

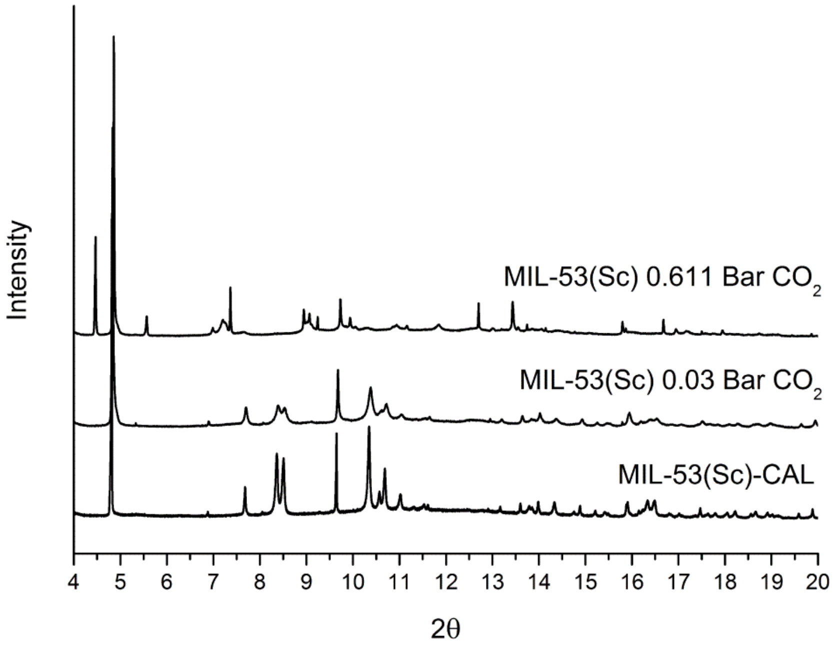

Figure 6.27: Comparison of the *in-situ* X-ray diffraction patterns of the MIL-53(Sc) with adsorbed CO_2.

At 0.611 Bar of CO_2, there was evidence for a mixture of phases in the pattern. Indexing the new phase (identified by the visibly narrower peak width at half maximum) gave the orthorhombic unit cell: a = 7.31 Å, b = 17.01 Å, c = 13.51 Å, $\alpha = \beta = \gamma$ = 90°. This cell was in good agreement with the cell resulting from the geometry optimization of the open form of MIL-53(Sc)-OPEN (orthorhombic : a = 7.419 Å, b = 17.913 Å, c = 12.570 Å, $\alpha = \beta = \gamma$ = 90°). Although the data was not of suitable quality to allow Reitveld refinement, the simulated pattern from the geometry optimized MIL-53(Sc)-OPEN was observed to be in good agreement with the indexed peaks of the second phase.

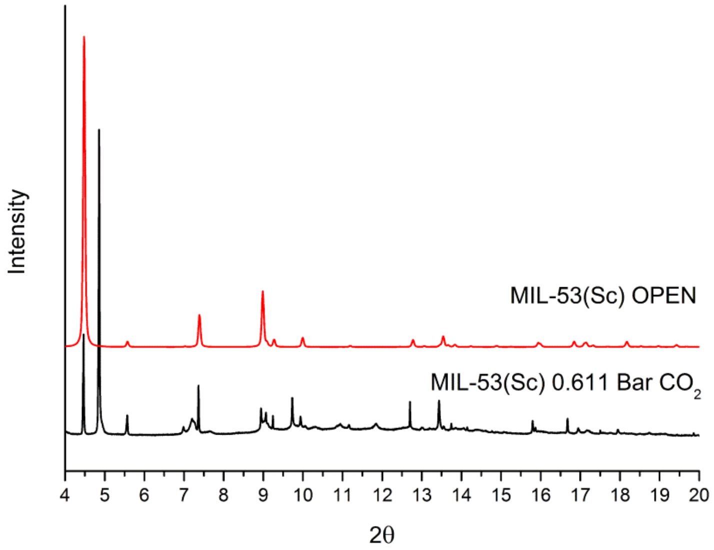

Figure 6.28: Experimental X-ray diffraction pattern of MIL-53(Sc) with adsorbed CO_2 compared with the simulated pattern of geometry optimized MIL-53(Sc)-OPEN

The large adsorption capacity for CO_2 observed at the higher P/P_0 combined with the *in-situ* X-ray diffraction data provide good evidence for the presence of a fully opened form of MIL-53(Sc) as predicted from the presence of similar large pore structural forms observed for other trivalent MIL-53(M) derivatives.

To support the theory that the presence of the $–NO_2$ group in the framework of MIL-53(Sc) prevents the channels from closing, the CO_2 adsorption behavior of the material was investigated. Comparison of the isotherms collected at 273 K clearly shows that where the unfunctionalised material begins with a non-porous phase, MIL-53(Sc)-NO_2 displays a type 1 isotherm with uptake from low pressure more representative of permanent microporosity (Figure 6.29).

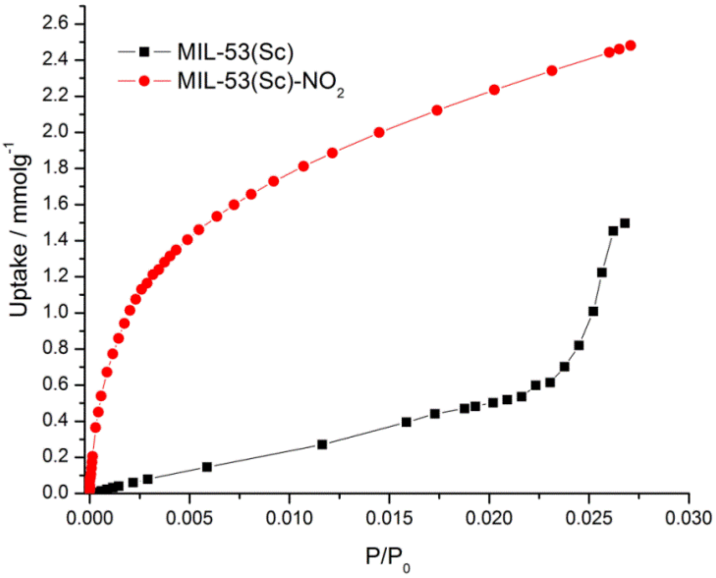

Figure 6.29: MIL-53(Sc)-NO_2 adsorption isotherms for CO_2 at 273 K.

Low temperature (196 K) CO_2 adsorption on MIL-53(Sc)-NO_2 (Figure 6.30) again shows evidence for permanent porosity with uptake of ~ 3.2 mmol g^{-1} up to $P/P_0 = 0.1$. At the higher partial pressure, the materials display a step, characteristic of the MIL-53 series, to the maximum uptake of 10.25 mmol g^{-1}. This pore volume is less than that observed in the unfunctionalised material due to the pore blocking effects arising from the presence of the bulky –NO_2 species.

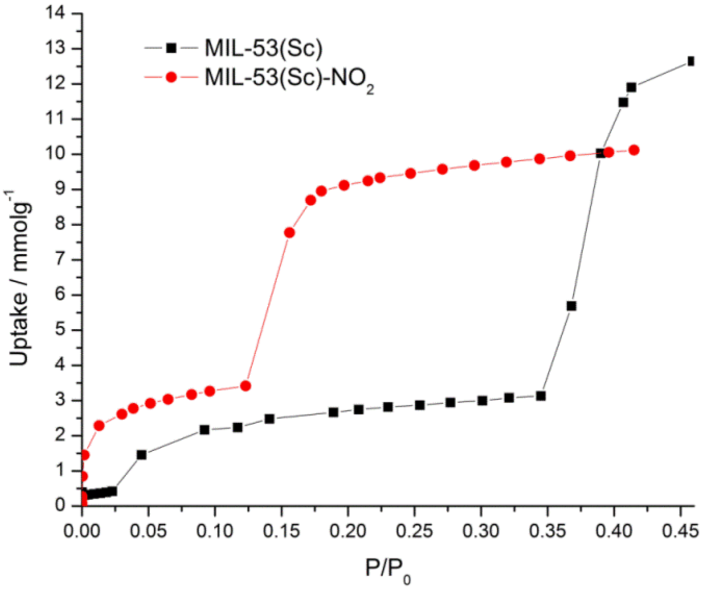

Figure 6.30: CO_2 adsorption isotherm at 196 K for MIL-53(Sc)-NO_2 at 196 K.

6.3 Summary

MIL-53(Sc) was prepared as the open pore, solvated MIL-53(Sc)-DMF. On removal of the solvent, the structure was found to close to the MIL-53(Sc)-CAL form, which possesses the smallest cell volume reported for a MIL-53(M) material. This is believed to be a result of the larger radium Sc^{3+} cation (0.885 Å) the only larger radius in the series is MIL-53(In) which is not stable to removal of terephthalic acid from the channels. This closed pore structure has not yet been observed for the Al^{3+}, Cr^{3+} or Fe^{3+}. Upon heating from 100 K – 573 K, the MIL-53(Sc)-CAL structure progressively opens with a cell volume expansion of 7.4 %, with no change to the space group used to model the structure. At 623 K, the structure changes to the higher symmetry, monoclinic *C2/c,* MIL-53(Sc)-HT form with a further 5.4% cell expansion from 573 K to 623 K. This expansion and symmetry change was found to be fully reversible upon cooling after which the structure reverted back to the MIL-53(Sc)-CAL form. ^2H wideline NMR indicated that there is restricted motion in the phenyl rings of the MIL-53(Sc)-CAL as a result of the narrow channel opening. The MIL-53(Sc)-HT structure, observed at the high temperature, may be in response to phenyl group motion and the associated entropic stabilization permitted by the more open configuration.

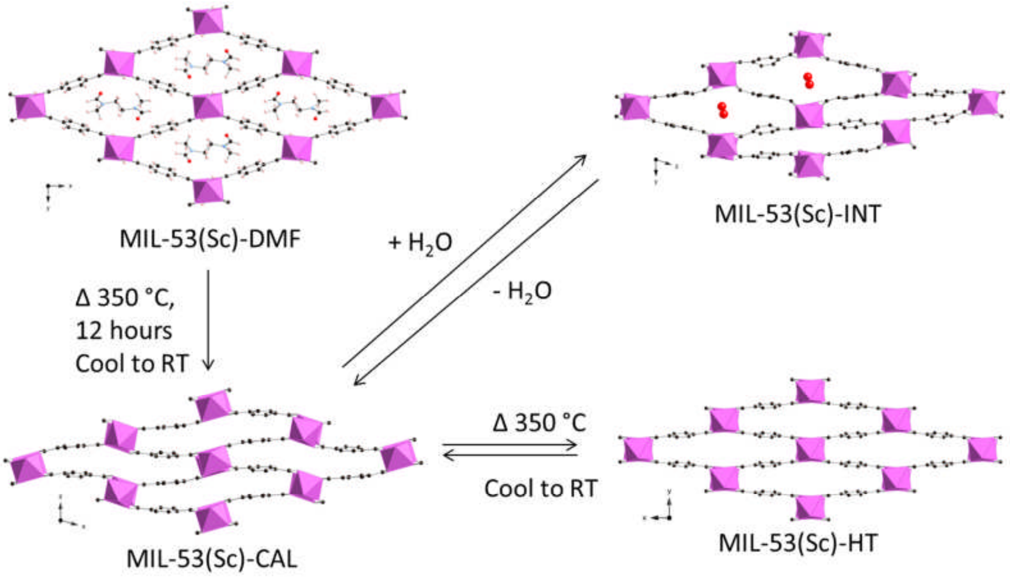

Figure 6.31: Summary of the structural forms identified for MIL-53(Sc). Scandium octahedra are shown in pink. Black, red and blue spheres represent the carbon, oxygen and nitrogen atoms of the organic linker respectively.

In addition to the pure terephthalate form of MIL-53(Sc), the functionalised 2-nitroterephthalic acid derivative MIL-53(Sc)-NO_2 was also prepared and characterized by single crystal X-ray diffraction, solid state NMR and elemental analysis.

The closed pore MIL-53(Sc)-CAL does not have permanent microporosity, rather the structure opens in response to a suitable pressure of CO_2 via a two-step mechanism to ultimately open fully to the high capacity MIL-53(Sc)-OPEN form. Comparison of the CO_2 adsorption of MIL-53(Sc)-CAL with MIL-53(Sc)-NO_2 showed that the steric effects of the bulky –NO_2 groups in the functionalised material prevent the structure from adopting the fully closed -CAL configuration. At the higher partial pressure, both MIL-53(Sc)-CAL with MIL-53(Sc)-NO_2 were observed to open to what is predicted to be the fully open framework configuration for the respective structures.

7 General summary and further work

7.1 General summary

The main aims of this project were to investigate the effects of structural flexibility and functionalization on the adsorption and separation properties of metal-organic framework materials. Initially materials were chosen to be suitable candidates for adsorption experiments. The aluminium methylphosphonate, AlMePO-α, was chosen as a starting point, based on the literature data on the dynamics of molecules such as benzene and xylene isomers. Modification of the framework was successful, by replacing one quarter of the aluminium with scandium (enough to substitute all the octahedral sites in the structure) in the reaction gel, the mixed metal ScAlMePO-α was prepared. The composition of the final product was determined by means of Rietveld analysis on laboratory X-ray powder diffraction, solid state NMR and elemental analysis confirming that the product was the mixed metal ScAlMePO-α with occupancy of the octahedral site calculated to be 97.5% scandium and 2.5% aluminium. By varying the metal source and the methylphosphonate precursor, it was possible to control the particle morphology and porosity of the product. Although some porosity was observed, the maximum capacity measured was still significantly lower than predicted for the fully activated structure, indicating that the synthesis and activation of ScAlMePO-α requires further optimization before column-based testing is possible.

A synthetic study on the piperazine-based bisphosphonate linkers **1**, **2** and **3** with the lighter and larger lanthanides La, Ce and Nd has been shown to produce three framework types. The structure which crystallises from the reaction depends on the pH of the starting gel which, in turn, influences the protonation state of the organic linker used. 2-methylpiperazine and 2,5-dimethylpiperazine derivatives of the ligand were found to have significant structure directing properties arising from the steric bulk of the methyl groups and the restricted channels in the structures. Detailed structural characterisation on the products was performed using single crystal X-ray diffraction, synchrotron powder X-ray diffraction and elemental analysis to identify the products before and after dehydration to understand the activated structures. The reversible hydration of structure type I was shown to be accompanied by a significant reduction in unit cell volume and an associated conformational flip from chair to boat configuration in the piperazine ring reversible upon subsequent rehydration. The metals adopt seven or eight fold coordination with the oxygen and nitrogen of the linker and additional water molecules in all cases producing metal phosphonate chains connected through the bisphosphonate linker. Despite the reversible hydration, the materials possessed no permanent porosity to gas molecules such as CO_2 and N_2 and as such were not suitable for column-based studies.

The large pore bisphosphonate STA-12(Ni) was chosen as a candidate for use in small molecule separation experiments. To this end, a large quantity of STA-12(Ni) was prepared and characterized by powder X-ray diffraction and gas adsorption. The resulting sample (~10 g) was used to prepare a packed column for measurement of breakthrough curves with pure components and gas mixtures. The results showed high selectivity values for CO_2 over CO and CH_4 the materials progressed to further testing as a stationary phase in a gas chromatography column. A PLOT column of STA-12(Ni) was prepared in collaboration with Agilent Technologies, Inc. and tested for a series of low boiling point hydrocarbons (C_1 – C_4). Again results were promising with effective, baseline separation observed for the components tested, separated in line with the boiling points for the individual components despite poor uniformity of the coating in the PLOT column, a result of the needle-like particle morphology. Further study on the column in a capillary GC oven in St Andrews used heavier liquid C_6 mixtures, again showing some interesting preliminary results which indicate that STA-12(Ni) could have applications in this area.

Exploratory solvothermal syntheses with scandium sources and terephthalic acid yielded a total of 4 framework topologies. The lower temperature reactions favoured the scandium trimer-based frameworks MIL-88B(Sc) and MIL-101(Sc). Solvent exchange experiments on MIL-88B(Sc) indicated that the scandium form shows similar solvent exchange properties to the literature chromium example. MIL-101(Sc) was prepared as the major component of a mixture with the polymorphic MIL-88B(Sc) but it was not possible to access the full extent of the porosity of this large pore framework. Attempts to activate the material, using methods reported for MIL-101(Cr), resulted in re-crystallisation of the materials into the more dense MIL-88B(Sc).

The lack of stability of MIL-101(Sc) suggests that the trimeric scandium cluster does not possess the same chemical stability as the chromium derivative, evidenced by the fact that the scandium trimer has only been observed in MOF structures and not as an isolated molecular complex. High temperature reactions (160 - 220°C) also using scandium sources and terephthalic acid yielded the porous MIL-53(Sc) and Sc_2BDC_3 frameworks. By careful control of the synthetic conditions, it was possible to optimize the reactions to favour large crystals of either material for use in structure solution. Following optimization of the synthesis with terephthalic acid, reactions were explored with the functionalised derivatives of the organic linker including the $–NH_2$, $-NO_2$ and –Br analogues of terephthalic acid to see if the same framework topology was observed with inclusion of these species. Ultimately, the $–NH_2$ and $–NO_2$ functionalised Sc_2BDC_3 and the $–NO_2$ functionalised MIL-53(Sc) were prepared and characterized successfully.

Following the success of the syntheses with terephthalic acid, the exploratory syntheses were expanded to include the tri-carboxylate, trimesic acid, and the tetra-carboxylate linkers, 3,3’,5,5’- azobenzenetetracarboxylic acid and pyromellitic acid. Reactions with trimesic acid, over a range of temperatures (100 – 220°C) yielded only the large pore MIL-100(Sc) framework. Adsorption experiments on the solid indicated that close to the maximum adsorption capacity for MIL-100(Sc) was accessible in the low temperature (196 K) CO_2 isotherm, despite a low apparent uptake measured by nitrogen adsorption. The large pore MIL-101(Sc) is a promising material for applications in heterogeneous catalysis as the large, accessible pore cavities are lined with the coordinatively unsaturated scandium sites, accessible to a wide range of organic molecules (up to ~8.6 Å in diameter the size of the window into the largest cage). The 3,3’,5,5’- azobenzenetetracarboxylic acid linker also only yielded one structure in the exploratory synthesis study. The framework produced, isostructural with socMOF(In), is again constructed form the scandium trimer and is best described as an array of corner sharing cubes creating a highly interconnected cubic lattice or pore cavities. The cubic cavities in socMOF(In) were found, from single crystal diffraction, to contain nitrate counter ions, as opposed to the hydroxide used to balance charge in the trimer units of MIL-88B(Sc) and MIL-100(Sc). From solid state

NMR and elemental analysis it is evident that the Sc-ABTC structure is consistent with that of the reported socMOF(In). Reaction of scandium and pyromellitic acid yielded the final structure obtained in the solvothermal syntheses. The structure, solved from single crystal X-ray diffraction, was found to contain small cavities, however, there were no suitable windows through which gas molecules could access this porosity and from adsorption experiments, the material possessed no permanent porosity.

The flexibility of the scandium terephthalate, MIL-53(Sc), was studied by powder X-ray diffraction and adsorption experiments. The as-prepared material was solved from single crystal diffraction on a solvated crystal, coated in oil to prevent loss of solvent on exposure to air. The structure, denoted MIL-53(Sc)-DMF, was the first of the extensively reported MIL-53(M) series to contain ordered, physisorbed DMF solvent molecules in the unidirectional channels. MIL-53(Fe) was reported with ordered DMF, but the carbonyl-oxygen of the solvent was incorporated as the corner-sharing oxygen of the Fe chain and therefore was not physisorbed. Calcination under flowing air was used to remove all guest molecules, including un-reacted or adsorbed terephthalate molecules or solvent, after which (if kept isolated from moisture) the structure was observed to possess a ‘closed’ pore geometry, denoted MIL-53(Sc)-CAL. This structure is also unique in the MIL-53(M) series and represents the narrowest channel opening reported for the flexible MIL-53 series. Heating the MIL-53(Sc)-CAL to 623 K and studying the structural evolution by *in situ* synchrotron powder X-ray diffraction, it was clear that the structure was opening progressively until a symmetry change was observed above 573 K to a higher symmetry form, isostructural with MIL-53(Fe) under the same conditions. Allowing the MIL-53(Sc)-CAL to contact with air resulted in hydration of the material to a triclinic structure, again similar to MIL-53(Fe) but with a doubling of the unit cell. The final structure MIL-53(Sc)-H_2O was found to have two different types of channel, one identified to contain adsorbed water molecules and the other empty. Adsorption isotherms collected on MIL-53(Sc) also suggested a unique behavior for MIL-53(Sc). The low pressure region was typical of a non-porous material, as expected for a material with the MIL-53(Sc)-CAL structure, which proceeded to open via a 2 step mechanism to what is predicted to be, from adsorption simulations and diffraction experiments, to be the fully open, large pore form of MIL-53(Sc). Comparison of the isotherm data for the pure terephthalate against that of the MIL-53(Sc)-NO_2 suggests that the addition of the $-NO_2$ groups prevents the structure from closing fully and induces permanent porosity. At higher partial pressure, the structure of MIL-53(Sc)-NO_2 was also observed to open to what is predicted to be the fully open pore geometry.

The small pore terephthalate, Sc_2BDC_3, was synthesised both hydro- and solvo-thermally using scandium oxide and scandium nitrate sources. Prior to this study, the only evidence for flexibility in Sc_2BDC_3 was the structural response to adsorption of CO_2 measured by *in situ* single crystal studies. Variable temperature synchrotron powder diffraction studies, on an evacuated capillary of Sc_2BDC_3, indicated that there was also a purely temperature dependent symmetry change to the monoclinic symmetry on cooling below 225 K, fully reversible on subsequent re- heating. Above 225 K the structure remained in the orthorhombic symmetry up to the final measurement temperature of 573 K. Comparison of the structures, solved using Rietveld analysis, indicated a linear, negative thermal expansivity which, on close inspection of the trends in the cell parameters, was found to arise from rotation in the carboxylate groups along the scandium – carboxylate chain resulting in a shortening of the Sc – Sc distance. It was also found to be possible to include $-NH_2$ and $-NO_2$ groups in the Sc_2BDC_3 framework using the relevant mono-functionalised organic linkers. Inclusion of the functional groups was observed to have a strong structure directing effect with respect to the symmetry of the observed product. $Sc_2(NH_2\text{-}BDC)_3$ was indexed in the orthorhombic, *Fddd* symmetry at room temperature and upon preserved that symmetry over the temperature range 100 – 473 K. The $Sc_2(NO_2\text{-}BDC)_3$ was indexed as the monoclinic, *C2/c* at room temperature and maintained that symmetry over the range 100 – 473 K. Finally breakthrough and column testing measurements on the pure terephthalate Sc_2BDC_3, indicated high selectivities for the adsorption of CO_2 over CH_4 and again preliminary results suggested that the column was effective in the size selective separation of branched and straight-chain hydrocarbons (C_5 - C_7).

7.2 Further work

It has been shown that ScAlMePO-α has been successfully prepared and characterized however, the full extent of the porosity is yet to be accessed. The pore size and chemistry of this and the parent AlMePO-α are of interest for applications in separation, however, further optimization of the synthesis and/or activation condition is required if the materials is to be suitable for column applications.

Synthetic studies in this work yielded five framework topologies previously unreported in the scandium system. With the increasing popularity of synthetic MOF work and longer and more elaborate organic linkers becoming more readily available, scandium would be an excellent choice for further exploratory synthesis. Scandium has been shown to produce high thermal stability, porous MOF materials and early results by colleagues in the group suggest that the large pore MIL-100(Sc) is a highly effective heterogeneous Lewis acid catalyst.

The structural response of the porous terephthalates Sc_2BDC_3 and MIL-53(Sc) to temperature variation has been characterized by synchrotron powder X-ray diffraction. To better understand the phase behaviour of these materials during adsorption of gas molecules, *in situ* powder X-ray diffraction studies will be conducted using the capillary gas cell at the Diamond Light Source, beamline I11. This work, scheduled for May, 2012, should give crystallographic evidence for the phases observed before and after the ‘steps’ in the experimental adsorption isotherms which have been predicted from simulation studies on both MIL-53(Sc) and Sc_2BDC_3. Further to this, multi component isotherms on Sc_2BDC_3 could be used to measure more accurate selectivity values for CO_2/CH_4, which from breakthrough curve analysis is expected to be very high.

Preliminary results on the PLOT column of STA-12(Ni) show high selectivity values and effective separation of hydrocarbon mixtures. To fully understand the separation potential for this material, a systematic screening process is required and could be combined with simulation work to help target specific separations that are challenging using the commercially available columns. The range of MOFs tested in the PLOT column could also be expanded to some literature examples of MOFs with suitable structural and adsorptive properties. One challenge in this area is to target the MOF synthesis to produce nano-sized particles of the MOF materials which is an area that is of interest for future investigations.

8 References

(1) Davis, M. E. *Nature* **2002**, *417*, 813.

(2) Ma, S. Q.; Zhou, H. C. *Chem. Commun.* **2010**, *46*, 44.

(3) Wang, B.; Cote, A. P.; Furukawa, H.; O'Keeffe, M.; Yaghi, O. M. *Nature* **2008**, *453*, 207.

(4) Llewellyn, P. L.; Bourrelly, S.; Serre, C.; Vimont, A.; Daturi, M.; Hamon, L.; De Weireld, G.; Chang, J. S.; Hong, D. Y.; Hwang, Y. K.; Jhung, S. H.; Férey, G. *Langmuir* **2008**, *24*, 7245.

(5) Yazaydin, A. O.; Snurr, R. Q.; Park, T. H.; Koh, K.; Liu, J.; LeVan, M. D.; Benin, A. I.; Jakubczak, P.; Lanuza, M.; Galloway, D. B.; Low, J. J.; Willis, R. R. *J. Am. Chem. Soc.* **2009**, *131*, 18198.

(6) Pan, L.; Olson, D. H.; Ciemnolonski, L. R.; Heddy, R.; Li, J. *Angew. Chem.-Int. Edit.* **2006**, *45*, 616.

(7) Fuertes, A. B. *J. Membr. Sci.* **2000**, *177*, 9.

(8) Bárcia, P. S.; Zapata, F.; Silva, J. A. C.; Rodrigues, A. E.; Chen, B. L. *J. Phys. Chem. B* **2007**, *111*, 6101.

(9) Garcia-Couceiro, U.; Castillo, O.; Cepeda, J.; Luque, A.; Pérez-Yáῃez, S.; Román, P. *Inorg. Chim. Acta* **2009**, *362*, 4212.

(10) Horcajada, P.; Serre, C.; Maurin, G.; Ramsahye, N. A.; Balas, F.; Vallet-Regí, M.; Sebban, M.; Taulelle, F.; Férey, G. *J. Am. Chem. Soc.* **2008**, *130*, 6774.

(11) Banerjee, M.; Das, S.; Yoon, M.; Choi, H. J.; Hyun, M. H.; Park, S. M.; Seo, G.; Kim, K. *J. Am. Chem. Soc.* **2009**, *131*, 7524.

(12) Férey, G. *Chem. Soc. Rev.* **2008**, *37*, 191.

(13) Park, K. S.; Ni, Z.; Côté, A. P.; Choi, J. Y.; Huang, R. D.; Uribe-Romo, F. J.; Chae, H. K.; O'Keeffe, M.; Yaghi, O. M. *Proc. Natl. Acad. Sci. U.S.A.* **2006**, *103*, 10186.

(14) Furukawa, H.; Yaghi, O. M. *J. Am. Chem. Soc.* **2009**, *131*, 8875.

(15) Tanabe, K.; Hölderich, W. F. *Appl.Cata., A* **1999**, *181*, 399.

(16) Corma, A.; Planelles, J.; Sanchezmarin, J.; Tomas, F. *J. Catal.* **1985**, *93*, 30.

(17) Costa, E.; Delucas, A.; Uguina, M. A.; Ruíz, J. C. *Ind. Eng. Chem. Res.* **1988**, *27*,

1291.

(18) Mueller, U.; Schubert, M.; Teich, F.; Puetter, H.; Schierle-Arndt, K.; Pastré, J. *J. Mater. Chem.* **2006**, *16*, 626.

(19) Keskin, S.; Sholl, D. S. *Ind. Eng. Chem. Res.* **2009**, *48*, 914.

(20) Devanssay, E.; Capilla, P.; Coscia, D.; Do, L.; Sternberg, R.; Raulin, F. *J. Chromatogr.* **1993**, *639*, 255.

(21) Bauer, S.; Serre, C.; Devic, T.; Horcajada, P.; Marrot, J.; Férey, G.; Stock, N. *Inorg. Chem.* **2008**, *47*, 7568.

(22) Morris, W.; Doonan, C. J.; Furukawa, H.; Banerjee, R.; Yaghi, O. M. *J. Am. Chem. Soc.* **2008**, *130*, 12626.

(23) Wang, Z. Q.; Cohen, S. M. *Chem. Soc. Rev.* **2009**, *38*, 1315.

(24) Groves, J. A.; Miller, S. R.; Warrender, S. J.; Mellot-Draznieks, C.; Lightfoot, P.; Wright, P. A. *Chem. Commun.* **2006**, 3305.

(25) Wharmby, M. T.; Mowat, J. P. S.; Thompson, S. P.; Wright, P. A. *J. Am. Chem. Soc.* **2011**, *133*, 1266.

(26) Kitagawa, S.; Kitaura, R.; Noro, S. *Angew. Chem.-Int. Edit.* **2004**, *43*, 2334.

(27) Miller, S. R.; Wright, P. A.; Serre, C.; Loiseau, T.; Marrot, J.; Férey, G. *Chem. Commun.* **2005**, 3850.

(28) Surblé, S.; Serre, C.; Mellot-Draznieks, C.; Millange, F.; Férey, G. *Chem. Commun.* **2006**, 284.

(29) Serre, C.; Millange, F.; Thouvenot, C.; Noguès, M.; Marsolier, G.; Louër, D.; Férey, G. *J. Am. Chem. Soc.* **2002**, *124*, 13519.

(30) Barthelet, K.; Adil, K.; Millange, F.; Serre, C.; Riou, D.; Férey, G. *J. Mater. Chem.* **2003**, *13*, 2208.

(31) Rowsell, J. L. C.; Yaghi, O. M. *Microporous Mesoporous Mater.* **2004**, *73*, 3.

(32) Li, H.; Eddaoudi, M.; O'Keeffe, M.; Yaghi, O. M. *Nature* **1999**, *402*, 276.

(33) Rowsell, J. L. C.; Yaghi, O. M. *Angew. Chem.-Int. Edit.* **2005**, *44*, 4670.

(34) Mohamed, M. M.; Zidan, F. I.; Fodail, M. H. *J. Mater. Sci.* **2007**, *42*, 4066.

(35) van den Brink, R. W.; Booneveld, S.; Pels, J. R.; Bakker, D. F.; Verhaak, M. *Appl. Catal., B* **2001**, *32*, 73.

(36) de Lill, D. T.; Cahill, C. L. *Chem. Commun.* **2006**, 4946.

(37) Cronstedt, A. F. *Kongl. Svenska Vetenskaps-Akademiens handl.* **1756**, *17*, 120.

(38) Adams, J. M.; Haselden, D. A.; Hewat, A. W. *J. Solid State Chem.* **1982**, *44*, 245.

(39) Barrer, R. M. *J. Chem. Soc.* **1948**, 2158.

(40) Wilson, S. T.; Lok, B. M.; Messina, C. A.; Cannan, T. R.; Flanigen, E. M. *J. Am. Chem. Soc.* **1982**, *104*, 1146.

(41) Corma, A. *J. Catal.* **2003**, *216*, 298.

(42) Maeda, K.; Akimoto, J.; Kiyozumi, Y.; Mizukami, F. *Chem. Commun.* **1995**, 1033.

(43) Maeda, K.; Akimoto, J.; Kiyozumi, Y.; Mizukami, F. *Angew. Chem. Int. Ed.* **1995**, *34*, 1199.

(44) Olson, D. H.; Kokotailo, G. T.; Lawton, S. L.; Meier, W. M. *J. Phys. Chem.* **1981**, *85*, 2238.

(45) Gonzalez, J.; Devi, R. N.; Wright, P. A.; Tunstall, D. P.; Cox, P. A. *J. Phys. Chem. B* **2005**, *109*, 21700.

(46) Herdes, C.; Valente, A.; Lin, Z.; Rocha, J.; Coutinho, J. A. P.; Medina, F.; Vega, L. F. *Langmuir* **2007**, *23*, 7299.

(47) Clearfield, A. *Current Opinion in Solid State & Materials Science* **1996**, *1*, 268.

(48) Serre, C.; Groves, J. A.; Lightfoot, P.; Slawin, A. M. Z.; Wright, P. A.; Stock, N.; Bein, T.; Haouas, M.; Taulelle, F.; Férey, G. *Chem. Mater.* **2006**, *18*, 1451.

(49) Miller, S. R.; Pearce, G. M.; Wright, P. A.; Bonino, F.; Chavan, S.; Bordiga, S.; Margiolaki, I.; Guillou, N.; Férey, G.; Bourrelly, S.; Llewellyn, P. L. *J. Am. Chem. Soc.* **2008**.

(50) Chae, H. K.; Siberio-Pérez, D. Y.; Kim, J.; Go, Y.; Eddaoudi, M.; Matzger, A. J.; O'Keeffe, M.; Yaghi, O. M. *Nature* **2004**, *427*, 523.

(51) Chui, S. S. Y.; Lo, S. M. F.; Charmant, J. P. H.; Orpen, A. G.; Williams, I. D. *Science* **1999**, *283*, 1148.

(52) Prestipino, C.; Regli, L.; Vitillo, J. G.; Bonino, F.; Damin, A.; Lamberti, C.; Zecchina, A.; Solari, P. L.; Kongshaug, K. O.; Bordiga, S. *Chem. Mater.* **2006**, *18*, 1337.

(53) Vitillo, J. G.; Regli, L.; Chavan, S.; Ricchiardi, G.; Spoto, G.; Dietzel, P. D. C.;

Bordiga, S.; Zecchina, A. *J. Am. Chem. Soc.* **2008**, *130*, 8386.

(54) Marx, S.; Kleist, W.; Baiker, A. *J. Catal.* **2011**, *281*, 76.

(55) Furukawa, H.; Ko, N.; Go, Y. B.; Aratani, N.; Choi, S. B.; Choi, E.; Yazaydin, A. O.; Snurr, R. Q.; O'Keeffe, M.; Kim, J.; Yaghi, O. M. *Science* **2010**, *329*, 424.

(56) Yan, Y.; Telepeni, I.; Yang, S. H.; Lin, X.; Kockelmann, W.; Dailly, A.; Blake, A. J.; Lewis, W.; Walker, G. S.; Allan, D. R.; Barnett, S. A.; Champness, N. R.; Schröder, M. *J. Am. Chem. Soc.* **2010**, *132*, 4092.

(57) Dietzel, P. D. C.; Johnsen, R. E.; Blom, R.; Fjellvåg, H. *Chem.-Eur. J.* **2008**, *14*, 2389.

(58) Rosi, N. L.; Kim, J.; Eddaoudi, M.; Chen, B. L.; O'Keeffe, M.; Yaghi, O. M. *J. Am. Chem. Soc.* **2005**, *127*, 1504.

(59) Dietzel, P. D. C.; Georgiev, P. A.; Eckert, J.; Blom, R.; Straessle, T.; Unruh, T. *Chem. Commun.* **2010**, *46*, 4962.

(60) Chavan, S.; Bonino, F.; Vitillo, J. G.; Groppo, E.; Lamberti, C.; Dietzel, P. D. C.; Zecchina, A.; Bordiga, S. *PCCP* **2009**, *11*, 9811.

(61) McKinlay, A. C.; Morris, R. E.; Horcajada, P.; Férey, G.; Gref, R.; Couvreur, P.; Serre, C. *Angew. Chem.-Int. Edit.* **2010**, *49*, 6260.

(62) Barthelet, K.; Marrot, J.; Riou, D.; Férey, G. *Angew. Chem.-Int. Edit.* **2002**, *41*, 281.

(63) Loiseau, T.; Serre, C.; Huguenard, C.; Fink, G.; Taulelle, F.; Henry, M.; Bataille, T.; Férey, G. *Chem.-Eur. J.* **2004**, *10*, 1373.

(64) Barthelet, K.; Marrot, J.; Férey, G.; Riou, D. *Chem. Commun.* **2004**, 520.

(65) Volkringer, C.; Meddouri, M.; Loiseau, T.; Guillou, N.; Marrot, J.; Férey, G.; Haouas, M.; Taulelle, F.; Audebrand, N.; Latroche, M. *Inorg. Chem.* **2008**, *47*, 11892.

(66) Serre, C.; Millange, F.; Surblé, S.; Férey, G. *Angew. Chem. Int. Ed..* **2004**, *43*, 6286.

(67) Serre, C.; Mellot-Draznieks, C.; Surblé, S.; Audebrand, N.; Filinchuk, Y.; Férey, G. *Science* **2007**, *315*, 1828.

(68) Férey, G.; Mellot-Draznieks, C.; Serre, C.; Millange, F.; Dutour, J.; Surblé, S.;

Margiolaki, I. *Science* **2005**, *309*, 2040.

(69) Latroche, M.; Surblé, S.; Serre, C.; Mellot-Draznieks, C.; Llewellyn, P. L.; Lee, J. H.; Chang, J. S.; Jhung, S. H.; Férey, G. *Angew. Chem. Int. Ed.* **2006**, *45*, 8227.

(70) Férey, G.; Serre, C.; Mellot-Draznieks, C.; Millange, F.; Surblé, S.; Dutour, J.; Margiolaki, I. *Angew. Chem. Int. Ed..* **2004**, *43*, 6296.

(71) Schlenker, J. L.; Dwyer, F. G.; Jenkins, E. E.; Rohrbaugh, W. J.; Kokotailo, G. T.; Meier, W. M. *Nature* **1981**, *294*, 340.

(72) Vimont, A.; Goupil, J. M.; Lavalley, J. C.; Daturi, M.; Surblé, S.; Serre, C.; Millange, F.; Férey, G.; Audebrand, N. *J. Am. Chem. Soc.* **2006**, *128*, 3218.

(73) Saedi, Z.; Tangestaninejad, S.; Moghadam, M.; Mirkhani, V.; Mohammadpoor-Baltork, I. *J. Coord. Chem.* **2012**, *65*, 463.

(74) Gu, Z. Y.; Yan, X. P. *Angew. Chem. Int. Ed.* **2010**, *49*, 1477.

(75) Corbin, D. R.; Abrams, L.; Jones, G. A.; Eddy, M. M.; Harrison, W. T. A.; Stucky, G. D.; Cox, D. E. *J. Am. Chem. Soc.* **1990**, *112*, 4821.

(76) Chen, B. L.; Liang, C. D.; Yang, J.; Contreras, D. S.; Clancy, Y. L.; Lobkovsky, E. B.; Yaghi, O. M.; Dai, S. *Angew. Chem. Int. Ed.* **2006**, *45*, 1390.

(77) Kobayashi, S. *Eur. J. Org. Chem.* **1999**, 15.

(78) Ishihara, K.; Kubota, M.; Kurihara, H.; Yamamoto, H. *J. Org. Chem.* **1996**, *61*, 4560.

(79) Shannon, R. D. *Acta Crystallogr. Sect. A* **1976**, *32*, 751.

(80) Bull, I.; Wheatley, P. S.; Lightfoot, P.; Morris, R. E.; Sastre, E.; Wright, P. A. *Chem. Commun.* **2002**, 1180.

(81) Riou, D.; Fayon, F.; Massiot, D. *Chem. Mater.* **2002**, *14*, 2416.

(82) Perles, J.; Iglesias, M.; Ruiz-Valero, C.; Snejko, N. *Chem. Commun.* **2003**, 346.

(83) Miller, S. R.; Wright, P. A.; Devic, T.; Serre, C.; Férey, G.; Llewellyn, P. L.; Denoyel, R.; Gaberova, L.; Filinchuk, Y. *Langmuir* **2009**, *25*, 3618.

(84) Dietzel, P. D. C.; Blom, R.; Fjellvag, H. *Dalton Trans.* **2006**, 2055.

(85) Alaerts, L.; Kirschhock, C. E. A.; Maes, M.; van der Veen, M. A.; Finsy, V.; Depla, A.; Martens, J. A.; Baron, G. V.; Jacobs, P. A.; Denayer, J. E. M.; De Vos, D. E. *Angew. Chem. Int. Ed.* **2007**, *46*, 4293.

(86) Sheldrick, G. M. *Acta Crystallogr. Sect. A* **2008**, *64*, 112.

(87) Maria Cristina Burla, M. C.; Caliandro, R.; Camalli, M.; Carrozzini, B.; Cascarano, G. L.; G., C.; Mallamo, M.; Annamaria Mazzone; Polidori, G.; R., S. *J. Appl. Crystallogr.* **2012**, *45*, 357.

(88) Huddleston, J. G.; Visser, A. E.; Reichert, W. M.; Willauer, H. D.; Broker, G. A.; Rogers, R. D. *Green Chem.* **2001**, *3*, 156.

(89) Boultif, A.; Louër, D. *J. Appl. Crystallogr.* **1991**, *24*, 987.

(90) Werner, P. E.; Eriksson, L.; Westdahl, M. *J. Appl. Crystallogr.* **1985**, *18*, 367.

(91) Altomare, A.; Burla, M. C.; Camalli, M.; Carrozzini, B.; Cascarano, G. L.; Giacovazzo, C.; Guagliardi, A.; Moliterni, A. G. G.; Polidori, G.; Rizzi, R. *J. Appl. Crystallogr.* **1999**, *32*, 339.

(92) Düren, T.; Millange, F.; Férey, G.; Walton, K. S.; Snurr, R. Q. *J. Phys. Chem. C* **2007**, *111*, 15350.

(93) Brandani, S.; Jama, M. A.; Ruthven, D. M. *Chem. Eng. Sci.* **2000**, *55*, 1205.

(94) Brandani, S.; Ruthven, D. M.; Karger, J. *Zeolites* **1995**, *15*, 494.

(95) Ruthven, D. M. In *9th International Conference on Fundamentals of Adsorption (FOA9)*; Springer: Sicily, ITALY, 2007, p 225.

(96) Brandani, S.; Jama, M.; Ruthven, D. *Microporous Mesoporous Mater.* **2000**, *35-6*, 283.

(97) Yang, Q. Y.; Xue, C. Y.; Zhong, C. L.; Chen, J. F. *AlChE J.* **2007**, *53*, 2832.

(98) Carter, V. J.; Wright, P. A.; Gale, J. D.; Morris, R. E.; Sastre, E.; PerezPariente, J. *J. Mater. Chem.* **1997**, *7*, 2287.

(99) Maeda, K. *Microporous Mesoporous Mater.* **2004**, *73*, 47.

(100) Groves, J. A.; Stephens, N. F.; Wright, P. A.; Lightfoot, P. *Solid State Sci.* **2006**, *8*, 397.

(101) Mowat, J. P. S., University of St. Andrews, **2007**.

(102) Wharmby, M. T., University of St. Andrews, **2012**.

(103) Mowat, J. P. S.; Groves, J. A.; Wharmby, M. T.; Miller, S. R.; Li, Y.; Lightfoot, P.; Wright, P. A. *J. Solid State Chem.* **2009**, *182*, 2769.

(104) Miller, S. R., University of St. Andrews, **2007**.

(105) Gándara, F.; Gómez-Lor, B.; Iglesias, M.; Snejko, N.; Gutiérrez-Puebla, E.; Monge, A. *Chem. Commun.* **2009**, 2393.

(106) Celeste Bernini, M.; Snejko, N.; Gutiérrez-Puebla, E.; Monge, A. *Crystengcomm* **2011**, *13*, 1797.

(107) Monge, A.; Gándara, F.; Gutiérrez-Puebla, E.; Snejko, N. *Crystengcomm* **2011**, *13*, 5031.

(108) Ibarra, I. A.; Lin, X. A.; Yang, S. H.; Blake, A. J.; Walker, G. S.; Barnett, S. A.; Allan, D. R.; Champness, N. R.; Hubberstey, P.; Schröder, M. *Chem.-Eur. J.* **2010**, *16*, 13671.

(109) Ibarra, I. A.; Yang, S.; Lin, X.; Blake, A. J.; Rizkallah, P. J.; Nowell, H.; Allan, D. R.; Champness, N. R.; Hubberstey, P.; Schröder, M. *Chem. Commun.* **2011**, *47*, 8304.

(110) Mowat, J. P. S.; Miller, S. R.; Slawin, A. M. Z.; Seymour, V. R.; Ashbrook, S. E.; Wright, P. A. *Microporous Mesoporous Mater.* **2011**, *142*, 322.

(111) Mowat, J. P. S.; Miler, S. R.; Griffin, J. M.; Seymour, V. R.; Ashbrook, S. E.; Thompson, S. P.; Fairen-Jimenez, D.; Banu, A.-M.; Dueren, T.; Wright, P. A. *Inorg. Chem.* **2011**, *50*, 10844.

(112) Mowat, J. P. S.; Seymour, V. R.; Griffin, J. M.; Thompson, S. P.; Slawin, A. M. Z.; Fairen-Jimenez, D.; Duren, T.; Ashbrook, S. E.; Wright, P. A. *Dalton Trans.* **2012**, *41*, 3937.

(113) Whitfield, T. R.; Wang, X. Q.; Liu, L. M.; Jacobson, A. J. *Solid State Sci.* **2005**, *7*, 1096.

(114) Wang, S. X.; Wang, X. M.; Li, L. J.; Advincula, R. C. *J. Org. Chem.* **2004**, *69*, 9073.

(115) Liu, Y.; Eubank, J. F.; Cairns, A. J.; Eckert, J.; Kravtsov, V. C.; Luebke, R.; Eddaoudi, M. *Angew. Chem. Int. Ed.* **2007**, *46*, 3278.

(116) Lock, N.; Wu, Y.; Christensen, M.; Cameron, L. J.; Peterson, V. K.; Bridgeman, A. J.; Kepert, C. J.; Iversen, B. B. *J. Phys. Chem. C* **2010**, *114*, 16181.

(117) Rodriguez-Carvajal, J. *Physica B.* **1990**, *192*, 55

(118) Kolokolov, D. I.; Jobic, H.; Stepanov, A. G.; Plazanet, M.; Zbiri, M.; Ollivier, J.; Guillerm, V.; Devic, T.; Serre, C.; Férey, G. *Eur. Phys. J.* **2010**, *189*, 263.

(119) Vold, R. L.; Hoatson, G. L. *J. Mag. Reson.* **2009**, *198*, 57.

(120) Torrisi, A.; Bell, R. G.; Mellot-Draznieks, C. *Cryst. Growth Des.* **2010**, *10*, 2839.

(121) Miller, S. R.; Wright, P. A.; Devic, T.; Serre, C.; Férey, G.; Llewellyn, P. L.; Denoyel, R.; Gaberova, L.; Filinchuk, Y. *Langmuir* **2009**, *25*, 3618.

(122) Deridder, D. J. A.; Schenk, H. *Acta Crystallogr., Sect. B. Struct. Sci.* **1995**, *51*, 221.

(123) Grabowski, S. J.; Krygowski, T. M. *Acta Crystallogr., Sect C: Ceyst. Struct. Commun.* **1985**, *41*, 1224.

(124) Férey, G.; Latroche, M.; Serre, C.; Millange, F.; Loiseau, T.; Percheron-Guégan, A. *Chem. Commun.* **2003**, 2976.

(125) Anokhina, E. V.; Vougo-Zanda, M.; Wang, X. Q.; Jacobson, A. J. *J. Am. Chem. Soc.* **2005**, *127*, 15000.

(126) Bourrelly, S.; Llewellyn, P. L.; Serre, C.; Millange, F.; Loiseau, T.; Férey, G. *J. Am. Chem. Soc.* **2005**, *127*, 13519.

(127) Millange, F.; Guillou, N.; Walton, R. I.; Grenèche, J. M.; Margiolaki, I.; Fereya, G. *Chem. Commun.* **2008**, 4732.

(128) Volkringer, C.; Loiseau, T.; Guillou, N.; Férey, G.; Elkaïm, E.; Vimont, A. *Dalton Trans.* **2009**, 2241.

(129) Serre, C.; Bourrelly, S.; Vimont, A.; Ramsahye, N. A.; Maurin, G.; Llewellyn, P. L.; Daturi, M.; Filinchuk, Y.; Leynaud, O.; Barnes, P.; Férey, G. *Adv. Mater.* **2007**, *19*, 2246.

(130) Coudert, F. X.; Jeffroy, M.; Fuchs, A. H.; Boutin, A.; Mellot-Draznieks, C. *J. Am. Chem. Soc.* **2008**, *130*, 14294.

(131) Ramsahye, N. A.; Maurin, G.; Bourrelly, S.; Llewellyn, P. L.; Serre, C.; Loiseau, T.; Devic, T.; Ferey, G. *J. Phys. Chem. C* **2008**, *112*, 514.

(132) Liu, Y.; Her, J. H.; Dailly, A.; Ramirez-Cuesta, A. J.; Neumann, D. A.; Brown, C. M. *J. Am. Chem. Soc.* **2008**, *130*, 11813.

(133) Vougo-Zanda, M.; Huang, J.; Anokhina, E.; Wang, X. Q.; Jacobson, A. J. *Inorg. Chem.* **2008**, *47*, 11535.

(134) Devic, T.; Horcajada, P.; Serre, C.; Salles, F.; Maurin, G.; Moulin, B.; Heurtaux, D.; Clet, G.; Vimont, A.; Grenèche, J. M.; Le Ouay, B.; Moreau, F.; Magnier, E.;

Filinchuk, Y.; Marrot, J.; Lavalley, J. C.; Daturi, M.; Férey, G. *J. Am. Chem. Soc.* **2010**, *132*, 1127.

Appendices: Attached CD

Appendix A: Crystallographic information files for the metal phosphonates

A1: ScAlMePO-α

A2: Lanthanide bisphosphonates

Appendix B: Crystallographic information files for the scandium carboxylates

B1: MIL-88(Sc)

B2: Sc_4PMA_3

B3: Sc_2BDC_3

B4: MIL-53(Sc)